

¹ Observation of the Higgs boson in the WW^*
² channel and search for Higgs boson pair
³ production in the $b\bar{b}b\bar{b}$ channel with the
⁴ ATLAS detector

⁵ A DISSERTATION PRESENTED
⁶ BY
⁷ TOMO LAZOVICH
⁸ TO
⁹ THE DEPARTMENT OF PHYSICS

¹⁰ IN PARTIAL FULFILLMENT OF THE REQUIREMENTS
¹¹ FOR THE DEGREE OF
¹² DOCTOR OF PHILOSOPHY
¹³ IN THE SUBJECT OF
¹⁴ PHYSICS

¹⁵ HARVARD UNIVERSITY
¹⁶ CAMBRIDGE, MASSACHUSETTS
¹⁷ MAY 2016

¹⁸ ©2016 – TOMO LAZOVICH

¹⁹ ALL RIGHTS RESERVED.

²⁰ **Observation of the Higgs boson in the WW^* channel and search
²¹ for Higgs boson pair production in the $b\bar{b}b\bar{b}$ channel with the
²² ATLAS detector**

²³ ABSTRACT

²⁴ This dissertation presents the observation and measurement of the Higgs boson in the $H \rightarrow WW^* \rightarrow$
²⁵ $\ell\nu\ell\nu$ channel at $\sqrt{s} = 7$ TeV and $\sqrt{s} = 8$ TeV and a search for Higgs pair production in the $HH \rightarrow$
²⁶ $b\bar{b}b\bar{b}$ channel at $\sqrt{s} = 13$ TeV with the ATLAS detector in pp collisions at the Large Hadron Collider.

²⁷ First, the discovery of a particle consistent with the Higgs boson in 4.8 fb^{-1} at $\sqrt{s} = 7$ TeV and
²⁸ 5.8 fb^{-1} at $\sqrt{s} = 8$ TeV is discussed. Then, the measurement of the Higgs boson signal strength
²⁹ and cross section in both the gluon fusion and vector boson fusion (VBF) production modes using
³⁰ 20.3 fb^{-1} of $\sqrt{s} = 8$ TeV data combined with 4.8 fb^{-1} of 7 TeV data is shown. The combined signal
³¹ strength is measured to be $\mu = 1.09^{+0.23}_{-0.21}$. The total observed significance of the $H \rightarrow WW^*$ process
³² is observed to be 6.1σ (with 5.8σ expected). Advanced methods for background reduction and estima-
³³ tion, particularly in same-flavor lepton final states, are shown. The VBF signal strength is measured to
³⁴ be $\mu_{\text{VBF}} = 1.27^{+0.53}_{-0.45}$ with an observed significance of 3.2σ (with 2.7σ expected). In the VBF chan-
³⁵ nel, a selection requirement based method, the precursor to the final multivariate technique used for the
³⁶ result, is detailed.

³⁷ Finally, a search for Higgs pair production in the $b\bar{b}b\bar{b}$ final state with 3.2 fb^{-1} at $\sqrt{s} = 13$ TeV is
³⁸ presented. A particular focus is placed on a tailored signal region for resonant production of Higgs pairs
³⁹ at high masses. No significant excesses are observed, and upper limits on cross sections are placed for
⁴⁰ spin-2 Randall Sundrum gravitons (RSG) and narrow spin-0 resonances. The cross section of $\sigma(pp \rightarrow$
⁴¹ $G_{\text{KK}}^* \rightarrow hh \rightarrow b\bar{b}b\bar{b})$ with $k/\bar{M}_{\text{Pl}} = 1$ is constrained to be less than 70 fb for masses in the range
⁴² $600 < m_{G_{\text{KK}}^*} < 3000$ GeV. The cross section upper limits for $\sigma(pp \rightarrow H \rightarrow hh \rightarrow b\bar{b}b\bar{b})$ ranges
⁴³ from 30 to 300 fb in the mass range of $500 < m_H < 3000$ GeV.

Contents

44

45	o INTRODUCTION	I
46	I Theoretical and Experimental Background	5
47	I THE PHYSICS OF THE HIGGS BOSON	6
48	1.1 The Standard Model of Particle Physics	6
49	1.2 Electroweak Symmetry Breaking and the Higgs	8
50	1.3 Higgs Boson Production and Decay	II
51	1.4 Higgs Pair Production in the Standard Model	16
52	1.5 Higgs Pair Production in Theories Beyond the Standard Model	17
53	1.6 Conclusion	22
54	2 THE ATLAS DETECTOR AND THE LARGE HADRON COLLIDER	23
55	2.1 The Large Hadron Collider	24
56	2.2 The ATLAS Detector	26
57	2.3 The ATLAS Muon New Small Wheel Upgrade	37
58	2.4 Object Reconstruction in ATLAS	42
59	II Observation and measurement of Higgs boson decays to WW^* in LHC	
60	Run 1 at $\sqrt{s} = 7$ and 8 TeV	52
61	3 $H \rightarrow WW^* \rightarrow \ell\nu\ell\nu$ ANALYSIS STRATEGY	53
62	3.1 Introduction	53
63	3.2 The $H \rightarrow WW^* \rightarrow \ell\nu\ell\nu$ signal in ATLAS	54
64	3.3 Background processes	55
65	3.4 Shared signal region selection requirements	59
66	3.5 Background reduction in same-flavor final states	62
67	3.6 Parameters of interest and statistical treatment	68
68	4 THE DISCOVERY OF THE HIGGS BOSON AND THE ROLE OF THE $H \rightarrow WW^* \rightarrow \ell\nu\ell\nu$ CHANNEL	
69	4.1 Introduction	73

71	4.2	Data and simulation samples	74
72	4.3	$H \rightarrow WW \rightarrow e\nu\mu\nu$ search	74
73	4.4	$H \rightarrow \gamma\gamma$ search	80
74	4.5	$H \rightarrow ZZ \rightarrow 4\ell$ search	80
75	4.6	Combined results	82
76	4.7	Conclusion	83
77	5	EVIDENCE FOR VECTOR BOSON FUSION PRODUCTION OF $H \rightarrow WW^* \rightarrow \ell\nu\ell\nu$	87
78	5.1	Introduction	87
79	5.2	Data and simulation samples	88
80	5.3	Object selection	92
81	5.4	Analysis selection	96
82	5.5	Background estimation	104
83	5.6	Systematic uncertainties	116
84	5.7	Results	120
85	6	COMBINED RUN I $H \rightarrow WW^* \rightarrow \ell\nu\ell\nu$ RESULTS	125
86	6.1	Introduction	125
87	6.2	Results of dedicated gluon fusion $H \rightarrow WW^* \rightarrow \ell\nu\ell\nu$ analysis	126
88	6.3	Signal strength measurements in ggF and VBF production	129
89	6.4	Measurement of Higgs couplings to vector bosons and fermions	132
90	6.5	Higgs production cross section measurement	134
91	6.6	Conclusion	135
92	III	Search for Higgs pair production in the $HH \rightarrow b\bar{b}b\bar{b}$ channel in LHC	
93		Run 2 at $\sqrt{s} = 13$ TeV	137
94	7	SEARCH FOR HIGGS PAIR PRODUCTION IN BOOSTED $b\bar{b}b\bar{b}$ FINAL STATES	138
95	7.1	Introduction	138
96	7.2	Motivation	139
97	7.3	Data and simulation samples	141
98	7.4	Event reconstruction and object selection	143
99	7.5	Event selection	146
100	7.6	Data-driven background estimation	151
101	7.7	Systematic uncertainties	156
102	7.8	Results	159

103	8 COMBINED LIMITS FROM BOOSTED AND RESOLVED SEARCHES	162
104	8.1 Introduction	162
105	8.2 Resolved results	163
106	8.3 Statistical technique and results	163
107	8.4 Limit setting	164
108	IV Looking ahead	168
109	9 CONCLUSION	169
110	APPENDIX A <i>b</i>-TAGGING PERFORMANCE AT HIGH p_T	173
111	A.1 Changes in MV2 score at high p_T	173
112	A.2 Effect of multiple <i>b</i> -quarks inside one jet	175
113	A.3 Changes in track quality at high p_T	177
114	REFERENCES	180

Listing of figures

116	I.1	The particles of the Standard Model and their properties [6].	7
117	I.2	The four most common Higgs boson production modes at the LHC: (a) gluon-gluon fusion, (b) vector boson fusion, (c) $W/Z + H$ production, (d) $t\bar{t}H$ production	11
118	I.3	Higgs production cross sections as a function of center of mass energy (\sqrt{s}) at a pp collider [18].	12
119	I.4	Higgs boson branching ratios as a function of m_H [18].	15
120	I.5	The two leading diagrams for Standard Model di-Higgs production at the LHC: (a) box diagram, (b) Higgs self coupling.	16
121	I.6	Diagrams with new vertices for non-resonant Higgs pair production arising in composite Higgs models.	18
122	I.7	Generic Feynman diagram for resonant Higgs pair production in BSM theories.	18
123	I.8	Branching ratios for a spin-2 Randall-Sundrum graviton as a function of mass computed in MadGraph with the CP3-Origins implementation [34, 40, 41].	19
124	I.9	$\sigma \times \text{BR}(HH)$ for Randall-Sundrum gravitons as a function of mass computed in MadGraph with the CP3-Origins implementation [34, 40, 41].	20
125	I.10	Randall-Sundrum graviton width as a function of mass computed in MadGraph with the CP3-Origins implementation [34, 40, 41]	21
126	I.11	Branching ratios for heavy Higgs H in Type I (left) and Type II (right) 2HDM models with $\tan \beta = 1.5$ and $\cos(\beta - \alpha) = 0.1(0.01)$ for Type I (Type II) [38].	22
127	2.1	A schematic view of the LHC ring [48]. Four main experiments are located at interaction points along the ring. ATLAS and CMS are general purpose experiments, while ALICE is dedicated to heavy ion collisions and LHCb is dedicated to studying B physics.	24
128	2.2	A full diagram of the ATLAS detector [44].	27
129	2.3	The ATLAS coordinate system. The z direction corresponds to the beam axis, while x and y define the transverse plane. θ is the angle relative to the beam axis and ϕ is the azimuthal angle. η , the pseudorapidity, approaches infinity at small angles relative to the beam axis. .	28
130	2.4	Layout of the ATLAS Inner Detector system [52].	29
131	2.5	Layout of the ATLAS calorimeter system [44].	31
132	2.6	Layout of the ATLAS muon system [44].	33
133	2.7	Predicted field integral as a function of $ \eta $ for the ATLAS magnet system [44].	35

146	2.8	ATLAS trigger rates for Level-1 triggers as a function of instantaneous luminosity in 2012	
147		and 2015 operation. These are single object triggers for electromagnetic clusters (EM),	
148		muons (MU), jets (J), missing energy (XE), and τ leptons (TAU). The threshold of the	
149		trigger is given in the name in GeV [54].	36
150	2.9	Instantaneous luminosity as a function of time for data recorded by ATLAS at different	
151		center of mass energies [55, 56].	38
152	2.10	MDT tube hit (solid) and segment (dashed) efficiency as a function of hit rate per tube [57].	39
153	2.11	Trigger rate as a function of p_T threshold with and without the NSW upgrade [57].	40
154	2.12	Illustrations of the geometry (left) and operating principle (right) of the micromegas de-	
155		tector [57]. When a muon passes through the drift gap and ionizes the gas, the timing and	
156		position of signals on the readout strips can be used to reconstruct the angle of traversal. .	41
157	2.13	Geometry of the sTGC detector [57]. The wire plane acts as the anode, while carbon cath-	
158		odes are capacitively coupled to pickup strips and pads.	41
159	2.14	Illustration of particle interactions in ATLAS [60].	43
160	2.15	Electron performance: (a) reconstruction efficiency as a function of electron E_T [62] (b)	
161		energy resolution in simulation as a function of $ \eta $ for different energy electrons [63]. .	44
162	2.16	Muon performance in $\sqrt{s} = 8$ TeV data: (a) reconstruction efficiency as a function of	
163		muon p_T (b) dimuon mass resolution as a function of average p_T [64].	46
164	2.17	Jet energy response after calibration as a function of true p_T in simulation. The calibra-	
165		tions applied are derived for use in Run 2 data and simulation by ATLAS [69].	47
166	2.18	Summary of the inputs to the MV2 b -tagging algorithm.	48
167	2.19	Light jet rejection (1/efficiency) vs. b -jet efficiency for MV1 and its input algorithms (a) [70]	
168		and MV2 (b) [71] in simulated $t\bar{t}$ events. The numbers in the algorithm names in (b) refer	
169		to the fraction of charm events used in the MV2 training.	49
170	2.20	Resolution of E_T^{miss} components as a function of $\sum E_T$ before pileup suppression with	
171		different pileup techniques [73].	51
172	3.1	Branching ratios for a WW system. q refers to quarks. ℓ can be either an electron or muon,	
173		and the leptonic branching ratios of the τ are included. For example, the $\ell\nu qq$ final state	
174		includes one W decaying to $e\nu$, $\mu\nu$, or $\tau\nu$. τ_h refer to hadronic decays of the τ	55
175	3.2	An illustration of the unique analysis signal regions [74]. The analysis is split by jet mul-	
176		tiplicity and lepton flavor after pre-selection requirements. The most sensitive regions for	
177		both gluon fusion and vector boson fusion production are underlined.	56
178	3.3	Feynman diagram for Standard Model WW production	56
179	3.4	Feynman diagrams for top pair production (left) and Wt production (right).	57
180	3.5	An example Feynman diagram of $W + \text{jets}$ production.	58
181	3.6	An example Feynman diagram of $Z + \text{jets}$ production.	58

182	3.7	A graphical illustration of the $E_{\text{T},\text{rel}}^{\text{miss}}$ calculation. The black arrows represent the directions 183 of the two leptons in the transverse plane. The dotted red arrow represents $E_{\text{T}}^{\text{miss}}$, while 184 the solid red arrow is the resulting $E_{\text{T},\text{rel}}^{\text{miss}}$ after projecting away from lepton 1.	60
185	3.8	Predicted backgrounds (compared with data) as a function of the number of jets, n_j (a 186 and b), and the number of b -tagged jets, n_b (c), after pre-selection requirements. Panel a 187 shows n_j in the same flavor sample, while panels b and c show the n_j and n_b distributions 188 in the different flavor sample.	61
189	3.9	A cartoon of the WW final state. Momenta are represented with thin arrows, spins with 190 thick arrows [74].	62
191	3.10	An event display of a $Z/\gamma^* + \text{jets}$ event illustrating the effect of pileup interactions.	63
192	3.11	The RMS of different missing transverse momentum definitions as a function of the av- 193 erage number of interactions per bunch crossing.	64
194	3.12	The difference between the true and reconstructed values of the missing transverse mo- 195 mentum in a gluon fusion signal sample using both track-based ($p_{\text{T}}^{\text{miss}}$) and calorimeter- 196 based $E_{\text{T}}^{\text{miss}}$ definitions [74]. $p_{\text{T}}^{\text{miss}}$ shows a significant improvement in resolution over 197 $E_{\text{T}}^{\text{miss}}$	65
198	3.13	Comparison of f_{recoil} distributions for $Z/\gamma^* + \text{jets}$, $H \rightarrow WW^*$, and other backgrounds 199 with real neutrinos.	67
200	3.14	Signal significance as a function of required value for f_{recoil} and $p_{\text{T},\text{rel}}^{\text{miss}(\text{trk})}$ in the ggF 201 $H \rightarrow WW^*$ with $n_j = 0$	67
202	3.15	The difference between the true and reconstructed values of m_{T} in a gluon fusion signal 203 sample using both track-based ($p_{\text{T}}^{\text{miss}}$) and calorimeter-based $E_{\text{T}}^{\text{miss}}$ definitions [74].	69
204	4.1	Jet multiplicity distribution in data and MC after applying lepton, jet, and $E_{\text{T},\text{rel}}^{\text{miss}}$ selec- 205 tions. The WW and top backgrounds have been normalized using control samples, and 206 the hashed band indicates the total uncertainty on the prediction [1].	76
207	4.2	Comparison of m_{T} between data and simulation in the $n_j = 0$ WW (a) and $n_j = 1$ top 208 (b) control samples [1].	78
209	4.3	m_{T} distribution in the $H \rightarrow WW \rightarrow e\nu\mu\nu$ $n_j \leq 1$ channels for 8 TeV data [1].	79
210	4.4	Diphoton mass spectrum in 7 and 8 TeV data. Panel a) shows the unweighted data dis- 211 tribution superimposed on the background fit, while panel c) shows the data where each 212 event category is weighted by its signal to background ratio. Panels b) and d) show the 213 respective distributions with background subtracted [1].	81
214	4.5	Four lepton invariant mass spectrum ($m_{4\ell}$) in 7 and 8 TeV data compared to background 215 estimate. A 125 GeV SM Higgs signal is shown in blue [1].	82

216	4.6 Local p_0 distribution as a function of hypothesized Higgs mass for the $H \rightarrow ZZ^* \rightarrow 4\ell$	
217	(a), $H \rightarrow \gamma\gamma$ (b), and $H \rightarrow WW^* \rightarrow \ell\nu\ell\nu$ (c) channels. Dashed curves show expected	
218	results, while solid curves show observed. Red curves are from 7 TeV data, blue curves	
219	from 8 TeV, and black curved combined [1].	84
220	4.7 Combined 95% CL limits (a), local p_0 values (b), and signal strength measurement (c) as a	
221	function of Higgs mass [1].	85
222	4.8 Comparison of measured signal strength μ for a 126 GeV Higgs in the 7 and 8 TeV datasets [1].	86
223	4.9 Two dimensional likelihood as a function of signal strength μ and Higgs mass m_H [1]. . .	86
224	5.1 A comparison of the subleading lepton p_T spectrum between VBF $H \rightarrow WW^*$ produc-	
225	tion and $t\bar{t}$ background.	89
226	5.2 Comparisons between data and Monte Carlo simulation for the calorimeter-based E_T^{miss}	
227	(left) and the track-based p_T^{miss} (right) in the same flavor VBF $H \rightarrow WW^*$ analysis chan-	
228	nels. Both distributions are shown after the pre-selection cuts on $m_{\ell\ell}$. The bottom panel	
229	shows the ratio between the data and the number of events expected from combining the	
230	signal and background. The hashed and orange bands include both statistical and system-	
231	atic uncertainties.	97
232	5.3 Comparisons between data and Monte Carlo simulation for the jet multiplicity n_j (left)	
233	and the number of b -tagged jets n_b (right) in the VBF $H \rightarrow WW^*$ analysis. n_j is shown	
234	after the pre-selection cuts on $m_{\ell\ell}$ and n_b is shown after the requirement that $n_j \geq 2$.	
235	The bottom panel shows the ratio between the data and the number of events expected	
236	from combining the signal and background. In the n_b distribution, the top background is	
237	normalized using the procedures described in section 5.5.2. The hashed and orange bands	
238	include both statistical and systematic uncertainties.	97
239	5.4 Leading jet η in VBF $H \rightarrow WW^*$ (red) and $t\bar{t}$ (black)	99
240	5.5 Distributions of (a) m_{jj} , (b) Δy_{jj} , (c) $C_{\ell 1}$, and (d) $\Sigma m_{\ell j}$, for the cut-based VBF analysis.	
241	The top panels compare simulation and data, while the bottom panels show normalized	
242	distributions for all background processes and signal for shape comparisons [74].	100
243	5.6 m_T distribution in simulation mapped to the three bins used in the final VBF cut-based	
244	analysis fit. The bin boundaries correspond 80 and 130 GeV. The solid black line cor-	
245	responds to the VBF Higgs signal and is overlaid on the backgrounds to allow for shape	
246	comparison. Hashed bands include both statistical and systematic uncertainties.	101
247	5.7 Event display of a VBF candidate event [74].	103
248	5.8 Higgs topology variables - $m_{\ell\ell}$ (top left), $\Delta\phi_{\ell\ell}$ (top right), and m_T (bottom) - used in	
249	the selection requirements of the cut-based signal region and as inputs to the BDT result.	
250	These are plotted after all of the BDT pre-training selection cuts [74]. The VBF Higgs	
251	signal cross section is multiplied by a factor of 50 to allow for shape comparisons.	106

252	5.9	VBF topology variables - m_{jj} (top left), Δy_{jj} (top right), $\sum C_\ell$ (bottom) - used in the selection requirements of the cut-based signal region and as inputs to the BDT result. These are plotted after all of the BDT pre-training selection cuts [74]. The VBF Higgs signal cross section is multiplied by a factor of 50 to allow for shape comparisons.	107
253			
254	5.10	Distributions of m_{jj} (a) and O_{BDT} (b) in the VBF $n_b = 1$ top CR [74].	109
255			
256	5.11	Comparison of m_{jj} shape in a same flavor $Z \rightarrow \ell\ell$ control region and the VBF cut-based signal region. The MC samples used for these distributions are given in table 5.4.	110
257			
258	5.12	General illustration of the ABCD region definitions for $Z/\gamma^* \rightarrow \ell\ell$ background estimation.	111
259			
260	5.13	Distribution of $m_{\text{T}2}$ in the WW validation region of the VBF analysis [74].	113
261			
262	5.14	Extrapolation factors for the $W + \text{jets}$ estimate derived for muons (a) and electrons (b) as a function of lepton p_{T} [74]. OC refers to the opposite charge $W + \text{jets}$ MC sample, while SC refers to the same charge $W + \text{jets}$ MC. The uncertainty bands have contributions from statistical uncertainty in the data and backgrounds to $Z + \text{jets}$ that are subtracted from the data, as well as systematic uncertainties due to variations in the extrapolation factor between the three MC samples shown.	115
263			
264	5.15	Background composition in final VBF signal region [74].	116
265			
266	5.16	Variations in the top background extrapolation factor in the cut-based analysis due to PDF uncertainties. The uncertainties are shown in the three bins of m_{T} used in the final cut-based statistical fit. Variations from the eigenvector of the nominal PDF, CT10, as well as the result from an alternate PDF (NNPDF10), are compared.	119
267			
268	5.17	Variations in the top background extrapolation factor in the cut-based analysis due to QCD scale uncertainties. The uncertainties are shown in the three bins of m_{T} used in the final cut-based statistical fit. Q_F is the QCD factorization scale, while Q_R is the QCD renormalization scale.	119
269			
270	5.18	Post-fit distributions in the cut-based VBF analysis. Panel (a) shows the one-dimensional m_{T} distribution, while (b) shows the data candidates split into the bins of m_{T} and m_{jj} used in the final fit [74].	123
271			
272	5.19	Postfit distributions in the BDT VBF analysis [74].	124
273			
274	5.20	Overlap between cut-based and BDT VBF signal region candidates in the m_{jj} - m_{T} plane. .	124
275			
276	6.1	Post-fit m_{T} distribution in the $n_j \leq 1$ regions for the same flavor ($ee/\mu\mu$) final states [74].	127
277			
278	6.2	Post-fit m_{T} distribution in the $n_j \leq 1$ regions [74].	129
279			
280	6.3	Best fit signal strength $\hat{\mu}$ as a function of hypothesized m_H [74].	130
281			
282	6.4	Local p_0 as a function of m_H [74].	131
283			
284	6.5	Likelihood as a function of $\mu_{\text{VBF}}/\mu_{\text{ggF}}$ [74].	132
285			
286	6.6	Two dimensional likelihood scan as a function of μ_{VBF} and μ_{ggF} [74].	133
287			
288	6.7	Likelihood scan as a function of κ_F and κ_V , the Higgs coupling scale factors [74].	134
289			
290	6.8	Comparison of signal strength measurements in different Higgs decay channels on ATLAS [108].	136
291			

289	7.1	Parton luminosity ratios as a function of resonance mass M_X for 13/8 TeV and 7/8 TeV [109].	139
290	7.2	Summary of HH branching ratios [110].	140
291	7.3	Minimum ΔR between B decay vertices for different RSG masses in a $G_{\text{KK}}^* \rightarrow HH \rightarrow 4b$ sample with $c = 1$.	141
292	7.4	Trigger efficiency for events passing all signal region selections as a function of mass in a $G_{\text{KK}}^* \rightarrow HH \rightarrow 4b$ sample with $c = 1$ [119]. In the trigger names, “j” refers to a jet or jets. “ht” refers to H_T , the scalar sum of transverse momenta in the event. “bloose” refers to a loose b -tagging requirement applied to the jet. “aor” refers to anti- k_T jets with $R = 1.0$. The numbers at the end of each trigger name are the thresholds on the given quantity in GeV.	143
293	7.5	Comparison of untrimmed and trimmed jet masses for large radius jets in a RSG sample with $m_{G_{\text{KK}}^*} = 1$ TeV. JES (JMS) refers to the standard jet energy (mass) scale calibration for ATLAS [69].	144
294	7.6	Efficiency of finding two b -jets from each Higgs in an RSG event using calorimeter jets with $R = 0.3$ and track jet radii of $R = [0.2, 0.3, 0.4]$ [123].	145
295	7.7	Illustration of the boosted selection requirements on Higgs candidates. Each large-radius calorimeter jet (Higgs candidate) must contain two track jets.	147
296	7.8	Estimated significance as a function of signal mass for RSG $c = 1$ models in the 3 b (a) and 4 b (b) regions for different b -tagging efficiency working points.	148
297	7.9	Acceptance \times efficiency as a function of mass for (a) RSG and (b) narrow heavy scalar signal models [126]. Each curve corresponds to one of the selection requirements used to define the signal region. The requirements are made sequentially in the order shown in the legend.	149
298	7.10	Efficiency of requiring 3 or 4 b -tagged track jets vs. RSG mass. The efficiency quoted is relative to the previous selection requirements (rather than an absolute efficiency).	150
299	7.11	MV2c20 b -tagging efficiency for each of the four track jets in the boosted 4 b selection as a function of RSG mass for $c = 1$ models.	151
300	7.12	M_J^{sublead} vs. M_J^{lead} in a 2 b -tag data sample. The signal region is defined by the inner black contour ($X_{hh} < 1.6$) and the sideband region is defined by the outer contour ($R_{hh} > 35.8$ GeV). The region between the black contours is the control region. The mass region which is enriched in $t\bar{t}$ background is also shown for illustration [126].	153
301	7.13	An illustration of the data-driven background estimation technique for the boosted analysis	154
302	7.14	Leading large-R jet mass in the 3 b (a) and 4 b (b) sideband regions. The multijet and $t\bar{t}$ backgrounds are estimated using the data-driven methods described in the text. Because their normalizations are derived in the sideband region, the total background normalization is constrained by default to match the normalization of the data [126].	155

325	7.15	Di-jet invariant mass (M_{2J}) in the 3 <i>b</i> (a) and 4 <i>b</i> (b) control regions. The multijet and $t\bar{t}$ backgrounds are estimated using the data-driven methods described in the text [126].	156
326			
327	7.16	Di-jet invariant mass (M_{2J}) in the 3 <i>b</i> (a) and 4 <i>b</i> (b) signal regions. The multijet and $t\bar{t}$ backgrounds are estimated using the data-driven methods described in the text. In the 3 <i>b</i> region, a graviton signal with $m_{G_{KK}^*} = 1.8$ TeV and $c = 1$ is overlaid, with the cross section multiplied by a factor of 50 so that the signal is visible. In the 4 <i>b</i> region, signals with $m_{G_{KK}^*} = 1.0$ TeV and $m_{G_{KK}^*} = 1.5$ TeV are overlaid, both with $c = 1$ and the yields multiplied by factors of 2 and 5 respectively [126].	161
328			
329			
330			
331			
332			
333	8.1	Di-jet invariant mass (M_{2J}) in the resolved signal region. The expected signal from a graviton with $m_{G_{KK}^*} = 800$ GeV and $c = 1$ is overlaid. [126].	164
334			
335	8.2	Expected and observed upper limit as a function of mass for G_{KK}^* in the RSG model with (a) $c = 1$ and (b) $c = 2$, as well as (c) H with fixed $\Gamma_H = 1$ GeV, at the 95% confidence level in the CL_s method [126].	167
336			
337			
338	9.1	Combined ATLAS and CMS measurements in Run 1 for (a) Higgs signal strength in gluon fusion and VBF and (b) Higgs couplings normalized to their SM predictions	171
339			
340	9.2	Discovery significance for RSG models at the HL-LHC in three different budget scenarios [133]. Systematic uncertainties on the background prediction (σ_B) of 2.5% and 5.0% are both tested.	172
341			
342			
343	A.1	p_T of the leading track jet in the leading calorimeter jet for different signal masses in RSG $c = 1$ models.	174
344			
345	A.2	MV _{2c2o} score for the leading track jet (a) and subleading track jet (b) of the leading calorimeter jet for different signal masses in RSG $c = 1$ models.	174
346			
347	A.3	IP _{3D} log-likelihood ratio ($\log(p_b/p_u)$) of the leading track jet in the leading calorimeter jet for different signal masses in RSG $c = 1$ models.	175
348			
349	A.4	Mass (a) and number of tracks (b) for the secondary vertices computed with the SV1 algorithm. When no secondary vertex is found, the quantities are assigned to default negative values.	176
350			
351			
352	A.5	Mass (a) and number of tracks (b) for vertices computed with the JetFitter algorithm. When no vertices are found, the quantities are assigned to default negative values.	176
353			
354	A.6	MV _{2c2o} score (a) and SV1 mass (b) for leading track jets with two truth b quarks ($n_{tb,lead} = 2$) compared to those with only one truth b ($n_{tb,lead} = 1$).	177
355			
356	A.7	Track fit χ^2/n_{DOF} (a) and number of pixel detector hits (b) for the leading track of the leading track jet in different mass RSG $c = 1$ samples.	178
357			
358	A.8	Distance traveled (in the transverse plane) by B -hadrons before decay for different signal masses in RSG $c = 1$ models. Vertical lines denote where the IBL and first pixel layers begin.	179
359			
360			

361	A.9 MV _{2c2o} score (a) and SV1 mass (b) for leading track jets whose leading track jet has at least	
362	four pixel hits ($N_{\text{pix}} \geq 4$) compared to those which do not ($N_{\text{pix}} < 4$)	179

Listing of tables

363

364	1.1	Production cross sections for a 125 GeV Higgs boson at $\sqrt{s} = 8$ TeV with scale and PDF uncertainties [18].	13
365	1.2	Theoretical branching ratios for a 125 GeV Higgs boson, quoted as a percentage of the total width of the Higgs. Uncertainties shown are relative to the branching ratio value [18].	15
366	1.3	Possible channels for Higgs searches. Checkmarks denote the most sensitive production modes for each decay channel [5].	16
367	1.4	Production cross sections for pair production of a 125 GeV Higgs boson at $\sqrt{s} = 14$ TeV with total uncertainty [29]. The uncertainties include QCD scale and PDF variations as well as uncertainties on α_S	17
370	2.1	Evolution of LHC machine conditions [50, 51].	26
371	2.2	Performance requirements for the ATLAS detector [44].	37
372	2.3	Signal efficiencies for WH production with $H \rightarrow b\bar{b}$ and $H \rightarrow WW^* \rightarrow \mu\nu qq$ under different trigger configurations [57].	42
373	3.1	A summary of backgrounds to the $H \rightarrow WW^* \rightarrow \ell\nu\ell\nu$ signal.	59
377	4.1	Monte carlo generators used to model signal and background for the Higgs search [1].	74
378	4.2	Normalization factors (ratio of data and MC yields in a control sample) for the Standard Model WW and top backgrounds in the $H \rightarrow WW^* \rightarrow \ell\nu\ell\nu$ analysis [1]. Only statistical uncertainties are shown.	77
379	4.3	Data and expected yields for signal and background in the final $H \rightarrow WW^* \rightarrow \ell\nu\ell\nu$ signal region. Uncertainties shown are both statistical and systematic [1].	79
380	4.4	Summary of the expected and observed significance and measured signal strengths in the combined 7 and 8 TeV datasets for the Higgs discovery analysis [1].	82
381	5.1	Single lepton triggers used for electrons and muons in the $H \rightarrow WW^* \rightarrow \ell\nu\ell\nu$ analysis. A logical “or” of the triggers listed for each lepton type is taken. Units are in GeV, and the i denotes an isolation requirement in the trigger.	90
382	5.2	Di-lepton triggers used for different flavor combinations in the $H \rightarrow WW^* \rightarrow \ell\nu\ell\nu$ analysis. The two thresholds listed refer to leading and sub-leading leptons, respectively. The di-muon trigger only requires a single lepton at level-1.	90

392	5.3	Trigger efficiency for signal events and relative gain of adding a dilepton trigger on top of the single lepton trigger selection. The first lepton is the leading, while the second is the sub-leading. Efficiencies shown here are for the ggF signal in the $n_j = 0$ category but are comparable for the VBF signal.	90
393			
394			
395			
396	5.4	Monte Carlo samples used to model the signal and background processes [74]. The table lists the cross section for each process, taking into account the branching ratio for the process producing two leptons.	92
397			
398			
399	5.5	p_T dependent isolation requirements for muons. Muons are required to have their calorimeter based or track based cone sums be less than this fraction of their p_T	94
400			
401	5.6	p_T dependent requirements for electrons. Electrons are required to have their calorimeter based or track based cone sums be less than this fraction of their E_T	94
402			
403	5.7	Summary of event selection for the $n_j \geq 2$ VBF analysis in the 8 TeV cut-based analysis [74].	102
404			
405	5.8	Background composition after each requirement in the $n_j \geq 2$ VBF analysis in the 8 TeV cut-based analysis [74].	103
406			
407	5.9	Summary of selections for the cut-based and BDT signal regions. “Input” denotes variables used as input to the BDT algorithm. Definitions and explanations of the variables can be found in sections 5.4.2 and 5.4.3.	105
408			
409			
410	5.10	Top normalization factors computed at each stage of the cut-based selection. Uncertainties are statistical only.	108
411			
412	5.11	Top normalization factors computed for each bin of O_{BDT} . Uncertainties are statistical only.	108
413			
414	5.12	$Z/\gamma^* \rightarrow \tau\tau$ correction factors for the VBF cut-based analysis. Uncertainties are statistical only.	III
415			
416	5.13	$Z/\gamma^* \rightarrow \ell\ell$ normalization factors for cut-based and BDT analyses. Uncertainties are statistical only.	II2
417			
418	5.14	Theoretical systematic uncertainties for various processes in the cut-based VBF analysis, given in units of percent change in yield. Values are given for the low m_{jj} signal region. The systematic shown for the WW background is relevant only to WW diagrams where the final state jets are the result of QCD vertices.	II8
419			
420			
421			
422	5.15	Experimental systematic uncertainties (expressed as % of the estimated yield) for the VBF signal [74].	120
423			
424	5.16	Composition of the post-fit uncertainties (in %) on the total signal (N_{sig}), total background (N_{bkg}), and individual background yields in the VBF analysis [74]. “Stat.” refers to statistical uncertainties, “Expt.” refers to experimental systematic uncertainties, and “Theo.” refers to theoretical systematic uncertainties.	121
425			
426			
427			

428	5.17 Event selection for the VBF BDT analysis. The event yields in (a) are shown after the pre-selection and the additional requirements applied before the BDT classification (see text). 429 430 The event yields in (b) are given in bins in O_{BDT} after the classification [74].	122
431	6.1 Summary of post-fit yields in ggF dedicated signal regions for the $ee/\mu\mu$ final states [74].	126
432	6.2 Post-fit background composition in ggF dedicated signal regions for the $ee/\mu\mu$ final states [74]. 433	127
434	6.3 All signal regions definitions input into final statistical fit [74].	128
435	6.4 Post-fit yields in the both ggF and VBF dedicated signal regions with all lepton flavor final 436 states combined [74].	128
437	7.1 Summary of requirements on objects used in the $X \rightarrow HH \rightarrow b\bar{b}b\bar{b}$ search.	146
438	7.2 Effect of boosted selection on data, RSG signal models, $t\bar{t}$, and $Z + \text{jets}$. The numbers 439 from simulation are normalized with the MC generator cross section and do not take into 440 account the data driven estimates described in section 7.6 [127].	151
441	7.3 Mass region definitions used for background estimation.	152
442	7.4 Parameters derived for exponential fit to background M_{2J} shape in the 3b and 4b signal 443 regions [127].	155
444	7.5 The number of events in data and predicted background events in the boosted 3-tag and 445 4-tag sideband and control regions [126]. The uncertainties shown are statistical only.	157
446	7.6 Summary of systematic uncertainties in the total background and signal event yields (ex- 447 pressed in %) in the boosted 3-tag and 4-tag signal regions. Systematic uncertainties on 448 the signal normalization are shown for models with $m_{G_{KK}^*} = 1.5$ TeV and both $c = 1$ 449 and $c = 2$ as well as a narrow width heavy scalar.	159
450	7.7 Alternate fit functions used to model the M_{2J} distribution in the QCD multijet back- 451 ground. In the equations, $x = M_{2J}/\sqrt{s}$	160
452	7.8 Observed yields in the 3-tag and 4-tag signal regions for the boosted analysis compared to 453 the predicted number of background events Errors correspond to the total uncertainties 454 in the predicted event yields. The yields for a graviton with $m_{G_{KK}^*} = 1$ TeV and $c = 1$ 455 are also shown [126].	160
456	8.1 Observed yields in the resolved selection 4-tag signal region compared to the predicted 457 number of background events Errors correspond to the total uncertainties in the pre- 458 dicted event yields. The yields for a graviton with $m_{G_{KK}^*} = 800$ GeV and $c = 1$ are 459 also shown [126].	163

Acknowledgments

462 I have been a member of the Harvard ATLAS group for many years now, first as an undergraduate and
 463 then as a graduate student. As a result, I have had the privilege of interacting with many amazing people
 464 there over the years and have accumulated a large list of folks to thank.

465 First and foremost, I must thank the two people who have effectively been my academic parents since I
 466 started in the Harvard group: João Guimarães da Costa and Melissa Franklin. Melissa Franklin and João
 467 Guimarães da Costa. They have both been so important to both my academic and personal development
 468 that I can't even put one before the other. João has been an excellent PhD advisor, showing me how to
 469 look at the big picture and helping me navigate the sometimes complicated politics of ATLAS. He got me
 470 started on my first projects with ATLAS as a young college sophomore before there was even beam in the
 471 LHC (go cosmic ray muons!). He has also been a constant source of advice and support, even when we
 472 have been on different continents. Melissa gave me my start in HEP as a summer student on CDF and
 473 has been an unbelievable mentor throughout my time at Harvard. I still remember our weekly chalkboard
 474 particle physics lessons after that first summer. She also graciously took me on as a co-advisee after João
 475 moved on to his new position at IHEP. I am incredibly lucky to have had both of them as advisors.

476 Another mentor who was essential to my development as a graduate student is Paolo Giromini. His un-
 477 canny knowledge and intuition about detectors is unmatched and I am very grateful to have had the chance
 478 to work with him on the micromegas for the ATLAS New Small Wheel upgrade project. I owe essentially
 479 all my practical knowledge about detectors (and building things in general) to him. I also appreciated his
 480 unique sense of humor which made sometimes difficult tasks much easier to get through.

481 I am grateful to John Huth and Masahiro Morii for their helpful advice as the other professors in the
 482 Harvard ATLAS group as well. I especially thank John for helping me get started on the micromegas
 483 trigger project and being a great professor to TF particle physics for. Additionally I thank Howard Georgi
 484 for serving as my third committee member and offering me feedback throughout my graduate career.

485 I also owe enormous thanks to Hugh Skottowe, the postdoc that I worked most closely with in my early
486 years as a graduate student. He was always able to help me through complicated tasks in everything from
487 writing code to understanding difficult physics concepts. I particularly enjoyed walking down to his office
488 in Palfrey at random times and talking through whatever problem I was tackling on that day.

489 Alex Tuna, the second postdoc that I worked closely with at Harvard, deserves great thanks as well. He
490 helped me push through to the end of my graduate career and offered great advice along the way.

491 Being at Harvard, I have seen an incredible array of graduate students graduate before me: Ben Smith,
492 Verena Martinez Outschoorn, Srivas Prasad, Michael Kagan, Giovanni Zevi Della Porta, Laura Jeanty,
493 Kevin Mercurio, William Spearman, and Andy Yen. I want to thank them all for showing me what a good
494 physicist looks like and for patiently answering my questions and offering insightful advice about physics
495 and life.

496 Getting through graduate school would not have been possible without the support and friendship of
497 the other students in our group. Thanks to Emma Tolley for geeking out with me about cool comput-
498 ing stuff, going to taste delicious beers with me, and helping start the Palfrey tradition of Taco Tuesdays.
499 Thanks to Brian Clark for being a great friend and housing companion both in Kirkland House and in our
500 tiny summer apartment in Geneva (and thanks to his partner Allison Goff for the same reasons!). Thanks
501 to Siyuan Sun for giving me my first aikido lesson and always being there for great conversations, big and
502 small. Tony (Baojia) Tong deserves special recognition for working with me on the 4b analysis and putting
503 up with my sometimes strange requests (and giving me rides to the Val Thoiry Migros so I wouldn't have
504 to pay exorbitant Geneva grocery prices!). Stephen Chan is probably the only student in the group who
505 both understands my references to the Sopranos and makes some of his own. To the younger graduate
506 students - Karri Di Petrillo, Jennifer Roloff, Julia Gonski, and Ann Wang - I want to say thank you for
507 making the group a fun and lively place to be and giving all of us energy that the older graduate students
508 like myself can sometimes lack.

509 I'd like to thank Annie Wei and Gray Putnam, the two undergraduates I have worked with as a graduate
510 student. Their unbelievable intuition and quickness in picking up difficult particle physics concepts is
511 inspiring.

512 I would also like to thank all of the postdocs that I have interacted with in my time in the Harvard group:
513 Kevin Black, Alberto Belloni (who would always ask me “Do you have it?”...I can now say that I do!),
514 Shulamit Moed, Corrinne Mills, Geraldine Conti, David Lopez Mateos, Chris Rogan, Valerio Ippolito,
515 and Stefano Zambito.

516 There are many people on ATLAS who have helped me get to this point as well. In the *WW* group, I
517 have to thank Jonathan Long, Joana Machado Miguens, Ben Cerio, Philip Chang, Bonnie Chow, Richard
518 Polifka, Heberth Torres, Tae Min Hong, and Jennifer Hsu for being wonderful colleagues and making the
519 entire analysis run smoothly. In the *4b* group, I have to thank Qi Zeng, Tony Tong, Alex Tuna, Michael
520 Kagan, Max Bellomo, John Alison, and Patrick Bryant.

521 Kirkland House was my home for the last three years of graduate school and was an wonderful envi-
522 ronment and support system. I want to thank my fellow tutors, especially Brian Clark and Allison Goff
523 (again), Zach Abel, Kelly Bodwin, Alex Lupsasca, John and Pam Park, Luke and Erin Walczewski, and
524 Philip Gant for their friendship and support. I also want to thank Kate Drizos Cavell, Bob Butler, and the
525 Faculty Deans Tom and Verena Conley.

526 There are still a few friends that haven’t been covered yet and deserve great thanks. Jake Connors and
527 Meredith MacGregor have been absolutely wonderful friends and I thank them in particular for the many
528 home-cooked meals and great conversations we’ve had in their apartment. Nihar Shah has been my friend
529 and confidant since we were both wee freshmen in Harvard Yard. Gareth Kafka, though he sits on the
530 “neutrino” side of Palfrey House, has made days there more fun and has also been an enthusiastic partici-
531 pant in the Palfrey Taco Tuesdays.

532 Being at Harvard necessarily means having to navigate through bureaucracy at some point or another.
533 I thank Lisa Cacciabuado, Carol Davis, Jacob Barandes, Korin Watras, and Angela Allen for always having
534 open doors and being the most kind, helpful people in the Physics department.

535 I thank Venky Narayananuriti for putting on a great SPU course that I was proud to be a part of and
536 TF for. I’d also like to thank Jim Waldo for offering me much advice about working in Computer Science
537 and giving me a fun data project to be a part of in my free time.

538 I grew up in a very tight knit Serbian community on the south side of Chicago which helped make me

539 the person I am today. I would like to thank all of the people at St. Simeon Mirotochivi Serbian Orthodox
540 Church who have always been sources of enthusiasm and support in my life.

541 I would not be here without the unconditional love and constant support and encouragement of my
542 family. To my pokojni Deda Branko and Miloje, my pokojni Baba Milka, and my Baba Desa, I want to
543 say thank you for instilling in me at an early age the love of curiosity and storytelling that I have carried
544 throughout my life. To my sister Angelina, I want to say thank you for always loving me and being my
545 partner in crime throughout our childhoods. To my parents, Miroljub and Nada, Tata and Mama, I really
546 cannot express how grateful I am to you and how much I owe you. As I look back now I see how I am
547 a combination of both of your best qualities. Every day I am in situations where I better understand the
548 lessons you taught me and the sacrifices you made to make sure I got the best possible education. I love
549 you all.

550 Finally, I have to thank my soul mate, the one person in my life who understands me more than anyone
551 else, my fiancée Kelly Brock. You are my sounding board, my support system, my cheerleader (figuratively
552 and literally!), my best friend, my role model, and my everything. I would not have gotten through grad-
553 uate school without you and my life would not be the same without you. I cannot wait to start our new
554 lives together as the married doctors, tackling whatever comes our way with the same zeal with which we
555 tackled graduate school. I love you with all my heart and soul.

0

556

557

Introduction

558 The Higgs boson is often described as one of the cornerstones of particle physics. When the Standard
559 Model was first developed as a theory to describe the fundamental particles and forces of nature, physicists
560 were faced with a dilemma. The electroweak theory beautifully characterized both electromagnetism and
561 the weak force with a single underlying framework. However, the mass of the weak W and Z bosons
562 was puzzling given the fact that their electromagnetic counterpart, the photon, is massless. The Higgs
563 mechanism was developed as the leading theory for the origin of this electroweak symmetry breaking. It
564 predicted the existence of an additional spin-0 boson in the Standard Model, the Higgs boson. Generations
565 of collider experiments searched for this elusive particle. This dissertation presents research work on the
566 Higgs boson from its discovery to its use as a tool in the search for physics beyond the Standard Model
567 with the ATLAS detector at the Large Hadron Collider (LHC).

568 One of the first priorities for the LHC when it began colliding proton beams in 2010 was the search
569 for the Higgs boson. This search was initially tackled in the $H \rightarrow WW^* \rightarrow \ell\nu\ell\nu$ channel, followed by

570 the $H \rightarrow \gamma\gamma$ and $H \rightarrow ZZ^* \rightarrow 4\ell$ channels. Each channel has its own merits, but the WW^* mode is
571 particularly suited to searching over a wide range of masses. The $H \rightarrow WW^*$ branching ratio is large and it
572 is the primary decay channel above the $2m_W$ mass threshold. Despite the fact that the full Higgs invariant
573 mass cannot be reconstructed in the $H \rightarrow WW^* \rightarrow \ell\nu\ell\nu$ channel, its signal to background ratio makes
574 it ideal for measurement of Higgs properties such as the production cross section and couplings.

575 In 2012, the ATLAS and CMS experiments announced the discovery of a new particle consistent with
576 the Higgs boson [1, 2]. In ATLAS, this discovery was made with 4.8 fb^{-1} collected at $\sqrt{s} = 7 \text{ TeV}$
577 and 5.8 fb^{-1} at $\sqrt{s} = 8 \text{ TeV}$. This dissertation first presents the search for gluon fusion production
578 of the Higgs in the $H \rightarrow WW^* \rightarrow \ell\nu\ell\nu$ channel, which played an important role in this discovery.
579 Selection requirements which were optimized to maximize the discovery significance in this channel, as
580 well as background estimation procedures, are discussed.

581 After its discovery, interest in the Higgs shifted to focus on the measurement of its properties. As a result,
582 extensions of the initial discovery analysis in larger datasets had two main goals. Improvement of signal
583 to background ratio was important to allow for precision measurements. Also, searches for production
584 modes of the Higgs with lower cross sections than gluon fusion were a priority. The first such extension
585 presented in this dissertation is a tailored selection for $\ell\nu\ell\nu$ final states with same flavor leptons. Novel
586 variables for the reduction of the $Z+\text{jets}$ background that could remain robust under increasing LHC
587 instantaneous luminosities are shown. The second post-discovery result shown is the first evidence of
588 Vector Boson Fusion (VBF) production of the Higgs boson.

589 VBF production of the Higgs boson is particularly interesting in the $H \rightarrow WW^* \rightarrow \ell\nu\ell\nu$ final state.
590 In this combination of production and decay modes, the Higgs boson couples exclusively to vector bosons,
591 allowing for precise measurement of the Higgs- W coupling constant. However, it is challenging to observe
592 VBF Higgs production because its cross section at the LHC is an order of magnitude lower than gluon
593 fusion production. The large $H \rightarrow WW^*$ branching ratio thus presents another advantage over other
594 final states. Additionally, VBF production of the Higgs boson creates two forward jets in addition to the
595 Higgs, and these jets can be used to isolate VBF Higgs events from other production modes. The VBF
596 $H \rightarrow WW^* \rightarrow \ell\nu\ell\nu$ analysis first created a selection requirement based signal region using variables

597 constructed specifically for the VBF Higgs production topology. This “cut-based” analysis is presented
598 in detail in this dissertation. These VBF topology variables, once validated in the cut-based analysis, were
599 then input into a multivariate boosted decision tree discriminant to achieve the first evidence of VBF Higgs
600 production with the full 20.3 fb^{-1} of $\sqrt{s} = 8 \text{ TeV}$ data in ATLAS. Additionally, combining these results
601 with the dedicated gluon fusion Higgs production analysis allowed for precise measurement of the Higgs
602 couplings.

603 After a two year shutdown, the LHC restarted in 2015 with a center of mass energy of $\sqrt{s} = 13 \text{ TeV}$.
604 This increase improved the LHC’s ability to probe for physics beyond the Standard Model, and the Higgs
605 sector remained one of the largest regions of unprobed phase space where such new physics could be dis-
606 covered. Production of high mass resonances benefit most from the center of mass energy increase. In
607 particular, the cross section for a generic gluon-initiated 2 TeV resonance increased tenfold with the in-
608 crease from 8 to 13 TeV. Therefore, a natural next step in studies of the Higgs was a search for a new
609 heavy resonance which decays into a pair of Higgs bosons. The final result shown in this dissertation is
610 a search for resonant di-Higgs production in the $X \rightarrow HH \rightarrow b\bar{b}b\bar{b}$ final state with 3.2 fb^{-1} recorded
611 by ATLAS at $\sqrt{s} = 13 \text{ TeV}$. This search has the unique advantage that it can both probe new physics
612 and gain further understanding of the Higgs potential through constraints on SM pair production of the
613 Higgs. It also extends the previous ATLAS results at $\sqrt{s} = 8 \text{ TeV}$ and probes higher mass resonances
614 that were not previously accessible. Additionally, it is an informative precursor to di-Higgs analyses at the
615 future High Luminosity LHC (HL-LHC), where a projected dataset of 3000 fb^{-1} at $\sqrt{s} = 14 \text{ TeV}$ will
616 begin to become sensitive to the SM Higgs self coupling.

617 As mentioned above, this dissertation begins by discussing the discovery of the Higgs and the role of
618 the $H \rightarrow WW^* \rightarrow \ell\nu\ell\nu$ channel. It then presents the first evidence for the VBF production mode using
619 the $H \rightarrow WW^* \rightarrow \ell\nu\ell\nu$ channel with the full ATLAS Run 1 dataset. It also shows the final combined
620 Run 1 measurements of gluon fusion Higgs production from this channel. Finally, it presents a search for
621 Higgs pair production in the $HH \rightarrow b\bar{b}b\bar{b}$ channel. It is organized into four parts.

622 Part 1 presents the theoretical and experimental background required for the subsequent parts. Chap-
623 ter 1 gives an overview of Higgs physics, particularly single and double Higgs production in the Standard

624 Model and beyond. Chapter 2 presents details regarding the Large Hadron Collider and the ATLAS experi-
625 ment. The evolution of machine conditions, descriptions of the ATLAS sub-detectors, and an overview of
626 object reconstruction in ATLAS are all shown. A brief interlude on the ATLAS Muon New Small Wheel
627 upgrade is also given, as this upgrade has been a focus of my graduate work and will have an important
628 impact on ATLAS' ability to study the Higgs at the High Luminosity LHC.

629 Part 2 discusses the observation and measurement of the Higgs in the $H \rightarrow WW^* \rightarrow \ell\nu\ell\nu$ channel
630 in the ATLAS Run 1 dataset at $\sqrt{s} = 7$ and 8 TeV. Because I worked in this channel from before the
631 discovery through to the final analysis of the Run 1 dataset, Part 2 is organized in such a way to allow
632 easy presentation of multiple analyses on different subsets of the full Run 1 dataset. Chapter 3 presents
633 a general overview of the $H \rightarrow WW^*$ analysis strategy and defines many of the variables and common
634 elements used in the rest of Part 2. Chapter 4 presents the discovery and subsequent measurements of
635 the Higgs boson, focusing on the role of the WW^* channel in this discovery. Chapter 5 presents the
636 first evidence for the VBF production mode of the Higgs, a result from the WW^* channel in the full
637 Run 1 ATLAS dataset. In this chapter, the focus is mainly on the cut-based VBF analysis. The cut-based
638 analysis was an important first step to the final VBF result which used a boosted decision tree. Where
639 appropriate, connections between the cut-based and BDT analyses are shown and their compatibility is
640 discussed. Finally, the VBF analysis was an important input into the combined Run 1 $H \rightarrow WW^* \rightarrow$
641 $\ell\nu\ell\nu$ result, which used both the gluon fusion and VBF channels in a combined fit to infer properties of
642 the Higgs, including its couplings to the gauge bosons and its production cross section. This is the topic
643 of Chapter 6.

644 Part 3 presents a search for Higgs pair production in the $HH \rightarrow b\bar{b}b\bar{b}$ channel. Chapter 7 presents
645 an overview of this search in the boosted regime, where the Higgs pairs are the result of the decay of a
646 heavy resonance. Chapter 8 shows the combined results between the boosted regime and the resolved
647 regime, which is sensitive to lower mass resonances and non-resonant Higgs pair production. Finally, Part
648 4 presents a conclusion and brief outlook of future Higgs physics with ATLAS.

649

Part I

650

Theoretical and Experimental Background

In modern physics, there is no such thing as “nothing.”

Richard Morris

1

651

652

The Physics of the Higgs Boson

653 This chapter presents an overview of the Standard Model of Particle Physics and in particular the physics
654 of the Higgs boson. First, a brief overview of the Standard Model is presented. Then, a description of
655 the Higgs mechanism of electroweak symmetry breaking is given. Next, the physics of single Higgs boson
656 production and decay is described. The Standard Model also allows for production of two Higgs bosons
657 and this is detailed as well. Finally, di-Higgs production in two beyond the Standard Model (BSM) theories
658 - Randall-Sundrum gravitons (RSG) and Two Higgs Doublet Models (2HDM) - is shown.

659 **I.I THE STANDARD MODEL OF PARTICLE PHYSICS**

660 The Standard Model (SM) of Particle Physics is a quantum field theory describing the fundamental parti-
661 cles of nature and the forces that govern their interactions. Several comprehensive pedagogical treatments
662 of the SM already exist in the literature [3–8] and this section will not rehash those. Rather, this section
663 presents a brief overview of the SM particles and forces in order to define them for subsequent discussions.

664 The Standard Model consists of two primary categories of fundamental particles: fermions (spin 1/2
 665 particles) and bosons (integer spin particles). The SM also describes three forces: electromagnetism, the
 666 weak nuclear force, and the strong nuclear force. Gravity is not included in the theory and is largely irrel-
 667 evant at the scales currently probed by collider experiments. Within the fermions, there are both quarks
 668 (which interact via all three forces) and leptons. The charged leptons interact via electromagnetic and weak
 669 interactions, while neutrinos (neutral leptons) interact only via the weak force. Within the bosons, there
 670 are the W^\pm and Z bosons (the mediators of the weak force), the gluon (g , the mediator of the strong
 671 force), and the photon (γ , the mediator of the electromagnetic force). Finally, there is the Higgs boson,
 672 a fundamental spin zero particle resulting from the Higgs mechanism of electroweak symmetry breaking.
 673 Figure 1.1 summarizes the fermions and bosons of the SM.

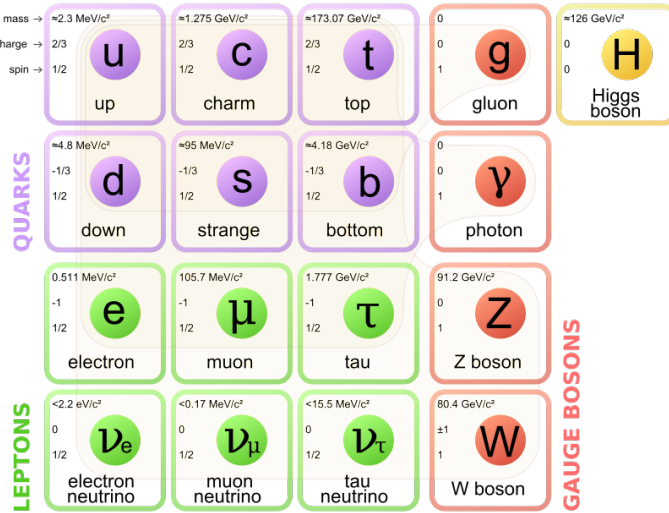


Figure 1.1: The particles of the Standard Model and their properties [6].

674 The Standard Model coalesced into a unified theoretical framework in the 1960s through the work
 675 of Glashow, Weinberg, Salam, and others on the theory of electroweak interactions [9–12]. This theory
 676 characterized both the electromagnetic and weak interactions as unified under a single gauge symmetry
 677 group, namely $SU(2) \times U(1)$. At low enough energy scales (on the order of the W and Z masses), the
 678 electroweak symmetry is broken, as evidenced by the fact that the weak bosons have mass while the photon
 679 does not. The discovery of the Higgs boson in 2012 confirmed the Higgs mechanism as the most likely
 680 candidate for this electroweak symmetry breaking [1, 2]. The complete SM consists of this electroweak

681 theory combined with the theory of quantum chromodynamics (which models the strong sector as a non-
 682 Abelian $SU(3)$ gauge group)¹.

683 **I.2 ELECTROWEAK SYMMETRY BREAKING AND THE HIGGS**

684 In the Standard Model Lagrangian, it is difficult to include mass terms for the W and Z bosons without
 685 breaking the fundamental gauge symmetry of the Lagrangian. A traditional mass term does not preserve
 686 the $SU(2) \times U(1)$ symmetry. Additionally, scattering of massive W and Z bosons violate unitarity and
 687 these diagrams diverge at high energy scales. In the 1960s, Higgs, Brout, Englert, Guralnik, Kibble, and
 688 Hagen developed a mechanism for spontaneous symmetry breaking via the addition of a complex scalar
 689 doublet to the SM. Three of the four real degrees of freedom of this complex field would go to the lon-
 690 gitudinal modes of the W^\pm and Z , thus allowing them to have mass [14–17]. The remaining degree of
 691 freedom would manifest as an additional scalar, known now as the Higgs boson.

692 The mechanism works by introducing a Lagrangian for the newly introduced field that still respects the
 693 symmetry of the Standard Model inherently, but with a minimum at a non-zero vacuum expectation value
 694 for the field. In this minimum of the potential, the electroweak symmetry is broken. Specifically, consider
 695 a complex scalar doublet Φ with four degrees of freedom, as shown in equation I.1.

$$\Phi = \begin{pmatrix} \phi^+ \\ \phi^0 \end{pmatrix} = \frac{1}{\sqrt{2}} \begin{pmatrix} \phi_1^+ + i\phi_2^+ \\ \phi_1^0 + i\phi_2^0 \end{pmatrix} \quad (\text{I.1})$$

696 The simplest potential of a self-interacting Higgs that still respects the SM symmetry is given in equa-
 697 tion I.2.

$$V(\Phi) = \mu^2 \Phi^\dagger \Phi + \lambda (\Phi^\dagger \Phi)^2 \quad (\text{I.2})$$

698 If the μ^2 term of this potential is positive, then the potential has a minimum at $\Phi = 0$ and the electroweak

¹For a pedagogical treatment of the physics of quantum chromodynamics, see reference [13].

⁶⁹⁹ symmetry is preserved. However, if instead $\mu^2 < 0$, then the minimum is at a finite value of Φ , namely

$$\Phi_{\min} = \frac{1}{\sqrt{2}} \begin{pmatrix} 0 \\ v \end{pmatrix} \quad (1.3)$$

⁷⁰⁰ where $v = \sqrt{\mu^2/\lambda}$. Because this is the location of the minimum, it corresponds to the vacuum expecta-
⁷⁰¹ tion value for the field ($\langle \Phi \rangle = \Phi_{\min}$). The excitations of the Higgs can then be parameterized as

$$\Phi = \frac{1}{\sqrt{2}} \begin{pmatrix} 0 \\ v + H \end{pmatrix} \quad (1.4)$$

⁷⁰² The full scalar Lagrangian, including the kinetic term, is then given as

$$\mathcal{L}_s = (D^\mu \Phi)^\dagger (D_\mu \Phi) - V(\Phi) \quad (1.5)$$

⁷⁰³ where the covariant derivative is defined as

$$D_\mu = \partial_\mu + \frac{ig}{2} \tau^a W_\mu^a + ig' Y B_\mu \quad (1.6)$$

⁷⁰⁴ and W^1, W^2, W^3 and B are the $SU(2)$ and $U(1)$ gauge fields of the electroweak theory, respectively. g
⁷⁰⁵ and g' are the corresponding coupling constants. The Pauli matrices are represented with τ . With the
⁷⁰⁶ scalar Lagrangian in place, the physical gauge fields can then be written as

$$W_\mu^\pm = \frac{1}{\sqrt{2}} (W_\mu^1 \mp i W_\mu^2) \quad (1.7)$$

⁷⁰⁷

$$Z_\mu = \frac{-g' B_\mu + g W_\mu^3}{\sqrt{g^2 + g'^2}} \quad (1.8)$$

⁷⁰⁸

$$A_\mu = \frac{g B_\mu + g' W_\mu^3}{\sqrt{g^2 + g'^2}} \quad (1.9)$$

⁷⁰⁹ Equation 1.7 corresponds to the charged W^+ and W^- bosons, equation 1.8 corresponds to the neutral Z
⁷¹⁰ boson, and equation 1.9 corresponds to the neutral photon. The masses of the particles also arise from the
⁷¹¹ Lagrangian. The photon has zero mass, while the masses of the W and Z bosons are given in equation 1.10.

⁷¹²

$$\begin{aligned} M_W^2 &= \frac{1}{4}g^2v^2 \\ M_Z^2 &= \frac{1}{4}(g^2 + g'^2)v^2 \end{aligned} \quad (1.10)$$

⁷¹³ The fermion masses also arise through a coupling with the Higgs via the Yukawa interaction (for a detailed
⁷¹⁴ description, see [8]). In this case the coupling between the Higgs and the fermions goes as

$$g_{hf\bar{f}} = \frac{m_f}{v} \quad (1.11)$$

⁷¹⁵ The full Lagrangian of Higgs interactions can be written as

$$\mathcal{L}_{\text{Higgs}} = -g_{hf\bar{f}}\bar{f}fh + \frac{g_{hhh}}{6}h^3 + \frac{g_{hhhh}}{24}h^4 + \delta_V V_\mu V^\mu \left(g_{hVV}H + \frac{g_{hhVV}}{2}h^2 \right) \quad (1.12)$$

⁷¹⁶ with

$$\begin{aligned} g_{hVV} &= \frac{2m_V^2}{v} & g_{hhVV} &= \frac{2m_V^2}{v^2} \\ g_{hhh} &= \frac{3m_h^2}{v} & g_{hhHH} &= \frac{3m_h^2}{v^2} \end{aligned} \quad (1.13)$$

⁷¹⁷ The last term of the Lagrangian appears twice, once for W bosons and once for Z bosons. V refers to
⁷¹⁸ the W^\pm and Z , and $\delta_W = 1$ while $\delta_Z = 1/2$. Phenomenologically, there are a few features of this
⁷¹⁹ Lagrangian that are useful to note. First, note that the Higgs mass is a free parameter of the theory that
⁷²⁰ must be determined experimentally. Second, note that the coupling of the Higgs to the vector bosons and
⁷²¹ fermions scales as a function of the masses of these particles, a fact that is important when considering
⁷²² both the production and decays of the Higgs. Finally, note the presence of the cubic and quartic Higgs self
⁷²³ interaction terms, which can lead to final states with multiple Higgs bosons produced.

724 1.3 HIGGS BOSON PRODUCTION AND DECAY

725 This section discusses the properties of Higgs production and decay mechanisms. The details presented
726 here will focus on the properties of a 125 GeV Higgs boson, as this is the mass closest to that of the newly
727 discovered Higgs.

728 1.3.1 HIGGS PRODUCTION

729 The Higgs is produced by four main production modes at the Large Hadron Collider - gluon-gluon fusion
730 (ggF), vector boson fusion (VBF), associated production with a W or Z boson, or associated production
731 with top quarks ($t\bar{t}H$). Figure 1.2 shows the Feynman diagrams for these four modes.

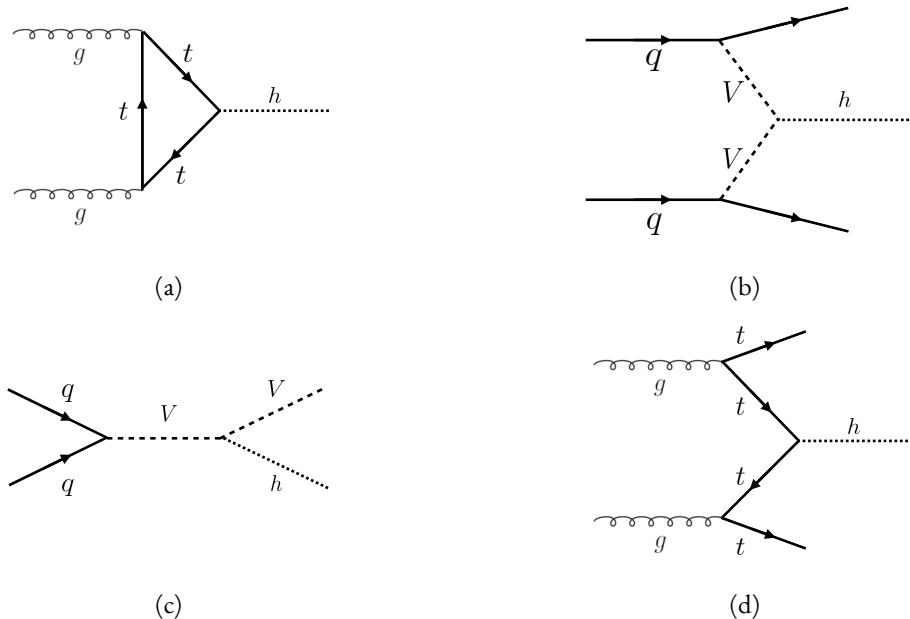


Figure 1.2: The four most common Higgs boson production modes at the LHC: (a) gluon-gluon fusion, (b) vector boson fusion, (c) $W/Z + H$ production, (d) $t\bar{t}H$ production

732 In gluon-gluon fusion, gluons from the incoming protons fuse via a top-quark loop to produce a Higgs.
733 The top quark is the dominant contribution in the loop due to its heavy mass and the fact that the Higgs-
734 fermion coupling constant scales with fermion mass. In vector boson fusion, the incoming quarks each
735 radiate a W or Z boson which fuse to produce the Higgs. This production mode results in a final state
736 with a Higgs boson and two additional jets which tend to be forward because they carry the longitudinal

737 momentum of the incoming partons. The Higgs can also be produced in association with a W or Z boson.
 738 The W/Z is produced normally and then radiates a Higgs². Finally, the Higgs can be produced in associa-
 739 tion with two top quarks. Each incoming gluon splits into a $t\bar{t}$ pair, and one of the top pairs combines to
 740 create a Higgs. Figure 1.3 shows the production cross section for a 125 GeV Higgs boson in each of these
 modes at a pp collider as a function of center of mass energy. In figure 1.3, note that gluon fusion has the

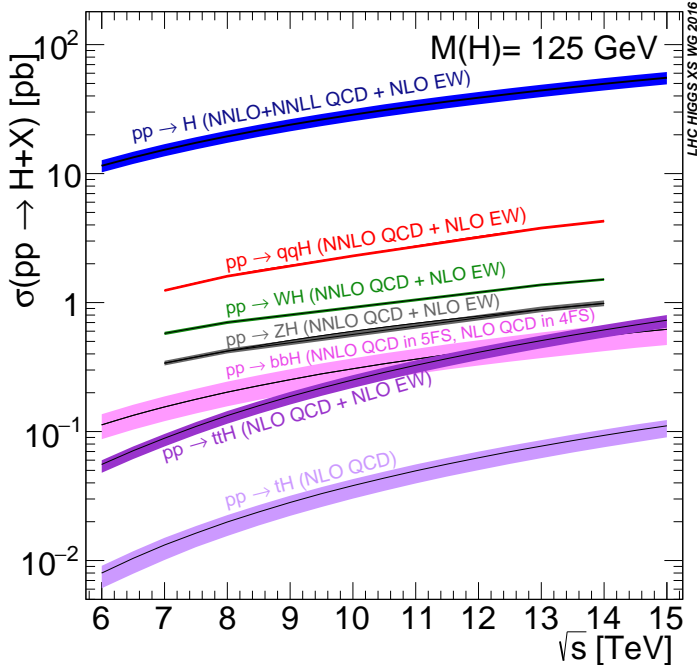


Figure 1.3: Higgs production cross sections as a function of center of mass energy (\sqrt{s}) at a pp collider [18].

741
 742 largest cross section, while VBF is the second largest at approximately a factor of 10 smaller. The figure also
 743 includes the less commonly studied $b\bar{b}H$ and tH modes. While the $b\bar{b}H$ mode has a larger cross section
 744 than $t\bar{t}H$, it also has larger backgrounds and is thus less sensitive. The tH mode is not as sensitive as $t\bar{t}H$
 745 due to its lower cross section. At $\sqrt{s} = 8$ TeV, ggF production of a 125 GeV Higgs has a cross section
 746 of $19.47^{+1.54}_{-1.67}$ pb, while VBF has a cross section of $1.601^{+0.036}_{-0.035}$ pb [18]. Both the gluon fusion and vector
 747 boson fusion cross sections have been computed to next-to-next-to-leading order (NNLO) in the QCD
 748 couplings and next-to-leading order in the electroweak couplings [19–26]. The gluon fusion cross section
 749 also includes next-to-next-to-leading logarithm (NNLL) resummation [27]. The cross sections of all of

²This mode is also sometimes known as “Higgs-strahlung”.

750 the main Higgs production modes at this center of mass energy, as well as their uncertainties from varying
 751 the QCD renormalization and factorization scales and PDFs, are summarized in table 1.1 for a 125 GeV
 752 Higgs. The relative uncertainty of the gluon fusion mode is larger than the relative uncertainty in the
 753 vector boson fusion mode due to the fact that gluon fusion production happens through a loop.

Production mode	σ (pb)	QCD scale uncert. (%)	PDF + α_s uncert. (%)
Gluon fusion	19.47	+7.3 / - 8.0	3.1
Vector boson fusion	1.601	+0.3 / - 0.2	2.2
WH	0.7026	+0.6 / - 0.9	2.0
ZH	0.4208	+2.9 / - 2.4	1.7
$b\bar{b}H$	0.2021	+20.7 / - 22.3	
$t\bar{t}H$	0.1330	+4.1 / - 9.2	4.3
tH (t -channel)	0.01869	+7.3 / - 16.5	4.6
tH (s -channel)	1.214×10^{-3}	+2.8 / - 2.4	2.8

Table 1.1: Production cross sections for a 125 GeV Higgs boson at $\sqrt{s} = 8$ TeV with scale and PDF uncertainties [18].

754 1.3.2 HIGGS BRANCHING RATIOS

755 The fact that the Higgs couples more strongly to more massive particles is crucial for understanding its
 756 branching ratios. The width for Higgs decays to fermions is given by equation 1.14 [5].

$$\Gamma(H \rightarrow f\bar{f}) = \frac{N_c \sqrt{2} G_F m_f^2 m_H}{8\pi} \quad (1.14)$$

757 In this case, N_c is the number of colors, G_F is the Fermi constant, m_f is the mass of the fermion, and
 758 m_H is the mass of the Higgs. Note that the width scales with the square of the fermion mass. (This also
 759 assumes that the Higgs mass is large enough to decay with both the fermions on shell.)

760 The decay width to WW , in the case where both W bosons are produced on shell ($m_H \geq 2m_W$), is
 761 given in equation 1.15 [5].

$$\Gamma(H \rightarrow W^+ W^-) = \frac{\sqrt{2} G_F M_W^2 m_H}{16\pi} \frac{\sqrt{1-x_W}}{x_W} (3x_W^2 - 4x_W + 4) \quad (1.15)$$

762 where m_W is the mass of the W and $x_W = 4M_W^2/m_H^2$. To get the branching ratio to ZZ (in the regime
 763 where $m_H \geq 2m_Z$), the equation is divided by 2 to account for identical particles in the final state, and
 764 x_W is replaced with $x_Z = 4M_Z^2/m_H^2$. This is shown in equation 1.16 [5].

$$\Gamma(H \rightarrow ZZ) = \frac{\sqrt{2}G_F M_Z^2 m_H}{32\pi} \frac{\sqrt{1-x_Z}}{x_Z} (3x_Z^2 - 4x_Z + 4) \quad (1.16)$$

765 The more general formula for Higgs branching into WW or ZZ , taking into account the case where one
 766 or both vector bosons is off-shell, is shown in equation 1.17 [28].

$$\Gamma(H \rightarrow V^*V^*) = \frac{1}{\pi^2} \int_0^{M_H^2} \frac{dq_1^2 M_V \Gamma_V}{(q_1^2 - M_V^2)^2 + M_V^2 \Gamma_V^2} \int_0^{(M_H - q_1)^2} \frac{dq_2^2 M_V \Gamma_V}{(q_2^2 - M_V^2)^2 + M_V^2 \Gamma_V^2} \Gamma_0 \quad (1.17)$$

767 Here, q_1^2 and q_2^2 are the invariant masses of the virtual gauge bosons, M_V is the W or Z mass, and Γ_V is
 768 the W or Z width. Γ_0 is the squared matrix element, which is given in equation 1.18 [28].

$$\Gamma_0 = \frac{G_F M_H^3}{8\sqrt{2}\pi} \delta_V \sqrt{\lambda(q_1^2, q_2^2, M_H^2)} \left[\lambda(q_1^2, q_2^2, M_H^2) + \frac{12q_1^2 q_2^2}{M_H^4} \right] \quad (1.18)$$

769 The function λ is defined as $\lambda(x, y, z) = (1 - x/z - y/z)^2 - 4xy/z^2$. The integral in the general
 770 off-shell boson case is much more difficult to interpret than the simpler on-shell branching ratios, but it
 771 can be evaluated numerically. These branching ratio formulas can also be visualized as a function of Higgs
 772 mass, as shown in figure 1.4. There are a few interesting features to note in this figure. First, note that at
 773 high Higgs masses, once on-shell production of both W and Z bosons is possible, these two decays are
 774 dominant due to the large masses of the W/Z . Also note that the branching ratio to W s is twice that of
 775 Z s at these large masses due to the fact that there are two charged W bosons (W^\pm) and only one Z boson³.
 776 At 125 GeV, the Higgs is accessible through many different decay modes. The largest branching ratio is
 777 the decay $H \rightarrow b\bar{b}$ at 58.24% [18]. This branching is larger than the WW/ZZ decays because one of
 778 the two bosons must be produced off-shell for $m_h = 125$ GeV. The second largest branching ratio is
 779 to WW^* at 21.37 % (before taking into account the branching ratios of the W). Table 1.2 summarizes

³In the Higgs Lagrangian, this extra symmetry factor is quantified by the δ_V noted in equation 1.12.

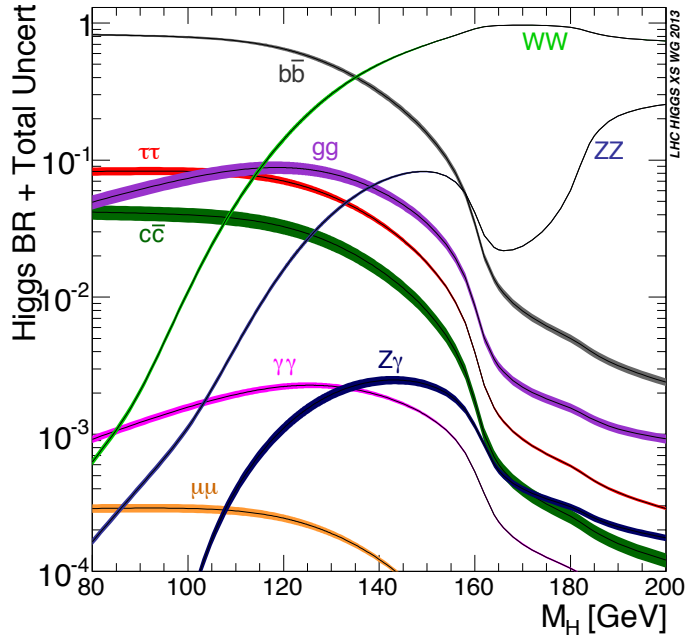


Figure 1.4: Higgs boson branching ratios as a function of m_H [18].

the theoretical branching ratios for a Higgs with a mass of 125 GeV. Note that there is a Higgs branching ratio to $\gamma\gamma$ even though photons are massless. This decay happens through a loop, which suppresses the branching ratio⁴.

Decay	Branching ratio (%)	Relative uncertainty (%)
bb	58.24	+0.25 / -0.25
WW^*	21.37	+0.99 / -0.99
gg	8.187	+3.40 / -3.41
$\tau\tau$	6.272	+1.17 / -1.16
cc	2.891	+1.20 / -1.20
ZZ^*	2.619	+0.99 / -0.99
$\gamma\gamma$	0.2270	+1.73 / -1.72
$Z\gamma$	0.1533	+5.71 / -5.71
$\mu\mu$	0.02176	+1.23 / -1.23

Table 1.2: Theoretical branching ratios for a 125 GeV Higgs boson, quoted as a percentage of the total width of the Higgs. Uncertainties shown are relative to the branching ratio value [18].

Note that the branching ratios alone do not tell the full story of which Higgs channels are the most

⁴The largest contributions to the loop are the top quark and W boson.

784 sensitive. For example, the $H \rightarrow b\bar{b}$ channel in gluon fusion production is incredibly difficult to observe
 785 due to the large QCD dijet background at the LHC. However, in associated production of the Higgs,
 786 where a W or Z gives additional final state particles that can be used to reduce background, a search for
 787 $H \rightarrow b\bar{b}$ can be sensitive. The combinations of production and decay modes that are most commonly
 788 studied at the LHC are summarized in table 1.3 [5].

Decay	Inclusive (incl. ggF)	VBF	WH/ZH	$t\bar{t}H$
$H \rightarrow \gamma\gamma$	✓	✓	✓	✓
$H \rightarrow b\bar{b}$			✓	✓
$H \rightarrow \tau^+\tau^-$		✓		
$H \rightarrow WW^* \rightarrow \ell\nu\ell\nu$	✓	✓	✓	
$H \rightarrow ZZ \rightarrow 4\ell$	✓			
$H \rightarrow Z\gamma \rightarrow \ell\ell\gamma$	very low			

Table 1.3: Possible channels for Higgs searches. Checkmarks denote the most sensitive production modes for each decay channel [5].

789 1.4 HIGGS PAIR PRODUCTION IN THE STANDARD MODEL

790 The Standard Model also allows for processes that produce two Higgs bosons in the final state, known
 791 as Higgs pair production or di-Higgs production. The two main production mechanisms are shown in
 figure 1.5. The two diagrams in figure 1.5 interfere destructively with one another, resulting in a low overall

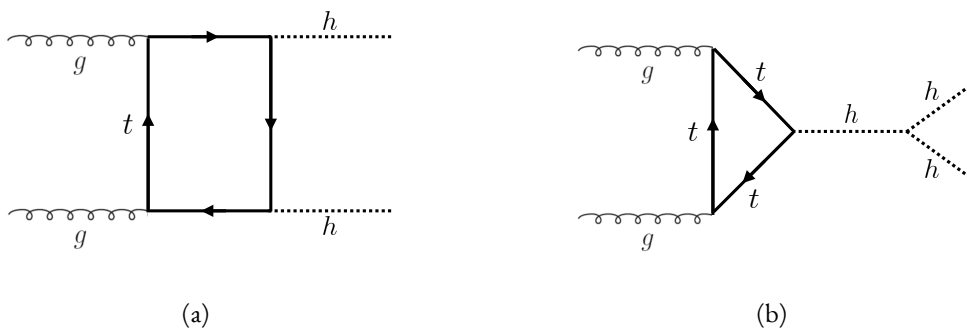


Figure 1.5: The two leading diagrams for Standard Model di-Higgs production at the LHC: (a) box diagram, (b) Higgs self coupling.

792
 793 cross section for di-Higgs production at the LHC. Nevertheless, Higgs pair production is quite interesting

794 to study because it gives direct access to the λ parameter of the Higgs potential, also known as the Higgs
795 self coupling. The diagram in figure 1.5(b) is sensitive to this coupling through the triple Higgs vertex.

796 One can substitute the gluon fusion production of diagram 1.5(b) with any of the other production
797 modes previously discussed. These alternate production modes have a lower cross section than the gluon
798 fusion mode, however. The cross sections for di-Higgs production in the different modes, as well as their
799 uncertainties, are shown in table 1.4 [29]. These are shown for $\sqrt{s} = 14$ TeV as this is the expected center
800 of mass energy for the High Luminosity LHC and this energy is more sensitive to di-Higgs production.

Note that the scale of cross section quoted is now in fb rather than pb.

Production mode	σ (fb)	Total uncert. (%)
Gluon fusion	33.89	+37.2 / -27.8
Vector boson fusion	2.01	+7.6 / -5.1
$W H H$	0.57	+3.7 / -3.3
$Z H H$	0.42	+7.0 / -5.5
$t \bar{t} H$	1.02	-

Table 1.4: Production cross sections for pair production of a 125 GeV Higgs boson at $\sqrt{s} = 14$ TeV with total uncertainty [29]. The uncertainties include QCD scale and PDF variations as well as uncertainties on α_S .

801

802 1.5 HIGGS PAIR PRODUCTION IN THEORIES BEYOND THE STANDARD MODEL

803 The Higgs pair production cross section in the Standard Model is rather small, and datasets on the scale of
804 the full 3000 fb^{-1} expected from the High Luminosity LHC will be required to obtain sensitive measure-
805 ments of the Higgs self-coupling [29]. However, the discovery of the Higgs also gives particle physicists
806 a new tool that can be exploited in the search for new physics beyond the Standard Model. In particular,
807 Higgs pair production is a promising channel in the search for new physics. The cross section for di-Higgs
808 production can be altered through both resonant and non-resonant production of Higgs pairs. In non-
809 resonant production, di-Higgs production vertices can arise from the presence of a new strong sector and
810 additional colored particles [30–32]. Figure 1.6 shows examples of the types of vertices that can arise. In
811 the resonant case, new heavy particle can decay to Higgs pairs. Such new particles can include heavy Higgs
812 bosons arising in two Higgs doublet models (2HDM) or Higgs portal models as well as heavy gravitons in

⁸¹³ Randall-Sundrum theories [30, 33–39]. Figure 1.7 shows a generic diagram for a heavy resonance decaying
⁸¹⁴ to two Higgs bosons. In the 2HDM, X corresponds to the heavy CP-even scalar H . In the Randall-
 Sundrum model, X corresponds to a heavy spin-2 graviton G_{KK}^* . The next sections provide more detail

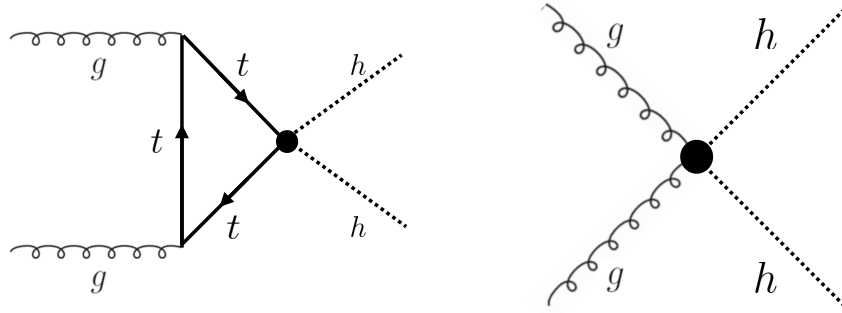


Figure 1.6: Diagrams with new vertices for non-resonant Higgs pair production arising in composite Higgs models.

⁸¹⁵
⁸¹⁶ on the phenomenology of resonant Higgs production in Randall-Sundrum and 2HDM models, as these
 models will later be tested in a dedicated search for resonant production of boosted Higgs pairs.

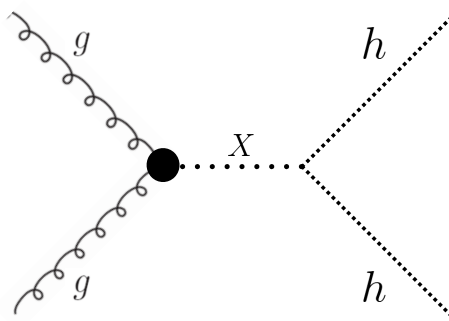


Figure 1.7: Generic Feynman diagram for resonant Higgs pair production in BSM theories.

⁸¹⁷

⁸¹⁸ 1.5.1 RANDALL-SUNDRUM GRAVITONS

⁸¹⁹ The Randall-Sundrum model is a proposed solution to the hierarchy problem that posits a five-dimensional
⁸²⁰ warped spacetime that contains two branes: one where the force of gravity is very strong and a second brane
⁸²¹ at the TeV scale corresponding to the known Standard Model sector [33]. In the theory, the branes are
⁸²² weakly coupled and the graviton probability function drops exponentially going from the gravity brane

823 to the SM brane, rendering gravity weak on the SM brane. The experimental consequence of this theory
 824 is a tower of widely spaced (in mass) Kaluza-Klein graviton resonances. In theories where the fermions
 825 are localized to the SM brane, production of gravitons from fermion pairs is suppressed and the primary
 826 mode of production is gluon fusion [34]. These gravitons have a substantial branching fraction to Higgs
 827 pairs, ranging from 6.43% for gravitons with a mass of 500 GeV to 7.66% at 3 TeV. Figure 1.8 shows the
 828 branching ratios of the spin-2 Randall Sundrum graviton (RSG) as a function of its mass. The predomi-
 829 nant decays are to $t\bar{t}$ above the mass threshold for that channel.

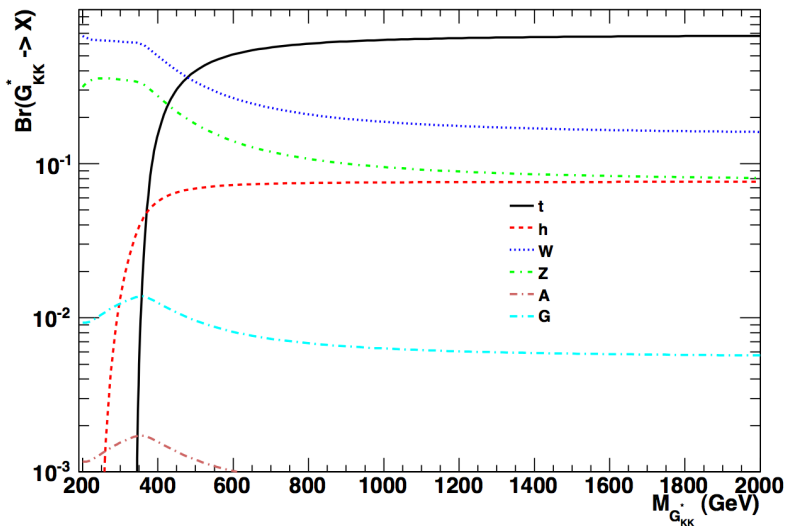


Figure 1.8: Branching ratios for a spin-2 Randall-Sundrum graviton as a function of mass computed in MadGraph with the CP3-Origins implementation [34, 40, 41].

830 Randall-Sundrum models have two free parameters - the mass of the graviton and a curvature parameter
 831 k . Typically, rather than k , the theory is parameterized using $c \equiv k/\bar{M}_{\text{pl}}$, where \bar{M}_{pl} is the reduced
 832 Planck mass. The cross section for production of the RSG decreases as a function of mass and is strongly
 833 dependent on the gluon PDF. The increase in center of mass energy from 8 to 13 TeV in LHC Run 2
 834 greatly increases the cross section at higher mass. Figure 1.9 shows the cross section as a function of graviton
 835 mass at $\sqrt{s} = 13$ TeV for RSG models with $c = 1.0$ and $c = 2.0$.

836 Another interesting feature of the theory is that the width of the graviton increases with both c and
 837 $m_{G_{KK}^*}$. Figure 1.10 shows the graviton width for both $c = 1.0$ and $c = 2.0$ as a function of mass. In
 838 $c = 1.0$, the width starts at 8.365 GeV for a mass of 300 GeV and increases to 187.2 GeV at a mass of

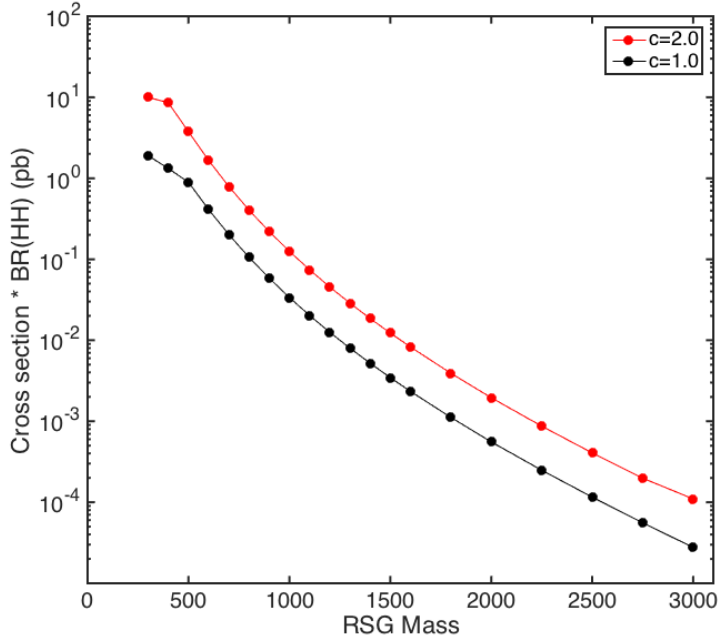


Figure 1.9: $\sigma \times \text{BR}(HH)$ for Randall-Sundrum gravitons as a function of mass computed in MadGraph with the CP3-Origins implementation [34, 40, 41].

839 3 TeV. Similarly, with $c = 2.0$, the width starts at 33.46 GeV for $m_G = 300$ GeV and increases to
 840 748.8 GeV at a mass of 3 TeV.

841 1.5.2 TWO HIGGS DOUBLET MODELS

842 In Two Higgs Doublet Models (2HDM), a second complex scalar doublet is added to the Standard Model [36–
 843 38]. In this case, all four degrees of freedom in the second doublet correspond to new particles, meaning
 844 that there are five total scalars from the two Higgs doublets - h (light CP-even Higgs), H (heavy CP-even
 845 Higgs), A (heavy CP-odd Higgs), and H^\pm (charged Higgs). The model is parameterized by two main pa-
 846 rameters. The first, $\tan \beta \equiv \frac{v_2}{v_1}$, is the ratio of the vacuum expectation values of the two Higgs doublets
 847 (where v_1 corresponds to the v in the SM Higgs model described above). The second parameter is α , a mix-
 848 ing angle between the heavy and light Higgs fields. Models are also often parameterized with $\cos(\beta - \alpha)$
 849 rather than α directly. The limit where $\cos(\beta - \alpha) = 0$ is called the alignment limit, and in this limit the
 850 light Higgs h has the same couplings as a Standard Model Higgs. Measurements of the Higgs boson have

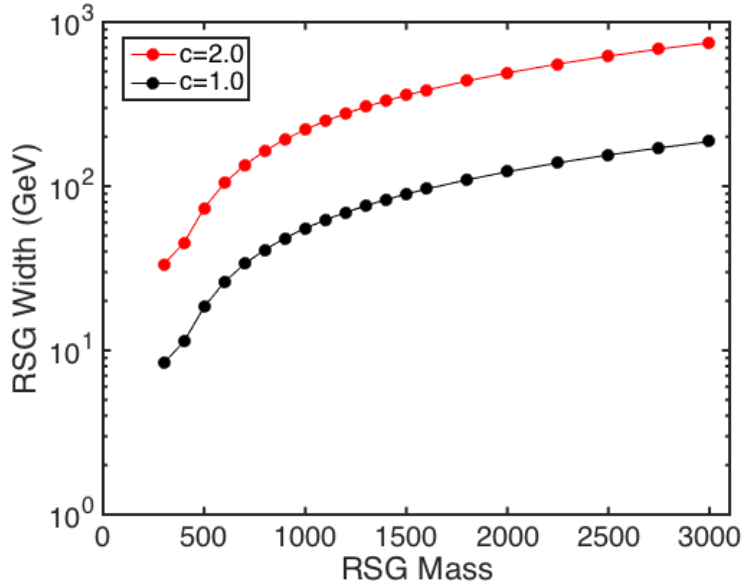


Figure 1.10: Randall-Sundrum graviton width as a function of mass computed in MadGraph with the CP3-Origins implementation [34, 40, 41]

851 put constraints on these two parameters, but near the alignment limit there is still much unprobed phase
 852 space depending on the exact models and values of $\tan \beta$ being considered [42].

853 2HDM models are usually separated into two main types - Type I and Type II. In Type I models, the
 854 charged fermions only couple to the second Higgs doublet, leading to a fermiophobic light Higgs. In
 855 Type II models, up-type quarks couple to the first doublet while down-type quarks couple to the second
 856 doublet. One specific realization of a Type II 2HDM is the Minimal Supersymmetric Standard Model
 857 (MSSM).

858 Resonant di-Higgs production in 2HDM models can proceed through decays of the heavy CP-even
 859 Higgs $H \rightarrow hh$. The branching ratio for $H \rightarrow hh$ depends on the model type as well as the values of
 860 $\tan \beta$ and $\cos \beta - \alpha$. Figure 1.11 shows the branching ratios as a function of the mass of the heavy scalar
 861 H for both Type I and Type II models. Depending on the type of model hh can be a substantial fraction
 862 of the decays of H .

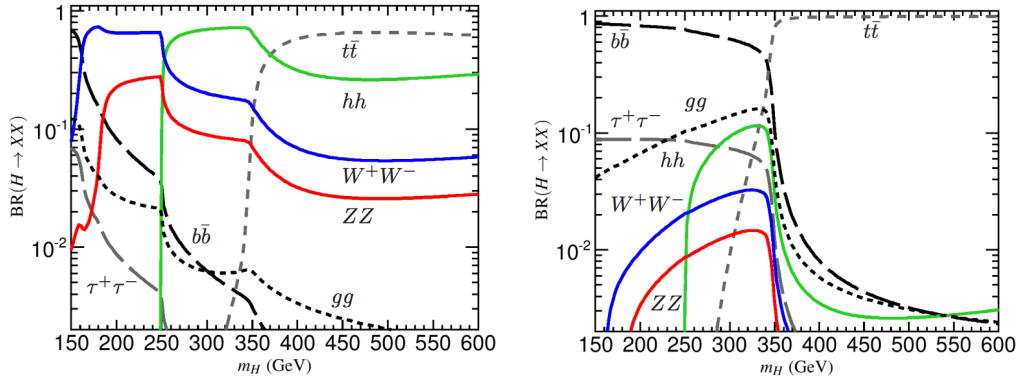


Figure 1.II: Branching ratios for heavy Higgs H in Type I (left) and Type II (right) 2HDM models with $\tan \beta = 1.5$ and $\cos(\beta - \alpha) = 0.1$ (0.01) for Type I (Type II) [38].

863 1.6 CONCLUSION

864 Studying the Higgs sector is essential for understanding the details of how mass arises in the Standard
 865 Model and how the electroweak symmetry is broken. The discovery of the Higgs boson also opens the
 866 door for its use as a tool to search for new physics, and Higgs pair production is an ideal candidate for
 867 this study. Even if no BSM physics is found in Higgs pair production, searches for Higgs pairs will put
 868 constraints on the Higgs self coupling and thus improve knowledge of the Standard Model and the details
 869 of the Higgs potential.

*The enthusiasm and motivation to explore particle physics
at the high-energy frontier knows no borders between the
nations and regions of the planet.*

Peter Jenni

2

870

871

872

The ATLAS detector and the Large Hadron Collider

873 This chapter presents an overview of the experimental systems used to conduct the measurements in this
874 thesis. First, a brief overview of the accelerator, the Large Hadron Collider, will be given, followed by a
875 summary of the accelerator conditions relevant to data-taking. Next, an overview of the ATLAS experi-
876 ment is given. The basics of each sub-detector's role are summarized, as well as the details of the datasets
877 accumulated. Then, a brief interlude on the ATLAS Muon New Small Wheel upgrade is presented. While
878 this new detector does not have a direct impact on any of the datasets recorded so far, it will have an im-
879 pact on future analyses and the work done on it is briefly summarized here. Finally, an overview of object
880 reconstruction in ATLAS is given. While the details of all of the algorithms will not be presented in detail,
881 aspects of the reconstruction performance are shown as these are relevant to the results presented later in
882 this thesis.

883 2.1 THE LARGE HADRON COLLIDER

884 The Large Hadron Collider (LHC) is a proton-proton collider at the CERN laboratory in Geneva, Switzer-
885 land [43]. It was designed for a maximum collision center of mass energy of $\sqrt{s} = 14 \text{ TeV}$ and has a
886 circumference of 26.7 kilometers. Four main experiments are located at the interaction points (IP) of
887 the accelerator: ATLAS (A Toroidal LHC ApparatuS), CMS (the Compact Muon Solenoid), ALICE (A
888 Large Ion Collider Experiment), and LHCb [44–47]. Figure 2.1 shows a schematic of the LHC ring and
889 its experiments.

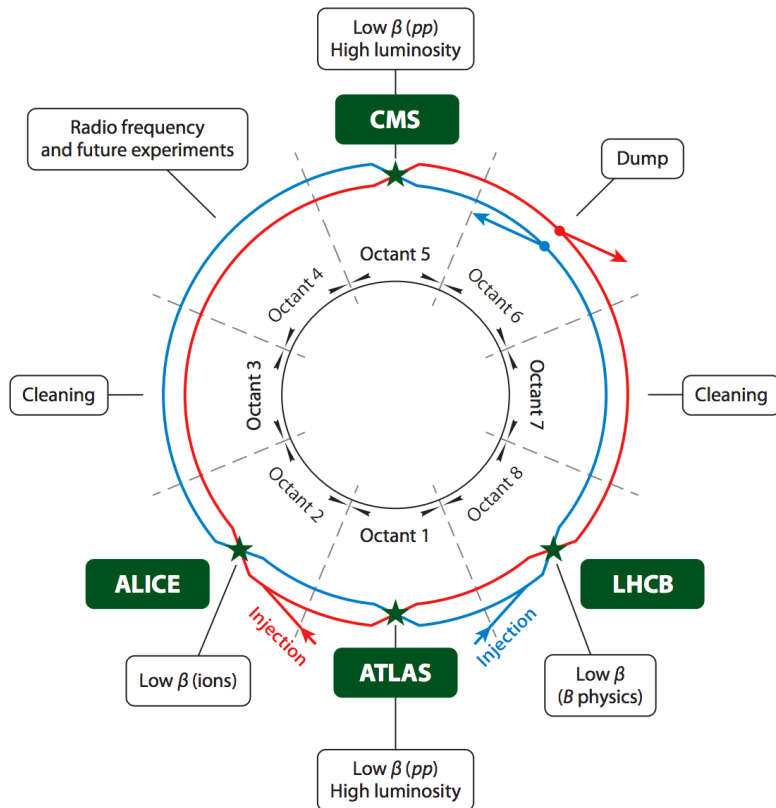


Figure 2.1: A schematic view of the LHC ring [48]. Four main experiments are located at interaction points along the ring. ATLAS and CMS are general purpose experiments, while ALICE is dedicated to heavy ion collisions and LHCb is dedicated to studying B physics.

890 One of the most interesting features of the LHC is its magnet design. Because the tunnel does not have
891 room for separate superconducting magnets for each of the beam pipes, the LHC employs a twin-bore
892 magnet design. Each magnet must hold an 8.3 Tesla magnetic field in order to bend the proton beams at

893 $\sqrt{s} = 14$ TeV. The superconducting magnets are cooled to a temperature of 1.9 Kelvin with superfluid
894 helium.

895 2.1.1 INSTANTANEOUS LUMINOSITY

896 The rate of physics events expected from the accelerator is dependent on the instantaneous luminosity
897 of the machine and the cross section of the physics process, $R_{\text{events}} = L\sigma$. Here, R_{events} is the num-
898 ber of events per second, L is the instantaneous luminosity of the machine, and σ is the cross section for
899 the physics process being measured. The instantaneous luminosity of the LHC is determined by numer-
900 ous factors related to beam conditions. Equation 2.1 gives the equation for instantaneous luminosity of a
901 Gaussian beam profile [48].

$$L = \frac{N_b^2 n_b f_{\text{rev}} \gamma_r}{4\pi \epsilon_n \beta^*} F \quad (2.1)$$

902 The LHC collides protons in bunches, and in the above equation N_b is the number of protons per bunch
903 while n_b is the number of bunches per beam. Nominally, the LHC can hold up to 2808 proton bunches.
904 f_{rev} is the revolution frequency. ϵ_n is the normalized transverse beam emittance, a measurement of the
905 average spread of the particles in position-momentum space which has the dimension of length. β^* is the
906 value of the β function for the beam at the interaction point. It relates the emittance to the Gaussian
907 width of the beam with $\sigma_{\text{beam}} = \sqrt{\epsilon \cdot \beta}$. F is a reduction factor that corrects for the fact that the beams
908 are colliding at an angle at the IP.

909 Another way of writing the instantaneous luminosity is shown in equation 2.2. In this case, the instan-
910 taneous luminosity is written as the ratio of the rate of inelastic collisions to the inelastic cross section [49].

911

$$L = \frac{R_{\text{inel}}}{\sigma_{\text{inel}}} = \frac{\mu n_b f_{\text{rev}}}{\sigma_{\text{inel}}} \quad (2.2)$$

912 In this case, μ is the average number of interactions per bunch crossing in the accelerator. μ is a useful
913 parameter for characterizing the amount of activity recorded in an experiment. As the instantaneous lu-
914 minosity and thus μ increase, there are more interactions per bunch crossing and more activity is present
915 in the detector. The level of activity is often characterized with $\langle \mu \rangle$, the measured per bunch crossing μ

value averaged over all bunch crossings. The interactions inside each bunch crossing that are not the main physics process of interest are often referred to as “pileup” interactions, and $\langle \mu \rangle$ is a measurement of the level of pileup in the detector.

2.1.2 EVOLUTION OF MACHINE CONDITIONS

This thesis uses datasets taken at three different center of mass energies: $\sqrt{s} = 7$ TeV data taken in the year 2011, $\sqrt{s} = 8$ TeV data taken in the year 2012, and $\sqrt{s} = 13$ TeV data taken in the year 2015. In addition to increasing center of mass energy, the instantaneous luminosity and parameters that determine it were evolving. Table 2.1 summarizes that machine conditions in each of these datasets.

	2011	2012	2015	Design
\sqrt{s} [TeV]	7	8	13	14
Number of bunches	1380	1380	1825	2808
Max. protons per bunch	1.45×10^{11}	1.7×10^{11}	1.2×10^{11}	1.15×10^{11}
Bunch spacing [ns]	50	50	25	25
Max. instantaneous luminosity [$\text{cm}^{-2}\text{s}^{-1}$]	3.7×10^{33}	7.7×10^{33}	5×10^{33}	10^{34}
β^* [m]	1.0	0.6	0.8	0.55
$\langle \mu \rangle$	11.6	20.7	13.7	-

Table 2.1: Evolution of LHC machine conditions [50, 51].

2.2 THE ATLAS DETECTOR

The ATLAS detector is the multi-purpose particle detector experiment located at the LHC’s Point 1 [44]. It has nearly 4π coverage in solid angle around the interaction point. It consists of an inner detector for measuring charged particles, electromagnetic and hadronic calorimeters, and a muon spectrometer. Figure 2.2 gives an overview of the detector.

2.2.1 COORDINATE SYSTEM

Before defining the properties of the individual detectors, it is important to establish the coordinate system used. Figure 2.3 shows a schematic of the coordinate system. The azimuthal plane (perpendicular to the

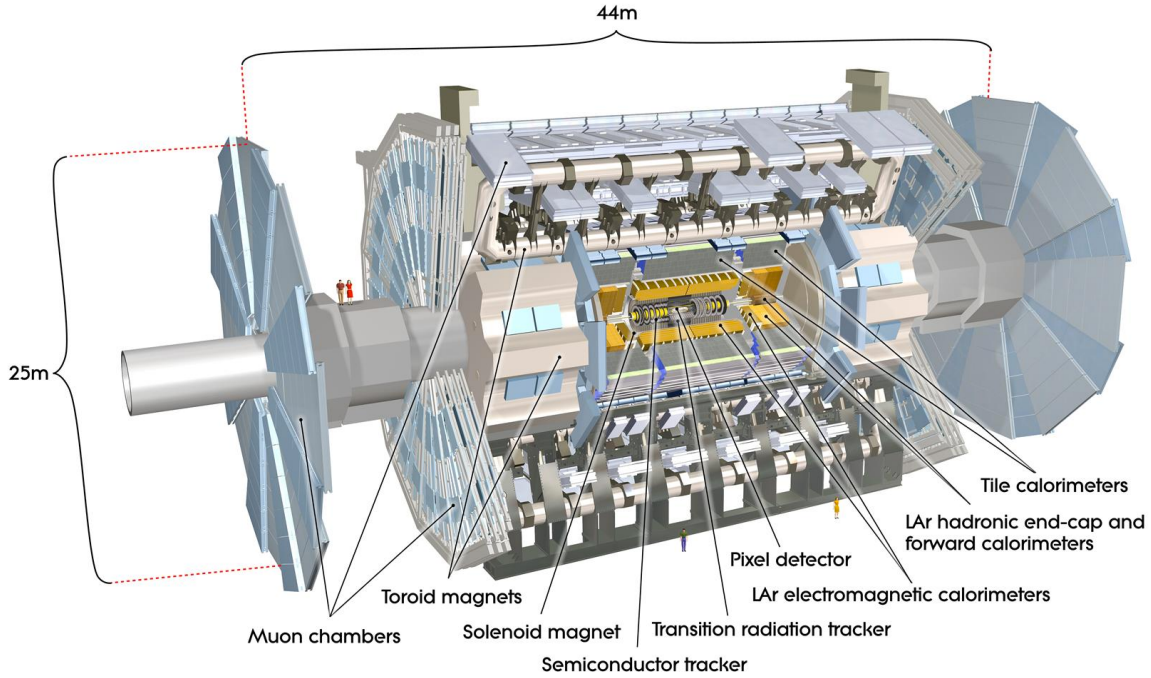


Figure 2.2: A full diagram of the ATLAS detector [44].

beam line) is defined as the x - y plane. The angle in this plane is referred to as ϕ . The angle relative to the beam axis is referred to as θ . Rather than using θ directly as a coordinate, the experiment often uses the pseudorapidity η , defined in equation 2.3.

$$\eta = -\ln \left(\tan \left(\frac{\theta}{2} \right) \right) \quad (2.3)$$

Pseudorapidity is the massless approximation of rapidity, the angle used to parameterize boosts in special relativity. This coordinate is useful in particle physics for two reasons. First, it means that differences in η are Lorentz invariant. Second, particle production is roughly constant in pseudorapidity. Particles with η close to zero are referred to as “central”, while those at high $|\eta|$ are called “forward”. In general, two main detector configurations can be seen in figure 2.2. There are “barrel” elements, which surround the beam line cylindrically and are in the central region of the detector. In the forward region, there are “endcap” regions which are arranged as disks perpendicular to the beam line.

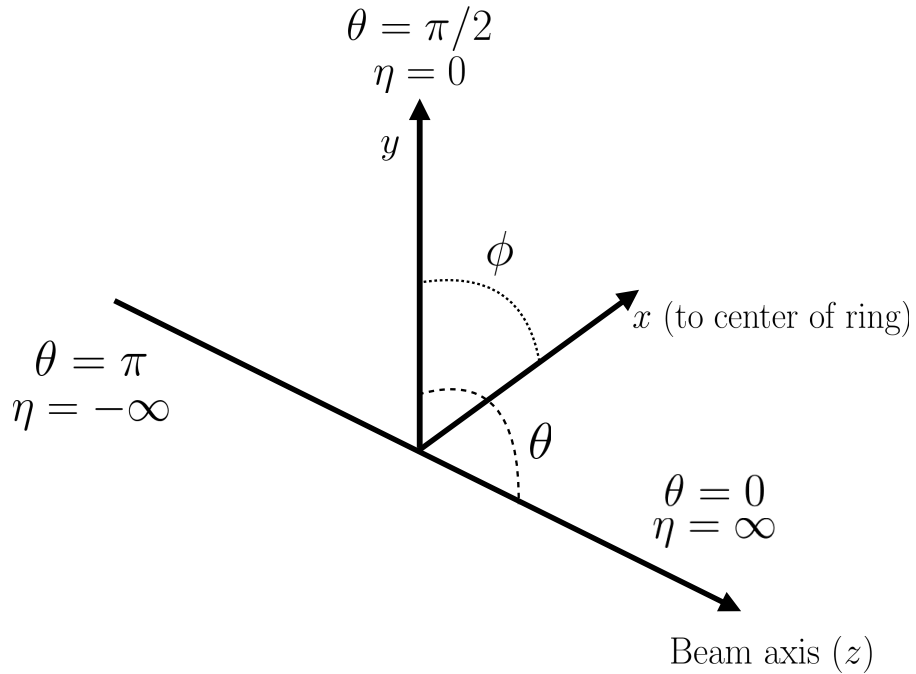


Figure 2.3: The ATLAS coordinate system. The z direction corresponds to the beam axis, while x and y define the transverse plane. θ is the angle relative to the beam axis and ϕ is the azimuthal angle. η , the pseudorapidity, approaches infinity at small angles relative to the beam axis.

942 2.2.2 INNER DETECTOR

943 The ATLAS Inner Detector (ID) system is built for precision tracking of charged particles. It covers the
 944 range $|\eta| < 2.5$. In this range, approximately 1000 particles are generated every bunch crossing in the de-
 945 tector [44]. This requires having fine granularity to achieve the resolutions required for good momentum
 946 measurement and vertex reconstruction.

947 The ID consists of three sub-components: the pixel detector, semiconductor tracker (SCT), and trans-
 948 sition radiation tracker (TRT). It is surrounded by a solenoid providing a 2 T axial magnetic field which
 949 bends particles in the transverse plane to allow for momentum measurement. Figure 2.4 shows the layout
 950 of each of these components.

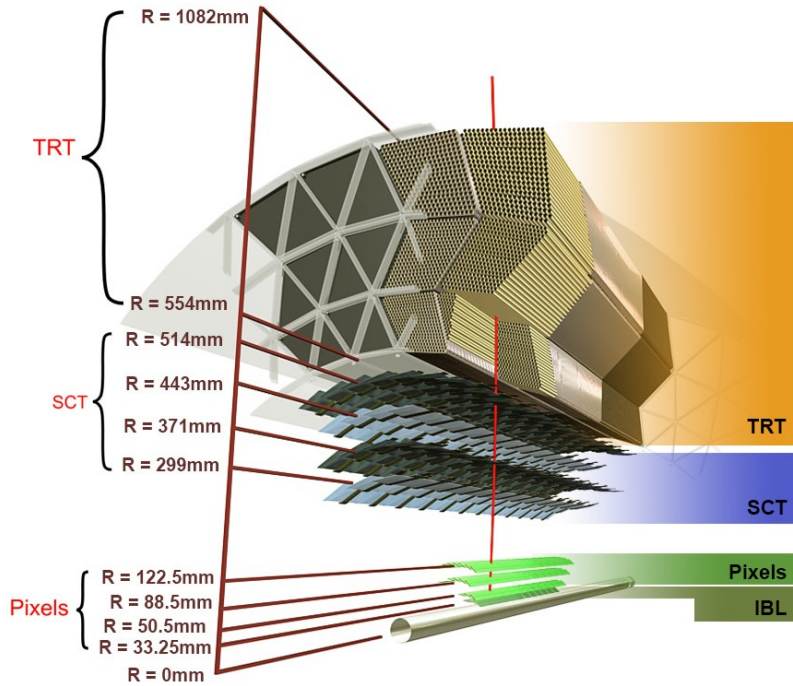


Figure 2.4: Layout of the ATLAS Inner Detector system [52].

951 PIXEL DETECTOR

952 The pixel detector is the first detector particles traverse after being generated in proton collisions and is
 953 the most granular detector. Its operation is crucial for precision tracking and vertex reconstruction as well
 954 as higher level object reconstruction like tagging of jets from b -quarks. The basic sensing element in this
 955 subdetector is a silicon pixel detector. The operating principle for the silicon pixels is that of a $p-n$ junction.
 956 When a charged particle passes through, it creates electron-hole pairs that are then separated by the electric
 957 field. The sensors are $250 \mu\text{m}$ thick and use oxygenated n -type wafers with readout pixels on the n^+ side
 958 of the detector [44]. Overall, the pixel detector has 1744 sensors and 80.4 million readout channels.

959 In the barrel region, the pixel detector has three concentric layers of sensors surrounding the beamline.
 960 In the endcap region, it consists of disks perpendicular to the beam axis. The detector is segmented in
 961 the $R-\phi$ plane and in z . Usually, three pixel layers are crossed by a charged particle track. The intrinsic
 962 accuracies of the sensors are $10 \mu\text{m}$ in $R-\phi$ and $115 \mu\text{m}$ in z (or R for the endcap).

963 **INSERTABLE B-LAYER**

964 In Run 2, a new innermost pixel layer, known as the insertable B-layer (IBL), was added to the Inner
965 Detector [53]. This layer was added to cope with the higher luminosities planned in LHC Run 2 and at the
966 high luminosity HL-LHC. Additionally it improves tracking position resolution which in turn improves
967 the vertexing and *b*-tagging capabilities in ATLAS. The detector sits directly on a new beam pipe, only
968 33.25 mm away from the collision points in the azimuthal plane.

969 **SEMICONDUCTOR TRACKER (SCT)**

970 The semiconductor tracker (SCT) consists of silicon microstrips and comprises the next four layers of
971 the ID. This sub-detector has 6.4 cm long sensors that are daisy-chained into strips with a strip pitch of
972 80 μm [44]. Some of the strips have a small stereo angle to allow for measurement of both angular co-
973 ordinates. In total there are 6.3 million readout channels. The intrinsic accuracies are 17 μm in $R\text{-}\phi$ and
974 580 μm in z (or R in the endcap).

975 **TRANSITION RADIATION TRACKER (TRT)**

976 The transition radiation tracker (TRT) serves two purposes. First, it consists of 4 mm diameter straw tubes
977 filled with a 70/27/3% gas mixture of xenon, carbon dioxide, and oxygen to provide tracking of charged
978 particles. Particles typically have 36 TRT straw tube hits per track. The material in between the straws
979 is designed to induce transition radiation which can be useful for particle identification. As particles pass
980 between media with different dielectric constants, they emit transition radiation that can cause additional
981 showers in the TRT. In particular it is useful for discrimination between electrons and pions or other
982 charged hadrons, as the amount of transition radiation is proportional to the Lorentz factor of the particle.

983 **2.2.3 CALORIMETERS**

984 The calorimeter system consists of two main sub-components: a fine granularity electromagnetic calorime-
985 ter tailored for the measurement of photons and electrons and multiple coarser hadronic calorimeters ded-
986 icated to the measurement of hadronic showers [44]. The calorimeter system has broader coverage than

987 the inner detector, covering the region out to $|\eta| < 4.9$. It is also designed to deliver good containment of
988 showers so as to limit leakage into the muon system. Figure 2.5 shows the layout of the calorimeter system.

989 Both the electromagnetic and hadronic calorimeters are sampling calorimeters. They alternate active
990 material for energy measurement with passive material for energy absorption. The materials used for each
991 purpose vary based on the type of calorimeter and its location in the detector.

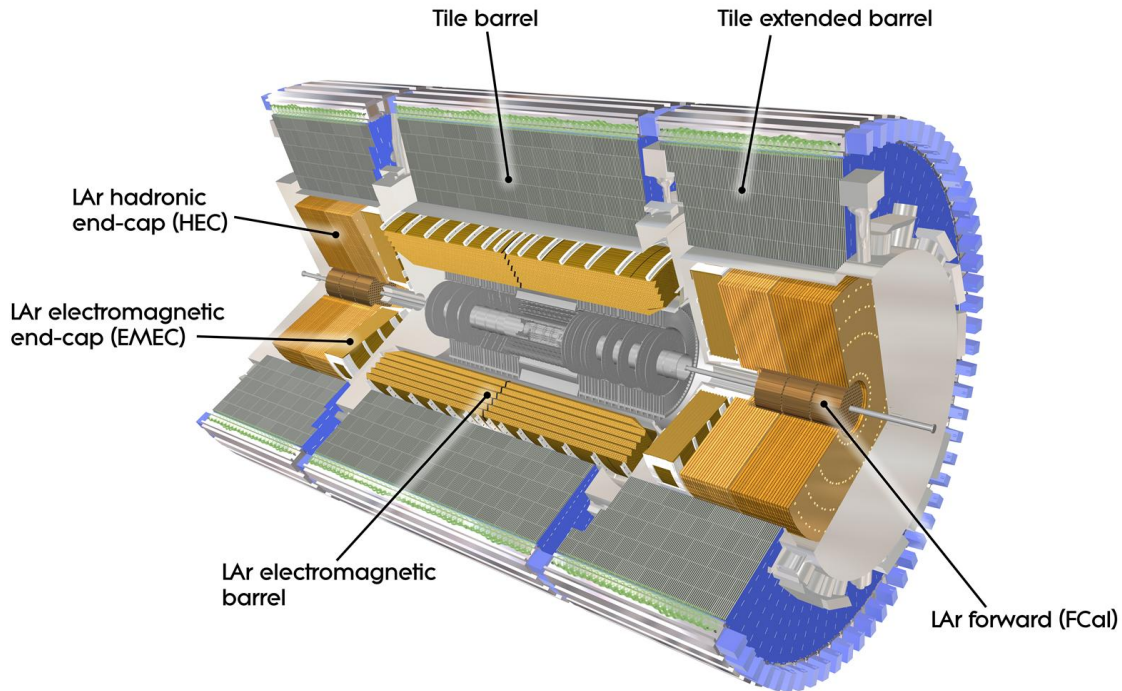


Figure 2.5: Layout of the ATLAS calorimeter system [44].

992 ELECTROMAGNETIC CALORIMETER

993 The electromagnetic calorimeter (EM calorimeter) use liquid Argon (LAr) as its active material and lead
994 as its passive material. It is arranged in an accordion geometry to increase the absorption area while still
995 allowing it to have no azimuthal cracks (complete symmetry in ϕ). The EM calorimeter is divided into a
996 barrel portion that extends to $|\eta| < 1.475$ and an endcap portion going from $1.375 < |\eta| < 3.2$. The
997 region where these two units overlap is called the “transition region”.

998 In order to provide good containment the calorimeter depth must be optimized. Typically, for elec-
999 tromagnetic calorimeters the depth is measured in radiation lengths. In general, the intensity of a particle
1000 beam attenuates exponentially in distance with an attenuation constant equal to the radiation length. That
1001 is, $I(x) = I_0 e^{-x/X_0}$, where I is the intensity, x is the distance traveled, and X_0 is the radiation length.
1002 The ATLAS EM calorimeter is designed to have > 22 radiation lengths in the barrel and > 24 in the
1003 endcap [44].

1004 HADRONIC CALORIMETERS

1005 There are three types of hadronic calorimeters present in ATLAS: the tile calorimeter (TileCal), hadronic
1006 endcap (HEC), and forward calorimeter (FCal). Each one is optimized for stopping of hadronic showers
1007 and the materials chosen are specific to their placement in the detector.

1008 The TileCal is a scintillating tile calorimeter placed directly outside the EM calorimeter. It uses steel as
1009 the absorber and plastic scintillator tiles as the active material. It has coverage in the barrel at $|\eta| < 1.0$
1010 and in the “extended barrel” region of $0.8 < |\eta| < 1.7$.

1011 The HEC had two wheels perpendicular to the beam line per endcap and is located directly behind the
1012 EM calorimeter endcap modules. The HEC covers the region from $1.5 < |\eta| < 3.2$, overlapping slightly
1013 with both the tile calorimeter and the forward calorimeter. Like the EM calorimeter, it uses liquid Argon
1014 as the active material, but it uses copper as the absorber.

1015 The FCal covers the most forward regions of the calorimeter system, extending to the region of $3.1 <$
1016 $|\eta| < 4.9$. It again uses liquid argon as its active material. For absorber, it consists of an innermost module
1017 made of copper followed by a module made of tungsten.

1018 The hadronic equivalent of radiation length is called the interaction length and is denoted as λ . In the
1019 barrel, the hadronic calorimeter depth is approximately 9.7λ , while in the endcap is is 10λ . The outer
1020 supports contribute an additional 1.3λ . This is been shown to be sufficient to limit punch-through of
1021 showers to the muon system [44].

1022 2.2.4 MUON SPECTROMETER

1023 The muon spectrometer is dedicated to measuring the momentum and position of muons. It consists
1024 of tracking and trigger chambers which are unique in the barrel and endcap regions. The magnetic field
1025 for bending of muons is provided by a system of three large air-core toroid magnets (from which ATLAS
1026 derives its name.) These magnets provide 1.5 to 5.5 Tm of bending power at $0 < |\eta| < 1.4$ and approx-
1027 imately 1 to 7.5 Tm in the endcap region of $1.6 < |\eta| < 2.7$. The entire muon system covers the range
1028 $0 < |\eta| < 2.7$. Monitored drift tubes (MDTs) are used for tracking in the barrel and the two outer layers
1029 of the endcap, while cathode strip chambers (CSCs) are used to provide tracking in the innermost endcap
1030 wheel. In the barrel, resistive plate chambers (RPCs) are used as trigger chambers while thin gap chambers
1031 (TGCs) are used in the endcap. Figure 2.6 shows the layout of the ATLAS muon system. The entire muon
1032 system is designed with the specification of providing a 10% momentum resolution for a 1 TeV muon.

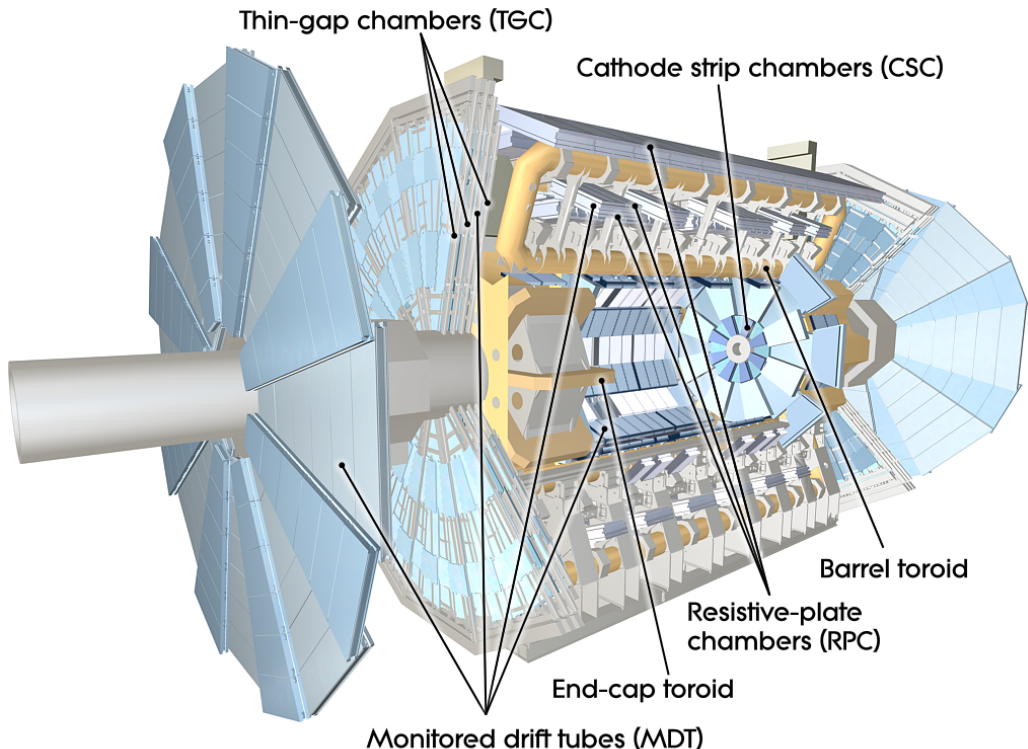


Figure 2.6: Layout of the ATLAS muon system [44].

1033 MONITORED DRIFT TUBES (MDTs)

1034 The monitored drift tubes (MDTs) are aluminum 3 cm diameter tubes filled with a 93/7 % mixture of
1035 Argon and CO₂, with trace amounts of water. As a charged particle traverses the tube, it ionizes the gas
1036 and the ions drift to a wire at the center of the tube. The radial distance of traversal of the particle in the
1037 tube is determined by the drift time of the electrons, allowing for fine position resolution. The tubes have
1038 an average resolution of 80 μm per tube and a maximum drift time of approximately 700 ns. The tubes
1039 are oriented so that they give precision measurement in η and run along ϕ . They cover $|\eta| < 2.7$, except
1040 in the innermost layer of the endcap where they only go to $|\eta| < 2.0$ [44].

1041 CATHODE STRIP CHAMBERS (CSCs)

1042 The cathode strip chambers cover a narrow window of the innermost endcap region at $2.0 < |\eta| <$
1043 2.7. In this region the background rates in the cavern are particularly high and the CSCs are designed to
1044 handle these higher rates. The CSCs are multiwire proportional chambers with wires pointing in the radial
1045 direction (away from the beam pipe). The wire serves as an anode and there are two types of segmented
1046 cathode strip, one perpendicular to the wires which gives the precision measurement and one parallel which
1047 provides the transverse coordinate. It has an 80/20% gas mixture of Argon and CO₂ [44].

1048 RESISTIVE PLATE CHAMBERS (RPCs)

1049 The resistive plate chambers (RPCs) are gaseous electrode-plate detectors covering the region $|\eta| < 1.05$.
1050 They consist of two resistive plates separated by a distance of 2 mm. The gas mixture used is a 94.7/5/0.3%
1051 mixture of C₂H₂F₄, Iso-C₄H₁₀, and SF₆. It has readout strips with a pitch of 23-35 mm for both η and
1052 ϕ measurement and thus provides measurement of the azimuthal coordinate in the barrel. The thin gas
1053 gap allows for a quick response time which makes it ideal for use in the trigger. Signals in the RPC have
1054 a width of approximately 5 ns. There are three layers of RPCs which are referred to as the three trigger
1055 stations. They allow for programmable thresholds in both a low p_T and high p_T trigger. The coincidence
1056 of hits in the innermost chambers allows for setting muon trigger thresholds between 6 and 9 GeV, while
1057 the outermost layer allows the trigger to set trigger thresholds in the range of 9 to 40 GeV [44].

1058 THIN GAP CHAMBERS (TGCs)

1059 The thin gap chambers (TGCs) are multiwire proportional chambers where the wire to cathode distance
1060 (1.4mm) is smaller than the wire-to-wire distance (1.8 mm). They contain a gas mixture of CO₂ and *n*-
1061 pentane and use a high electric field to gain good time resolution. They serve two functions in the end-cap
1062 system. First, they serve as the trigger chambers. Second, they also provide azimuthal coordinate measure-
1063 ment. They sit on the inner and middle layers of the endcap. The outermost layer's azimuthal coordinate
1064 is determined by extrapolation [44]. As with the RPCs, the TGCs also are capable of triggering with pro-
1065 grammable thresholds in the same p_T range specified for the RPCs above.

1066 2.2.5 MAGNET SYSTEM

1067 As mentioned previously, there are two independent magnet systems in ATLAS. The first is a 2 T solenoid
1068 field in the inner detector which provides bending in the azimuthal plane. The second is an approximately
1069 0.5 T toroidal field in the muon system which provides bending in η . Figure 2.7 shows the predicted field
1070 integral as a function of $|\eta|$ [44].

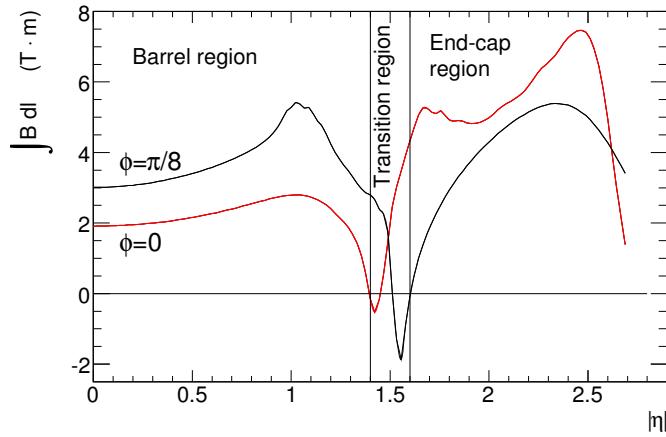


Figure 2.7: Predicted field integral as a function of $|\eta|$ for the ATLAS magnet system [44].

1071 2.2.6 TRIGGER SYSTEM

1072 The ATLAS trigger system searches for signatures of muons, electrons, photons, hadronically decaying τ
 1073 leptons, and jets in order to save these events for further analysis. The trigger system in ATLAS is designed
 1074 to reduce the maximum LHC event rate of 40 MHz to a more reasonable rate that can be recorded. The
 1075 trigger first consists of a fast, hardware based system called the Level-1 (L1) trigger. The L1 trigger consists
 1076 of independent dedicated detector sub-components that can seed regions of interest (RoIs) for further
 1077 analysis downstream. For muons, the RPCs and TGCs are used, while in the calorimeter coarsely grained
 1078 sections of calorimeter cells called towers are used. Once regions of interest are seeded, a software based
 1079 system called the High Level Trigger (HLT) is used to reconstruct objects and integrate information from
 1080 different parts of the detector. In Run 1 of ATLAS, the HLT consisted of two separate stages: the level 2
 1081 (L2) trigger and the event filter (EF).

1082 The maximum trigger rate that the L1 trigger can handle is 75 kHz. In the HLT, the rate of events
 1083 written to disk is approximately 400 Hz. Figure 2.8 shows the trigger rates for different L1 triggers in 2012
 1084 and 2015 for ATLAS [54].

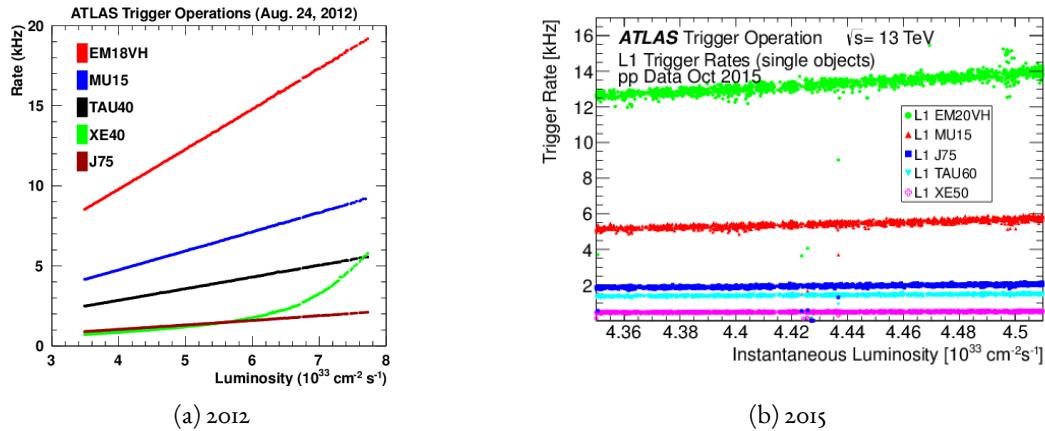


Figure 2.8: ATLAS trigger rates for Level-1 triggers as a function of instantaneous luminosity in 2012 and 2015 operation. These are single object triggers for electromagnetic clusters (EM), muons (MU), jets (J), missing energy (XE), and τ leptons (TAU). The threshold of the trigger is given in the name in GeV [54].

1085 2.2.7 ATLAS DATASETS

1086 ATLAS has collected data at center of mass energies of 7, 8, and 13 TeV. Figure 2.9 shows the integrated
1087 luminosity as a function of time for each of the three datasets. In the 2011 dataset with $\sqrt{s} = 7$ TeV,
1088 ATLAS recorded 5.08 fb^{-1} . Increased instantaneous luminosity in 2012 led to a larger dataset of 21.3 fb^{-1}
1089 recorded at $\sqrt{s} = 8$ TeV. After Long Shutdown 1 (LS1) of the LHC and a restart in 2015, ATLAS
1090 recorded 3.9 fb^{-1} of data at $\sqrt{s} = 13$ TeV [55, 56]. The data recorded by ATLAS can only be used for
1091 analysis if the required sub-detectors were in a stable state when the data was being taken. The fraction
1092 of recorded ATLAS data that was labeled as being good for physics analysis was 90%, 95%, and 82% in
1093 the 7, 8, and 13 TeV data respectively. Thus, the Run 1 results presented in this thesis use 4.6 fb^{-1} at
1094 $\sqrt{s} = 7$ TeV and 20.3 fb^{-1} at $\sqrt{s} = 8$ TeV¹. The Run 2 results use 3.2 fb^{-1} at $\sqrt{s} = 13$ TeV.

1095 2.2.8 DETECTOR PERFORMANCE

1096 Table 2.2 summarizes the design requirements for each of the different sub-detectors. This table shows the
1097 energy and momentum resolution of tracking, calorimetry, and muon measurements.

	Required resolution
Tracking	$\sigma_{p_T}/p_T = 0.05\% p_T \oplus 1\%$
EM calorimetry	$\sigma_E/E = 10\%/\sqrt{E} \oplus 0.7\%$
Hadronic calorimetry	
Barrel and end-cap	$\sigma_E/E = 50\%/\sqrt{E} \oplus 3\%$
Forward	$\sigma_E/E = 100\%/\sqrt{E} \oplus 10\%$
Muon spectrometer	σ_{p_T}/p_T at $p_T = 1$ TeV

Table 2.2: Performance requirements for the ATLAS detector [44].

1098 2.3 THE ATLAS MUON NEW SMALL WHEEL UPGRADE

1099 As the LHC continues operation, it is scheduled to be upgraded in several phases to allow it to reach higher
1100 instantaneous luminosities and thus collect larger datasets. These conditions will open new doors for study

¹The analyses combined in the Higgs discovery (presented in chapter 4) use between 4.6 and 4.8 fb^{-1} at 7 TeV depending on which detectors are required to be in a stable state. The discovery also only uses the 5.8 fb^{-1} of 8 TeV data that was available at the time of the analysis.

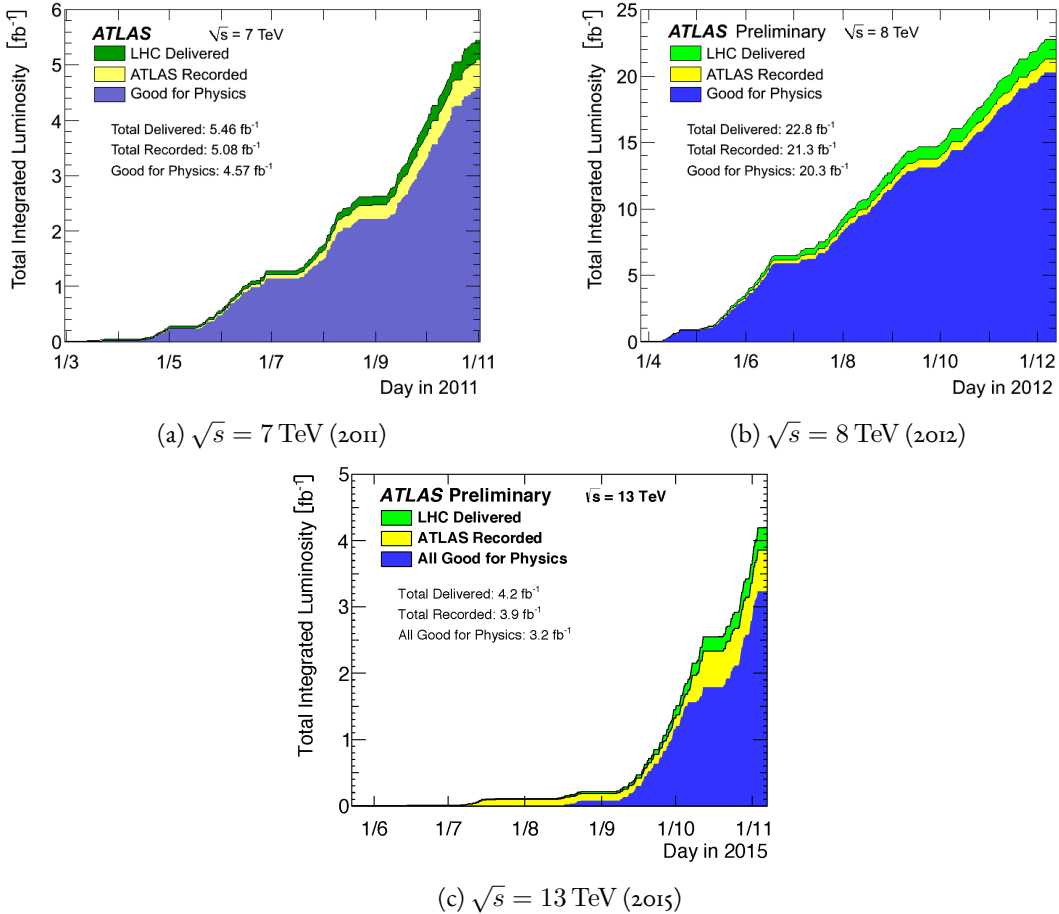


Figure 2.9: Instantaneous luminosity as a function of time for data recorded by ATLAS at different center of mass energies [55, 56].

of rare physics processes but will also present interesting challenges that must be faced. ATLAS will require new detector technologies to cope with the increased background rates in the cavern in these high luminosity conditions. One such upgrade, scheduled to be installed during Long Shutdown 2 (LS2) of the LHC in 2018, is the ATLAS Muon New Small Wheel (NSW) [57]. The NSW will replace the innermost end-cap wheel of the muon system with new technologies. This is the part of the muon detector closest to the beam line and thus experiences the highest rates of particle flux in the muon system.

1107 2.3.1 MOTIVATION

1108 The motivation of the NSW is two-fold. The first objective is to alleviate the decreased tracking efficiency
1109 that comes in a high rate environment. As shown in figure 2.10, at the LHC design luminosity both the
1110 efficiency of recording hits and reconstructing track segments in the MDTs decreases. While the MDTs
1111 were designed to cope with the hit rates at the LHC design luminosity, the High Luminosity LHC will
1112 exceed these design specifications and the MDTs will have to be replaced.

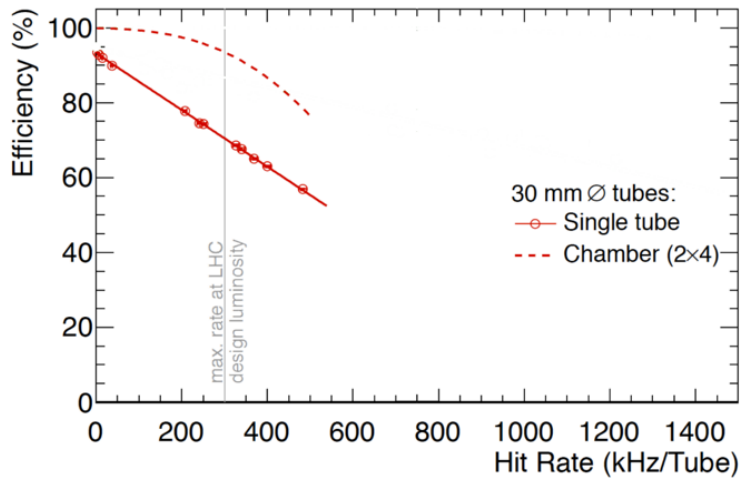


Figure 2.10: MDT tube hit (solid) and segment (dashed) efficiency as a function of hit rate per tube [57].

1113 The NSW will also work to alleviate the rate of fake triggers arising in the endcap. Figure 2.11 shows the
1114 extrapolated trigger rates as a function of the p_T threshold with and without the NSW upgrade. As the
1115 figure shows, the NSW upgrade will reduce the trigger rate considerably compared to the current endcap
1116 trigger system. At a p_T threshold of 20 GeV, the level-1 trigger rate drops from 20 kHz to 7 kHz. This
1117 reduction allows the p_T thresholds on muons to remain low, increasing the phase space of possible physics
1118 studies and in particular maintaining good acceptance for Higgs physics.

1119 2.3.2 NSW DETECTOR TECHNOLOGIES

1120 The NSW will use two new detector technologies - micromesh gaseous structure detectors (micromegas)
1121 and small-strip thin gap chambers (sTGCs) [57, 58]. The micromegas is more suited to tracking because

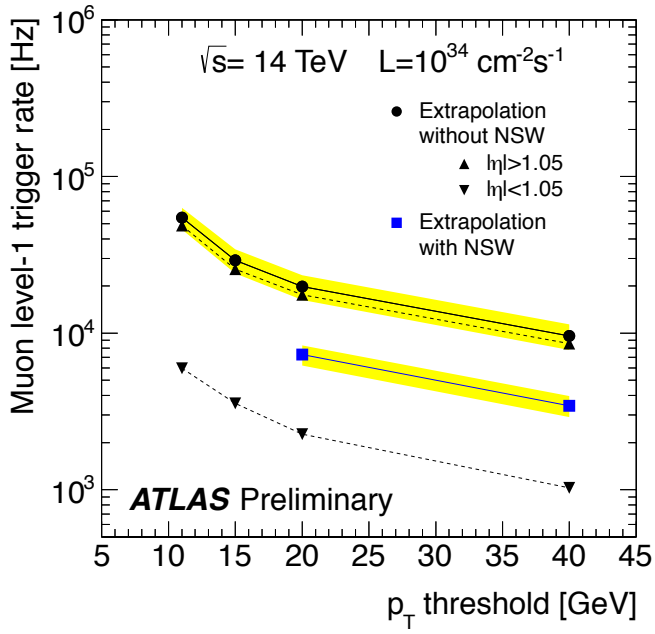


Figure 2.11: Trigger rate as a function of p_T threshold with and without the NSW upgrade [57].

of its good spatial resolution, while the sTGCs have better time resolution and are more suited for the trigger. However, both systems are capable of providing tracking and trigger information. To maintain full redundancy in cases of detector failure, both technologies will be used for tracking and trigger in the NSW.

1126 MICROMEGAS

1127 Micromegas detectors operate using a thin metallic mesh that sits approximately $100\ \mu\text{m}$ away from the
 1128 readout electrodes to create the amplification region. Above this mesh, there is a drift region on the order
 1129 of a few mm in length capped by a drift electrode. As a charged particle traverses the detector, it ionizes gas
 1130 and the electrons drift down towards readout strips. The timing of the drift can be used to reconstruct the
 1131 angle of traversal of the particle. This is illustrated in figure 2.12. The micromegas used in ATLAS will be
 1132 resistive micromegas, where the readout electrodes are topped with resistive strips [59]. This alleviates the
 1133 risk of sparking in the large area detectors that ATLAS will use.

1134 In ATLAS, the micromegas drift gap will be 5 mm and the amplification gap will be $128\ \mu\text{m}$. They are

1135 filled with the same gas mixture as the MDTs. They will be stacked in an octuplet in an XXUV-UVXX
 1136 geometry, where X refers to nominal strips and U and V refer to stereo strips at an angle of $\pm 1.5^\circ$. This
 1137 arrangement allows for measurement of the azimuthal coordinate and gives a large lever arm between the
 1138 straight strips for triggering purposes. Figure 2.12 shows the geometry of a single micromegas detector as
 1139 well as its operating principle [57].

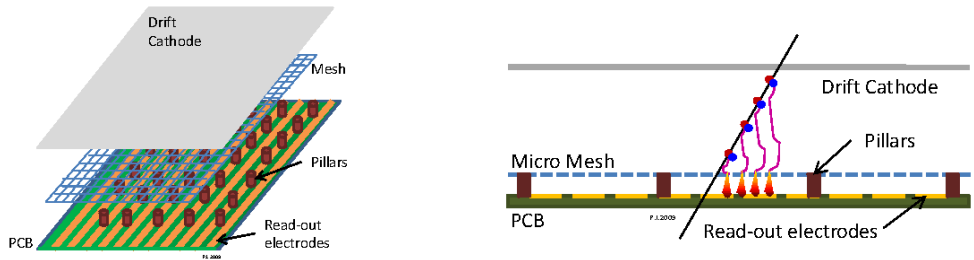


Figure 2.12: Illustrations of the geometry (left) and operating principle (right) of the micromegas detector [57]. When a muon passes through the drift gap and ionizes the gas, the timing and position of signals on the readout strips can be used to reconstruct the angle of traversal.

1140 sTGCs

1141 The sTGCs are similar to the TGCs currently in the ATLAS endcap muon system [44]. They consist
 1142 of gold-plated tungsten wires (with a 1.8 mm pitch) between two graphite cathode planes 1.4 mm away
 1143 from the wire plane. One cathode plane is capacitively coupled to pickup strips with a 3.2 mm pitch
 1144 (much smaller pitch than the TGCs), while the other is coupled to coarser pads that are used for defining
 1145 regions of interest in the sTGC trigger algorithm. Figure 2.13 shows the basic detector geometry.

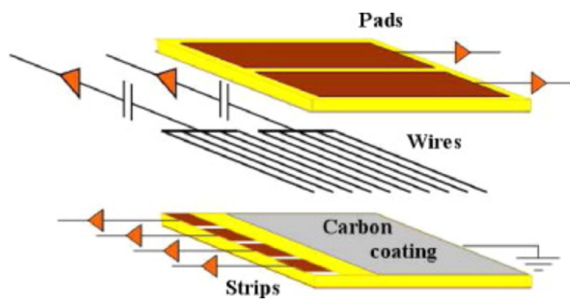


Figure 2.13: Geometry of the sTGC detector [57]. The wire plane acts as the anode, while carbon cathodes are capacitively coupled to pickup strips and pads.

1146 2.3.3 PHYSICS IMPACT

1147 Maintaining low p_T thresholds for muons while still staying within the trigger rate budget at Level 1 for the
1148 muon system (20 kHz) is crucial for physics analyses to be successful in high luminosity conditions. One
1149 realm where the lepton trigger threshold is especially important is in Higgs physics. In the $H \rightarrow WW^*$
1150 analysis, one of the W bosons is off shell and tends to decay to soft leptons. In associated production of a
1151 Higgs with a W , the lepton is also important because it provides the main handle which allows the event
1152 to be triggered. Without the NSW, analyses would be required to either raise the muon p_T threshold or
1153 only use muons triggered from the barrel muon system. Table 2.3 shows that both of these alternatives
1154 significantly reduce the Higgs signal efficiency. With the NSW, the signal efficiency is largely maintained
1155 and the triggers can remain unprescaled at lower p_T thresholds.

Threshold	$H \rightarrow b\bar{b}$ (%)	$H \rightarrow WW^*$ (%)
$p_T > 20 \text{ GeV}$	93	94
$p_T > 40 \text{ GeV}$	61	75
$p_T > 20 \text{ GeV} (\text{barrel only})$	43	72
$p_T > 20 \text{ GeV} (\text{with NSW})$	90	92

Table 2.3: Signal efficiencies for WH production with $H \rightarrow b\bar{b}$ and $H \rightarrow WW^* \rightarrow \mu\nu qq$ under different trigger configurations [57].

1156 2.4 OBJECT RECONSTRUCTION IN ATLAS

1157 ATLAS analyses first start by requiring the presence of certain reconstructed physics objects in the event.
1158 This section will present a brief overview of the algorithms used to reconstruct electrons, muons, jets (in-
1159 cluding b -jets), and missing energy². The performance of physics object reconstruction and identification
1160 will also be discussed as these are relevant to the analyses presented later. Figure 2.14 gives an overview of
1161 the different sub-detectors that each type of particle will interact with in ATLAS.

²Reconstruction algorithms for other objects, such as photons and hadronically decaying τ leptons, are not detailed here as these objects are not used in the results presented in this dissertation.

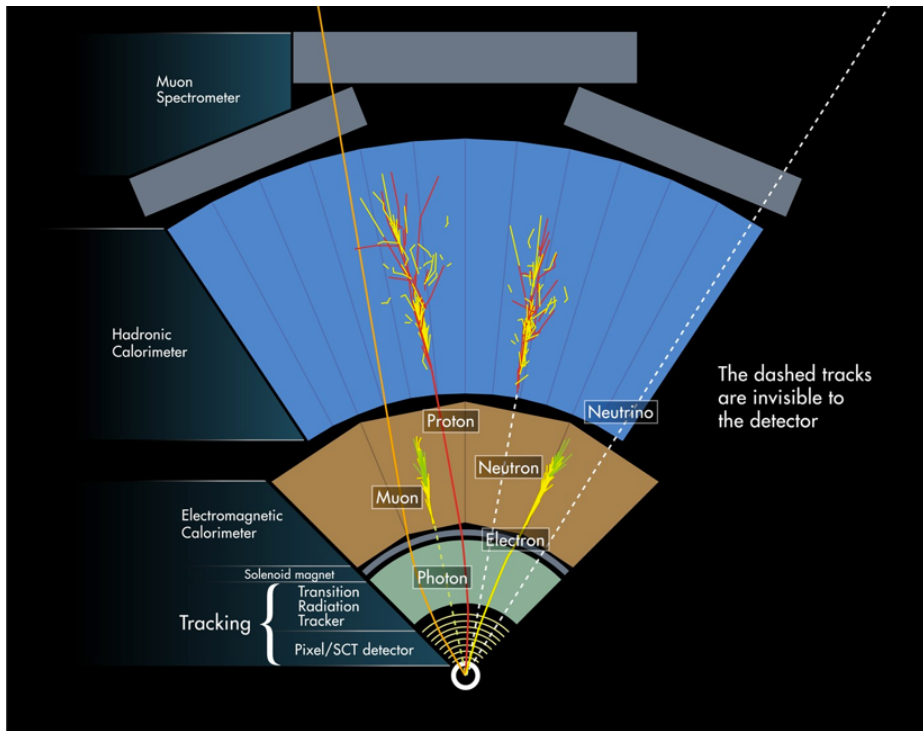


Figure 2.14: Illustration of particle interactions in ATLAS [60].

1162 2.4.I ELECTRONS

1163 Electrons in ATLAS will leave tracks in the inner detector and energy deposits in the electromagnetic
1164 calorimeter. The algorithm for recognizing the signature of electrons proceeds in two steps: reconstruction
1165 and identification.

1166 In reconstruction, an electron candidate is formed by matching EM calorimeter deposits with ID tracks.
1167 The algorithm first chooses seed clusters in the EM calorimeter by using a sliding window algorithm that
1168 searches for towers with transverse energy larger than 2.5 GeV. In addition to seed clusters, track candi-
1169 dates must be identified in the ID. The algorithm selects seed tracks with $p_T > 1$ GeV that do not fit well
1170 with a pion hypothesis. Once candidate tracks are selected, they are re-fit with a Gaussian Sum Filter (GSF)
1171 algorithm to estimate electron parameters [61]. Finally, an electron candidate is formed if at least one track
1172 matches to a seed cluster in the calorimeter. The full details of the reconstruction algorithm can be found
1173 in reference [62].

1174 Once an electron candidate is present, identification criteria must be applied in order to reject fake elec-

trons from background. Many different variables are used for this identification. They include information about the shower shape in the EM calorimeter and the amount of leakage into the hadronic calorimeter, as well as information from the ID and in particular the TRT. There are both selection requirement based and likelihood-based criteria that range from “loose” to “very tight”. For details, see reference [62]. In the $H \rightarrow WW^*$ analysis, both medium and very tight likelihood electrons are used depending on the electron p_T .

Figure 2.15 shows the algorithm’s reconstruction efficiency for true electrons with different identification criteria as well as the electron energy resolution in simulation [62, 63]. The reconstruction efficiency is measured using both the Z and J/ψ with 8 TeV data.

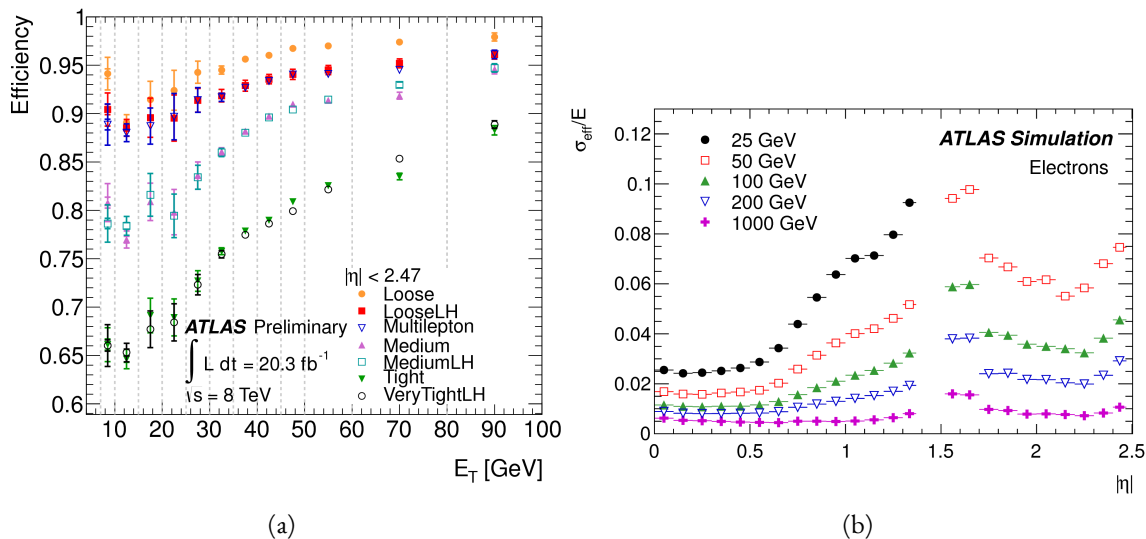


Figure 2.15: Electron performance: (a) reconstruction efficiency as a function of electron E_T [62] (b) energy resolution in simulation as a function of $|\eta|$ for different energy electrons [63].

2.4.2 MUONS

The ATLAS detector is designed to stop most particles before they reach the muon spectrometer. Muons, however, are minimum ionizing particles, meaning that they will not lose a significant amount of energy through interactions with the detector and will thus pass through. Therefore, the muon reconstruction works to match tracks in the muon spectrometer with tracks in the inner detector.

1189 The first step of reconstruction is to reconstruct local straight line tracks, called segments, in each muon
1190 chamber. Segments are then fit to larger tracks that traverse the entire muon spectrometer. Such muon
1191 tracks are referred to as “standalone” tracks (SA) as they only use information from the muon spectrometer.
1192 The standalone tracks are then matched to tracks in the inner detector to form “combined” (CB) muons,
1193 and both tracks are used to determine the momentum and direction of the muon. To improve acceptance,
1194 segment-tagged and calorimeter-tagged muons are also reconstructed. In these cases, ID tracks are matched
1195 to segments in the MS and calorimeter deposits consistent with a minimum ionizing particle, respectively.
1196 The details of the reconstruction can be found in reference [64].

1197 As with electrons, once muon candidates are reconstructed they have identification criteria applied to
1198 reduce background. These criteria include the χ^2 match between the ID and MS tracks, the number of
1199 hits in the ID, overall ID and MS track fit quality, and additional variables. In Run 1, the muons used are
1200 simply referred to as combined muons [64]. In Run 2, an improved reconstruction algorithm is used and
1201 criteria ranging from “loose” to “tight” are defined (similar to what is done with electrons) [65]. Figure 2.16
1202 shows the muon reconstruction efficiency (measured with the Z and J/ψ) and invariant mass resolution
1203 in $\sqrt{s} = 8$ TeV data.

1204 2.4.3 JETS

1205 When a quark or gluon is produced in collisions, it is not measured directly in ATLAS. Rather, due to
1206 QCD effects, it produces a collimated spray of hadrons in the direction of the original parton, which is
1207 known as a jet. Jets are reconstructed in ATLAS using energy deposits in the hadronic calorimeter. The
1208 first step is build “topological clusters” out of energy deposits in calorimeter cells [66, 67]. This is done
1209 using strategy where seed cells are chosen by picking cells whose energy measurements are four times the
1210 amount of noise expected for that cell. Adjacent cells with at least 2σ energy measurements are added to
1211 the cluster, then a final layer of clusters with energy above 0σ are added. Once calorimeter clusters are
1212 formed, they are clustered further into jet candidates. The analyses presented in this thesis use the anti- k_T
1213 jet clustering algorithm [68]. This algorithm defines a parameter R that appears in the denominator of
1214 the clustering distance metric and defines the radial size of the jet in η - ϕ space.

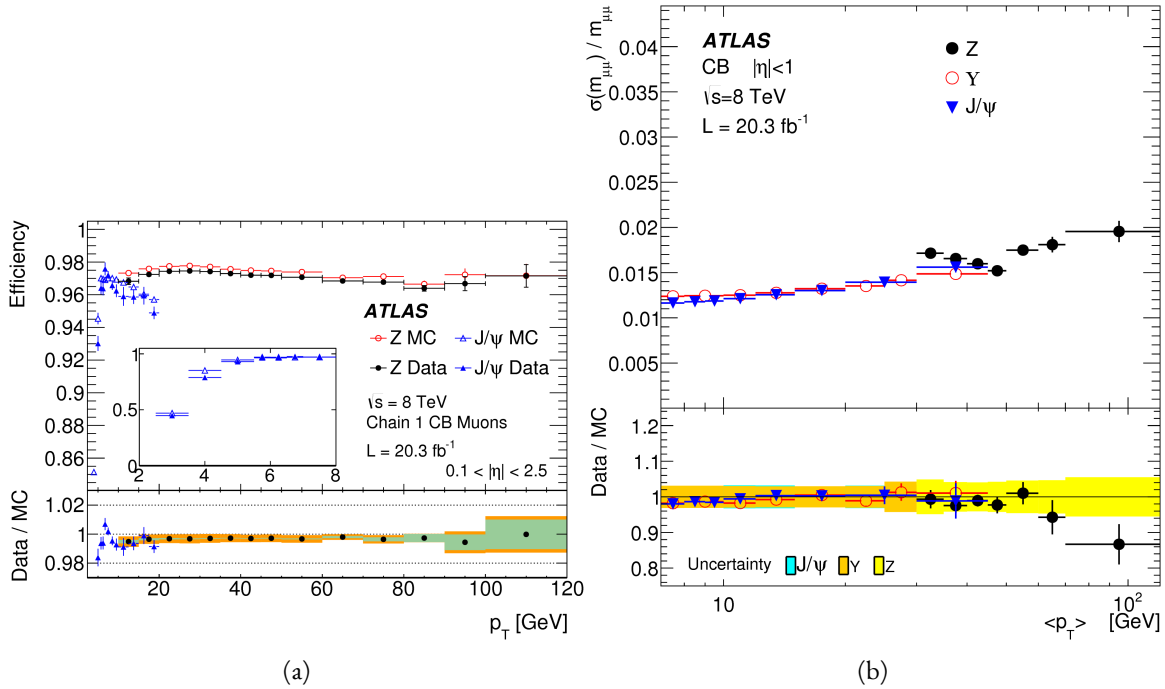


Figure 2.16: Muon performance in $\sqrt{s} = 8$ TeV data: (a) reconstruction efficiency as a function of muon p_T (b) dimuon mass resolution as a function of average p_T [64].

1215 The energy response of the calorimeter must be properly characterized in order to reconstruct the true
 1216 jet energy. Calorimeter clusters can be calibrated either with the EM calibration, where each cluster is as-
 1217 sumed to have come from the energy deposit of an electron or photon, or the LCW calibration, where local
 1218 cluster weights are computed to allow for local calibration of clusters as hadronic or electromagnetic. The
 1219 details of the jet energy calibration are not discussed here and are presented in reference [69]. Figure 2.17
 1220 shows the jet energy response after calibration in Monte Carlo as a function of the true p_T of the jet [69].

1221 Analyses often need to know how consistent a particular jet is with the primary vertex of the event in
 1222 order to avoid contamination from pileup interactions. One measure of this consistency is known as the
 1223 jet vertex fraction (JVF). The JVF is the ratio of tracks associated with a primary vertex to the total number
 1224 of tracks inside a jet. Jets from the primary interaction in the event should have a large fraction of tracks
 1225 consistent with the primary vertex and therefore have a large JVF value.

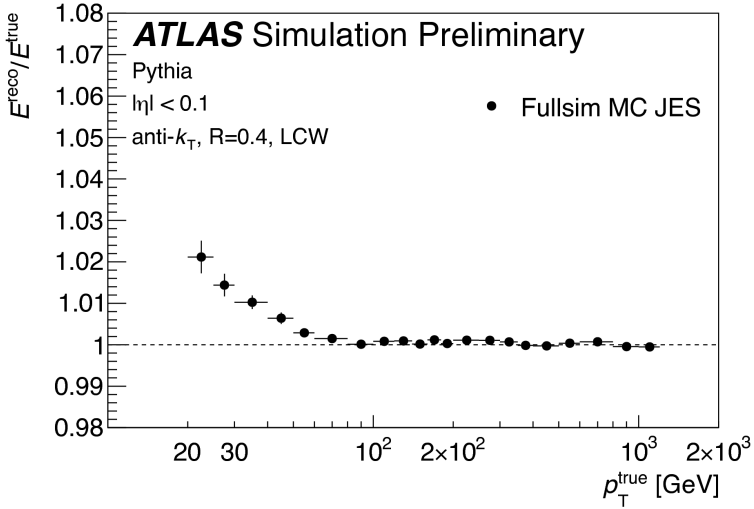


Figure 2.17: Jet energy response after calibration as a function of true p_T in simulation. The calibrations applied are derived for use in Run 2 data and simulation by ATLAS [69].

1226 2.4.4 b -TAGGING

1227 One important aspect of jet physics is the task of identifying the flavor of parton that produced the mea-
 1228 sured jet. While in general this is very difficult, jets from b -quarks offer an interesting case where such
 1229 identification is possible. B mesons have a lifetime on the order of 10^{-12} seconds, which makes a $c\tau$ of
 1230 0.5 mm [6]. This type of displaced decay vertex can be identified in detectors like ATLAS and allows b -jets
 1231 to be distinguished from other flavors of jets³. With boosts, B mesons can travel for several millimeters
 1232 before decaying.

1233 ATLAS uses several algorithms, including a multivariate machine learning technique, to identify jets
 1234 from b -quarks. The inputs to the multivariate algorithm are determined from lower level reconstruction
 1235 algorithms. There are three distinct algorithms that reconstruct variables which are used as input to the
 1236 multivariate technique.

1237 The first family of algorithms is referred to as IPxD (where the x can either be 2 or 3). These algorithms
 1238 use the transverse and longitudinal impact parameters d_0 and z_0 of the tracks inside a jet to determine their
 1239 consistency with the primary vertex. They use two or three dimensional (hence the x) templates for light

³Jets from charm quarks can also be detected in this way but they do not live quite as long so the displacement of the vertex is harder to distinguish

1240 flavor, charm, and bottom jets and then evaluate the likelihood of the jet coming from each of these types.

1241 The likelihood ratios are used as inputs to the multivariate algorithm.

1242 The next two algorithms used as input are referred to as the secondary vertex (SV) and JetFitter (JF)
1243 algorithms. The SV algorithm uses tracks inside the jet to fit for vertices that are displaced from the pri-
1244 mary vertex. The JF algorithm attempts to reconstruct the full flight path of the b by looking for multiple
1245 displaced vertices along the same line (as B decays often result in subsequent charm meson decays).

1246 In Run 1, the multivariate b -tagging algorithm used a neural network and was referred to as MV1. The
1247 details of this algorithm and its inputs are given in reference [70]. This algorithm is used for defining
1248 a veto on b -jets in the $H \rightarrow WW^* \rightarrow \ell\nu\ell\nu$ analysis presented in Part 2. In Run 2, the number of
1249 inputs was simplified and a boosted decision tree with 24 input variables was used, referred to as MV2 [71].
1250 The MV2 algorithm is a boosted decision tree incorporating twenty-four input variables constructed from
1251 three lower level input algorithms described above. This algorithm is used for b -tagging in the $X \rightarrow$
1252 $HH \rightarrow b\bar{b}b\bar{b}$ search presented in Part 3. Figure 2.18 summarizes the inputs to MV2. Figure 2.19 shows the
1253 performance of each of these algorithms in Run 1 and Run 2.

IP2D and IP3D (6 inputs)	SV1 (8 inputs)	JetFitter (8 inputs)
$\log(p_b/p_u)$	Mass	Mass
$\log(p_b/p_c)$	Energy fraction	Energy fraction
$\log(p_c/p_u)$	# tracks at vertex	# vertices
	# 2 track vertices	# tracks at vertex
	Lxy	# 1 track vertices
	L3d	# 2 track vertices
	3D significance	3D significance
	ΔR	ΔR
Kinematics (2 inputs)		
	p_T	
	η	

Figure 2.18: Summary of the inputs to the MV2 b -tagging algorithm.

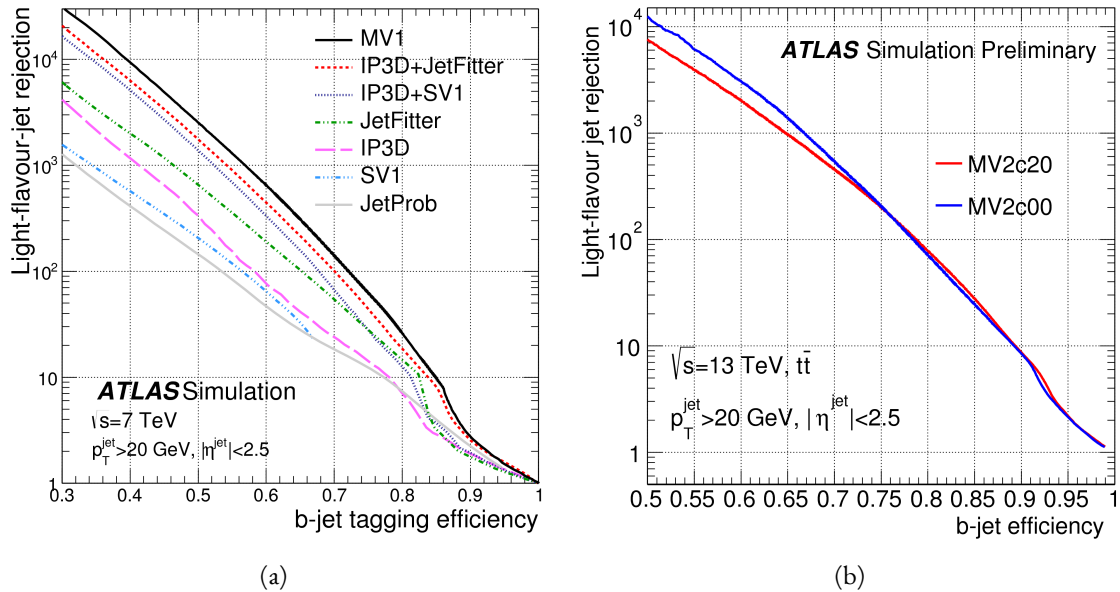


Figure 2.19: Light jet rejection ($1/\text{efficiency}$) vs. b -jet efficiency for MV1 and its input algorithms (a) [70] and MV2 (b) [71] in simulated $t\bar{t}$ events. The numbers in the algorithm names in (b) refer to the fraction of charm events used in the MV2 training.

1254 2.4.5 MISSING TRANSVERSE ENERGY

1255 As noted in figure 2.14, neutrinos produced in ATLAS will pass through the detector without interacting.
 1256 The only way of detecting the presence of weakly interacting particles like neutrinos (or BSM particles
 1257 that are long-lived) is to use missing transverse momentum. The basic principle of missing transverse en-
 1258 ergy is to use the momentum balance of the incoming protons to infer the presence of missing particles.
 1259 The net longitudinal momentum of the incoming partons that collide is not known (since each carries
 1260 an unknown fraction of the proton's momentum). However, the protons (and thus incoming partons)
 1261 have essentially no net momentum in the plane transverse to the beam line (the x - y plane). Therefore, if
 1262 there are no undetected particles in the final state, the transverse momenta of all of the final state particles
 1263 should balance. The magnitude of the imbalance in the transverse plane is known as missing transverse
 1264 momentum (E_T^{miss}).

1265 The basic calculation of missing transverse momentum from calorimeter cells is given in equation 2.4 [72].

1266

$$\begin{aligned} E_x^{\text{miss}} &= -\sum_{i=1}^{N_{\text{cell}}} E_i \sin \theta_i \cos \phi_i \\ E_y^{\text{miss}} &= -\sum_{i=1}^{N_{\text{cell}}} E_i \sin \theta_i \sin \phi_i \end{aligned} \quad (2.4)$$

1267 The E_T^{miss} calculation is separated into different terms based on the objects that the calorimeter clusters
 1268 are associated with. This way, each cell's contribution is calibrated appropriately according to the object.
 1269 This separation of terms used to define the E_T^{miss} in Run 1 is shown in equation 2.5 [72].

$$\begin{aligned} E_{x(y)}^{\text{miss,calo}} &= E_{x(y)}^{\text{miss},e} + E_{x(y)}^{\text{miss},\gamma} + E_{x(y)}^{\text{miss},\tau} + E_{x(y)}^{\text{miss,jets}} \\ &\quad + E_{x(y)}^{\text{miss,softjets}} + E_{x(y)}^{\text{miss},\mu} + E_{x(y)}^{\text{miss,CellOut}} \end{aligned} \quad (2.5)$$

1270 The CellOut term of the above equation corresponds to calorimeter cells with energy deposits that are
 1271 not associated with other objects. The soft jets term comes from cells associated to jets with p_T between
 1272 7 and 20 GeV, while the jets term comes from jets with $p_T > 20$ GeV. Because muons do not deposit
 1273 significant energy in the calorimeter, the muon momentum (after correction for the energy deposited in
 1274 the calorimeter for non-isolated muons) is used for the muon term [72]. The final E_T^{miss} is calculated using
 1275 equation 2.6.

$$E_T^{\text{miss}} = \sqrt{(E_x^{\text{miss}})^2 + (E_y^{\text{miss}})^2} \quad (2.6)$$

1276 Figure 2.20 shows the resolution of the components of the E_T^{miss} with different pileup suppression tech-
 1277 niques [73].

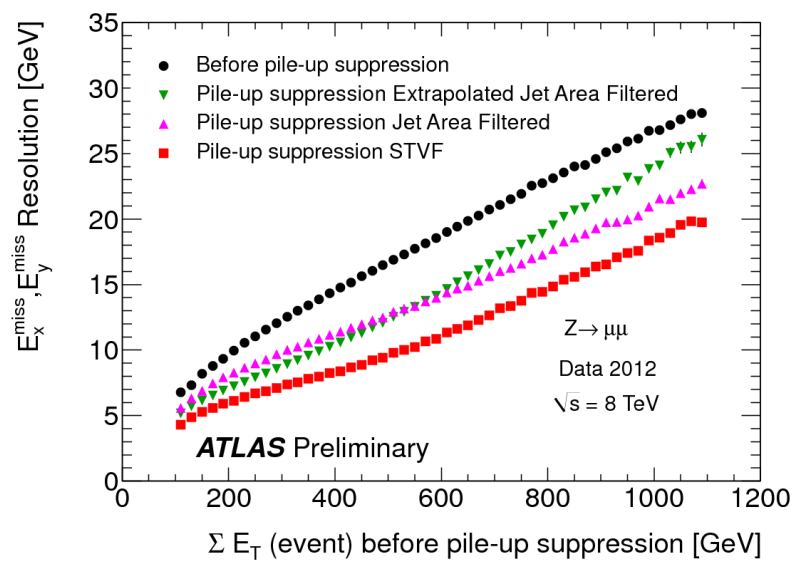


Figure 2.20: Resolution of E_T^{miss} components as a function of $\sum E_T$ before pileup suppression with different pileup techniques [73].

1278

Part II

1279

Observation and measurement of Higgs

1280

boson decays to WW^* in LHC Run I at

1281

$\sqrt{s} = 7$ and 8 TeV

*Basic research is what I am doing when I don't know what
I am doing.*

Wernher von Braun

3

1282

1283

$H \rightarrow WW^* \rightarrow \ell\nu\ell\nu$ Analysis Strategy

1284 3.1 INTRODUCTION

1285 This chapter presents an overview of the strategy for searching for a Higgs boson in the $H \rightarrow WW^* \rightarrow$
1286 $\ell\nu\ell\nu$ decay topology. Its purpose is to define in broad terms how the search and measurement are under-
1287 taken, discussing common aspects of the analysis before going into the details of individual sub-categories.
1288 First, the properties of the Higgs signal are discussed and the associated backgrounds are presented. Next,
1289 the observables used to enhance the signal to background ratio are defined. Finally, the parameters of in-
1290 terest in the search and measurement will be shown, along with a brief overview of the statistical treatment
1291 of the final Higgs candidates.

1292 Following this chapter, three different results from the $H \rightarrow WW^* \rightarrow \ell\nu\ell\nu$ channel are shown.
1293 Chapter 4 presents the discovery and subsequent measurement of Higgs boson production in gluon fusion
1294 mode and the role of the $H \rightarrow WW^*$ channel. Chapter 5 shows the search and first evidence in ATLAS
1295 for the Vector Boson Fusion (VBF) production mode of the Higgs. Finally, chapter 6 shows the combined

1296 Run 1 $H \rightarrow WW^*$ results for the measurement of the Higgs cross section and relative coupling strengths
1297 to other SM particles.

1298 3.2 THE $H \rightarrow WW^* \rightarrow \ell\nu\ell\nu$ SIGNAL IN ATLAS

1299 The signal studied in this and subsequent chapters is the Higgs boson in the WW^* final state, where each
1300 W boson subsequently decays into a charged lepton and a neutrino. In the simplest decay path, the final
1301 state consists of two neutrinos and two charged leptons, each of which can be either an electron or a muon.
1302 If a W decays to a τ lepton, only leptonic decays of the τ are considered. The τ leptons produce additional
1303 neutrinos in the final state but still yield two charged leptons (where each lepton is an electron or muon).
1304 Neutrinos are not detected in ATLAS, so the final state ultimately consists of two reconstructed leptons
1305 and missing transverse momentum. Final states where both of the charged leptons are electrons or muons
1306 are referred to as the “same flavor” ($ee/\mu\mu$) final states, while those with one electron and one muon are
1307 referred to as “different flavor” ($e\mu$ or μe).

1308 There can be additional jets produced in association with the Higgs boson. As described in detail in
1309 Chapter 1, if the Higgs is produced via vector boson fusion production, there will be two additional forward
1310 jets in the event. In gluon fusion, one or more jets can be produced through initial state radiation from
1311 the incoming gluons. Because of the varying background composition as a function of jet multiplicity,
1312 each bin in this variable has its own dedicated requirements applied in the search and measurement. The
1313 $n_j = 0$ and $n_j = 1$ bins are dedicated to gluon fusion production, while the $n_j \geq 2$ bin has separate
1314 dedicated searches for ggF and VBF production.

1315 Figure 3.1 shows the relative branching fractions for the $H \rightarrow WW^*$ process, calculated from the Par-
1316 ticle Data Group values for the W and τ branching ratios [6]. The largest branching ratio corresponds
1317 to both W bosons decaying to quark pairs at 45.44%. The second largest ratio is for one W decaying lep-
1318 tonically and the other decaying to quarks, a branching ratio of 34.18%. In all cases, ℓ denotes either an
1319 electron or muon, and the leptonic branching ratios of the τ are included. For example, the $\ell\nu qq$ final
1320 state includes one W decaying to $e\nu$, $\mu\nu$, or $\tau\nu$. In the case of the $W \rightarrow \tau\nu$ decay, the τ lepton then
1321 decays to an electron or muon via $\tau \rightarrow \nu_\tau \ell \nu_\ell$. Final states with a τ_h refer to hadronic decays of the τ . The

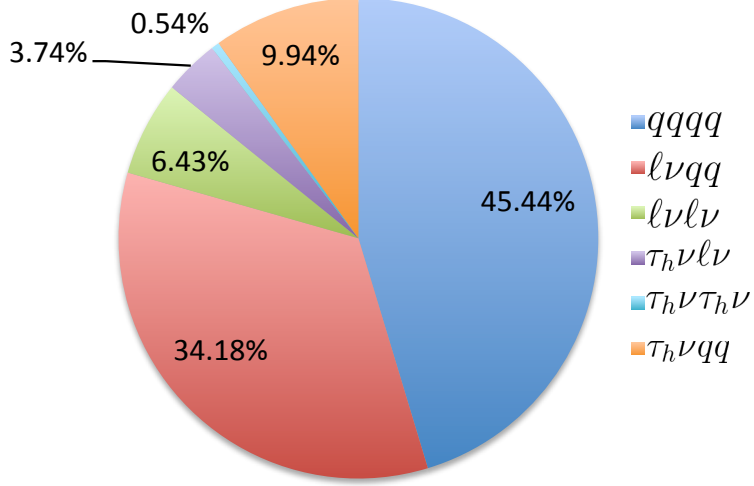


Figure 3.1: Branching ratios for a WW system. q refers to quarks. ℓ can be either an electron or muon, and the leptonic branching ratios of the τ are included. For example, the $\ell\nu qq$ final state includes one W decaying to $e\nu$, $\mu\nu$, or $\tau\nu$. τ_h refer to hadronic decays of the τ .

branching ratio of the $\ell\nu\ell\nu$ final state is 6.43%.

While the $\ell\nu\ell\nu$ final state is not a large fraction of the branching ratio, there are significant advantages to using this channel in an analysis. First, both the $qqqq$ and $\ell\nu qq$ channels suffer from a large QCD multijet background, which is often difficult to model. Second, events in the the $\ell\nu\ell\nu$ channel in data can be triggered more efficiently due to the presence of two leptons.

Figure 3.2 delineates the different signal regions used in the gluon fusion and vector boson fusion analyses of $H \rightarrow WW^*$. Signal regions are defined using jet multiplicity and the flavor combination of the final state leptons.

3.3 BACKGROUND PROCESSES

Many processes from the Standard Model can also produce a final state with two leptons and missing transverse momentum. This section describes the dominant backgrounds to Higgs production and further explains how they can be reduced. Table 3.1 summarizes the different background processes.

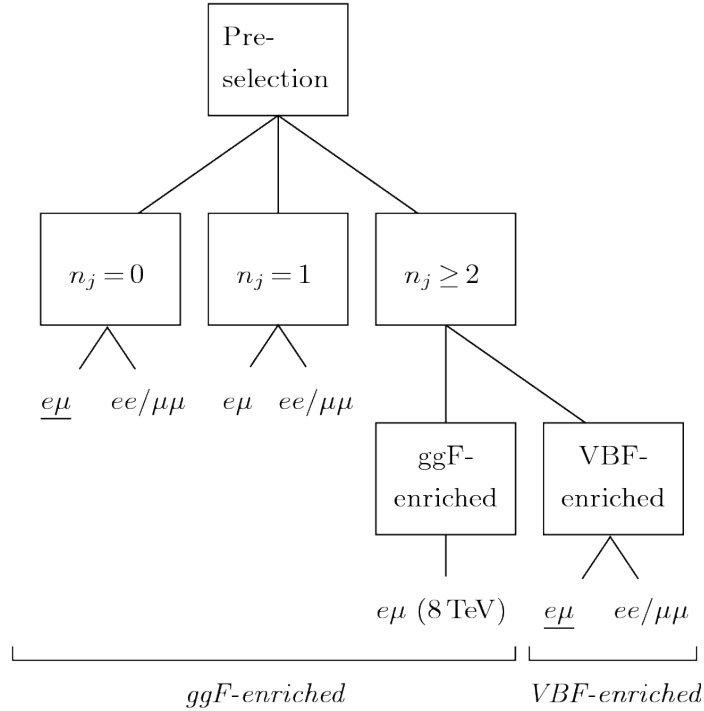


Figure 3.2: An illustration of the unique analysis signal regions [74]. The analysis is split by jet multiplicity and lepton flavor after pre-selection requirements. The most sensitive regions for both gluon fusion and vector boson fusion production are underlined.

1334 3.3.1 STANDARD MODEL WW PRODUCTION

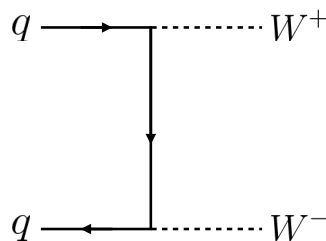


Figure 3.3: Feynman diagram for Standard Model WW production

1335 Non-resonant Standard Model diboson production, as shown in figure 3.3, is an irreducible background
1336 to Higgs boson production in the WW final state. It produces the same exact final state objects, namely
1337 leptonically decaying W bosons. There are no additional objects in the final state that allow for back-
1338 ground reduction. Therefore the analysis solely relies on the correlations between the leptons to reduce
1339 this background.

1340 3.3.2 TOP QUARK PRODUCTION

1341 Top quark production can mimic the Higgs in the WW^* final state as well. Top quarks can be produced
1342 either in pairs ($t\bar{t}$ production) or singly (s -channel, t -channel, or associated production Wt). The domi-
1343 nant top background are $t\bar{t}$ and Wt production.

1344 Because top quarks decay via $t \rightarrow Wb$, top pair production can produce a final state with two W bosons
1345 that then decay leptonically. In Wt production, there are two real W bosons produced, as with $t\bar{t}$. In
1346 both cases, there is at least one b -jet in the final state. By vetoing on the presence of b -jets, these top quark
1347 backgrounds can be reduced. Figure 3.4 shows the Feynman diagrams for $t\bar{t}$ and Wt production.

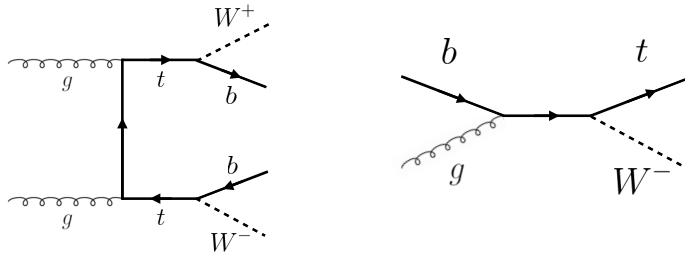


Figure 3.4: Feynman diagrams for top pair production (left) and Wt production (right).

1348 3.3.3 W +JETS BACKGROUND

1349 Single W boson production in association with jets is a unique background to Higgs production. The
1350 other backgrounds considered thus far have all included two prompt leptons, each decaying from a W
1351 boson, in the final state. In W +jets production, however, only one reconstructed lepton originates from
1352 a W . The second reconstructed lepton is either an algorithmic “fake” or the result of non-prompt decays.
1353 In the first case, the lepton is a jet misidentified as a lepton by either the electron or muon reconstruction
1354 algorithms. In the second case, the lepton may be a real lepton but coming from semi-leptonic decays of
1355 particles inside the shower of the jet. This background can be reduced by requiring that the reconstructed
1356 lepton have little activity in the surrounding region of the calorimeter (also known as an “isolation”). Fig-
1357 ure 3.5 shows the Feynman diagram for W +jets production.

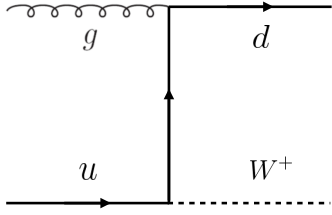


Figure 3.5: An example Feynman diagram of $W + \text{jets}$ production.

1358 3.3.4 $Z/\gamma^* + \text{JETS BACKGROUND}$

1359 Production of a Z boson or virtual photon (also known as Drell-Yan and denoted with Z/γ^*) in associa-
 1360 tion with jets is also a background to Higgs production. The Z boson decays to two leptons of the same
 1361 flavor. However, the background is present in both the same flavor and different flavor samples. When the
 1362 Z/γ^* decays directly to electrons or muons, the background enters the same flavor final state sample, and
 1363 when it decays to two τ leptons the background can enter the different flavor sample as well. Figure 3.6
 1364 shows the production of a Z in association with one jet. Because there are no neutrinos in this final state,
 1365 variables like E_T^{miss} can be used to reduce the background¹.

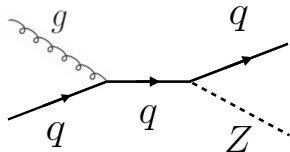


Figure 3.6: An example Feynman diagram of $Z + \text{jets}$ production.

1366 3.3.5 SUBDOMINANT BACKGROUNDS

1367 There are additional processes which contribute to the background composition. These backgrounds are
 1368 subdominant and contribute less to the total background estimate than those discussed previously. The

¹The E_T^{miss} cut is much more effective for the reduction of Z/γ^* production in the same flavor final state. If the background enters the different flavor final state through τ decays, there will be neutrinos present. Other requirements on the lepton invariant mass are made to reduce the $Z/\gamma^* \rightarrow \tau\tau$ background.

1369 first process is referred to as VV or “Other diboson” processes and includes multiple Standard Model
1370 diboson processes, including WZ , ZZ , $W\gamma$, $W\gamma^*$, and $Z\gamma$ production. Additionally, there is a back-
1371 ground contribution from QCD multijet production. While the cross section for this process is large, its
1372 contribution to the WW^* final state is small because two jets must be misidentified as leptons.

Category	Process	Description
SM WW	$WW \rightarrow \ell\nu\ell\nu$	Real leptons and neutrinos
Top quark production	$t\bar{t} \rightarrow WbW\bar{b} \rightarrow \ell\nu b\ell\nu\bar{b}$	Real leptons, untagged b s
	$tW \rightarrow WbW \rightarrow \ell\nu\ell\nu b$	Real leptons, untagged b
	$t\bar{b}, t\bar{q}\bar{b}$	Untagged b , jet misidentified as lepton
Drell-Yan	$Z/\gamma^* \rightarrow ee, \mu\mu$	“Fake” E_T^{miss}
	$Z/\gamma^* \rightarrow \tau\tau \rightarrow \ell\nu\nu\ell\nu\nu$	Real leptons and neutrinos
Other dibosons	$ZZ \rightarrow \ell\ell\nu\nu$	Real leptons and neutrinos
	$W\gamma^*, WZ \rightarrow \ell\nu\ell\ell, ZZ \rightarrow \ell\ell\ell\ell$	Unreconstructed leptons
	$W\gamma, Z\gamma$	γ reconstructed as e , unreconstructed lepton
$W + \text{jets}$	$Wj \rightarrow \ell\nu j$	Jet reconstructed as lepton
QCD multijet	jj	Jets reconstructed as leptons

Table 3.1: A summary of backgrounds to the $H \rightarrow WW^* \rightarrow \ell\nu\ell\nu$ signal.

1373 3.4 SHARED SIGNAL REGION SELECTION REQUIREMENTS

1374 As presented in section 3.2, there are many different combinations of physics objects that can define a
1375 $H \rightarrow WW^* \rightarrow \ell\nu\ell\nu$ final state. The multiplicity of jets and the flavor combinations of the leptons
1376 both lead to many potential signal regions. Additionally, signal regions can be optimized separately to be
1377 sensitive to the distinct production modes of the Higgs. Gluon fusion, vector boson fusion, and associated
1378 production of a Higgs all lead to unique final state topologies. While there are different optimizations
1379 possible in each signal region, there are also some commonly shared selections that will be described here.

1380 3.4.1 EVENT PRE-SELECTION

1381 Before being sorted into the distinct signal regions, basic requirements are applied to the reconstructed
1382 objects in the event to select Higgs-like event candidates. First, two oppositely charged leptons are required.
1383 Once the leptons are selected, the last requirement for event pre-selection is the presence of neutrinos.
1384 E_T^{miss} is used as a proxy for the combined neutrino momentum in the transverse plane.

1385 In general, the signal tends to have higher values of E_T^{miss} than backgrounds, especially if these back-
 1386 grounds do not contain neutrinos in the final state. It is possible mis-measurements of objects in the detec-
 1387 tor can lead to imbalances in the transverse plane. When such a mis-measurement occurs, the E_T^{miss} vector
 1388 in the transverse plane will often point in the same direction as the mis-measured object. Therefore, a new
 1389 variable, $E_{T,\text{rel}}^{\text{miss}}$, is used in the pre-selection. $E_{T,\text{rel}}^{\text{miss}}$ is defined in equation 3.1.

$$E_{T,\text{rel}}^{\text{miss}} = \begin{cases} E_T^{\text{miss}} \sin \Delta\phi_{\text{near}} & \text{if } \Delta\phi_{\text{near}} < \pi/2 \\ E_T^{\text{miss}} & \text{otherwise,} \end{cases} \quad (3.1)$$

1390 If the closest object to the E_T^{miss} vector is within $\pi/2$ radians in the transverse plane, the E_T^{miss} is projected
 1391 away from this object. Otherwise, the normal E_T^{miss} vector is used. Figure 3.7 shows a graphical illustration
 of this concept.

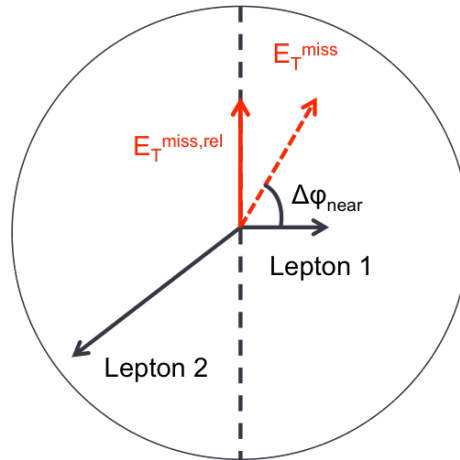


Figure 3.7: A graphical illustration of the $E_{T,\text{rel}}^{\text{miss}}$ calculation. The black arrows represent the directions of the two leptons in the transverse plane. The dotted red arrow represents E_T^{miss} , while the solid red arrow is the resulting $E_{T,\text{rel}}^{\text{miss}}$ after projecting away from lepton 1.

1392 Once the lepton and E_T^{miss} pre-selections are made, the analysis is divided into different regions accord-
 1393 ing to jet multiplicity.
 1394

1395 3.4.2 JET MULTIPLICITY

1396 Jet multiplicity, denoted as n_j , is used to sub-divide the analysis into distinct signal regions. By creating
 1397 separate signal regions, each bin in jet multiplicity becomes sensitive to different modes of Higgs produc-
 1398 tion and different backgrounds. For example, the $n_j \geq 2$ region is more sensitive to VBF production
 1399 because of the two high momentum jets produced at matrix element level. For gluon fusion production
 1400 to enter this bin, two initial state radiation jets must be emitted.

1401 Figure 3.8 shows the jet multiplicity in both the different flavor and same flavor regions after the pre-
 1402 selection. It also shows the background composition in the bins of the number of b -tagged jets, n_b . A
 1403 few trends from this distribution are worth noting. The first is that the Drell-Yan background dominates
 1404 in the same flavor channels for $n_j \leq 1$. Second, the top background becomes a clear contributor to the
 1405 total background for $n_j \geq 1$. Lastly, the SM WW production dominates in the $n_j = 0$ bin, as it is an
 1406 irreducible background to $H \rightarrow WW^*$ production. Because of these distinct features, each jet multiplicity
 1407 bin is treated separately.

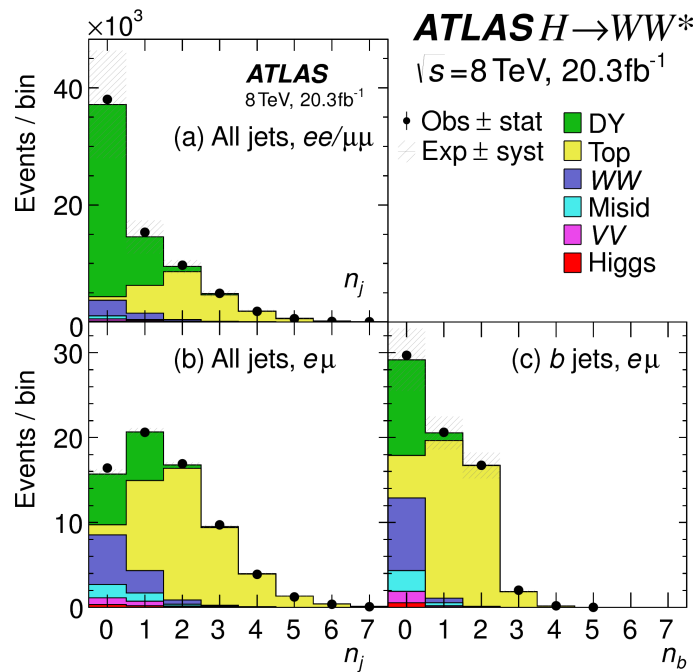


Figure 3.8: Predicted backgrounds (compared with data) as a function of the number of jets, n_j (a and b), and the number of b -tagged jets, n_b (c), after pre-selection requirements. Panel a shows n_j in the same flavor sample, while panels b and c show the n_j and n_b distributions in the different flavor sample.

1408 3.4.3 LEPTON CORRELATIONS IN $H \rightarrow WW^* \rightarrow \ell\nu\ell\nu$

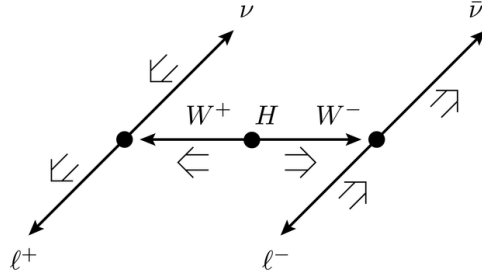


Figure 3.9: A cartoon of the WW final state. Momenta are represented with thin arrows, spins with thick arrows [74].

1409 The final state leptons in the $H \rightarrow WW^* \rightarrow \ell\nu\ell\nu$ channel will exhibit unique correlations due
 1410 to the fact that they arise from the decay of a spin zero resonance. These characteristics are present in
 1411 $H \rightarrow WW^* \rightarrow \ell\nu\ell\nu$ decays regardless of the production mode being studied. In particular, the spins
 1412 of the final state leptons and neutrinos must all cancel, as shown in figure 3.9. Because the neutrino has a
 1413 left handed chirality and the anti-neutrino has a right handed chirality (in the massless neutrino approx-
 1414 imation), the spin and momentum of the particles will be anti-aligned and aligned, respectively. In the
 1415 transverse plane, the momenta of all four final state objects must cancel as well. With the constraint of
 1416 having both the momenta and the spin alignments cancel, the final state kinematics strongly prefer having
 1417 a small angle between the leptons in the transverse plane (low $\Delta\phi_{\ell\ell}$). This angular correlation will also
 1418 lead to low values of the di-lepton invariant mass $m_{\ell\ell}$. These unique signal final state kinematic correla-
 1419 tions are exploited to define the ultimate signal region in both the gluon fusion and vector boson fusion
 1420 signal regions.

1421 3.5 BACKGROUND REDUCTION IN SAME-FLAVOR FINAL STATES

1422 As described in section 3.4.2, the background composition of the same flavor final states is different from
 1423 that of the different flavor states. In particular, Drell Yan processes play a much larger role because the
 1424 Z/γ^* decays to same flavor leptons. Because real neutrinos are absent in the Z/γ^* decays to ee and $\mu\mu$, a
 1425 requirement on E_T^{miss} should largely reduce the background. However, as this section will demonstrate,

1426 with increasing pileup conditions the resolution of the calorimeter-based E_T^{miss} degrades greatly. There-
1427 fore, two new variables for Z/γ^* background reduction are constructed and described in this section.

1428 **3.5.1 PILEUP AND E_T^{miss} RESOLUTION**

1429 Secondary interactions of protons in the colliding bunches of the LHC (known as pileup interactions,
1430 described in detail in Chapter 2) deposit energy into the ATLAS calorimeter in addition to the energy that
1431 comes from the hard scatter process of interest. The calculation of E_T^{miss} is fundamentally like a Poisson
1432 process - summing up all of the energy deposits in individual calorimeter cells or clusters is similar to a
1433 counting experiment. The error on a mean of N in a Poisson distribution is \sqrt{N} , so the energy resolution
1434 scales as \sqrt{E} . As more energy is deposited in the calorimeter, the E_T^{miss} resolution degrades, meaning that
1435 the E_T^{miss} resolution is particularly sensitive to LHC instantaneous luminosity conditions.

1436 Figure 3.10 shows an event display of a Z/γ^* + jets event candidate with the twenty-five reconstructed
1437 primary vertices. This display illustrates that while the interaction of interest only has tracks coming from
1438 the hardest primary vertex, all of the secondary interactions deposit energy in the calorimeter as well.

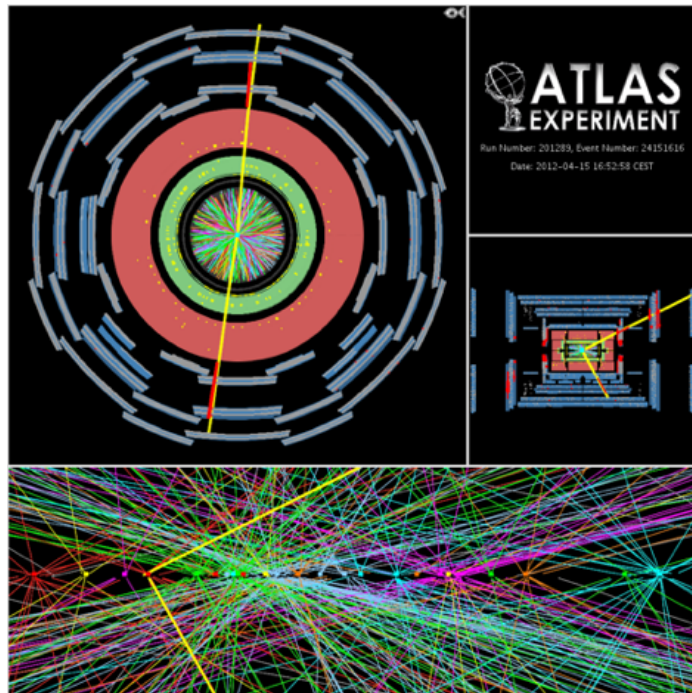


Figure 3.10: An event display of a Z/γ^* + jets event illustrating the effect of pileup interactions.

1439 Figure 3.11 shows the RMS of the E_T^{miss} distribution in $Z \rightarrow \mu\mu$ events (where there are no real neutrinos) as a function of the number of the average number of interactions. Under 2011 LHC conditions, this
 1440 RMS was approximately 9 GeV, while under 2012 running conditions the resolution worsened to 12 GeV.
 1441 The increase in pileup dilutes the ability of the E_T^{miss} variable to reduce the Z/γ^* background.
 1442

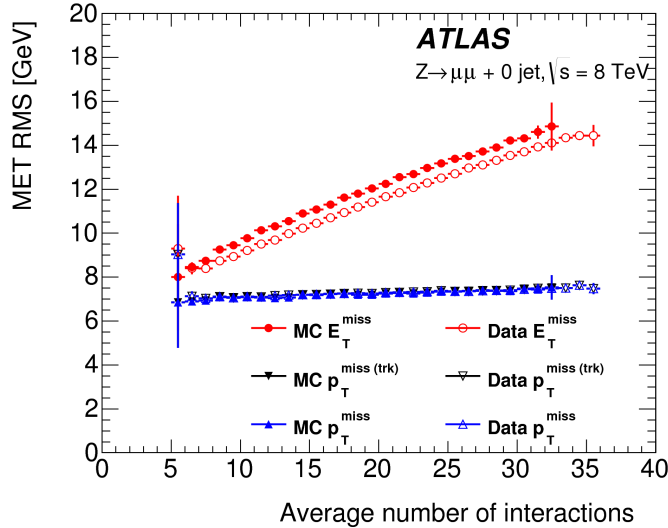


Figure 3.11: The RMS of different missing transverse momentum definitions as a function of the average number of interactions per bunch crossing.

1443 3.5.2 TRACK-BASED DEFINITIONS OF MISSING TRANSVERSE MOMENTUM

1444 Because the increasing number of secondary proton-proton interactions degrades calorimeter-based E_T^{miss}
 1445 resolution, a new variable using only contributions from the primary interaction vertex is necessary to
 1446 further reduce the Z/γ^* background. While it is not possible to associate calorimeter energy deposits
 1447 with a particular vertex, individual charged particle tracks in the Inner Detector are associated to unique
 1448 vertices. Thus, two track-based definitions of missing transverse momentum, using only tracks coming
 1449 from the primary vertex in the event, are used in the analysis. These variables are not intended to substitute
 1450 E_T^{miss} , as they only account for charged particles and do not measure neutrals. However, the track-based
 1451 variables serve as a confirmation that any measured momentum imbalance is coming from real particles
 1452 and not detector effects. The simplest variable, $p_T^{\text{miss}(\text{trk})}$, is the vectorial sum of the p_T of all of the tracks
 1453 from the primary vertex and the selected leptons (excluding the tracks associated with the selected leptons)

¹⁴⁵⁴ to avoid double counting). Equation 3.2 defines $p_T^{\text{miss}(\text{trk})}$.

$$p_T^{\text{miss}(\text{trk})} = - \left(\sum_{\text{selected leptons}} p_T + \sum_{\text{other tracks}} p_T \right), \quad (3.2)$$

¹⁴⁵⁵ To further improve the resolution on the missing transverse momentum, the variable p_T^{miss} is used as de-
¹⁴⁵⁶ fined in equation 3.3. For selected leptons and jets, the nominal p_T measurements are used, as the calorime-
¹⁴⁵⁷ ter information improves the p_T resolution of the objects by taking into account the presence of neutral
¹⁴⁵⁸ particles in showers. The soft component of the missing transverse momentum, which is more suscep-
¹⁴⁵⁹ tible to spurious contributions from pileup interactions, is estimated using tracks instead of calorimeter
¹⁴⁶⁰ measurements.

$$p_T^{\text{miss}} = - \left(\sum_{\text{selected leptons}} p_T + \sum_{\text{selected jets}} p_T + \sum_{\text{other tracks}} p_T \right), \quad (3.3)$$

¹⁴⁶¹ Figure 3.11 illustrates that these two new variables accomplish their intended purpose. The resolution as a
¹⁴⁶² function of mean number of interactions for both $p_T^{\text{miss}(\text{trk})}$ and p_T^{miss} is much flatter than the dependence
for E_T^{miss} . Figure 3.12 shows the difference between the true and reconstructed values of missing transverse

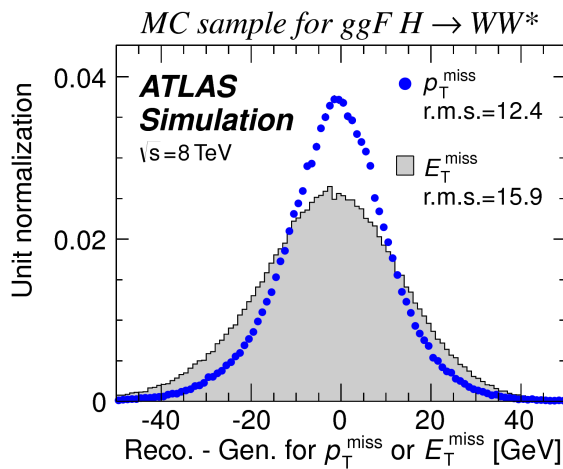


Figure 3.12: The difference between the true and reconstructed values of the missing transverse momentum in a gluon fusion signal sample using both track-based (p_T^{miss}) and calorimeter-based E_T^{miss} definitions [74]. p_T^{miss} shows a significant improvement in resolution over E_T^{miss} .

¹⁴⁶³

¹⁴⁶⁴ momentum using both the track-based p_T^{miss} and calorimeter based E_T^{miss} . The RMS of the distribution

1465 improves by 3.5 GeV when using p_T^{miss} .

1466 3.5.3 DISTINGUISHING Z/γ^* +JETS AND $H \rightarrow WW^*$ TOPOLOGIES

1467 In addition to measuring missing transverse momentum, another variable can be constructed to exploit
1468 kinematic and topological differences between the Z/γ^* background and $H \rightarrow WW^*$ signal. Because
1469 there are no real neutrinos in the final state (in the case of $Z/\gamma^* \rightarrow ee, \mu\mu$ decays), the dilepton system
1470 will be balanced with the jets produced in the hard scatter. A new variable, f_{recoil} , is constructed to es-
1471 timate the balance between the dilepton system and recoiling jets and is defined in equation 3.4. The
1472 transverse plane is divided into four sections, or quadrants, with one quadrant centered on the dilepton
1473 vector. The numerator of f_{recoil} is the magnitude of the vectorial sum of the p_T of jets in the quadrant
1474 opposite the dilepton system, weighted the Jet Vertex Fraction (JVF, described in chapter 2) of each jet.
1475 The denominator is the magnitude of the dilepton p_T .

$$f_{\text{recoil}} = \left| \sum_{\text{jets } j \text{ in } \wedge} \text{JVF}_j \cdot \mathbf{p}_T^j \right| / p_T^{\ell\ell}. \quad (3.4)$$

1476 Figure 3.13 shows a shape comparison of the f_{recoil} distribution in a simulated Z/γ^* + jets sample, a
1477 $H \rightarrow WW^*$ signal sample, and other backgrounds that contain real neutrinos. The Z/γ^* + jets events
1478 tend to be more balanced between the dilepton system and recoiling jets, while the processes containing
1479 real neutrinos are less balanced in the transverse plane. Thus, a requirement on f_{recoil} will reduce the Z/γ^*
1480 + jets background while maintaining a good signal efficiency.

1481 3.5.4 OPTIMIZING BACKGROUND REDUCTION SELECTION REQUIREMENTS

1482 The requirements on $p_T^{\text{miss}(\text{trk})}$ and f_{recoil} used to reduce the Z+jets background must be optimized to
1483 maximize expected signal significance in the same flavor channels. Figure 3.14 shows an optimization of
1484 the combination of the two requirements in the gluon fusion zero jet bin. Each bin shows the expected
1485 signal significance if the $p_{T,\text{rel}}^{\text{miss}(\text{trk})}$ (the track-based version of $E_{T,\text{rel}}^{\text{miss}}$) is required to be greater than the left
1486 edge of the bin and the f_{recoil} is required to be less than the top edge of the bin. The figure shows that the
1487 best signal significance comes from requiring low values of $f_{\text{recoil}} (< 0.05)$ and $p_{T,\text{rel}}^{\text{miss}(\text{trk})}$ values greater

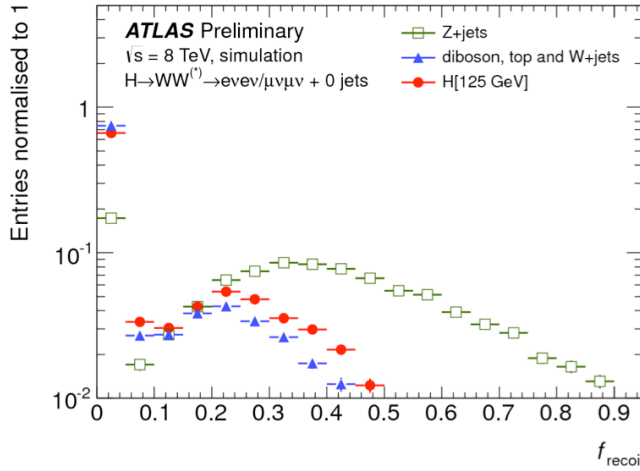


Figure 3.13: Comparison of f_{recoil} distributions for $Z/\gamma^* + \text{jets}$, $H \rightarrow WW^*$, and other backgrounds with real neutrinos.

than 45 GeV.

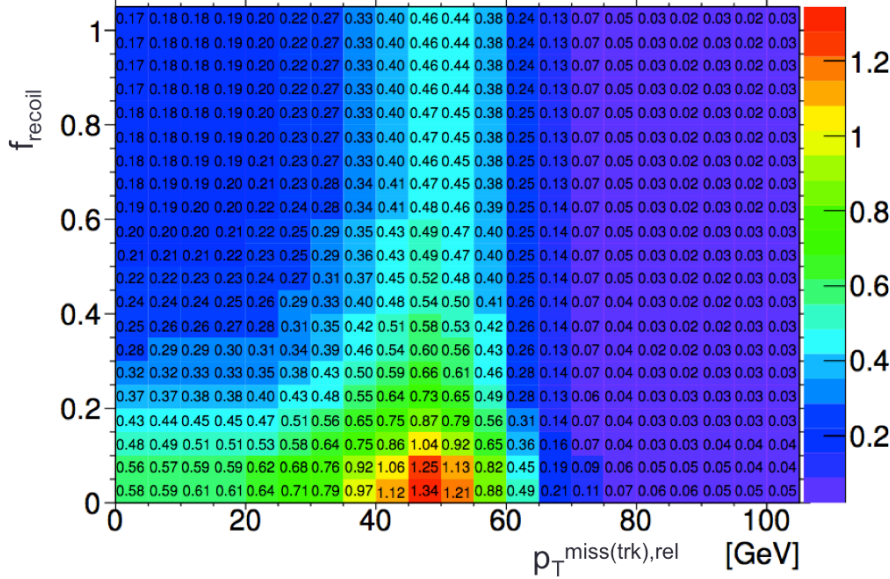


Figure 3.14: Signal significance as a function of required value for f_{recoil} and $p_{\text{T},\text{rel}}^{\text{miss(trk)}}$ in the ggF $H \rightarrow WW^*$ with $n_j = 0$.

1489 3.6 PARAMETERS OF INTEREST AND STATISTICAL TREATMENT

1490 As with any search or measurement, there are particular parameters of the Higgs that the $H \rightarrow WW^*$
1491 analysis is interested in measuring. In this case, the parameters of interest are the mass of the Higgs boson
1492 and its production cross section. In the $H \rightarrow WW^* \rightarrow \ell\nu\ell\nu$ final state, it is not possible to measure
1493 the full invariant mass of the Higgs due to the presence of neutrinos. However, a proxy for the invariant
1494 mass is defined using transverse plane information and detailed in section 3.6.1. The second parameter of
1495 interest is the cross section σ , which in this analysis is measured relative to the theoretical prediction for a
1496 Standard Model Higgs. This ratio, μ , is defined in equation 3.5.

$$\mu = \frac{\sigma}{\sigma_{\text{SM}}} \quad (3.5)$$

1497 All of the likelihoods used in the statistical analysis of the final signal region events are parameterized as a
1498 function of μ . μ is a natural variable for hypothesis testing, as $\mu = 0$ corresponds to a background only
1499 hypothesis and $\mu = 1$ corresponds exactly to a Standard Model Higgs.

1500 3.6.1 TRANSVERSE MASS

1501 The $H \rightarrow WW^* \rightarrow \ell\nu\ell\nu$ analysis cannot reconstruct the full invariant mass of the Higgs because of the
1502 neutrinos in the final state. The transverse mass serves as a proxy for the full invariant mass by exploiting
1503 information from the transverse plane. The transverse mass is defined in equation 3.6.

$$m_T = \sqrt{(E_T^{\ell\ell} + p_T^{\text{miss}})^2 - |\vec{p}_T^{\ell\ell} + \vec{p}_T^{\text{miss}}|^2}, \quad (3.6)$$

1504 Here the $E_T^{\ell\ell}$ and $p_T^{\ell\ell}$ are the transverse energy and momentum of the dilepton system, while p_T^{miss} is
1505 a proxy for the transverse momentum of the di-neutrino system. The track-based p_T^{miss} is used in the
1506 m_T rather than the calorimeter based E_T^{miss} because it has a better resolution on the true transverse mass.
1507 Figure 3.15 shows the improvement in the RMS of the difference between the true and reconstructed trans-
1508 verse mass in a ggF signal sample. The RMS improves by 4.7 GeV using p_T^{miss} in the m_T calculation. The

1509 m_T variable is used as the final discriminant for the Higgs signal in most of the $H \rightarrow WW^*$ signal regions
1510 (specifically, all gluon fusion regions and the selection requirement based vector boson fusion region).

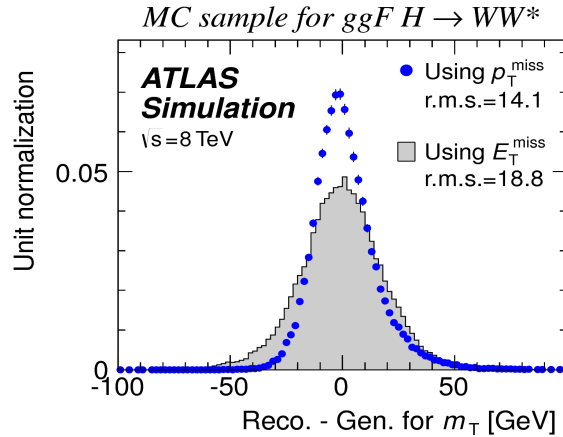


Figure 3.15: The difference between the true and reconstructed values of m_T in a gluon fusion signal sample using both track-based (p_T^{miss}) and calorimeter-based E_T^{miss} definitions [74].

1511 3.6.2 STATISTICAL TREATMENT

1512 LIKELIHOOD FUNCTION

1513 The statistical analysis² of final event candidates is framed as a hypothesis test, where the null hypothesis is
1514 background-only (no Standard Model Higgs). The first step in the analysis is to form a likelihood function
1515 for the data. In its simplest form, this likelihood is the probability of observing the number of events seen
1516 in the final signal region given knowledge of the signal strength. Because observation of events is funda-
1517 mentally a Poisson counting experiment, this simple likelihood can be expressed as a Poisson probability of
1518 observing N events given a total number of predicted signal and background events. This basic likelihood
1519 is shown in equation 3.7.

$$\mathcal{L}(\mu) = P(N|\mu S + B) \quad (3.7)$$

1520 Here, P is the Poisson probability density function, N is the total number of observed events, μ is the
1521 signal strength, S is the predicted number of signal events, and B is the predicted number of background
1522 events.

²Many thanks to Aaron Armbruster, whose thesis [75] inspired parts of this section.

1523 Generally, in searches, certain background estimates are commonly normalized in so-called “control” re-
 1524 gions and those predictions are scaled by the same normalization factor in the signal region. This method
 1525 allows for more precise background estimation by using data as a constraint, reducing the impact of theo-
 1526 retical uncertainties on the background model. This leads to a slightly more complicated likelihood, which
 1527 is a function of both the signal strength and the background normalization. This is shown in equation 3.8.

1528

$$\mathcal{L}(\mu, \theta) = P(N|\mu S + \theta B) P(N_{\text{CR}}|\theta B_{\text{CR}}) \quad (3.8)$$

1529 Here, θ serves as a “nuisance parameter”, or a parameter that is not of primary interest but still enters the
 1530 likelihood. The second Poisson term enforces that the background normalization be consistent with the
 1531 number of observed events in data in the control region, N_{CR} .

1532 So far, these two formulations of likelihoods have assumed a single signal region and do not take into
 1533 account any shape information of potential discriminating variables. The $H \rightarrow WW^*$ analysis is divided
 1534 into many different categories, and the counting experiment described above can be performed in each
 1535 individual category. As mentioned in section 3.6.1, the transverse mass is used as the primary discriminating
 1536 variable in many of the $H \rightarrow WW^*$ signal regions. The same counting experiment can be performed
 1537 in each bin of the m_T distribution to incorporate some shape information. Thus, the total likelihood
 1538 becomes a product over signal regions and bins of the m_T distribution. Finally, there are usually many
 1539 background sources that are normalized in control regions. The new formulation of the likelihood takes
 1540 this into account by including a product over control regions in the second Poisson term. All of these
 1541 modifications are shown in equation 3.9.

$$\mathcal{L}(\mu, \theta) = \prod_{\substack{\text{SRs } i \\ \text{bins } b}} P\left(N_{ib} \middle| \mu S_{ib} + \sum_{\text{bkg } k} \theta_k B_{kib}\right) \prod_{\text{CRs } l} P\left(N_l \middle| \sum_{\text{bkg } k} \theta_k B_{kl}\right) \quad (3.9)$$

1542 Here, the variable i counts over the different signal regions, b counts over bins of m_T , k counts over the
 1543 backgrounds, and l counts over the control regions.

1544 The final step to obtain the full likelihood used in the analysis is to add nuisance parameters for the
 1545 systematic uncertainties. In cases where the uncertainty does not affect the shape of m_T bin-by-bin, each

systematic uncertainty ϵ is allowed to affect the expected event yields through a linear response function of the nuisance parameter, namely $\nu(\theta) = (1 + \epsilon)\theta$. If instead the uncertainty does affect the shape, the effect is instead parameterized by $\nu_b(\theta) = 1 + \epsilon_b\theta$. The value of the nuisance parameters for the systematic uncertainty are constrained with a Gaussian term that is added to the likelihood as well. This is of the form $g(\delta|\theta) = e^{-(\delta-\theta)^2/2}/\sqrt{2\pi}$, where δ is the central value and θ is a nuisance parameter. Finally, a last term is added to account for the statistical uncertainty in the Monte Carlo samples used, which adds an additional poisson term. The full likelihood used in the final statistical analysis is defined in equation 3.10.

$$\begin{aligned}
 \mathcal{L}(\mu, \boldsymbol{\theta}) = & \prod_{\substack{\text{SRs i} \\ \text{bins b}}} P \left(N_{ib} \middle| \mu S_{ib} \cdot \prod_{\substack{\text{sig.} \\ r}} \nu_{br}(\theta_r) + \sum_{\text{bkg k}} \theta_k B_{kib} \cdot \prod_{\substack{\text{bkg.} \\ s}} \nu_{bs}(\theta_s) \right) \\
 & \cdot \prod_{\text{CRs l}} P \left(N_l \middle| \sum_{\text{bkg k}} \theta_k B_{kl} \right) \\
 & \cdot \prod_{\substack{\text{syst} \\ t}} g(\delta_t|\theta_t) \cdot \prod_{\text{bkg k}} P(\xi_k|\zeta_k \theta_k)
 \end{aligned} \tag{3.10}$$

Here, $\boldsymbol{\theta}$ represents the full vector of nuisance parameters, r is an index for signal systematics, s is an index for background systematics, and t is an index for Monte Carlo samples. The fourth term of the equation quantifies the uncertainty due to finite Monte Carlo sample size. Here, ξ represents the central value of the background prediction, θ is the associated nuisance parameter, $\zeta = (B/\delta B)^2$, where δB is the statistical uncertainty of B .

The best fit value of the signal strength μ is determined by finding the values of μ and $\boldsymbol{\theta}$ that maximize the likelihood, while setting $\delta = 0$ and $\xi = \zeta$. Once the likelihood is defined, a test statistic must be built for use in hypothesis testing.

TEST STATISTIC

To distinguish whether the data match a background only or background and signal hypothesis, a test statistic must be used. The $H \rightarrow WW^*$ analysis uses the profile likelihood technique [76]. The first step

1564 in formulating this test statistic is to define the profile likelihood ratio, shown in equation 3.11.

$$\lambda(\mu) = \frac{\mathcal{L}(\mu, \hat{\theta}_\mu)}{\mathcal{L}(\hat{\mu}, \hat{\theta})} \quad (3.11)$$

1565 Here $\hat{\theta}_\mu$ is the value of θ that maximizes the likelihood for the choice of μ being tested. Additionally, $\hat{\theta}$
1566 and $\hat{\mu}$ represent the values of θ and μ that gives the overall maximum value of the likelihood.

1567 Once this is defined, a test statistic q_μ is constructed. This is shown in equation 3.12.

$$q_\mu = -2 \ln \lambda(\mu) \quad (3.12)$$

1568 A higher value of q_μ indicates that the data are more incompatible with the hypothesized value of μ , and
1569 q_0 then corresponds to the value of the test statistic for the background only hypothesis. A p_0 value is
1570 then defined to quantify the compatibility between the data and the null hypothesis. The p_0 value is the
1571 probability of obtaining a value of q_0 larger than the observed value, and this is shown in equation 3.13.

$$p_0 = \int_{q_0^{\text{obs}}}^{\infty} f(q_\mu | \mu = 0) dq_\mu \quad (3.13)$$

1572 Here $f(q_\mu)$ is the probability distribution function of the test statistic. Finally, the p_0 value can be con-
1573 verted into a signal significance, using the formula in equation 3.14, or the one-sided tail of the Gaussian
1574 distribution.

$$Z_0 = \sqrt{2} \operatorname{erf}^{-1}(1 - 2p_0) \quad (3.14)$$

1575 The threshold for discovery used in particle physics is $Z_0 \geq 5$, more commonly known as a value of 5σ .

The real voyage of discovery consists not in seeking new landscapes, but in having new eyes.

Marcel Proust

4

1576

1577 The discovery of the Higgs boson and the role 1578 of the $H \rightarrow WW^* \rightarrow \ell\nu\ell\nu$ channel

1579 4.1 INTRODUCTION

1580 This chapter presents the results of the search for the Higgs boson in 4.8 fb^{-1} collected at $\sqrt{s} = 7 \text{ TeV}$
1581 and 5.8 fb^{-1} at $\sqrt{s} = 8 \text{ TeV}$. The results of three searches at $\sqrt{s} = 8 \text{ TeV}$ in the $H \rightarrow WW^* \rightarrow \ell\nu\ell\nu$
1582 , $H \rightarrow \gamma\gamma$, and $H \rightarrow ZZ \rightarrow 4\ell$ channels are shown. These results at 8 TeV are combined with the
1583 results of searches at $\sqrt{s} = 7 \text{ TeV}$ in the same channels along with $H \rightarrow \tau\tau$ production and associated
1584 production searches for $H \rightarrow b\bar{b}$. The results of this combination are a 5.9σ detection of a new particle
1585 consistent with a Higgs boson produced via gluon fusion. Rather than going into detail for all of the
1586 different Higgs decay searches, this chapter will discuss the three most sensitive channels and in particular
1587 focus on $H \rightarrow WW^* \rightarrow \ell\nu\ell\nu$, the topic of this thesis. While the focus is on WW^* , some of the ZZ^*

1588 and $\gamma\gamma$ results are shown for completeness. The results not discussed here can be found in the ATLAS
1589 Higgs discovery publication [1].

1590 **4.2 DATA AND SIMULATION SAMPLES**

1591 The data sample used for the following results was taken in 2011 and 2012 at center of mass energies of 7 and
1592 8 TeV, respectively, with 4.8 fb^{-1} collected at 7 TeV and 5.8 fb^{-1} collected at 8 TeV. Higgs production
1593 in the gluon fusion and vector boson fusion modes is modeled with **POWHEG** for the hard scattering event
1594 and **PYTHIA** for the showing and hadronization. Associated production of a Higgs with a vector boson
1595 or top quarks is modeled via **PYTHIA**. Table 4.1 shows the Monte Carlo generators used for modeling the
1596 signal and background processes relevant for the three analyses to be discussed.

Process	Generator
$ggF, VBF H$	POWHEG + PYTHIA
$WH, ZH, t\bar{t}H$	PYTHIA
$W + \text{jets}, Z/\gamma^* + \text{jets}$	ALPGEN + HERWIG
$t\bar{t}, tW, tb$	MC@NLO + HERWIG
tqb	ACERMC + PYTHIA
$q\bar{q} \rightarrow WW$	MC@NLO + HERWIG
$gg \rightarrow WW$	GG2WW+ HERWIG
$q\bar{q} \rightarrow ZZ$	POWHEG + PYTHIA
$gg \rightarrow ZZ$	GG2ZZ+ HERWIG
WZ	MADGRAPH+ PYTHIA , HERWIG
$W\gamma + \text{jets}$	ALPGEN + HERWIG
$W\gamma^*$	MADGRAPH+ PYTHIA
$q\bar{q}/gg \rightarrow \gamma\gamma$	SHERPA

Table 4.1: Monte carlo generators used to model signal and background for the Higgs search [1].

1597 **4.3 $H \rightarrow WW \rightarrow e\nu\mu\nu$ SEARCH**

1598 As discussed in chapter 3, the $H \rightarrow WW \rightarrow e\nu\mu\nu$ search is unique compared to the ZZ and $\gamma\gamma$ channels.
1599 The Higgs mass cannot be fully reconstructed due to the presence of neutrinos in the final state, so the
1600 transverse mass m_T is used as the final discriminating variable. This channel also has a wider variety of

1601 backgrounds compared to other channels. The same flavor final states are excluded from the 8 TeV dataset
1602 due to high pileup conditions¹. These final states were later included in results with the full Run 1 dataset,
1603 as discussed in chapters 5 and 6.

1604 4.3.1 EVENT SELECTION

1605 The analysis requires two opposite charge isolated leptons, with the leading (sub-leading) lepton required
1606 to have $p_T > 25(15)$ GeV. The events are separated into different signal regions depending on which
1607 flavor of lepton is leading ($e\mu$ for leading electron, μe for leading muon). Strict lepton quality cuts are
1608 applied to the sample to reduce backgrounds from mis-reconstructed leptons.

1609 Jets are reconstructed with the anti- k_T algorithm with a radius parameter $R = 0.4$. The jets are re-
1610 quired to have $p_T > 25$ GeV and $|\eta| < 4.5$, with jets in the tracking volume required to have a jet vertex
1611 fraction of 0.5 and jets in the forward region required to have $p_T > 30$ GeV. The analysis is separated
1612 into three different signal regions based on jet multiplicity: $n_j = 0, 1, \geq 2$.

1613 To indicate the presence of neutrinos in the event, a requirement of $E_{T,\text{rel}}^{\text{miss}} > 25$ GeV is made². This
1614 requirement significantly reduces the QCD multijet and Z/γ^* + jets backgrounds. Figure 4.1 shows the
1615 distribution of n_j in data and simulation after applying these “pre-selection” requirements.

1616 Additional selections are applied to require the dilepton topology to correspond to that of a Standard
1617 Model Higgs boson. The requirements are presented here - more detailed discussion on the motivation for
1618 each requirement can be found in section 3.4.3. In all of the jet multiplicity channels, the dilepton system
1619 is required to have a small gap in azimuthal angle, $\Delta\phi_{\ell\ell} < 1.8$. Similarly, the dilepton invariant mass,
1620 $m_{\ell\ell}$, is required to be less than 50 GeV in the lower jet multiplicity channels and less than 80 GeV in the
1621 $n_j \geq 2$ channel. In the $n_j = 0$ channel, the magnitude of the dilepton p_T , $p_T^{\ell\ell}$, is required to be greater
1622 than 30 GeV.

1623 In the higher jet multiplicity channels ($n_j \geq 1$), the top background is a larger fraction of the total
1624 background and must be reduced more carefully. The magnitude of the vectorial sum of the E_T^{miss} with
1625 the p_T of the leptons and jets, also known as p_T^{sum} , is thus required to be less than 30 GeV. Additionally,

¹The less sensitive 7 TeV search result includes both different flavor and same flavor final states.

²For the definition of $E_{T,\text{rel}}^{\text{miss}}$, see section 3.4.1.

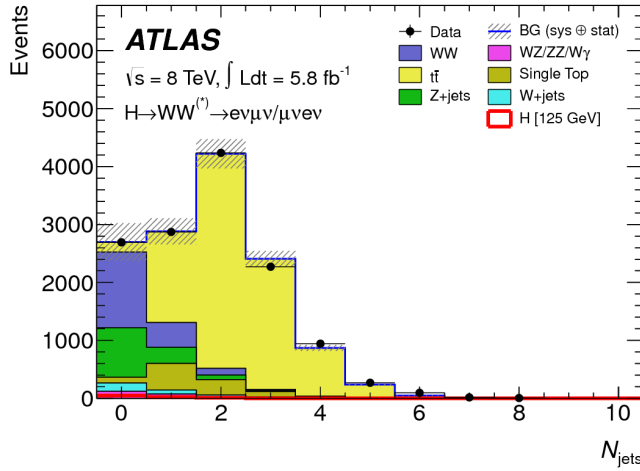


Figure 4.1: Jet multiplicity distribution in data and MC after applying lepton, jet, and $E_{\text{T},\text{rel}}^{\text{miss}}$ selections. The WW and top backgrounds have been normalized using control samples, and the hashed band indicates the total uncertainty on the prediction [1].

the di- τ invariant mass $m_{\tau\tau}$ (dilepton mass computed under the assumption that the neutrinos from the τ decay are emitted collinear to the charged leptons [77]) is used to reject $Z \rightarrow \tau\tau$ events by requiring $|m_{\tau\tau} - m_Z| > 25 \text{ GeV}$.

In the $n_j \geq 2$ channel, requirements are made to isolate the VBF contribution to Higgs production. The kinematics of the two leading jets are used to make these requirements. In particular, the event must have $\Delta y_{jj} > 3.8$ and $m_{jj} > 500 \text{ GeV}$, along with a veto on having any additional jets with rapidity between the two leading jets. This channel contributed little to the Higgs discovery but became important with the full dataset. This updated analysis is discussed in depth in chapter 5.

The final discriminating variable used to distinguish the presence of the Higgs signal is the transverse mass, m_{T} . As discussed in chapter 3, this variable acts as a substitute for the true invariant mass of the Higgs in final states with neutrinos.

4.3.2 BACKGROUND ESTIMATION

The details of the background estimation techniques used in the $H \rightarrow WW^* \rightarrow \ell\nu\ell\nu$ analysis are discussed with the full Run 1 dataset in section 5.5. The dominant backgrounds are SM WW production and top (both pair and single) production, and these backgrounds have their normalizations estimated

1641 from dedicated control regions while their shapes are taken from simulation.

1642 The control sample for the Standard Model WW background is defined by making the same require-
1643 ments as the signal region with the $m_{\ell\ell}$ requirement inverted (now requiring $m_{\ell\ell} > 80$ GeV) and remov-
1644 ing the $\Delta\phi_{\ell\ell}$ requirement. This creates a control sample that is 70% (40%) pure in the 0(1)-jet region. The
1645 correction to the pure MC-based background estimate is quantified by defining a normalization factor β
1646 which is the ratio of the data yield to the MC yield ($N_{\text{data}}/N_{\text{MC}}$) in this control sample. Table 4.2 shows
1647 the WW normalization factors in the $n_j = 0$ and $n_j = 1$ bins (the $n_j \geq 2$ estimate is taken directly
1648 from MC).

n_j	β_{WW}	β_t
$= 0$	1.06 ± 0.06	1.11 ± 0.06
$= 1$	0.99 ± 0.15	1.11 ± 0.05
≥ 2	-	1.01 ± 0.26

Table 4.2: Normalization factors (ratio of data and MC yields in a control sample) for the Standard Model WW and top backgrounds in the $H \rightarrow WW^* \rightarrow \ell\nu\ell\nu$ analysis [1]. Only statistical uncertainties are shown.

1649 The top background estimate is also computed separately in each jet multiplicity bin. In the $n_j = 0$
1650 channel, the background is first normalized using data after pre-selection requirements with no selection
1651 on n_j . Then, a dedicated b -tagged control sample is used to evaluate the ratio of one-jet to two-jet events in
1652 data. The details of this technique are shown in reference [78]. In the $n_j = 1$ and the $n_j \geq 2$ regions, the
1653 top background is normalized in a control sample where the signal region selections are applied, but the
1654 b -jet veto is reversed and the Higgs topology requirements on $m_{\ell\ell}$ and $\Delta\phi_{\ell\ell}$ are removed. The resulting
1655 normalization factors for these techniques are shown in table 4.2.

1656 The control samples which are used for background normalization can also be used to validate the mod-
1657eling of the m_T distribution for each background. Figure 4.2 shows the comparison between data and MC
1658 for the m_T distribution after correcting the normalization of the backgrounds in the WW and top control
1659 regions. Good agreement between data and simulation is seen in both cases.

1660 The $W + \text{jets}$ background estimate is taken entirely from data using a control sample with one well recon-
1661structed lepton and one anti-identified lepton. All other backgrounds are taken purely from simulation.

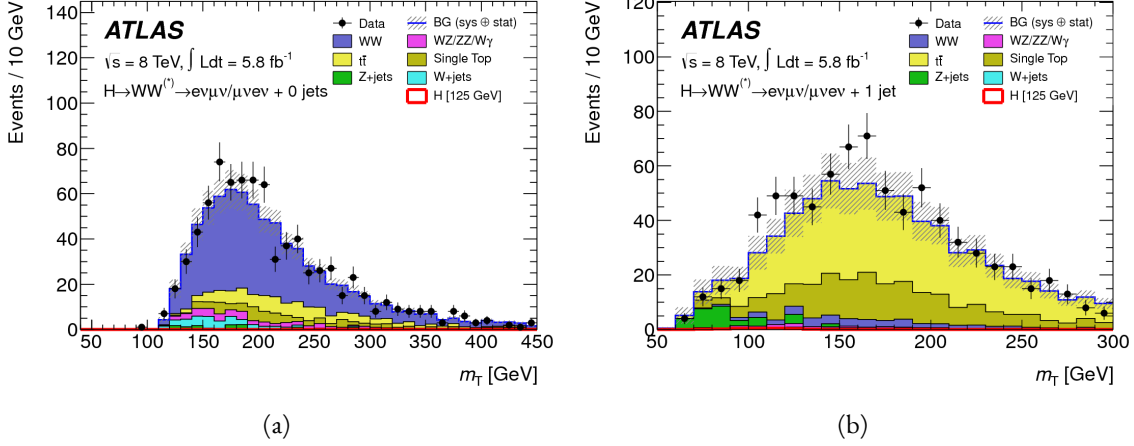


Figure 4.2: Comparison of m_T between data and simulation in the $n_j = 0$ WW (a) and $n_j = 1$ top (b) control samples [1].

1662 4.3.3 SYSTEMATIC UNCERTAINTIES

1663 The systematic uncertainties that have the largest impact on the analysis are the theoretical uncertainties
 1664 associated with the signal cross section, which are shared with the ZZ^* and $\gamma\gamma$ channels. The uncertainties
 1665 resulting from variations of the QCD scale are $+7\% / -8\%$ on the final signal yield. Those coming from
 1666 variations of the parton distribution function (PDF) used in the simulation add a $\pm 8\%$ uncertainty on
 1667 the yield. The uncertainties on the branching ratios of the Higgs are $\pm 5\%$.

1668 The main experimental uncertainties come from variations of the jet energy scale (JES), jet energy reso-
 1669 lution (JER), pile-up, E_T^{miss} , b -tagging efficiency, $W+jets$ background estimate, and integrated luminos-
 1670 ity. The largest impacts of the JES uncertainty are a 7% uncertainty on the signal yield in the $n_j = 0$
 1671 bin and a 4% uncertainty on the background yield in the $n_j = 1$ bin. The JER uncertainty affects the
 1672 $n_j = 1$ bin primarily, and it gives a 4% (2%) uncertainty on the signal (background) yield in this bin.
 1673 The E_T^{miss} uncertainty is approximately 3% on both the signal and background yields. The b -tagging ef-
 1674 ficiency uncertainty is 10% on the background yield in the $n_j = 1$ bin. The total uncertainty on the
 1675 $W+jets$ background estimate is 40%, ultimately contributing an additional 5% uncertainty to the total
 1676 background yield. For more details on these systematic uncertainties, see reference [1].

¹⁶⁷⁷ 4.3.4 RESULTS

¹⁶⁷⁸ Table 4.3 shows the signal and background yields in the final signal region after normalizing the back-
¹⁶⁷⁹ grounds according to the methods described above.

	$n_j = 0$	$n_j = 1$	$n_j \geq 2$
Signal	20 ± 4	5 ± 2	0.34 ± 0.07
WW	101 ± 13	12 ± 5	0.10 ± 0.14
Other dibosons	12 ± 3	1.9 ± 1.1	0.10 ± 0.10
$t\bar{t}$	8 ± 2	6 ± 2	0.15 ± 0.10
Single top	3.4 ± 1.5	3.7 ± 1.6	-
$Z/\gamma^* + \text{jets}$	1.9 ± 1.3	0.10 ± 0.10	-
$W + \text{jets}$	15 ± 7	2 ± 1	-
Total background	142 ± 16	26 ± 6	0.35 ± 0.18
Observed in data	185	38	0

Table 4.3: Data and expected yields for signal and background in the final $H \rightarrow WW^* \rightarrow e\nu\mu\nu$ signal region.
Uncertainties shown are both statistical and systematic [1].

¹⁶⁸⁰ Figure 4.3 shows the m_T distribution in the $n_j \leq 1$ channels for 8 TeV data. (No events are observed
¹⁶⁸¹ in data in the $n_j \geq 2$ channels in this dataset). The excess shown here is relatively flat as a function of
¹⁶⁸² hypothesized Higgs mass. The combined 7 and 8 TeV data gives an excess with local significance of 2.8σ
¹⁶⁸³ with an expected significance of 2.3σ , corresponding to a μ measurement of 1.3 ± 0.5 .

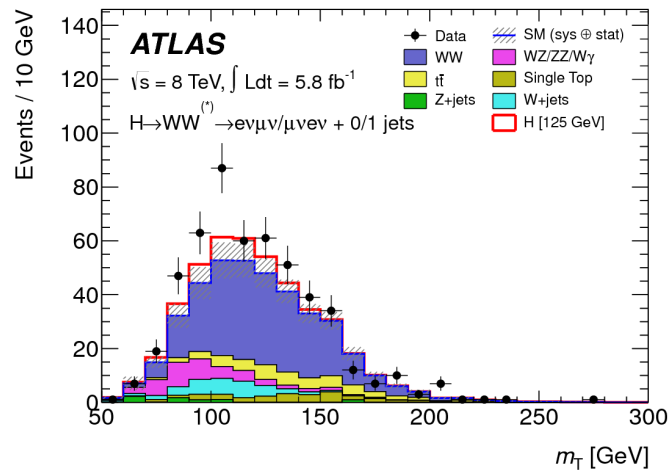


Figure 4.3: m_T distribution in the $H \rightarrow WW \rightarrow e\nu\mu\nu$ $n_j \leq 1$ channels for 8 TeV data [1].

1684 4.4 $H \rightarrow \gamma\gamma$ SEARCH

1685 The $H \rightarrow \gamma\gamma$ analysis is a search for a peaked excess above a falling SM diphoton mass spectrum, with
1686 $m_{\gamma\gamma}$ as the ultimate discriminating variable³. Events are selected by requiring two isolated photons, with
1687 the leading (sub-leading) photon required to have $E_T > 40(30)$ GeV. In the 8 TeV data, the photons are
1688 required to pass identification criteria consistent with a photonic shower in the electromagnetic calorimeter
1689 and little leakage in the hadronic calorimeter.

1690 The main challenges for this analysis are accurate mass reconstruction and $m_{\gamma\gamma}$ background shape es-
1691 timation. In order to accurately reconstruct the invariant mass of the di-photon system, both the energy
1692 and direction of the photons must be measured well. Therefore, the identification of the primary vertex of
1693 the hard interaction is particularly important, and is done using a multivariate likelihood which combines
1694 information about the photon direction and vertex position. The background is modeled with a falling
1695 spectrum in $m_{\gamma\gamma}$ that is parameterized by different functions depending on the category of the event.

1696 The resulting diphoton mass spectrum is shown in figure 4.4. The best fit mass value in the $\gamma\gamma$ channel
1697 alone in the combined 7 and 8 TeV data is 126.5 GeV. The local significance at this mass value is 4.5σ ,
1698 with an expected significance of 2.5σ . Therefore, the measured signal strength μ is 1.8 ± 0.5 in this
1699 channel.

1700 4.5 $H \rightarrow ZZ \rightarrow 4\ell$ SEARCH

1701 The $H \rightarrow ZZ \rightarrow 4\ell$ analysis searches for a Standard Model Higgs boson decaying to two Z bosons, each
1702 of which decays to a pair of same flavor, opposite charge isolated leptons. The ultimate discriminating
1703 variable is $m_{4\ell}$, or the invariant mass of the four selected leptons. The ℓ denotes an e or μ as with the
1704 $H \rightarrow WW^* \rightarrow \ell\nu\ell\nu$ analysis. Four distinct signal regions are constructed depending on the flavors of
1705 the final state, additionally separated by the flavor of the leading lepton pair. These are referred to as $4e$,
1706 $2e2\mu$, $2\mu2e$, 4μ .

1707 The main backgrounds in the $H \rightarrow ZZ \rightarrow 4\ell$ search are continuum ZZ^* production, $Z +$ jets pro-

³The ultimate shape of the SM $\gamma\gamma$ mass spectrum depends on the requirements used to define the signal region in the analysis.

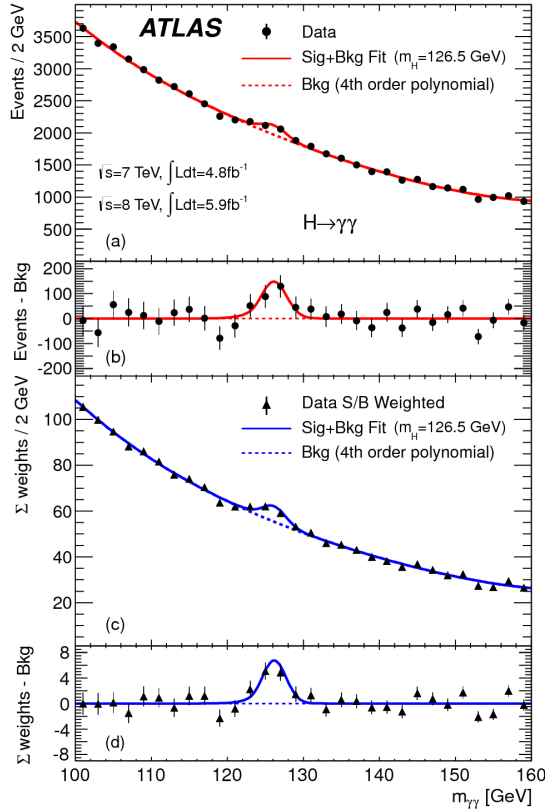


Figure 4.4: Diphoton mass spectrum in 7 and 8 TeV data. Panel a) shows the unweighted data distribution superimposed on the background fit, while panel c) shows the data where each event category is weighted by its signal to background ratio. Panels b) and d) show the respective distributions with background subtracted [1].

duction, and $t\bar{t}$. The $m_{4\ell}$ distribution for background is estimated from simulation. The normalization of the SM ZZ^* background is also taken from MC simulation, while the $Z + \text{jets}$ and $t\bar{t}$ normalizations are taken from data-driven methods.

Figure 4.5 shows the $m_{4\ell}$ spectrum measured in the 7 and 8 TeV datasets. There are 13 total events observed in the window between 120 and 130 GeV, with 6 events in the 4μ channel, 2 events in the $4e$ channel, and 5 events in the $2e2\mu/2\mu2e$. The best fit μ value in the combined 7 and 8 TeV data occurs at 125 GeV and is measured to be 1.2 ± 0.6 . The observed significance at this mass is 3.6σ , with an expected significance of 2.7σ .

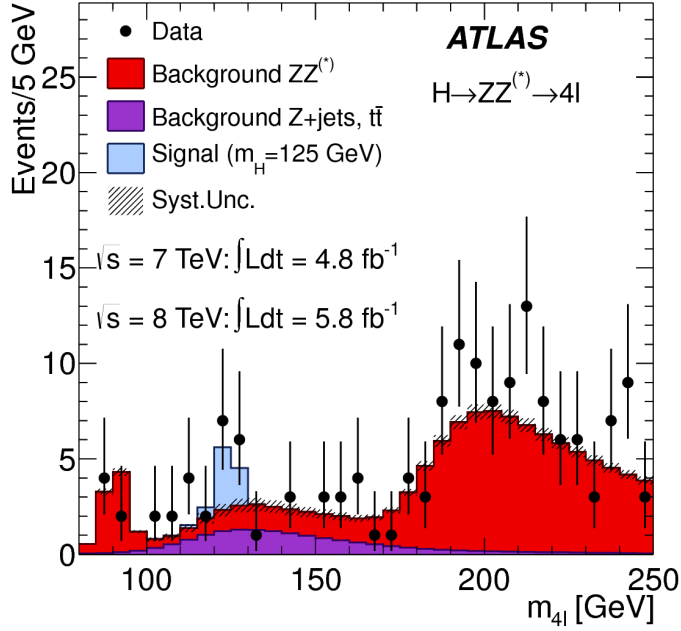


Figure 4.5: Four lepton invariant mass spectrum ($m_{4\ell}$) in 7 and 8 TeV data compared to background estimate. A 125 GeV SM Higgs signal is shown in blue [1].

1716 4.6 COMBINED RESULTS

1717 The statistical interpretation of the combined results is undertaken as described in section 3.6.2, with a hy-
 1718 pothesis test based on a likelihood ratio parameterized by the Higgs signal strength μ . The null hypothesis
 1719 corresponds to $\mu = 0$, while the SM Higgs corresponds to $\mu = 1$.

Channel	Fit var.	Observed Z_l	Expected Z_l	$\hat{\mu}$
$H \rightarrow ZZ^* \rightarrow 4\ell$	$m_{4\ell}$	3.6	2.7	1.2 ± 0.6
$H \rightarrow \gamma\gamma$	$m_{\gamma\gamma}$	4.5	2.5	1.8 ± 0.5
$H \rightarrow WW^* \rightarrow e\nu\mu\nu$	m_T	2.8	2.3	1.3 ± 0.5
Combined	-	6.0	4.9	1.4 ± 0.3

Table 4.4: Summary of the expected and observed significance and measured signal strengths in the combined 7 and 8 TeV datasets for the Higgs discovery analysis [1].

1720 Table 4.4 summarizes the properties of the individual channels as well as the significances of the ex-
 1721 cesses seen. The most significant observed local excess comes from the $\gamma\gamma$ channel. Figure 4.6 shows
 1722 a comparison of the observed local p_0 values as a function of hypothesized mass for the three different

1723 search channels. Both the ZZ^* and $\gamma\gamma$ channels have very peaked excesses, while the WW^* excess can
1724 be seen as very broad because the m_T distribution does not provide detailed information about the true
1725 Higgs mass. Note that all three channels shown have very similar expected significances for the Higgs sig-
1726 nal. While the 4ℓ and $\gamma\gamma$ channels measure excesses in data larger than that expected from the SM Higgs,
1727 the $H \rightarrow WW^* \rightarrow \ell\nu\ell\nu$ channel is still very comparable in sensitivity. Figure 4.7 shows the combined
1728 exclusion limit, p_0 , and signal strength. The highest local excess comes at a value of 126.5 GeV and corre-
1729 sponds to a 6.0σ observed excess.

1730 Figure 4.8 and table 4.4 show a comparison of the measured signal strengths between the different Higgs
1731 search channels. All measured μ are consistent with unity within their uncertainty, and the combined μ
1732 measurement is 1.4 ± 0.3 . This indicates that the observed Higgs is consistent with the expectation from
1733 a SM Higgs in this dataset.

1734 The likelihood can also be computed in a two-dimensional plane of m_H and μ , and this is shown in
1735 figure 4.9. The results show that while the $\gamma\gamma$ and ZZ^* channels have very good mass resolution, the
1736 excess in WW^* covers a broad mass range. The banana shape of the WW^* result is due to the fact that
1737 the excess in this channel can either be explained by increasing the signal strength or by changing the mass
1738 (and thus the cross section). The two parameters are correlated due to the lack of mass sensitivity in this
1739 channel.

1740 Because multiple Higgs mass points are searched for, the local significance must be corrected for a look-
1741 elsewhere effect to compute a true global significance. The global significance for finding a Higgs anywhere
1742 in the mass range of 110 GeV to 600 GeV is 5.1σ . This increases slightly to 5.3σ if only mass range from
1743 110 to 150 GeV are considered.

1744 4.7 CONCLUSION

1745 A new particle consistent with the Higgs boson was observed using 4.8 fb^{-1} collected at $\sqrt{s} = 7 \text{ TeV}$
1746 and 5.8 fb^{-1} at $\sqrt{s} = 8 \text{ TeV}$. The measured mass of the particle is 126.5 GeV with a global (local)
1747 significance of $5.1(6.0)\sigma$. This discovery was achieved using the $H \rightarrow WW^* \rightarrow \ell\nu\ell\nu$, $H \rightarrow \gamma\gamma$,
1748 and $H \rightarrow ZZ \rightarrow 4\ell$ channels. All three of these channels had very similar expected significances for

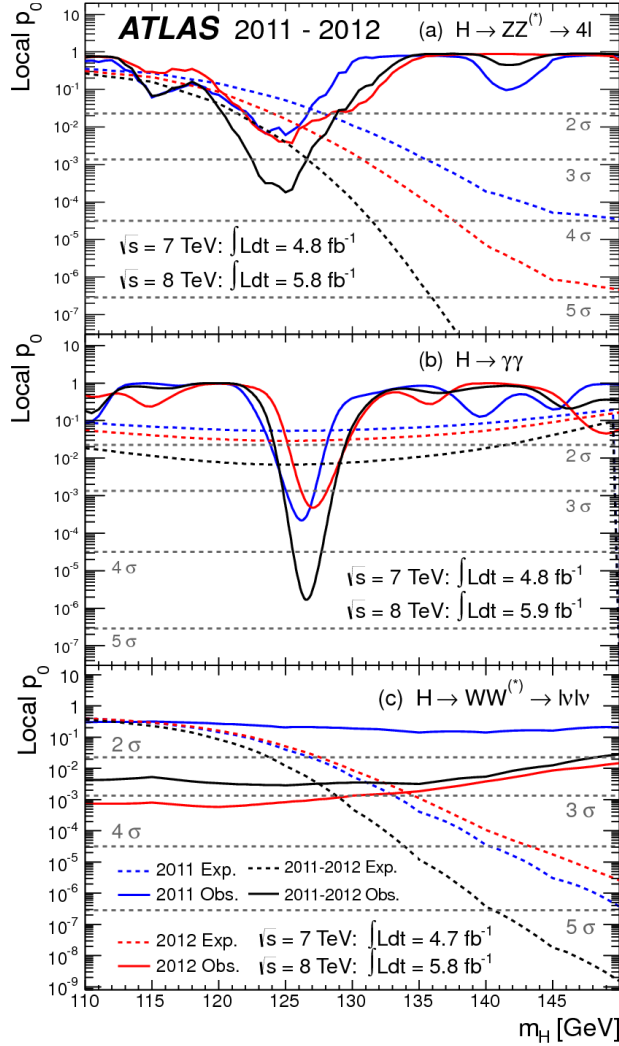


Figure 4.6: Local p_0 distribution as a function of hypothesized Higgs mass for the $H \rightarrow ZZ^* \rightarrow 4\ell$ (a), $H \rightarrow \gamma\gamma$ (b), and $H \rightarrow WW^* \rightarrow \ell\nu\ell\nu$ (c) channels. Dashed curves show expected results, while solid curves show observed. Red curves are from 7 TeV data, blue curves from 8 TeV, and black curved combined [1].

¹⁷⁴⁹ observing the SM Higgs (2.3-2.7 σ in each channel). Even with worse mass resolution, the WW^* channel
¹⁷⁵⁰ contributed to the expected sensitivity due to the large branching ratio of the Higgs to this final state. The
¹⁷⁵¹ observed significances were 2.8 σ in the WW^* channel, 3.6 σ in the ZZ^* channel, and 4.5 σ in the $\gamma\gamma$
¹⁷⁵² channel. This result is the first discovery level observation of a particle consistent with the Higgs.

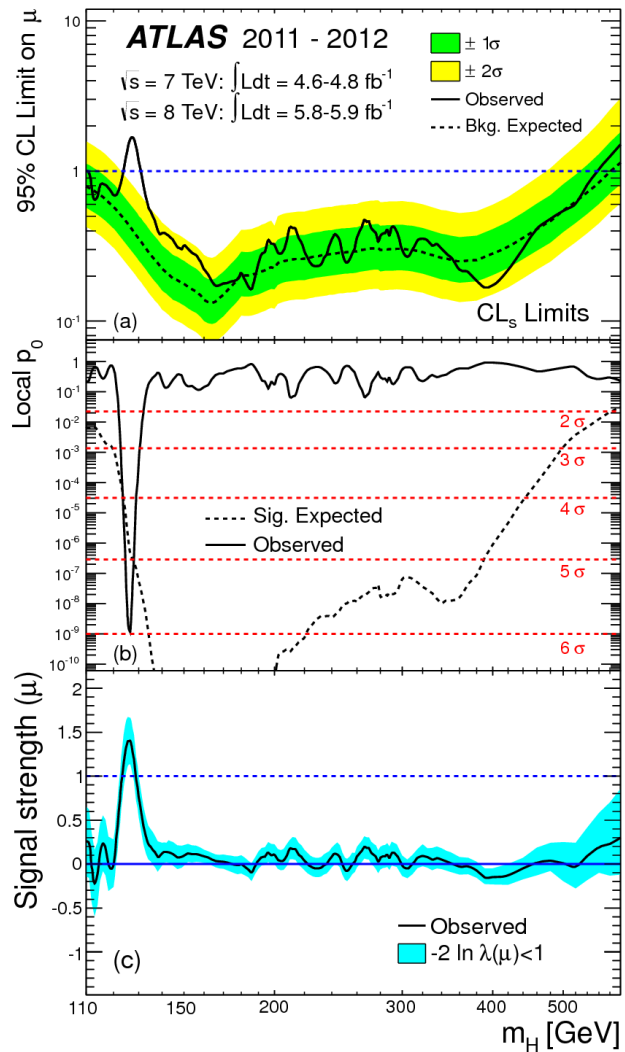


Figure 4.7: Combined 95% CL limits (a), local p_0 values (b), and signal strength measurement (c) as a function of Higgs mass [1].

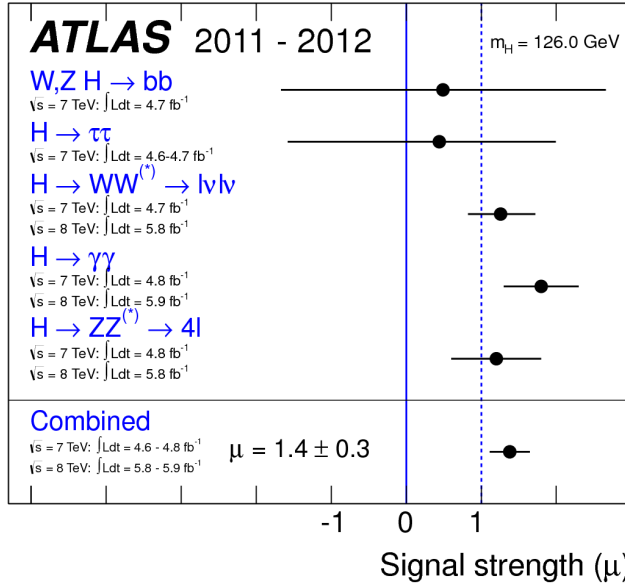


Figure 4.8: Comparison of measured signal strength μ for a 126 GeV Higgs in the 7 and 8 TeV datasets [1].

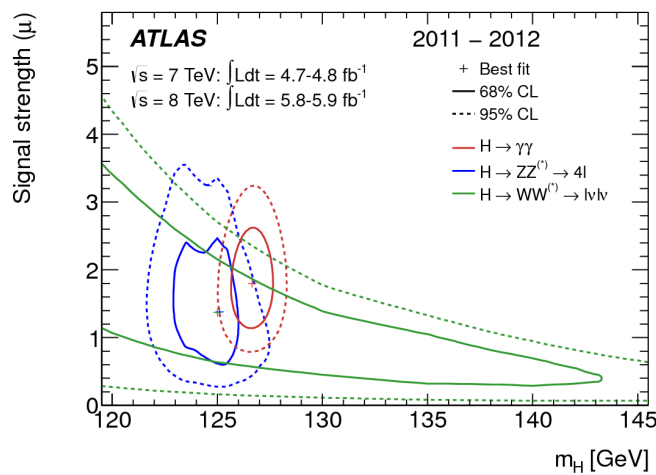


Figure 4.9: Two dimensional likelihood as a function of signal strength μ and Higgs mass m_H [1].

The imagination of nature is far, far greater than the imagination of man.

Richard Feynman

5

1753

1754 Evidence for Vector Boson Fusion production

1755

$$\text{of } H \rightarrow WW^* \rightarrow \ell\nu\ell\nu$$

1756 5.1 INTRODUCTION

1757 After the discovery of the Higgs boson, the $H \rightarrow WW^*$ analysis had two main goals. The first goal was
1758 to increase the sensitivity of the analysis to fully confirm that the $H \rightarrow WW^*$ process did indeed exist.
1759 The second goal was to characterize the particle as much as possible, including searching for the lower
1760 cross-section production modes. This chapter presents a dedicated search for Vector Boson Fusion (VBF)
1761 production of a Higgs boson decaying via the $H \rightarrow WW^* \rightarrow \ell\nu\ell\nu$ mode. First, the data and Monte
1762 Carlo samples are detailed, along with trigger and physics object selections. Then, the details of the analysis
1763 are shown, including signal region definition, background estimation techniques, and systematic uncer-
1764 tainties. Finally, the results of the analysis are presented. As will be shown, this analysis is the first and

1765 most sensitive evidence for VBF production of the Higgs at the LHC.

1766 The VBF $H \rightarrow WW^* \rightarrow \ell\nu\ell\nu$ analysis defines two signal regions. The first is a more standard
1767 selection, referred to as “cut-based”, that applies requirements on VBF topology variables and uses m_T as
1768 the final discriminating variable. The second is a looser selection that uses an algorithm known as a Boosted
1769 Decision Tree (BDT). A BDT is a multivariate technique that uses an ensemble of decision trees to split the
1770 phase space of input variables into signal-like and background-like regions in order to provide separation
1771 power [79–81]. The output score of a BDT trained to distinguish the VBF Higgs signal from background
1772 processes is used as the final discriminating variable in the second signal region. While the BDT-based
1773 signal region is ultimately more sensitive, the cut-based result is an important component of the analysis.
1774 First, the cut-based analysis allows for confirming the modeling and validity of the variables used as input
1775 to the BDT. Second, because this is the first use of a multivariate technique in the $H \rightarrow WW^*$ analysis,
1776 the cut-based selection allows confirmation of the final BDT result with a more traditional analysis. The
1777 cut-based techniques are the focus of this chapter, but connections to the BDT result will be illustrated
1778 when appropriate.

1779 One important note is that because this analysis is dedicated to the measurement of the VBF pro-
1780 duction mode of the Higgs, events coming from gluon fusion production with the Higgs decaying via
1781 $H \rightarrow WW^* \rightarrow \ell\nu\ell\nu$ are treated as background events. This will be seen throughout the background
1782 predictions shown below.

1783 5.2 DATA AND SIMULATION SAMPLES

1784 The results presented here are with 20.3 fb^{-1} taken at $\sqrt{s} = 8 \text{ TeV}$ and 4.5 fb^{-1} taken at $\sqrt{s} = 7 \text{ TeV}$.
1785 The details of the LHC and detector conditions during this period are given in Chapter 2. The trigger
1786 selection defining the dataset is discussed in section 5.2.1. The simulation samples used for signal and back-
1787 ground modeling are given in section 5.2.2.

1788 5.2.1 TRIGGERS

1789 The analysis uses a combination of single lepton and dilepton triggers to allow lowering of the p_T thresh-
1790 olds and increased signal acceptance. The p_T threshold on the leptons is a particularly important con-
1791 sideration for this signal. Because the W^* produced in the decay is off-shell, it tends to produce lower
1792 momentum leptons. Thus, being able to lower the p_T threshold while still maintaining a low background
1793 rate is critical. Figure 5.1 shows an example of the subleading lepton p_T for a VBF $H \rightarrow WW^*$ signal com-
1794 pared to the corresponding $t\bar{t}$ background. Note that the lepton p_T spectrum is considerably softer in the
1795 signal sample. The spectrum shown here is also similar in gluon fusion production of the Higgs as well.

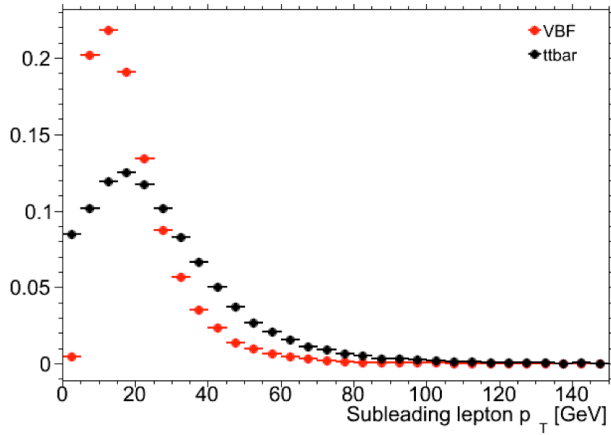


Figure 5.1: A comparison of the subleading lepton p_T spectrum between VBF $H \rightarrow WW^*$ production and $t\bar{t}$ background.

1796 As discussed in Chapter 2, there are multiple levels in the ATLAS trigger system, and there are different
1797 p_T thresholds imposed for the leptons at each level. Additionally, some triggers have a loose selection on
1798 the isolation of the lepton (looser than that applied offline in the analysis object selection). Table 5.1 shows
1799 the p_T thresholds used for single lepton triggers, while table 5.2 shows the p_T thresholds coming from
1800 di-lepton triggers. The single lepton trigger efficiency for muons that pass the analysis object selection is
1801 70% for muons in the barrel region ($|\eta| < 1.05$) and 90% in the endcap region. The electron trigger
1802 efficiency increases with electron p_T but the average is approximately 90%. These efficiencies are measured
1803 by combined performance and trigger signature groups [82, 83].

	Level-1 threshold	High-level threshold
Electron	18	$24i$
	30	60
Muon	15	$24i$
		36

Table 5.1: Single lepton triggers used for electrons and muons in the $H \rightarrow WW^* \rightarrow \ell\nu\ell\nu$ analysis. A logical “or” of the triggers listed for each lepton type is taken. Units are in GeV, and the i denotes an isolation requirement in the trigger.

	Level-1 threshold	High-level threshold
ee	10 and 10	12 and 12
$\mu\mu$	15	18 and 8
$e\mu$	10 and 6	12 and 8

Table 5.2: Di-lepton triggers used for different flavor combinations in the $H \rightarrow WW^* \rightarrow \ell\nu\ell\nu$ analysis. The two thresholds listed refer to leading and sub-leading leptons, respectively. The di-muon trigger only requires a single lepton at level-1.

1804 The combination of all listed triggers gives good efficiency for signal events. This efficiency is summa-
 1805 rized in table 5.3. The relative improvement in efficiency by adding the dilepton triggers is also shown
 1806 in the same table. The largest gain comes in the $\mu\mu$ channel. Overall the trigger selection shows a good
 1807 efficiency for $H \rightarrow WW^*$ signal events.

Channel	Trigger efficiency	Gain from 2ℓ trigger
ee	97%	9.1%
$\mu\mu$	89%	18.5%
$e\mu$	95%	8.3%
μe	81%	8.2%

Table 5.3: Trigger efficiency for signal events and relative gain of adding a dilepton trigger on top of the single lepton trigger selection. The first lepton is the leading, while the second is the sub-leading. Efficiencies shown here are for the ggF signal in the $n_j = 0$ category but are comparable for the VBF signal.

1808 5.2.2 MONTE CARLO SAMPLES

1809 In both the gluon fusion and vector boson fusion focused analyses, modeling of signal and background
 1810 processes in the signal region is an important consideration for the final interpretation of the analysis.
 1811 Therefore, careful consideration must be paid to which Monte Carlo (MC) generators are used for specific

1812 processes. With the exception of the $W + \text{jet}$ and multijet backgrounds, the m_T shape used as the final
1813 discriminant is taken from simulation¹.

1814 Table 5.4 shows the MC generators used for the signal and background processes, as well as the cross
1815 sections of each process. In order to include corrections up to next-to-leading order (NLO) in the QCD
1816 coupling constant α_s , the `POWHEG` [84] generator is often used. In some cases, only leading order gener-
1817 ators like `ACERMC` [85] and `GG2VV` [86] are available for the process in question. If the process requires
1818 good modeling for very high parton multiplicities, the `SHERPA` [87] and `ALPGEN` [88] generators are used
1819 to provide merged calculations for five or fewer additional partons. These matrix element level calculations
1820 must then be additionally matched to models of the underlying event, hadronization, and parton shower.
1821 There are four generators used for this purpose: `SHERPA`, `PYTHIA 6` [89], `PYTHIA 8` [90], or `HERWIG`
1822 [91] + `JIMMY` [92]. The simulation additionally requires an input parton distribution function (PDF).
1823 The `CT10` [93] PDFs are used for `SHERPA` and `POWHEG` simulated samples, while `CTEQ6L1` [94] is used
1824 for `ALPGEN + HERWIG` and `ACERMC` simulations. The Drell-Yan samples are reweighted to the `MRST` [95]
1825 PDFs, as these are found to give the best agreement between data and simulation. The branching ratio
1826 for Higgs to WW^* and ZZ^* is computed with `PROPHECY4f` [96], while the width of all other decays is
1827 computed with `HDECAY`[97].

1828 Once the basic hard scattering process is simulated, it must be passed through a detector simulation and
1829 additional pile-up events must be overlaid. The pile-up events are modeled with `PYTHIA 8`, and the ATLAS
1830 detector is simulated with `GEANT4` [98]. Because of the unique phase space of the $H \rightarrow WW^*$ analysis,
1831 events are sometimes filtered at generator level to allow for more efficient generation of relevant events.
1832 The efficiency of the trigger in MC simulation does not always match the measured efficiency in data, so
1833 trigger scale factors are applied to correct the MC efficiency to the data. The details of these corrections are
1834 given in reference [82] for muons and reference [83] for electrons.

¹Many backgrounds are normalized from data, as described in section 5.5.

Process	MC generator	$\sigma \cdot \mathcal{B}$ (pb)
Signal		
ggF $H \rightarrow WW^*$	POWHEG +PYTHIA 8	0.435
VBF $H \rightarrow WW^*$	POWHEG +PYTHIA 8	0.0356
VH $H \rightarrow WW^*$	PYTHIA 8	0.0253
WW		
$q\bar{q} \rightarrow WW$ and $qg \rightarrow WW$	POWHEG +PYTHIA 6	5.68
$gg \rightarrow WW$	GG2VV +HERWIG	0.196
$(q\bar{q} \rightarrow W) + (q\bar{q} \rightarrow W)$	PYTHIA 8	0.480
$q\bar{q} \rightarrow WW$	SHERPA	5.68
VBS $WW + 2$ jets	SHERPA	0.0397
Top quarks		
$t\bar{t}$	POWHEG +PYTHIA 6	26.6
Wt	POWHEG +PYTHIA 6	2.35
$t\bar{q}\bar{b}$	ACERMC +PYTHIA 6	28.4
$t\bar{b}$	POWHEG +PYTHIA 6	1.82
Other dibosons (VV)		
$W\gamma$ ($p_T^\gamma > 8$ GeV)	ALPGEN +HERWIG	369
$W\gamma^*$ ($m_{\ell\ell} \leq 7$ GeV)	SHERPA	12.2
WZ ($m_{\ell\ell} > 7$ GeV)	POWHEG +PYTHIA 8	12.7
VBS $WZ + 2$ jets	SHERPA	0.0126
($m_{\ell\ell} > 7$ GeV)		
$Z\gamma$ ($p_T^\gamma > 8$ GeV)	SHERPA	163
$Z\gamma^*$ (min. $m_{\ell\ell} \leq 4$ GeV)	SHERPA	7.31
ZZ ($m_{\ell\ell} > 4$ GeV)	POWHEG +PYTHIA 8	0.733
$ZZ \rightarrow \ell\ell\nu\nu$ ($m_{\ell\ell} > 4$ GeV)	POWHEG +PYTHIA 8	0.504
Drell-Yan		
Z ($m_{\ell\ell} > 10$ GeV)	ALPGEN +HERWIG	16500
VBF $Z + 2$ jets	SHERPA	5.36
($m_{\ell\ell} > 7$ GeV)		

Table 5.4: Monte Carlo samples used to model the signal and background processes [74]. The table lists the cross section for each process, taking into account the branching ratio for the process producing two leptons.

1835 5.3 OBJECT SELECTION

1836 In order to define the signal region, the analysis must first select the reconstructed physics objects to be
 1837 considered. The details of the object reconstruction algorithms were discussed in Chapter 2, while this

1838 section gives specific selection requirements used in the $H \rightarrow WW^*$ analysis. The first step in this process
1839 is to select a primary vertex candidates. The event's primary vertex is chosen to be the vertex with the largest
1840 sum of p_T^2 for its associated tracks. It is required to have at least three tracks with $p_T > 450$ MeV. Many
1841 of the object selection cuts are then made relative to this chosen primary vertex.

1842 **5.3.1 MUONS**

1843 The analysis uses combined muon candidates, where a track in the Inner Detector has been matched to a
1844 standalone track in the Muon Spectrometer. The track parameters are combined statistically in the muon
1845 reconstruction algorithm [64]. The muons are required to be within $|\eta| < 2.5$ and have a $p_T > 10$ GeV.
1846 To reduce backgrounds coming from mis-reconstructed leptons, there are requirements on the impact
1847 parameter of the muon relative to the primary vertex. The transverse impact parameter d_0 is required to
1848 be small relative to its estimated uncertainty, the exact cut value being $d_0/\sigma_{d_0} < 3$. The longitudinal
1849 impact parameter z_0 must satisfy $|z_0 \sin \theta| < 1$ mm.

1850 As discussed previously, the muons must also be isolated. There are two types of lepton isolations
1851 that are calculated: track-based and calorimeter-based. For muons, the track-based isolation is defined
1852 using the scalar sum $\sum p_T$ for tracks with $p_T > 1$ GeV (excluding the muon track) within a cone of
1853 $\Delta R = 0.3$ (0.4) around the track for muons with $p_T > 15$ GeV ($10 < p_T < 15$ GeV). The final
1854 isolation requirement is made by requiring that this scalar sum be no more than a certain fraction of the
1855 muon p_T . This requirement varies with muon p_T and the exact requirements are defined in table 5.5.

1856 The calorimeter-based muon isolation is defined using the $\sum E_T$ calculated from calorimeter cells with
1857 the same cone size as the track-based isolation but excluding cells within $\Delta R < 0.05$ around the muon.
1858 This isolation is also defined as a requirement on the ratio of the sum to the muon p_T and varies with
1859 muon p_T . The requirement values as a function of p_T are also given in table 5.5.

1860 The isolation requirements loosen as a function of p_T to allow for larger signal acceptance. At low p_T ,
1861 the isolation is tightened to reduce the $W + \text{jets}$ background which arises from a misidentified lepton.

p_T range (GeV)	Calorimeter isolation	Track isolation
10 – 15	0.06	0.06
15 – 20	0.12	0.08
20 – 25	0.18	0.12
> 25	0.30	0.12

Table 5.5: p_T dependent isolation requirements for muons. Muons are required to have their calorimeter based or track based cone sums be less than this fraction of their p_T .

1862 5.3.2 ELECTRONS

1863 Electrons are identified and reconstructed using the methods previously described in chapter 2. The elec-
 1864 trons are required to have $|\eta| < 2.47$, and candidates in the transition region between the barrel and
 1865 endcap ($1.37 < |\eta| < 1.52$) are excluded. As the muons, the electrons are required to have transverse
 1866 impact parameter significance < 3 , while in the longitudinal direction they must have $|z_0 \sin \theta| < 0.4$
 1867 mm. Some electron requirements also vary with electron E_T , and these requirements are summarized in
 1868 table 5.6.

1869 The isolation for electrons is defined similarly to the muons but with unique requirements on the ob-
 1870 jects included. The track-based isolation is constructed using tracks with $p_T > 400$ MeV with cone sizes
 1871 as defined for the muons. The calorimeter-based isolation also uses the same cone size as the muon, but
 1872 here the cells within a 0.125×0.175 area in $\eta \times \phi$ around the electron cluster's barycenter are excluded.
 1873 The other difference with respect to muons is that the denominator of the isolation ratio is the electron
 1874 E_T rather than p_T . The isolation cuts very with electron E_T and are defined in table 5.6. The electron is
 1875 also required to not be consistent with a vertex coming from a photon conversion.

p_T range (GeV)	Quality cut	Calorimeter isolation	Track isolation
10 – 15	Very tight LH	0.20	0.06
15 – 20	Very tight LH	0.24	0.08
20 – 25	Very tight LH	0.28	0.10
> 25	Medium	0.28	0.10

Table 5.6: p_T dependent requirements for electrons. Electrons are required to have their calorimeter based or track based cone sums be less than this fraction of their E_T .

1876 5.3.3 JETS

1877 Jets are clustered with the anti- k_T reconstruction algorithm using a radius parameter of $R = 0.4$. They
1878 are required to have a jet vertex fraction (JVF) of at least 50%, meaning that half of the tracks associated with
1879 the jet originated from the primary vertex. Jets with no tracks associated (i.e. those outside the acceptance
1880 of the ID) do not have this requirement applied. Jets are required to have $p_T > 25$ GeV if they are within
1881 the tracking acceptance ($|\eta| < 2.4$). Jets with $2.4 < |\eta| < 4.5$ are required to have $p_T > 30$ GeV. This
1882 tighter requirement reduces jets from pileup in the region where JVF requirements cannot be applied. The
1883 two highest p_T jets in the event are referred to as the “VBF” jets and used to compute variables used in the
1884 analysis selection.

1885 Identification of b -jets is done using the MV₁ algorithm and is limited to the acceptance of the ID ($|\eta| <$
1886 2.5) [70]. The operating point of MV₁ used is 85% efficient for identifying true b -jets. This operating
1887 point has a 10.3% probability of mis-tagging a light quark jet as a b -jet. The analysis vetoes events that
1888 contain b -tagged jets with $p_T > 20$ GeV.

1889 5.3.4 OVERLAP REMOVAL

1890 There are some cases where reconstructed objects will overlap and one will have to be chosen (for example,
1891 an electron and a jet in the calorimeter). First, the case of lepton overlap is dealt with. If an electron
1892 candidate extends into the muon spectrometer, it is removed. If a muon and electron are within $\Delta R < 0.1$
1893 of each other, the electron is removed and the muon is kept. If two electron candidates overlap within the
1894 same radius, then the higher E_T electron is kept. Next, the overlap between leptons and jets is considered.
1895 If an electron and jet are within $\Delta R < 0.3$ of one another, the electron is kept and the jet is removed.
1896 However, if a muon and jet overlap within $\Delta R < 0.3$, the jet is kept (as it is likely that the muon is the
1897 result of a semileptonic decay inside the jet²). Once the overlap removal is complete, the final set of objects
1898 used in the analysis is defined.

²Electrons can also result from semileptonic decays inside a jet. However, these electrons are more difficult to reconstruct than muons. When electrons overlap with jets, the electron is kept because every electron candidate will also be reconstructed as a jet by the anti- k_T algorithm.

1899 5.4 ANALYSIS SELECTION

1900 This section discusses the variables used to distinguish VBF production of the Higgs in the $H \rightarrow WW^* \rightarrow$
1901 $\ell\nu\ell\nu$ final state. First, pre-selection requirements are presented. Then, the definitions of analysis variables
1902 and the cut-based signal region are shown. Finally, the BDT signal region is defined and the commonalities
1903 between the two signal regions are discussed.

1904 5.4.1 PRE-SELECTION

1905 Both the cut-based and BDT analyses have a common pre-selection that is applied before the signal region
1906 requirements. The requirements on leptons are common to all n_j bins. The analysis requires two oppo-
1907 sitely charged leptons, with the leading lepton required to have $p_T > 22$ GeV while the subleading lepton
1908 must have $p_T > 10$ GeV. Next, to remove low mass Z/γ^* events, a requirement on the dilepton mass
1909 $m_{\ell\ell} > 10$ (12) GeV is applied in the different (same) flavor channel. In the same flavor channels, there is
1910 an additional veto placed on the region around the Z peak, requiring that $|m_{\ell\ell} - m_Z| > 15$ GeV.

1911 There are also requirements on the amount of missing transverse momentum in the event. These
1912 are only applied in the same flavor channels, where $Z/\gamma^* + \text{jets}$ production is one of the dominant back-
1913 grounds. The BDT analysis requires $p_T^{\text{miss}} > 40$ GeV and $E_T^{\text{miss}} > 45$ GeV. The cut-based analysis
1914 must select more tightly on these variables to have maximal sensitivity and thus requires $p_T^{\text{miss}} > 50$ GeV
1915 and $E_T^{\text{miss}} > 55$ GeV. Figure 5.2 shows the distributions of both E_T^{miss} and p_T^{miss} compared between
1916 data and simulation in the same flavor channels. Both variables are modeled fairly well in the bulk of the
1917 distribution, with some mis-modeling arising in the tails. Additionally, it is interesting to note that the
1918 $Z/\gamma^* \rightarrow \ell\ell$ backgrounds tends to have lower values of both variables compared to the VBF signal, as
1919 expected.

1920 Finally, because this analysis is focused on VBF Higgs production, a requirement on the jet multiplicity
1921 is placed, with $n_j \geq 2$. Additionally, the analysis requires that there are no jets identified as b-quarks in the
1922 event, or $n_b = 0$. Figure 5.3 shows the jet multiplicity distributions in data and Monte Carlo simulation
1923 for both n_j and n_b . The n_j variable is seen to be very well modeled for $n_j \leq 7$, with some discrepancies
1924 appearing at very high jet multiplicities (where events are a small fraction of the total sample). Similarly,

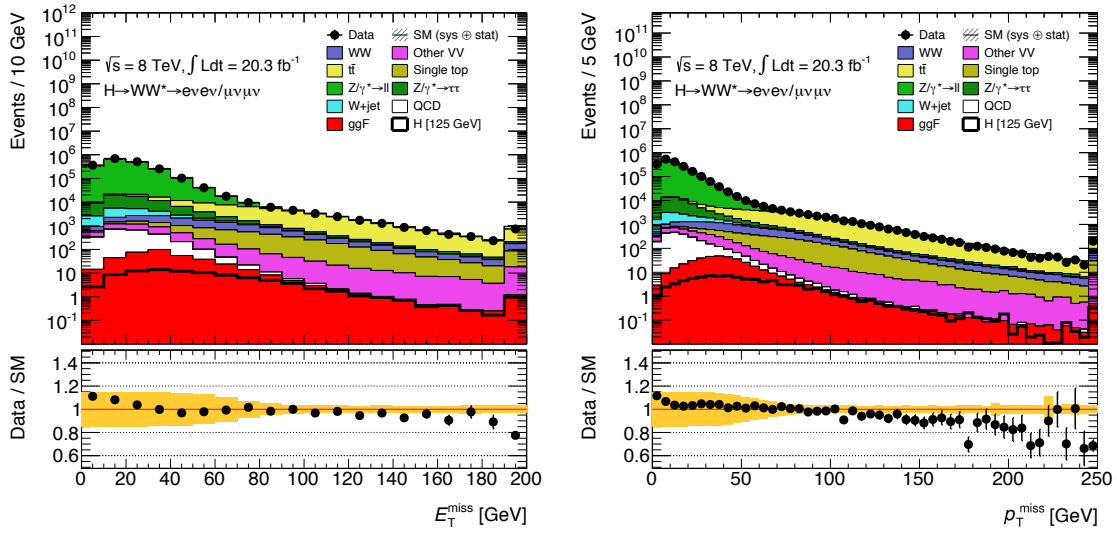


Figure 5.2: Comparisons between data and Monte Carlo simulation for the calorimeter-based E_T^{miss} (left) and the track-based p_T^{miss} (right) in the same flavor VBF $H \rightarrow WW^*$ analysis channels. Both distributions are shown after the pre-selection cuts on $m_{\ell\ell}$. The bottom panel shows the ratio between the data and the number of events expected from combining the signal and background. The hashed and orange bands include both statistical and systematic uncertainties.

the n_b variable is modeled very well for $n_b \leq 2$, with some discrepancies at higher values.

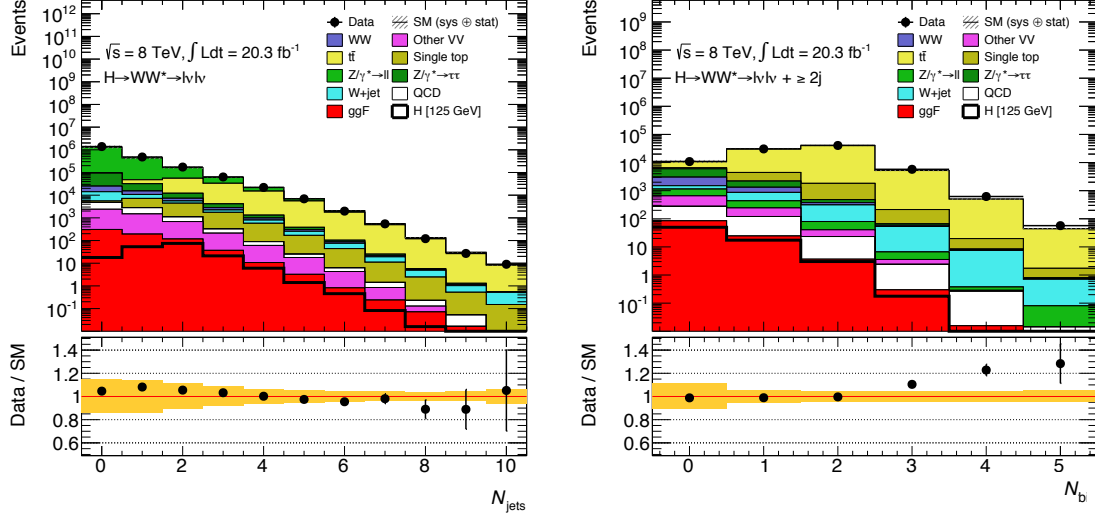


Figure 5.3: Comparisons between data and Monte Carlo simulation for the jet multiplicity n_j (left) and the number of b -tagged jets n_b (right) in the VBF $H \rightarrow WW^*$ analysis. n_j is shown after the pre-selection cuts on $m_{\ell\ell}$ and n_b is shown after the requirement that $n_j \geq 2$. The bottom panel shows the ratio between the data and the number of events expected from combining the signal and background. In the n_b distribution, the top background is normalized using the procedures described in section 5.5.2. The hashed and orange bands include both statistical and systematic uncertainties.

1926 5.4.2 ANALYSIS VARIABLE DEFINITIONS AND CUT-BASED SELECTION

1927 The cut-based selection places sequential requirements on variables reconstructed from the VBF jets in
1928 order to increase the signal to background ratio. This section defines the variables that are used in the
1929 cut-based selection and details the requirements that are placed on these variables.

1930 GENERAL BACKGROUND REDUCTION

1931 Top pair production is the primary background in the $n_j \geq 2$ bin. Even though $n_b = 0$ is required, an
1932 additional variable is constructed to further suppress the top background. There is often additional QCD
1933 radiation that accompanies the $t\bar{t}$ system when it is produced. Therefore, a variable which tests for the
1934 presence of this additional radiation, p_T^{sum} , is constructed. It is defined in equation 5.1.

$$p_T^{\text{sum}} = p_T^{\ell\ell} + p_T^{\text{miss}} + \sum p_T^j \quad (5.1)$$

1935 After pre-selection, the cut-based analysis requires the event to have $p_T^{\text{sum}} < 15$ GeV to further suppress
1936 $t\bar{t}$ production.

1937 In the different flavor channels, a requirement is made to reduce the contamination from $Z \rightarrow \tau\tau$
1938 decays. The di- τ invariant mass, $m_{\tau\tau}$, is constructed by assuming that the neutrinos from the τ decays
1939 were collinear with the leptons [77]. The analysis requires that this mass satisfy $m_{\tau\tau} < m_Z - 25$ GeV so
1940 that it is not consistent with the mass of the Z boson.

1941 VBF TOPOLOGICAL CUTS

1942 The characteristic feature of VBF production of the Higgs is the presence of two additional forward jets
1943 coming from the incoming partons which radiate the vector bosons that make the Higgs. These jets are
1944 forward because the outgoing partons still carry the longitudinal momentum of the incoming partons.
1945 Figure 5.4 shows the distribution of the η for the leading jet in a VBF event compared to a background top
1946 pair production event. As can be seen, the VBF jets tend to be more forward in η , while the $t\bar{t}$ jets are more
1947 central. Because the cross section for VBF production is an order of magnitude smaller than gluon fusion

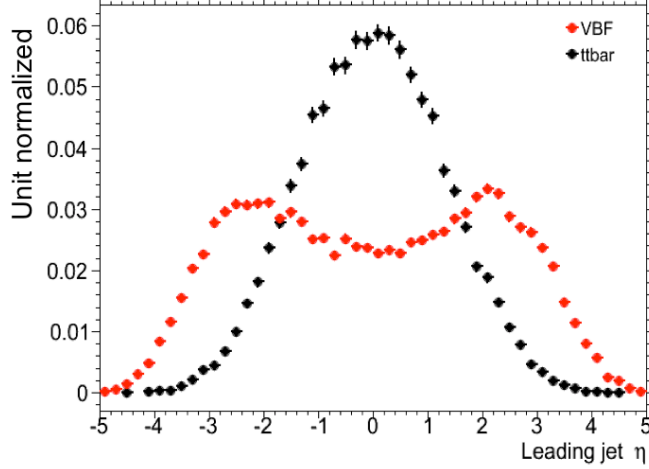


Figure 5.4: Leading jet η in VBF $H \rightarrow WW^*$ (red) and $t\bar{t}$ (black)

1948 production, these forward jets must be used in order to reduce background and achieve a good signal to
 1949 background ratio. The dedicated VBF search selection requirements are constructed to maximally exploit
 1950 the features of the unique VBF topology.

1951 Requirements on the VBF jets are collectively referred to as the “VBF topological cuts”. First, a require-
 1952 ment on the dijet invariant mass of the VBF jets, m_{jj} , is placed, requiring $m_{jj} > 600$ GeV. Next, the
 1953 event is required to have a large gap in rapidity between the two VBF jets, or $\Delta y_{jj} > 3.6$. Both of these
 1954 are tight requirements on the presence of two forward, high p_T jets moving in opposite directions in the
 1955 longitudinal plane.

1956 Beyond requiring the presence of the two forward VBF jets, the analysis also vetoes on the presence of
 1957 any additional jets that fall between the two VBF jets. This requirement is referred to as the central jet
 1958 veto, or CJV. Events are vetoed if they have a third jet with $p_T > 20$ GeV whose rapidity is between the
 1959 region defined by the two VBF jets. This requirement can be expressed in terms of a variable called the jet
 1960 centrality, defined in equation 5.2.

$$C_{j3} = \left| \eta_{j3} - \frac{\eta_{j1} + \eta_{j2}}{2} \right| / \frac{|\eta_{j1} - \eta_{j2}|}{2}, \quad (5.2)$$

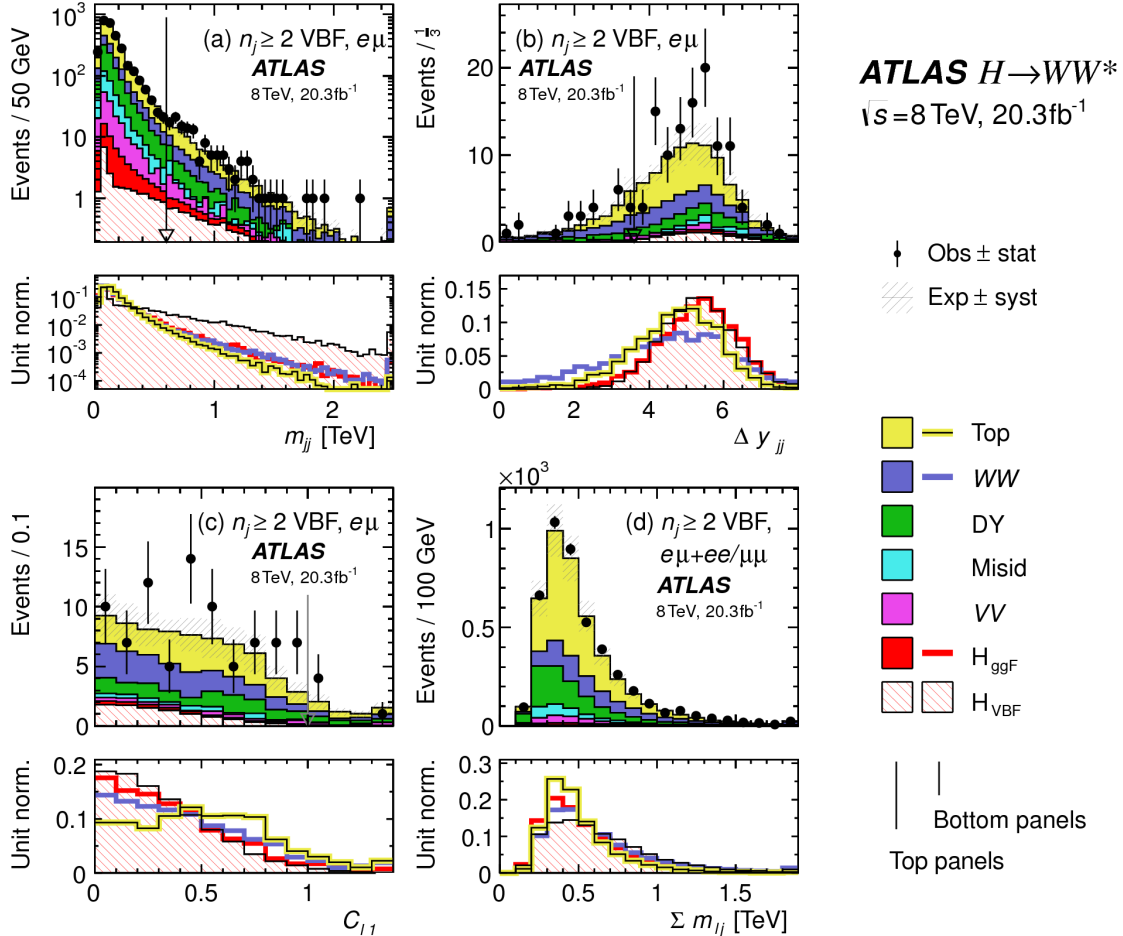


Figure 5.5: Distributions of (a) m_{jj} , (b) Δy_{jj} , (c) $C_{\ell 1}$, and (d) $\Sigma m_{\ell j}$, for the cut-based VBF analysis. The top panels compare simulation and data, while the bottom panels show normalized distributions for all background processes and signal for shape comparisons [74].

1961 Here, η_{j1} and η_{j2} are the pseudorapidities of the leading and subleading jets, respectively, while η_{j3} is
 1962 the pseudorapidity of the extra jet in the event (if one exists). Intuitively, C_{j3} is zero when η_{j3} is directly
 1963 centered between the two jets and unity when η_{j3} is aligned with either of the VBF jets. Thus, the CJV
 1964 can be expressed as a requirement that $C_{j3} > 1$.

1965 The decay products of the Higgs tend to be central as well. Thus, the analysis also requires that both
 1966 leptons in the analysis fall within the rapidity gap defined by the jets. This cut is referred to as the outside
 1967 lepton veto, or OLV. Stated another way, leptons are required to have a centrality (defined analogously to
 1968 that of the third jet in equation 5.2) within the jet rapidity gap, or $C_{\ell} < 1$ for both leptons.

1969 Figure 5.5a-c shows the m_{jj} , Δy_{jj} , and $C_{\ell 1}$ variables at the stage where all previous requirements in the
 1970 sequence have been made. The agreement between data and Monte Carlo is good, and the bottom panels
 1971 show their power in discriminating the VBF signal from the background processes.

1972 The final signal region is also split into two bins of m_{jj} , with the first bin corresponding to $600 \text{ GeV} <$
 1973 $m_{jj} < 1 \text{ TeV}$ and the second bin corresponding to $m_{jj} > 1 \text{ TeV}$. The first bin has more events but also
 1974 a larger contribution from background, while the second bin has a lower expected number of events but a
 1975 1:1 signal to background ratio.

1976 HIGGS TOPOLOGICAL CUTS

1977 As described in section 3.4.3, the final state leptons in $H \rightarrow WW^* \rightarrow \ell\nu\ell\nu$ are correlated due to the spin
 1978 zero nature of the Higgs. Two requirements on dilepton kinematics are made that are common with lower
 1979 multiplicity jet bins as well. The angle between leptons in the transverse plane, $\Delta\phi_{\ell\ell}$, is required to be less
 1980 than 1.8 radians. Additionally, the dilepton invariant mass, $m_{\ell\ell}$, is required to be less than 50 GeV.

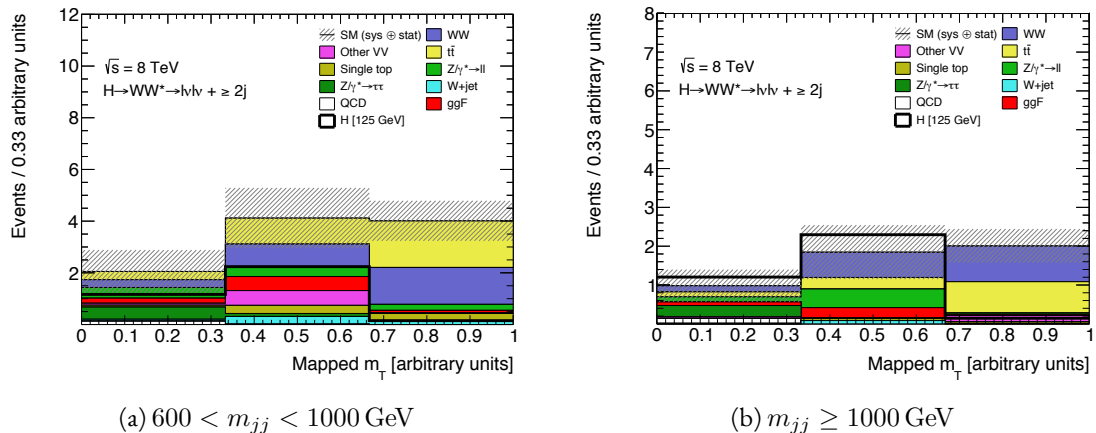


Figure 5.6: m_T distribution in simulation mapped to the three bins used in the final VBF cut-based analysis fit. The bin boundaries correspond 80 and 130 GeV. The solid black line corresponds to the VBF Higgs signal and is overlaid on the backgrounds to allow for shape comparison. Hashed bands include both statistical and systematic uncertainties.

1981 The cut-based analysis uses m_T as the final discriminating variable as in the ggF focused analysis. The
 1982 optimal number of bins in m_T was found to be three bins, with the bin boundaries at 80 and 130 GeV.
 1983 Figure 5.6 shows the m_T distribution in the three bins used in the fit (also known as the “mapped” m_T)

1984 for both the $600 < m_{jj} < 1000$ GeV bin and the $m_{jj} \geq 1000$ GeV bin. As can be seen, both m_{jj}
1985 bins offer discriminating power for the VBF Higgs, with the lower m_{jj} bin providing more events and the
1986 higher m_{jj} bin providing better signal to background ratio.

1987 Table 5.7 shows a summary of the data and estimated signal and background yields from simulation
1988 as each requirement described above is made. The table shows how the overall signal to background ra-
1989 tio grows through the various selection requirements. Table 5.8 shows the background composition after
1990 each selection requirement, illustrating which backgrounds are reduced most by certain requirements. Fig-
1991 ure 5.7 shows an ATLAS event display of a candidate event in the final signal region.

Selection	Summary					
	$N_{\text{obs}}/N_{\text{bkg}}$	N_{obs}	N_{bkg}	N_{signal}		
				N_{ggF}	N_{VBF}	N_{VH}
$e\mu$ sample	1.00 ± 0.00	61434	61180	85	32	26
$n_b = 0$	1.02 ± 0.01	7818	7700	63	26	16
$p_T^{\text{sum}} < 15$	1.03 ± 0.01	5787	5630	46	23	13
$m_{\tau\tau} < m_Z - 25$	1.05 ± 0.02	3129	2970	40	20	9.9
$m_{jj} > 600$	1.31 ± 0.12	131	100	2.3	8.2	—
$\Delta y_{jj} > 3.6$	1.33 ± 0.13	107	80	2.1	7.9	—
$C_{j3} > 1$	1.36 ± 0.18	58	43	1.3	6.6	—
$C_{\ell 1} < 1, C_{\ell 2} < 1$	1.42 ± 0.20	51	36	1.2	6.4	—
$m_{\ell\ell}, \Delta\phi_{\ell\ell}, m_T$	2.53 ± 0.71	14	5.5	0.8	4.7	—
$ee/\mu\mu$ sample	0.99 ± 0.01	26949	27190	31	14	10.1
$n_b, p_T^{\text{sum}}, m_{\tau\tau}$	1.03 ± 0.03	1344	1310	13	8.0	4.0
$m_{jj}, \Delta y_{jj}, C_{j3}, C_\ell$	1.39 ± 0.28	26	19	0.4	2.9	0.0
$m_{\ell\ell}, \Delta\phi_{\ell\ell}, m_T$	1.63 ± 0.69	6	3.7	0.3	2.2	0.0

Table 5.7: Summary of event selection for the $n_j \geq 2$ VBF analysis in the 8 TeV cut-based analysis [74].

1992 5.4.3 BDT-BASED SELECTION

1993 The boosted decision tree based analysis uses many of the variables defined in the cut-based selection as
1994 inputs to the BDT. The output BDT score (O_{BDT}) is used as the final discriminant rather than m_T ³.

3For the final discriminant analysis, the O_{BDT} distribution is divided into four bins, with boundaries at $[-1, -0.48, -0.3, 0.78, 1]$.

	Composition of N_{bkg}									
	N_{WW}		$N_{t\bar{t}}$		N_{misid}		N_{VV}		$N_{\text{Drell-Yan}}$	
	N_{WW}^{QCD}	N_{WW}^{EW}	$N_{t\bar{t}}$	N_t	N_{Wj}	N_{jj}	N_{VV}^{QCD}	$N_{ee/\mu\mu}$	$N_{\tau\tau}^{\text{QCD}}$	$N_{\tau\tau}^{\text{EW}}$
$e\mu$ sample	1350	68	51810	2970	847	308	380	51	3260	46
$n_b = 0$	993	43	3000	367	313	193	273	35	2400	29
$p_T^{\text{sum}} < 15$	781	38	1910	270	216	107	201	27	2010	23
$m_{\tau\tau} < m_Z - 25$	484	22	1270	177	141	66	132	7.6	627	5.8
$m_{jj} > 600$	18	8.9	40	5.3	1.8	2.4	5.1	0.1	15	1.0
$\Delta y_{jj} > 3.6$	11.7	6.9	35	5.0	1.6	2.3	3.3	—	11.6	0.8
$C_{j3} > 1$	6.9	5.6	14	3.0	1.3	1.3	2.0	—	6.8	0.6
$C_{\ell 1} < 1, C_{\ell 2} < 1$	5.9	5.2	10.8	2.5	1.3	1.3	1.6	—	5.7	0.6
$m_{\ell\ell}, \Delta\phi_{\ell\ell}, m_T$	1.0	0.5	1.1	0.3	0.3	0.3	0.6	—	0.5	0.2
$ee/\mu\mu$ sample	594	37	23440	1320	230	8.6	137	690	679	16
$n_b, p_T^{\text{sum}}, m_{\tau\tau}$	229	12.0	633	86	26	0.9	45	187	76	1.5
$m_{jj}, \Delta y_{jj}, C_{j3}, C_\ell$	3.1	3.1	5.5	1.0	0.2	0.0	0.7	3.8	0.7	0.1
$m_{\ell\ell}, \Delta\phi_{\ell\ell}, m_T$	0.4	0.2	0.6	0.2	0.2	0.0	0.1	1.5	0.3	0.1

Table 5.8: Background composition after each requirement in the $n_j \geq 2$ VBF analysis in the 8 TeV cut-based analysis [74].

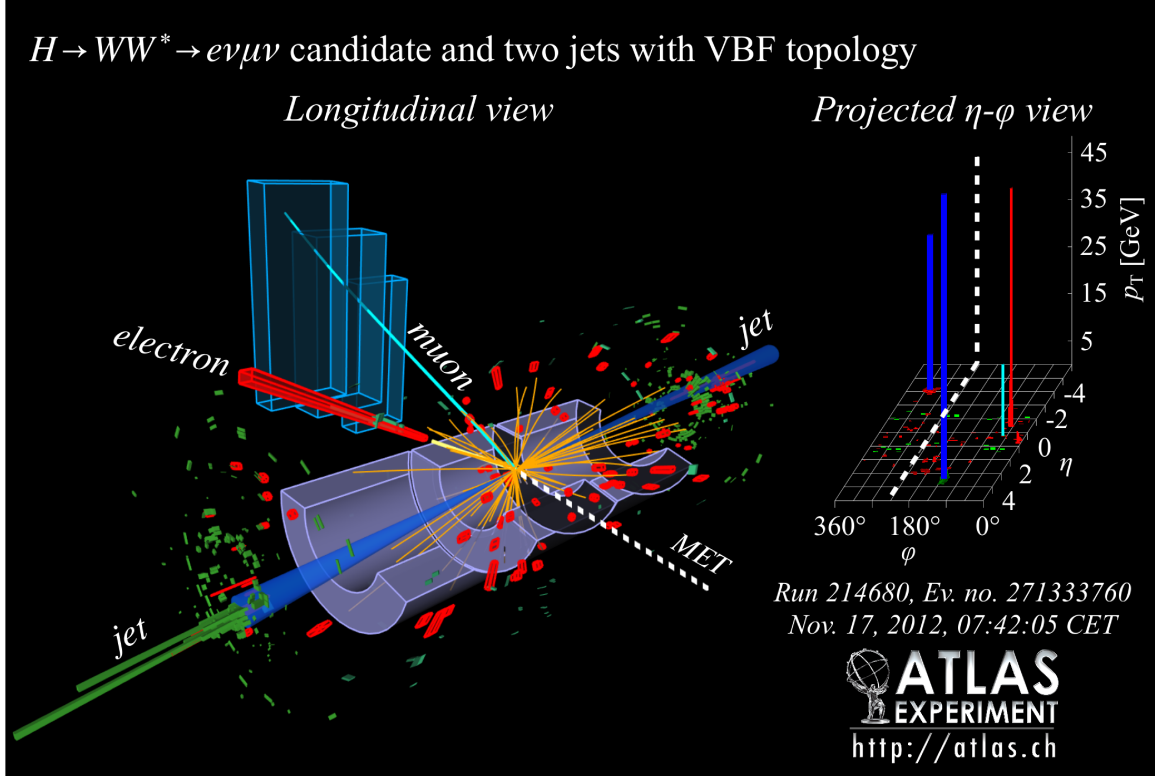


Figure 5.7: Event display of a VBF candidate event [74].

1995 The BDT is trained with the VBF $H \rightarrow WW^*$ simulation as the signal samples and all other processes as
1996 background, including ggF $H \rightarrow WW^*$ production. While the BDT based analysis is ultimately treated
1997 as a separate result, it has significant overlap with the cut-based selection.

1998 **PRE-TRAINING SELECTION AND BDT INPUTS**

1999 Before training, the common pre-selection cuts described in section 5.4.1 are applied. Additionally, the
2000 central jet veto and outside lepton veto described in section 5.4.2 are applied. The BDT has eight input
2001 variables, six of which are also variables that are used in the cut-based analysis. The six shared variables
2002 are p_T^{sum} , m_{jj} , Δy_{jj} , $m_{\ell\ell}$, $\Delta\phi_{\ell\ell}$, and m_T . The seventh variable input in the BDT is a combination of
2003 the variables used to define the OLV in the cut-based analysis. The BDT uses as input the sum of lepton
2004 centralities, or $\sum C_\ell = C_{\ell 1} + C_{\ell 2}$. The final BDT input variable, $\Sigma m_{\ell j}$, is constructed to account for
2005 the correlations between the jets and leptons in the event. It is the sum of the invariant masses of all four
2006 possible lepton-jet combinations. Table 5.9 summarizes the cuts applied for the cut-based and analyses, as
2007 well as which variables are used as input to the BDT.

2008 Figure 5.5d shows the agreement between data and simulation for the $\Sigma m_{\ell j}$ variable, as well as showing
2009 its discriminating power. Figure 5.8 shows the distributions of the Higgs topological variables that are
2010 shared between the cut-based and BDT analyses. Figure 5.9 shows the distributions of the VBF topological
2011 variables shared between the cut-based and BDT analyses. In both cases, the VBF yield has been scaled by
2012 a factor of 50 to better show the shape difference compared to the backgrounds.

2013 **5.5 BACKGROUND ESTIMATION**

2014 This section describes the procedures used to estimate backgrounds for the VBF analysis in both the cut-
2015 based and BDT analyses. First, the general strategy is presented. Then, specific procedures for each back-
2016 ground in both signal regions are shown.

Category	Selection	Cut-based value	BDT-based value
Pre-selection	Leptons	2 oppositely charged	
	Leading lepton p_T	$> 22 \text{ GeV}$	
	Subleading lepton p_T	$> 10 \text{ GeV}$	
	$m_{\ell\ell}$	$> 10 (12) \text{ GeV for } e\mu/\mu e (ee/\mu\mu)$ $ m_{\ell\ell} - m_Z > 15 \text{ GeV for } ee/\mu\mu$	
	E_T^{miss} ($ee/\mu\mu$ only)	$> 55 \text{ GeV}$	$> 45 \text{ GeV}$
	p_T^{miss} ($ee/\mu\mu$ only)	$> 50 \text{ GeV}$	$> 40 \text{ GeV}$
	b -veto	$n_b = 0$	
Bkg. rejection	p_T^{sum}	$< 15 \text{ GeV}$	Input
VBF topology	m_{jj}	$> 600 \text{ GeV}$	Input
	Δy_{jj}	> 3.6	Input
	CJV and OLV	applied	
	$\sum C_\ell$	-	Input
	$\sum m_{\ell j}$	-	Input
Higgs topology	$m_{\ell\ell}$	$< 50 \text{ GeV}$	Input
	$\Delta\phi_{\ell\ell}$	< 1.8	Input
	m_T	Three bins with boundaries at 80 and 130 GeV	Input

Table 5.9: Summary of selections for the cut-based and BDT signal regions. “Input” denotes variables used as input to the BDT algorithm. Definitions and explanations of the variables can be found in sections 5.4.2 and 5.4.3.

2017 5.5.1 GENERAL STRATEGY

2018 Most of the backgrounds in both the gluon fusion and VBF Higgs analyses have shapes estimated from
 2019 Monte Carlo simulation but normalizations derived from control regions in data. In essence, a normaliza-
 2020 tion factor (denoted with β or abbreviated as NF) is derived by scaling the MC yield in the control region
 2021 to the corresponding yield in data. Once this factor is derived, it can be used to scale the MC estimate of
 2022 the background in the signal region. This is illustrated in equation 5.3.

$$B_{\text{SR}}^{\text{est}} = B_{\text{SR}} \times \frac{N_{\text{CR}}}{B_{\text{CR}}} \equiv B_{\text{SR}} \times \beta \quad (5.3)$$

2023 Here, B is the MC yield prediction in the denoted region, while N is the observed number of events in
 2024 data in the denoted region.

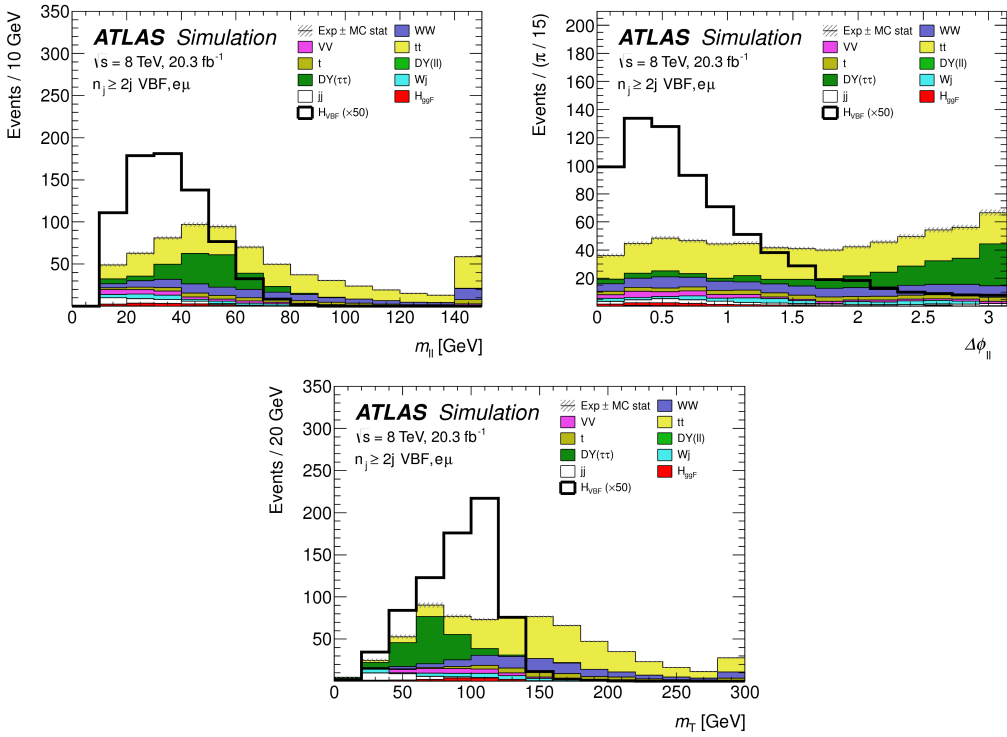


Figure 5.8: Higgs topology variables - $m_{\ell\ell}$ (top left), $\Delta\phi_{\ell\ell}$ (top right), and m_T (bottom) - used in the selection requirements of the cut-based signal region and as inputs to the BDT result. These are plotted after all of the BDT pre-training selection cuts [74]. The VBF Higgs signal cross section is multiplied by a factor of 50 to allow for shape comparisons.

2025 There is an alternative way of writing the same equation in terms of an extrapolation factor α rather
 2026 than a normalization factor β . The overall calculation is exactly the same. However, when phrased in
 2027 this way, it shows how the uncertainty on the background estimation can be reduced. This is shown in
 2028 equation 5.4.

$$B_{\text{SR}}^{\text{est}} = N_{\text{CR}} \times \frac{B_{\text{SR}}}{B_{\text{CR}}} \equiv N_{\text{CR}} \times \alpha \quad (5.4)$$

2029 Phrased this way, the equation shows that with enough events in the control region, a large theoretical
 2030 uncertainty on the overall background yield in the signal region can be replaced by a small statistical un-
 2031 certainty coming from the number of data events in the CR and a smaller theoretical uncertainty on the
 2032 extrapolation from the control region to the signal region.

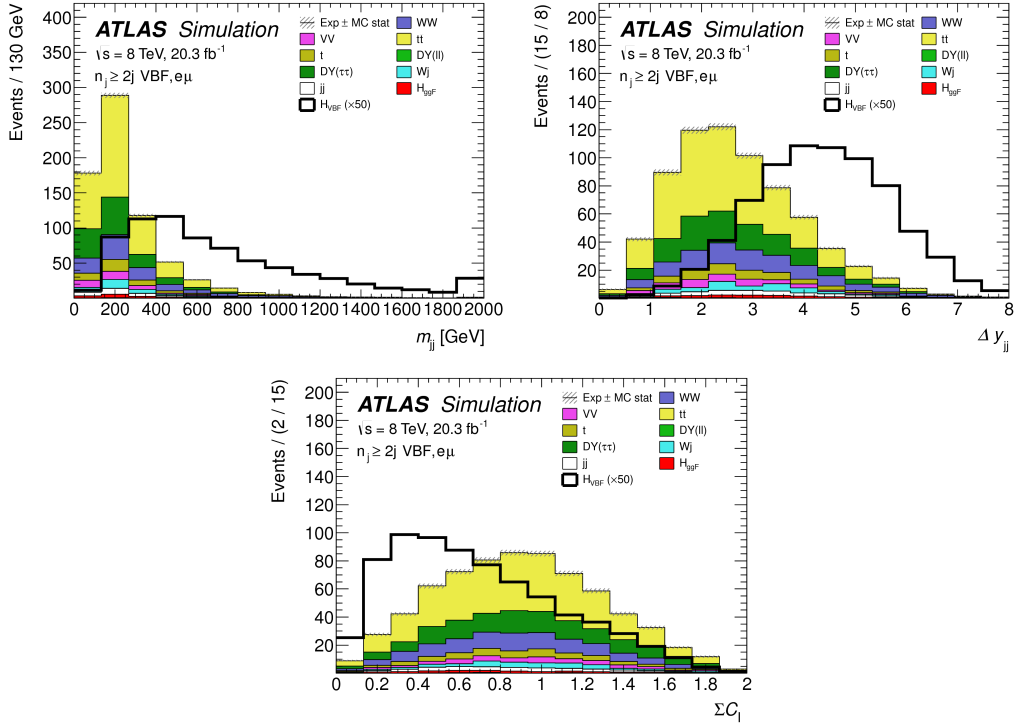


Figure 5.9: VBF topology variables - m_{jj} (top left), Δy_{jj} (top right), $\sum C_\ell$ (bottom) - used in the selection requirements of the cut-based signal region and as inputs to the BDT result. These are plotted after all of the BDT pre-training selection cuts [74]. The VBF Higgs signal cross section is multiplied by a factor of 50 to allow for shape comparisons.

5.5.2 TOP BACKGROUND

The normalization factor β_t for the top background in the VBF analysis is derived in a region required to have one b -tagged jet, or $n_b = 1$. In the cut-based analysis, normalization factors are computed after every selection requirement by making the same requirements in the CR. These NF are then applied to the $t\bar{t}$ and single top event yields in the SR. In the BDT analysis, a single normalization factor is computed for each bin of O_{BDT} after applying the BDT pre-training cuts described previously. The computed normalization factors are derived with all flavor combinations combined in order to decrease statistical uncertainty. Additionally, in the BDT analysis, BDT bins 2 and 3 are merged for the same reason.

Table 5.10 shows the evolution of the β_t through the cut-based selection. Table 5.11 shows the value of the β_t in each bin of O_{BDT} . The computed factors are almost all relatively consistent with unity, except for bin 1 of O_{BDT} which requires a larger correction. The normalization factors in bins 2 and 3 of O_{BDT} are also

2044 consistent with those derived in the cut-based signal region, increasing confidence in the BDT estimation.

Figure 5.10 shows the m_{jj} and O_{BDT} distributions in the top control region. Overall the modeling looks

Cut	β_t
$p_T^{\text{sum}} < 15 \text{ GeV}$	1.03 ± 0.01
$m_{\tau\tau} < m_Z - 25$	1.05 ± 0.01
$m_{jj} > 600 \text{ GeV}$	0.96 ± 0.06
$\Delta y_{jj} > 3.6$	1.02 ± 0.08
CJV	1.13 ± 0.16
OLV	1.01 ± 0.19
$m_{jj} < 1 \text{ TeV}$	0.94 ± 0.19
$m_{jj} > 1 \text{ TeV}$	1.48 ± 0.66

Table 5.10: Top normalization factors computed at each stage of the cut-based selection. Uncertainties are statistical only.

O_{BDT}	β_t
Bin 0	1.09 ± 0.02
Bin 1	1.58 ± 0.15
Bin 2	0.95 ± 0.31
Bin 3	0.95 ± 0.31

Table 5.11: Top normalization factors computed for each bin of O_{BDT} . Uncertainties are statistical only.

2045

2046 consistent with the data. While these normalization factors can be computed and applied to the expected
 2047 background yields listed in tables like table 5.8, the final normalization of the top background is profiled
 2048 (meaning there is a dedicated Poisson constraint) and allowed to float in the final statistical fit.

2049 5.5.3 $Z/\gamma^* \rightarrow \tau\tau$ BACKGROUND

2050 In the different flavor channels, the $Z/\gamma^* \rightarrow \tau\tau$ background is an important one. Di-tau production can
 2051 produce an $e\mu$ final state if each τ lepton decays to a different flavor lepton.

2052 In the BDT analysis, a single normalization factor for the background is derived. A control region
 2053 is defined using the pre-training selection cuts, except requiring that $|m_{\tau\tau} - m_Z| < 25 \text{ GeV}$ so that
 2054 the region is enriched in $Z/\gamma^* \rightarrow \tau\tau$ background. Additional requirements of $m_{\ell\ell} < 80(75) \text{ GeV}$
 2055 in the different (same) flavor channel, as well as $O_{\text{BDT}} > -0.48$ are applied to increase the purity of the

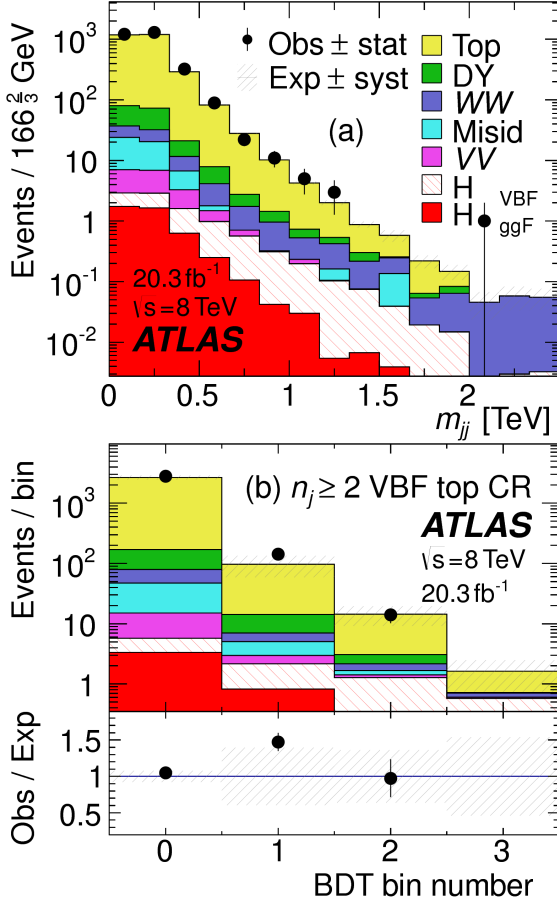


Figure 5.10: Distributions of m_{jj} (a) and O_{BDT} (b) in the VBF $n_b = 1$ top CR [74].

region. The final $\beta_{Z/\gamma^* \rightarrow \tau\tau}$ is calculated to be 0.9 ± 0.3 (statistical uncertainty only). Because of the small contribution of this background in the BDT analysis and the large statistical uncertainty, no additional systematics are calculated. The final SR estimate is scaled by this β and not allowed to float in the fit.

The cut-based corrections are a bit more involved because they need to be applied selection by selection, as well as in the final signal region for the fit. The control region is defined including all SR requirements up to the $Z/\gamma^* \rightarrow \tau\tau$ veto, which is instead turned into a Z mass peak requirement as for the BDT region. The $m_{\ell\ell}$ cut from the BDT region is included as well. The cut-based approach aims to correct the normalization of the $Z/\gamma^* \rightarrow \tau\tau$ background in two ways. First, an overall normalization factor is computed from the control region. However, the VBF topological cuts are not included in this region, and applying them as is done in the top CR is not feasible due to limited statistics. So, instead, correction

2066 factors (CF) to the cut efficiencies of the VBF cuts are derived in a same flavor $Z \rightarrow \ell\ell$ control region,
 2067 which has significantly more statistics. The CF is simply the ratio of the cut efficiencies in data and MC
 2068 derived in this region. In the end, the overall background estimate is given by equation 5.5.

$$N_{Z/\gamma^* \rightarrow \tau\tau}^{\text{est}} = B_{Z/\gamma^* \rightarrow \tau\tau}^{\text{SR}} \times \beta_{\tau\tau} \times \frac{\epsilon_{\text{VBF cuts}}^{\text{data}}}{\epsilon_{\text{VBF cuts}}^{\text{MC}}} \quad (5.5)$$

2069 The hypothesis is that while the normalization correction must be derived in a dedicated region, the effi-
 2070 ciency of the VBF topology requirements should not be sensitive to the type of Z/γ^* process and thus the
 2071 higher number of events can be exploited to derive the CF. Figure 5.11 shows a shape comparison for the
 2072 m_{jj} variable in $Z \rightarrow \tau\tau$ events in the signal region and $Z \rightarrow \ell\ell$ events in the control region. The figure
 2073 shows that the shapes are indeed comparable and thus any CF derived in the same flavor control region
 2074 can reliably be applied in the signal region.

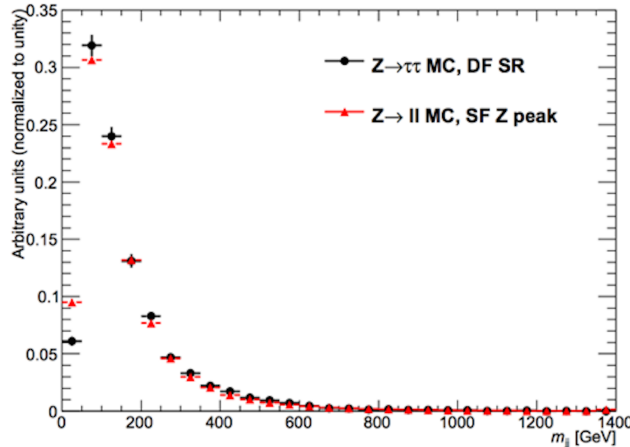


Figure 5.11: Comparison of m_{jj} shape in a same flavor $Z \rightarrow \ell\ell$ control region and the VBF cut-based signal region.
 The MC samples used for these distributions are given in table 5.4.

2075 Table 5.12 shows the overall normalization factor $\beta_{\tau\tau}$ and the efficiency correction factors for the various
 2076 VBF topological cuts. In general, the statistical uncertainties on the cut efficiency corrections are quite
 2077 good, and the MC tends to underestimate the efficiency of the VBF cuts for the $Z/\gamma^* \rightarrow \tau\tau$ background.
 2078 The overall normalization factor is also consistent with that calculated for the BDT analysis.

$\beta_{\tau\tau}$	0.97 ± 0.04
Cut	Correction factors (CF)
$m_{jj} > 600 \text{ GeV}$	1.09 ± 0.01
$\Delta y_{jj} > 3.6$	1.14 ± 0.02
CJV	1.20 ± 0.02
OLV	1.17 ± 0.03
$m_{jj} < 1 \text{ TeV}$	1.17 ± 0.06
$m_{jj} > 1 \text{ TeV}$	1.18 ± 0.13

Table 5.12: $Z/\gamma^* \rightarrow \tau\tau$ correction factors for the VBF cut-based analysis. Uncertainties are statistical only.

2079 5.5.4 $Z/\gamma^* \rightarrow \ell\ell$ BACKGROUND

2080 In the same flavor channels, the $Z/\gamma^* \rightarrow \ell\ell$ background is dominant and thus must be estimated cor-
 2081 rectly. In both the BDT and cut-based analyses, the background is estimated using the so-called “ABCD”
 2082 method. The ABCD method creates four different regions by defining requirements on two variables.
 2083 One of the regions (A) is the signal region, while the other regions are defined by inverting one of both of
 2084 the requirements. in this case, the two variables used are $m_{\ell\ell}$ and E_T^{miss} , because inverting either of the
 2085 SR cuts on these variables will give regions rich in the $Z/\gamma^* \rightarrow \ell\ell$ background. Figure 5.12 illustrates the
 2086 definitions of each region.

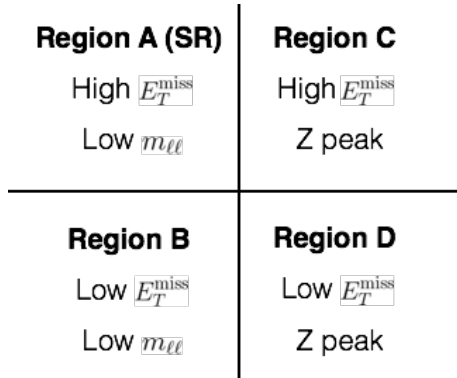


Figure 5.12: General illustration of the ABCD region definitions for $Z/\gamma^* \rightarrow \ell\ell$ background estimation.

2087 In both of the cut-based and BDT analyses, the Z peak region is defined with $|m_{\ell\ell} - m_Z| < 15 \text{ GeV}$.
 2088 In the cut-based analysis, low $m_{\ell\ell}$ corresponds to $m_{\ell\ell} < 50 \text{ GeV}$ (this defines the cut-based SR) while
 2089 in the BDT it is $m_{\ell\ell} < 75 \text{ GeV}$. In the cut-based, high and low E_T^{miss} are defined as opposite ends of

2090 the 55 GeV cut applied for the signal region definition. The BDT low E_T^{miss} region is between 25 and
 2091 45 GeV, while the high E_T^{miss} region is $E_T^{\text{miss}} > 45$ GeV.

2092 Once the regions are defined, the background in the signal region is estimated by extrapolating the
 2093 estimate in region B to region A. This extrapolation is done by multiplying the number of events in region
 2094 B by the ratio of the number of events in regions C and D. Effectively, the Z peak region is used to estimate
 2095 the efficiency of the E_T^{miss} requirement in data, and then this efficiency is applied in the low $m_{\ell\ell}$ region.
 2096 The method assumes that the E_T^{miss} efficiency is uncorrelated with $m_{\ell\ell}$. The method can be applied in
 2097 MC as a check on this assumption, and an additional correction, f_{corr} , is applied for the non-closure of
 2098 the method in MC. This is summarized in equations 5.6 and 5.7.

$$N_{Z/\gamma^* \rightarrow \ell\ell}^{\text{SR}} = N_{Z/\gamma^* \rightarrow \ell\ell}^{\text{B}} \times \frac{N_{Z/\gamma^* \rightarrow \ell\ell}^{\text{C}}}{N_{Z/\gamma^* \rightarrow \ell\ell}^{\text{D}}} \times f_{\text{corr}} \quad (5.6)$$

$$f_{\text{corr}} = \frac{B_{\text{MC}}^{\text{A}}/B_{\text{MC}}^{\text{B}}}{B_{\text{MC}}^{\text{C}}/B_{\text{MC}}^{\text{D}}} \quad (5.7)$$

2100 Here, the N refer to data yields in each region with the non Z/γ^* backgrounds subtracted, while B refer
 2101 to the Z/γ^* yields in MC in each region.

2102 A normalization factor $\beta_{\ell\ell}$ is computed for each analysis as the ratio of the predicted data yield to the
 2103 MC yield in the SR. The shape of the BDT distribution is taken from data region B, while the shape of
 2104 the m_T distribution in the cut-based analysis is taken from Z/γ^* MC in the SR. The values of $\beta_{\ell\ell}$ in the
 2105 cut-based and BDT analyses from this method are summarized in table 5.13. They are quite consistent
 2106 with one another within the statistical uncertainties. The value of f_{corr} is found to be 0.77 ± 0.13 . In the
 2107 cut-based analysis, the same cut efficiency correction factors shown in table 5.12 are also applied (in product
 2108 with the $\beta_{\ell\ell}$) to obtain the final estimate of the Z/γ^* background in the same flavor channels.

	$\beta_{\ell\ell}$
BDT Bin 1	1.01 ± 0.15
BDT Bin 2	0.89 ± 0.28
Cut-based	0.81 ± 0.21

Table 5.13: $Z/\gamma^* \rightarrow \ell\ell$ normalization factors for cut-based and BDT analyses. Uncertainties are statistical only.

2109 5.5.5 WW AND OTHER DIBOSON BACKGROUNDS

2110 The Standard Model WW and other diboson backgrounds (WZ , ZZ , $W\gamma$, $W\gamma^*$, and $Z\gamma$) have both
 2111 their shape and normalization taken from MC simulation as they are subdominant in the VBF analysis.
 2112 They are validated in dedicated control regions and found to agree with data well.

2113 As SM WW production is the largest of these backgrounds and is irreducible, validating the estimate
 2114 is of particular importance. A validation region is constructed by requiring the pre-selection requirements
 2115 on leptons and $m_{\ell\ell}, n_b = 0$, and $m_T > 100$ GeV. The m_{T2} variable is an additional discriminant that
 2116 has been shown to have the ability to isolate the SM WW background [99]. It is calculated by scanning
 2117 over all possible values of neutrino momentum for both W bosons and taking the minimum result. A
 2118 requirement of $m_{T2} > 160$ GeV is placed to define the WW validation region. This requirement gives a
 2119 60% purity for the validation region. The derived normalization factor in this region is 1.15 ± 0.19 and
 2120 is thus consistent with unity. Figure 5.13 shows the m_{T2} distribution and how it distinguishes the WW
 2121 background.

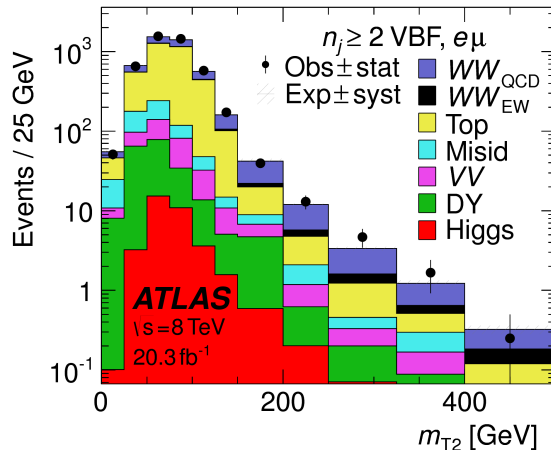


Figure 5.13: Distribution of m_{T2} in the WW validation region of the VBF analysis [74].

2122 5.5.6 HIGGS PRODUCTION VIA GLUON-GLUON FUSION

2123 Because this analysis is dedicated to measuring the VBF contribution to Higgs production, the component
 2124 of Higgs production from gluon-gluon fusion is treated as a background. The shape is taken directly from

2125 simulation, using the generators described in table 5.4. In the final combined fit of all different Higgs
2126 signal regions, the normalization is controlled by either a combined signal strength parameter μ , which
2127 controls the normalization of both ggF and VBF production, or a separate parameter μ_{ggF} depending on
2128 the interpretation being presented in the final results.

2129 5.5.7 BACKGROUNDS WITH MISIDENTIFIED LEPTONS

2130 As discussed previously, the $W+\text{jets}$ and QCD multijet backgrounds are derived with fully data-driven
2131 methods. These backgrounds do not make a large contribution to the final VBF signal region but their es-
2132 timation methods are discussed briefly here. Because both backgrounds involve at least one mis-identified
2133 lepton, they are labeled as “misid” throughout this chapter.

2134 $W+\text{jets}$ BACKGROUND

2135 The $W+\text{jets}$ background enters the signal region by having one of the jets mis-reconstructed as a lepton.
2136 The background is estimated by constructing a control sample with two leptons, where one lepton passes
2137 the usual lepton quality requirements but the second lepton fails one of those requirements (also known
2138 as the “anti-identified” lepton). This control region is rich in the $W+\text{jets}$ contribution because if a second
2139 lepton is reconstructed in a $W+\text{jets}$ event it is likely to be of poor quality. The purity of this $W+\text{jets}$ control
2140 sample is 85% to 90% depending on the exact configuration of leptons in the final state.

2141 The $W+\text{jets}$ content of the signal region is estimated by extrapolation from the control sample to the
2142 signal region using extrapolation factors derived in a $Z+\text{jets}$ control sample in data. The assumption of
2143 the method is that the probability of a jet being misidentified as a lepton does not change between $W+\text{jets}$
2144 and $Z+\text{jets}$ samples, and systematic uncertainties are assigned for differences in sample composition. The
2145 extrapolation factor is defined as the ratio of the number of lepton candidates satisfying all quality criteria
2146 to the number of lepton candidates anti-identified. This ratio is measured in bins of p_T and η . Thus, the
2147 final signal region estimate (binned as the extrapolation factor is binned) is simply the number of events in
2148 the anti-identified lepton control sample multiplied by the extrapolation factor derived from the $Z+\text{jets}$
2149 control sample. Figure 5.14 shows the extrapolation factors derived for electrons and muons. The extrap-

2150 olation factor can be seen in the figure to be an order of magnitude larger for muons than electrons, but
 2151 this does not indicate that jets have a larger probability to be mis-identified as a muon than an electron.
 2152 Values of the extrapolation factor are actually determined by the specific requirements used to define an
 2153 anti-identified lepton. The difference between the muon and electron extrapolation factors comes from
 2154 different definitions of the anti-identified lepton in each case.

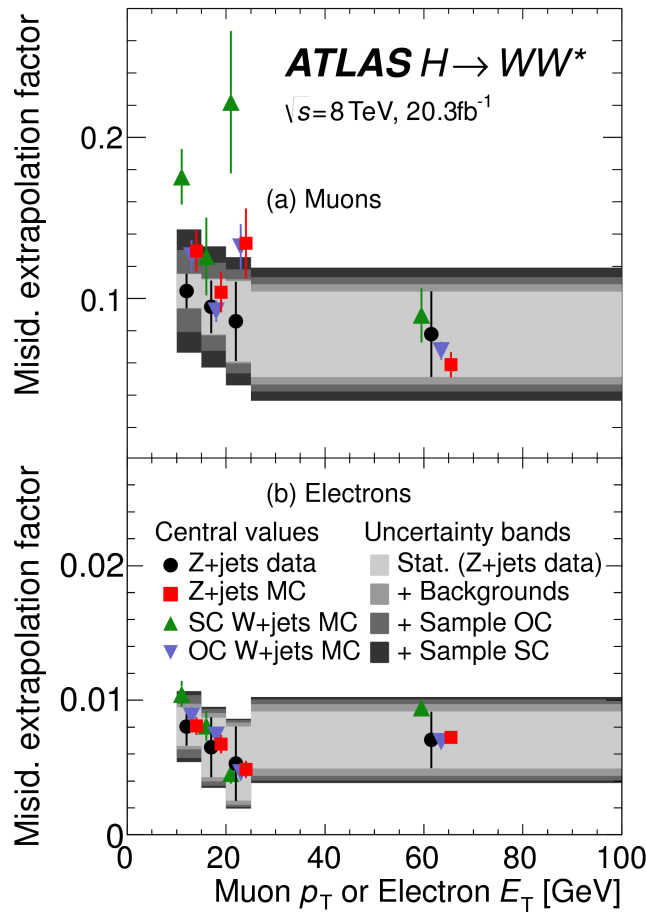


Figure 5.14: Extrapolation factors for the $W + \text{jets}$ estimate derived for muons (a) and electrons (b) as a function of lepton p_T [74]. OC refers to the opposite charge $W + \text{jets}$ MC sample, while SC refers to the same charge $W + \text{jets}$ MC. The uncertainty bands have contributions from statistical uncertainty in the data and backgrounds to $Z + \text{jets}$ that are subtracted from the data, as well as systematic uncertainties due to variations in the extrapolation factor between the three MC samples shown.

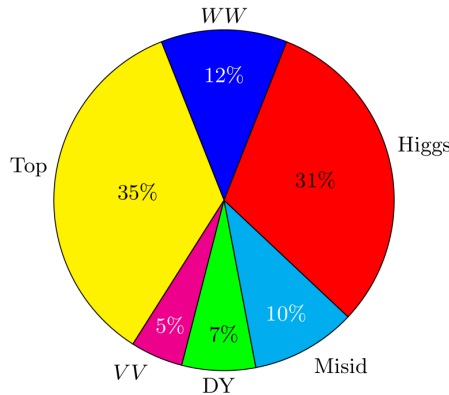
2155 **QCD MULTIJET BACKGROUND**

2156 The method for estimating the multijet background is very similar to the $W + \text{jets}$ estimation method. The
2157 control sample in this case has two anti-identified leptons but otherwise satisfies all signal region require-
2158 ments. The extrapolation factor is estimated from a multijet sample and applied twice to the control sam-
2159 ple.

2160 **5.5.8 BACKGROUND COMPOSITION IN SIGNAL REGION**

2161 After all of these estimation procedures, the signal region background composition can be calculated. The
2162 estimated yields are all shown in table 5.8. Figure 5.15 shows the relative percentages of the different back-
2163 ground for the different flavor and same flavor final states. In $e\mu$, the leading backgrounds are top back-
2164 grounds, ggF Higgs, and SM WW production. In $ee/\mu\mu$, the leading background is Drell-Yan, followed
2165 by top and ggF Higgs.

(a) $n_j \geq 2$ VBF, $e\mu$



(b) $n_j \geq 2$ VBF, $ee/\mu\mu$

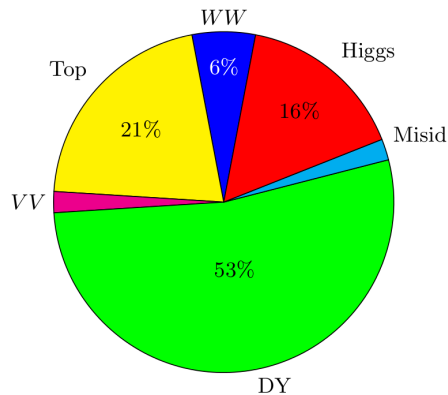


Figure 5.15: Background composition in final VBF signal region [74].

2166 **5.6 SYSTEMATIC UNCERTAINTIES**

2167 There are two main types of systematic uncertainties that are assessed for the analysis. First, theoretical
2168 uncertainties associated with the signal and background yield estimates are discussed. Then, experimental
2169 uncertainties due to detector effects are shown. Normalization uncertainties refer to uncertainties that

2170 affect the cross section of the process in question in the signal region being probed. Shape uncertainties
2171 refer to systematic uncertainties that affect the shape of the final discriminating variable (either m_T or
2172 O_{BDT}).

2173 **5.6.1 THEORETICAL UNCERTAINTIES**

2174 There are four main components to theoretical uncertainties assigned to signal and background processes
2175 taken from Monte Carlo. Each one is a different source of variation in the overall acceptance for that
2176 process. The first involves variation of the QCD renormalization and factorization scales used in the cal-
2177 culation. In this case, the two scales are varied both independently and simultaneously by factors of two
2178 high or low. The resulting variation in normalization and shape for the process is taken as a systematic
2179 uncertainty (referred to as scale uncertainty). This uncertainty approximates the level of the correction
2180 to the cross section that would come from including the next order of the QCD calculation. Next, there
2181 is an uncertainty associated with the PDF set used in generating the events. The uncertainty eigenvec-
2182 tors for the given PDF set are inspected, and the envelope of maximal variation is taken as an uncertainty
2183 (referred to as PDF uncertainty). Finally, there are two uncertainties associated with the choice of MC
2184 software. An uncertainty associated with the generator chosen for the hard scattering process is evaluated
2185 by keeping the parton showering software constant but varying the matrix element generator and taking
2186 the maximal variation as an uncertainty (referred to as the generator uncertainty). The converse variation
2187 can also be done, where the matrix element generator remains constant and the generator used for the un-
2188 derlying event/parton shower modeling is varied (referred to as the UE/PS uncertainty). In cases where
2189 the background is normalized in a control region, the systematic uncertainty arises from variations of the
2190 extrapolation factor α between the CR and the SR, which can affect the normalization of the background
2191 in the SR.

2192 There are two additional uncertainties that are applied to the Higgs processes as well. First, there are
2193 uncertainties assigned to the Higgs total production cross section. Then, there are uncertainties assigned
2194 based on the fact that the analysis is done in exclusive jet bins and it is possible for signal events to migrate
2195 from one bin to the next depending on the presence or absence of jets. These are assigned using the Jet Veto

2196 Efficiency (JVE) procedure [18, 100] for ggF events and the Stewart-Tackmann (ST) method [101] for VBF
 2197 production. Table 5.14 shows the total theory uncertainties on the backgrounds in the cut-based analysis.
 2198 These are the sum in quadrature of the uncertainties from each of the variations described above.

Process	Theory syst. (%)
ggF H	48
Top	26
QCD WW	37
$Z/\gamma^* \rightarrow \tau\tau$	6.1

Table 5.14: Theoretical systematic uncertainties for various processes in the cut-based VBF analysis, given in units of percent change in yield. Values are given for the low m_{jj} signal region. The systematic shown for the WW background is relevant only to WW diagrams where the final state jets are the result of QCD vertices.

2199 Figures 5.16 and 5.17 show the variations in the extrapolation factor from the PDF and QCD uncertain-
 2200 ties on the top background estimate, binned in m_T , for the cut-based analysis. In both cases, there was
 2201 no significant shape uncertainty but normalization uncertainties were assigned according to the maximal
 2202 variation. These uncertainties enter into the 26% total uncertainty on top quark production quoted in
 2203 table 5.14

2204 While the estimate for the same-flavor $Z/\gamma^* \rightarrow \ell\ell$ background is data-driven, there is still a systematic
 2205 uncertainty taken for the non-closure of the method in Monte Carlo. This is taken as the maximum of the
 2206 deviation of the non-closure factor f_{corr} from unity and its uncertainty, or $\max(|1 - f_{\text{corr}}|, \delta f_{\text{corr}})$. For
 2207 the cut-based analysis this non-closure uncertainty 23%, while for the BDT analysis it is 17%.

2208 5.6.2 EXPERIMENTAL UNCERTAINTIES

2209 In this analysis, the theoretical uncertainties are the most dominant after statistical, but there are some
 2210 experimental uncertainties that make a contribution as well. The first is the uncertainty on the measured
 2211 integrated luminosity, which affects the signal estimate and backgrounds whose normalizations are taken
 2212 from MC. It is measured to be 2.8% in the 8 TeV dataset [102]. The dominant sources of uncertainty over-
 2213 all are uncertainties on the jet energy scale and resolution and the b -tagging efficiency. Additional sources
 2214 include lepton uncertainties on identification, resolution, and trigger efficiency, as well as uncertainties on
 2215 the missing transverse momentum.

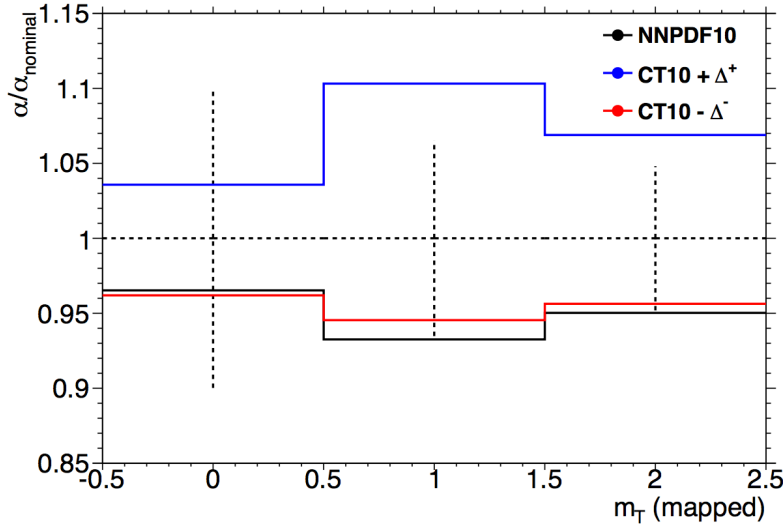


Figure 5.16: Variations in the top background extrapolation factor in the cut-based analysis due to PDF uncertainties. The uncertainties are shown in the three bins of m_T used in the final cut-based statistical fit. Variations from the eigenvector of the nominal PDF, CT10, as well as the result from an alternate PDF (NNPDF10), are compared.

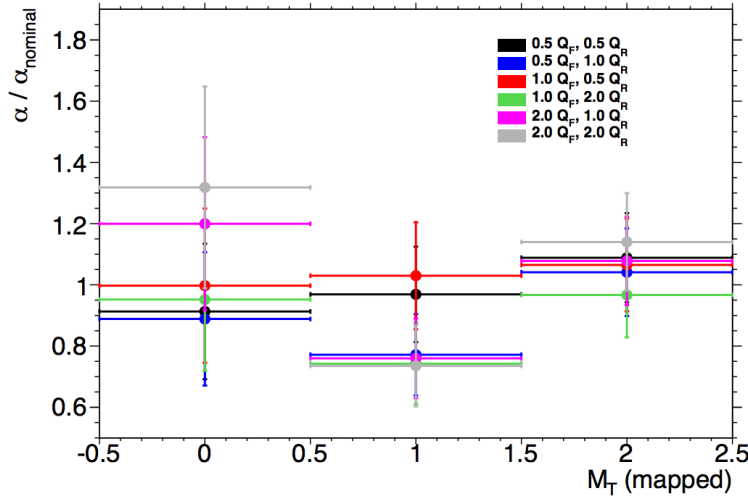


Figure 5.17: Variations in the top background extrapolation factor in the cut-based analysis due to QCD scale uncertainties. The uncertainties are shown in the three bins of m_T used in the final cut-based statistical fit. Q_F is the QCD factorization scale, while Q_R is the QCD renormalization scale.

The jet energy scale uncertainty is split into several independent components, including jet-flavor dependent calorimeter response uncertainties, uncertainties on modeling of pile-up interactions, uncertainties on extrapolation from the central to forward detector regions, and MC non-closure [103]. The uncer-

tainty on energy scale for jets used in this analysis ranges from 1% to 7% depending on the jet p_T and η .
The jet energy resolution varies from 5% to 20%, with uncertainties ranging from 2% to 40% (the largest
uncertainties occurring at the selection threshold).

The b-tagging efficiency is independently measured in data samples enriched in dileptonic decays of $t\bar{t}$
events or in events where a muon is reconstructed in the vicinity of a jet [104, 105]. The efficiencies and
their uncertainties are binned in p_T and decomposed into uncorrelated components using an eigenvector
method [106]. Uncertainties on the efficiency range from 1% to 7.8%. The uncertainty on the rate of
misidentification of c -jets as b -jets ranges from 6-14%, while the uncertainty on the rate of light jet mis-
tagging ranges from 9-19% depending on p_T and η . These efficiency uncertainties are applied to each
individual jet in the event.

Table 5.15 shows the effect of the experimental uncertainties on the VBF signal yield. The largest ex-
perimental uncertainty is the jet energy scale and resolution. Object uncertainties associated with p_T^{miss} ,
electrons, and muons also make a small contribution, as well as the uncertainty on the trigger efficiency.

Uncertainty source	Impact on signal yield (%)
Jet energy scale and resolution	5.4
Luminosity	2.8
p_T^{miss} scale and resolution	1.2
Electron uncertainties	1.0
Muon uncertainties	0.9
Trigger efficiency	0.4

Table 5.15: Experimental systematic uncertainties (expressed as % of the estimated yield) for the VBF signal [74].

The total experimental uncertainties on different signal and background components are summarized
in table 5.16. They are compared to the level of other statistical and systematic uncertainties as well. Overall,
the experimental uncertainties are sub-dominant compared to the statistical and theoretical uncertainties.

5.7 RESULTS

While the combined results of all the $H \rightarrow WW^*$ sub-analyses will be discussed in the next chapter, this
section presents the results of the VBF specific analysis and interpretations. As table 5.7 shows, the final

Sample	Total uncert.	Stat. uncert.	Expt. uncert.	Theo. uncert.
$n_j \geq 2$ VBF-enriched				
N_{sig}	13	—	6.8	12
N_{bkg}	9.2	4.7	6.4	4.5
N_{WW}	32	—	14	28
N_{top}	15	9.6	7.6	8.5
N_{misid}	22	—	12	19
N_{VV}	20	—	12	15
$N_{\tau\tau}$ (DY)	40	25	31	2.9
$N_{ee/\mu\mu}$ (DY)	19	11	15	—

Table 5.16: Composition of the post-fit uncertainties (in %) on the total signal (N_{sig}), total background (N_{bkg}), and individual background yields in the VBF analysis [74]. “Stat.” refers to statistical uncertainties, “Expt.” refers to experimental systematic uncertainties, and “Theo.” refers to theoretical systematic uncertainties.

cut-based signal region contains 20 events in data with $m_T < 150$ GeV, 14 coming from the $e\mu$ channel and 6 coming from the $ee + \mu\mu$ channel. The BDT analysis has many more candidates due to its looser selection, and the yields in each bin of O_{BDT} are shown in table 5.17. Most of the information about the VBF signal comes from bins 2 and 3 which have significantly better signal to background ratios than bin 1. Additionally, the same-flavor channels contribute roughly the same sensitivity as the different flavor channels, highlighting the gain from adding these channels post-discovery with the techniques discussed in chapter 3.

Figure 5.18(a) shows the final distribution of data candidates compared to the expected m_T distribution for signal and background in the cut-based signal region. The data are very consistent with a VBF Higgs hypothesis. Figure 5.18(b) shows where the data candidates fall in the two-dimensional binning of m_T and m_{jj} used in the fit for the cut-based analysis. Figure 5.19 shows the distributions of O_{BDT} and m_T in the VBF BDT analysis. Again the data are quite consistent with a VBF Higgs hypothesis.

Because the cut-based result is used as a validation for the BDT analysis and the two signal regions are not fully orthogonal, it is interesting to explore which events overlap between the two analyses. Of the twenty events in the cut-based signal region, only seven were not selected by the BDT analysis, while the other thirteen also enter the BDT signal region. Figure 5.20 shows where the different analysis candidates lie in the m_{jj} - m_T plane. This shows clearly that the advantage of the BDT analysis is that it can extract

(a) Before the BDT classification

Selection	Summary						Composition of N_{bkg}										
	$N_{\text{obs}}/N_{\text{bkg}}$	N_{obs}	N_{bkg}	N_{signal}	N_{ggF}	N_{VBF}	N_{VH}	N_{WW}^{QCD}	N_{WW}^{EW}	$N_{t\bar{t}}$	N_t	N_{Wj}	N_{jj}	N_{VV}	$N_{\text{Drell-Yan}}$	$N_{ee/\mu\mu}^{\text{QCD}}$	$N_{\tau\tau}^{\text{EW}}$
$e\mu$ sample	1.04 ± 0.04	718	689	13	15	2.0		90	11	327	42	29	23	31	2.2	130	2
$ee/\mu\mu$ sample	1.18 ± 0.08	469	397	6.0	7.7	0.9		37	3	132	17	5.2	1.2	10.1	168	23	1

(b) Bins in O_{BDT}

$e\mu$ sample																	
Bin 0 (not used)	1.02 ± 0.04	661	650	8.8	3.0	1.9		83	9	313	40	26	21	28	2.2	126	1
Bin 1	0.99 ± 0.16	37	37	3.0	4.2	0.1		5.0	1.0	17	3.1	3.3	1.8	2.6	—	4.0	0.2
Bin 2	2.26 ± 0.63	14	6.2	1.2	4.2	—		1.5	0.5	1.8	0.3	0.4	0.3	0.8	—	0.3	0.3
Bin 3	5.41 ± 2.32	6	1.1	0.4	3.1	—		0.3	0.2	0.3	0.1	—	—	0.1	—	0.1	0.1
$ee/\mu\mu$ sample																	
Bin 0 (not used)	1.91 ± 0.08	396	345	3.8	1.3	0.8		33	2	123	16	4.1	1.1	8.8	137	20.5	0.5
Bin 1	0.82 ± 0.14	53	45	1.5	2.2	0.1		3.0	0.5	10.4	1.8	0.8	0.2	0.9	26	1.7	0.1
Bin 2	1.77 ± 0.49	14	7.9	0.6	2.5	—		0.8	0.3	1.1	0.2	0.2	—	0.3	4.4	0.3	0.1
Bin 3	6.52 ± 2.87	6	0.9	0.2	1.7	—		0.1	0.2	0.2	—	—	—	0.7	—	—	

Table 5.17: Event selection for the VBF BDT analysis. The event yields in (a) are shown after the pre-selection and the additional requirements applied before the BDT classification (see text). The event yields in (b) are given in bins in O_{BDT} after the classification [74].

2255 signal candidates from the lower m_{jj} region due to its ability to recognize correlations with other variables.

2256 While the context of these results in the broader $H \rightarrow WW^*$ statistical analysis will be presented in the
 2257 next chapter, the statistical significance of the VBF Higgs result is shown here. In the BDT analysis, the
 2258 expected signal significance was 2.7σ , while the observed significance was 3.1σ . In the cut-based analysis,
 2259 the expected significance was 2.1σ and the observed significance was 3.0σ . The compatibility between
 2260 these two results can be evaluated by computing the probability of observing a larger difference in Z_0 values
 2261 than the one measured. Using toy Monte Carlo with the ggF signal strength fixed to unity and considering
 2262 only statistical uncertainties, this probability is computed to be 79%, indicating good agreement between
 2263 the analyses. This result represents the first evidence of the vector boson fusion production of a Higgs
 2264 boson.

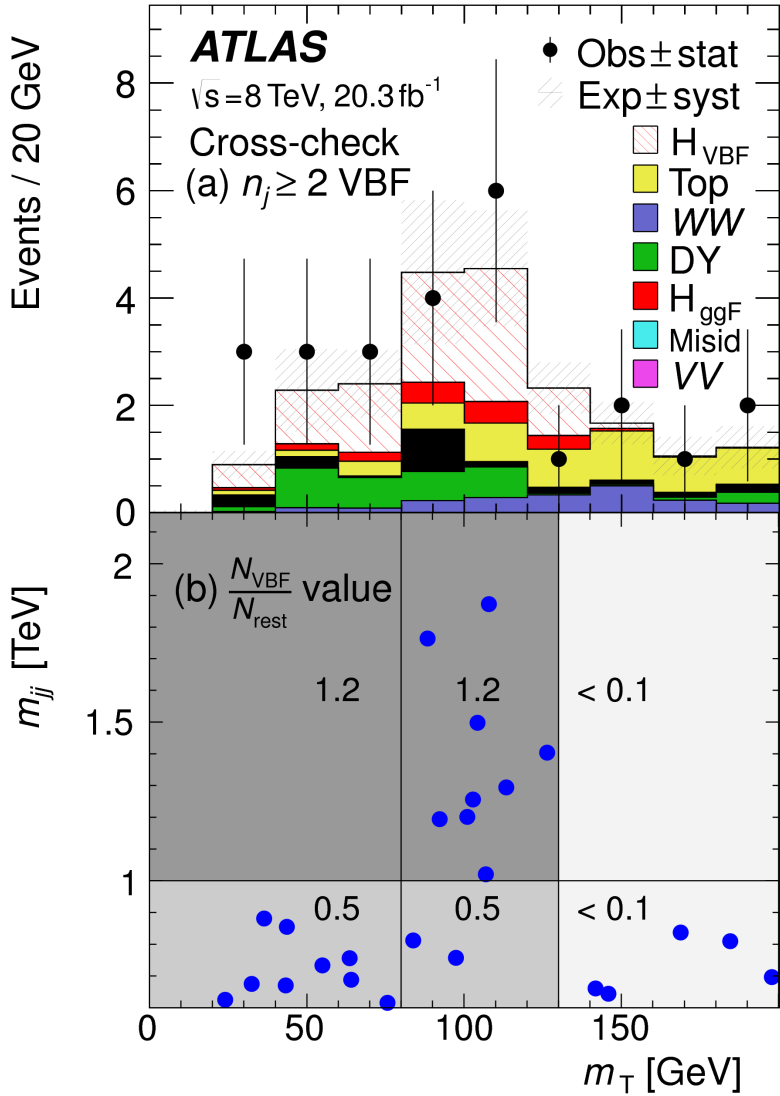


Figure 5.18: Post-fit distributions in the cut-based VBF analysis. Panel (a) shows the one-dimensional m_T distribution, while (b) shows the data candidates split into the bins of m_T and m_{jj} used in the final fit [74].

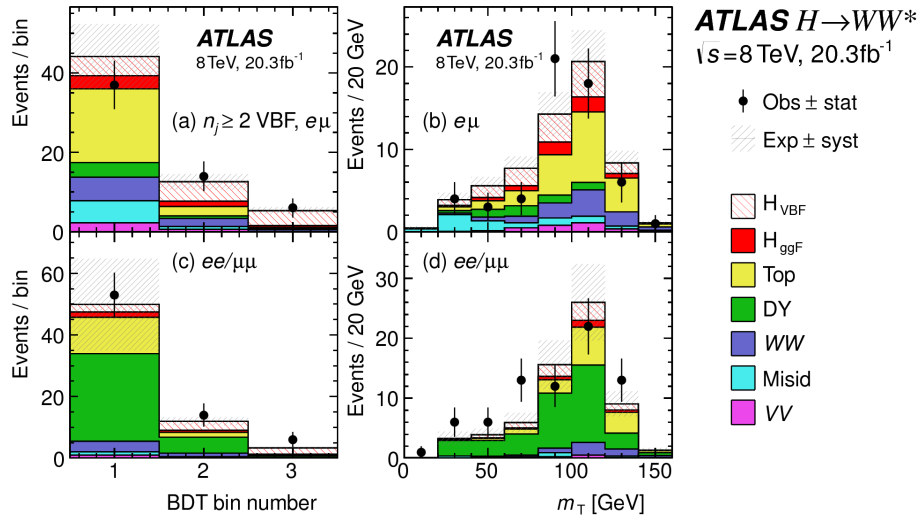


Figure 5.19: Postfit distributions in the BDT VBF analysis [74].

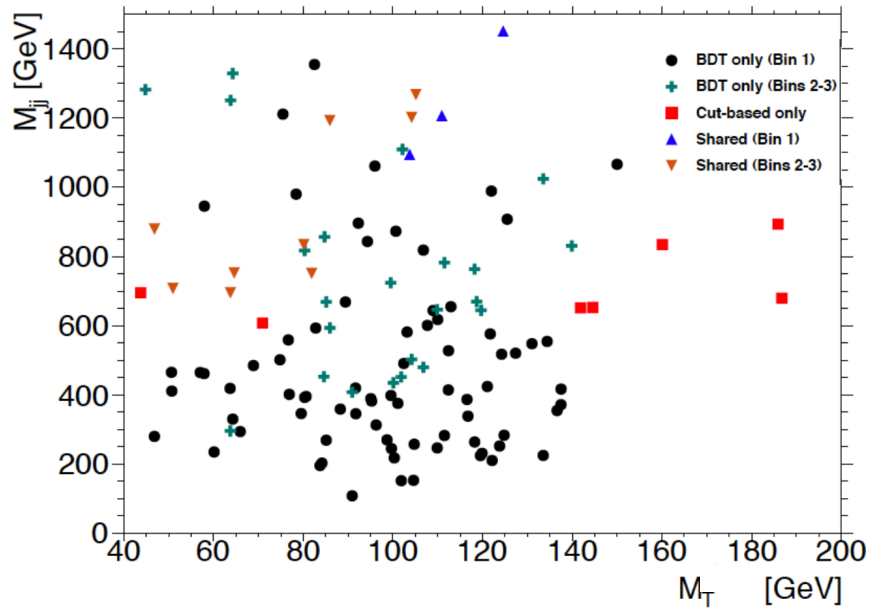


Figure 5.20: Overlap between cut-based and BDT VBF signal region candidates in the m_{jj} - m_T plane.

*The feeling is less like an ending than just another starting
point.*

Chuck Palahniuk

6

2265

2266

Combined Run I $H \rightarrow WW^* \rightarrow \ell\nu\ell\nu$

2267

results

2268

6.1 INTRODUCTION

2269 In the final statistical analysis of $H \rightarrow WW^* \rightarrow \ell\nu\ell\nu$, the dedicated gluon-gluon fusion and vector
2270 boson fusion sensitive signal regions are all combined into a single fit to determine the main parameters
2271 of interest, the Higgs signal strength μ and mass m_H . This chapter presents the combined interpretation
2272 of results in the $H \rightarrow WW^* \rightarrow \ell\nu\ell\nu$ analysis for gluon fusion and vector boson fusion Higgs produc-
2273 tion. First, the results of the dedicated gluon fusion search are presented. These results are an extension
2274 of the discovery analysis (presented in chapter 4) to the full Run I dataset. Next, a comparison of the in-
2275 dividual production mode signal strengths (μ_{ggF} and μ_{VBF}) and a measurement of the combined signal
2276 strength (μ) are shown. Then, the measured values of the Higgs couplings to fermions and vector bosons

2277 are presented. Finally, the cross section measurement for ggF and VBF production are shown.

2278 **6.2 RESULTS OF DEDICATION GLUON FUSION $H \rightarrow WW^* \rightarrow \ell\nu\ell\nu$ ANALYSIS**

2279 The analysis of gluon fusion Higgs production which led to the discovery of the Higgs, as presented in
2280 chapter 4, was also extended to the full Run 1 dataset. This new result included many improvements, such
2281 as more robust E_T^{miss} definitions, a lower sub-leading lepton p_T threshold (10 GeV), and the inclusion of
2282 the same flavor final states [74]. This section presents the results from the gluon fusion dedicated signal
2283 regions in the full Run 1 data. A special focus is placed on the results from the same flavor final state
2284 channels.

2285 **6.2.1 RESULTS IN SAME FLAVOR ($ee/\mu\mu$) FINAL STATES**

2286 Final states of the $H \rightarrow WW^* \rightarrow \ell\nu\ell\nu$ channel where both leptons have the same flavor ($ee/\mu\mu$)
2287 were not included in the discovery result due to increased pileup conditions in the $\sqrt{s} = 8$ TeV data.
2288 Dedicated techniques for background reduction in the same flavor final states were developed, as described
2289 in section 3.5. The results shown in this section are the first published results using the same flavor channels
2290 in the $H \rightarrow WW^*$ analysis.

	N_{obs}	N_{bkg}	N_{ggF}	N_{VBF}
$n_j = 0$	1108	1040 ± 40	77 ± 15	2.4 ± 1.7
$n_j = 1$	467	427 ± 21	22 ± 6	3.6 ± 1.8

Table 6.1: Summary of post-fit yields in ggF dedicated signal regions for the $ee/\mu\mu$ final states [74].

2291 Table 6.1 shows the background estimate, expected signal yield, and event count in data for the same
2292 flavor channels in the $n_j \leq 1$ signal regions. The dedicated same flavor background reduction techniques
2293 allow this channel to preserve a signal to background ratio (0.074 for $n_j = 0$) similar to that of the different
2294 flavor channels (0.087 for $n_j = 0$). Table 6.2 shows the breakdown of the background composition in the
2295 same flavor channels. It can be seen there that after using background reduction requirements, the Z/γ^*
2296 background only contributes approximately 5% (7%) of the total background in the $n_j = 0$ (1) bin.

2297 Figure 6.1 shows the final m_T distribution in data for the $n_j \leq 1$ same flavor channels. The data is very

Background	$n_j = 0$	$n_j = 1$
N_{WW}	740 ± 40	184 ± 15
N_t	39 ± 3	46 ± 4
$N_{t\bar{t}}$	65 ± 5	119 ± 10
N_{Wj}	82 ± 16	19 ± 4
N_{jj}	2 ± 0.5	0.2 ± 0.1
N_{VV}	64 ± 7	31 ± 4
N_{DY}	50 ± 21	28 ± 12

Table 6.2: Post-fit background composition in ggF dedicated signal regions for the $ee/\mu\mu$ final states [74].

consistent with the Higgs hypothesis and it can be seen that the same flavor channels are indeed sensitive to gluon fusion production of the Higgs.
 2298 to gluon fusion production of the Higgs.
 2299

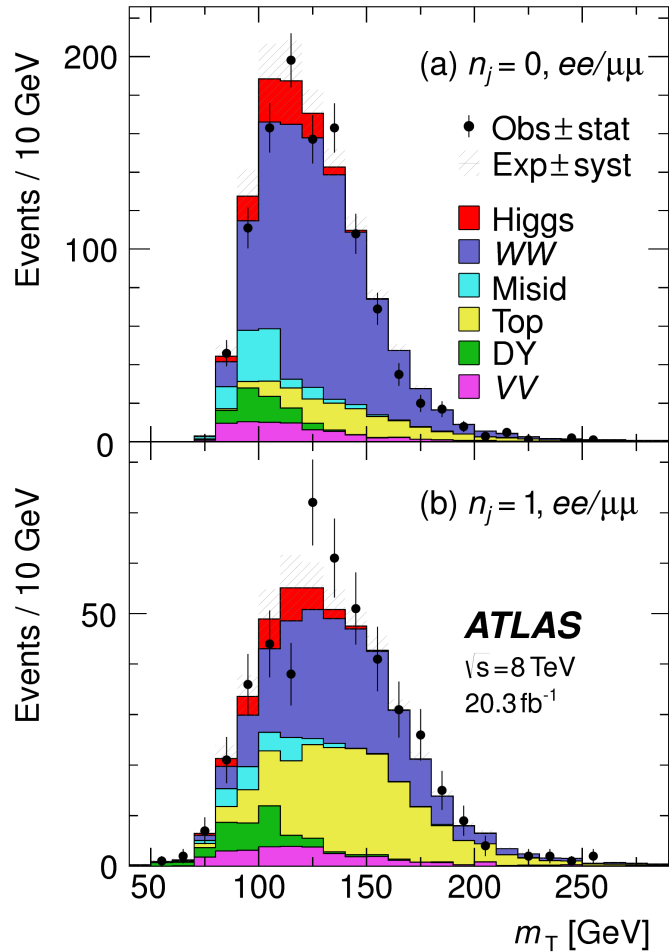


Figure 6.1: Post-fit m_T distribution in the $n_j \leq 1$ regions for the same flavor ($ee/\mu\mu$) final states [74].

SR category i				Fit var.	
n_j , flavor	$\otimes m_{\ell\ell}$	$\otimes p_T^{\ell 2}$	$\otimes \ell_2$		
$n_j = 0$	$e\mu$	$\otimes [10, 30, 55]$	$\otimes [10, 15, 20, \infty]$	$\otimes [e, \mu]$	m_T
	$ee/\mu\mu$	$\otimes [12, 55]$	$\otimes [10, \infty]$		m_T
$n_j = 1$	$e\mu$	$\otimes [10, 30, 55]$	$\otimes [10, 15, 20, \infty]$	$\otimes [e, \mu]$	m_T
	$ee/\mu\mu$	$\otimes [12, 55]$	$\otimes [10, \infty]$		m_T
$n_j \geq 2$ ggF	$e\mu$	$\otimes [10, 55]$	$\otimes [10, \infty]$		m_T
$n_j \geq 2$ VBF	$e\mu$	$\otimes [10, 50]$	$\otimes [10, \infty]$		O_{BDT}
	$ee/\mu\mu$	$\otimes [12, 50]$	$\otimes [10, \infty]$		O_{BDT}

Table 6.3: All signal regions definitions input into final statistical fit [74].

2300 6.2.2 COMBINED GLUON FUSION RESULTS

2301 Table 6.3 shows the individual signal regions that were input into the final statistical fit. The ggF dedicated
 2302 bins use m_T as their discriminating variable and are separated into bins of p_T of the subleading lepton as
 2303 well.

2304 Table 6.4 shows the yields in the various signal regions in both data and expected signal and back-
 2305 grounds. The yields for signal and background are all scaled according to the final normalizations cal-
 2306 culated in the fit.

	N_{obs}	N_{bkg}	N_{ggF}	N_{VBF}
$n_j = 0$	3750	3430 ± 90	300 ± 50	8 ± 4
$n_j = 1$	1596	1470 ± 40	102 ± 26	17 ± 5
$n_j \geq 2$, ggF $e\mu$	1017	960 ± 40	37 ± 11	13 ± 1.4
$n_j \geq 2$, VBF	130	99 ± 9	7.7 ± 2.6	21 ± 3

Table 6.4: Post-fit yields in the both ggF and VBF dedicated signal regions with all lepton flavor final states combined [74].

2307 Figure 6.2 shows the final post-fit m_T distribution in the $n_j \leq 1$ regions. The data are very consistent

with the hypothesis of ggF Higgs production. These yields are used as input, along with the VBF results

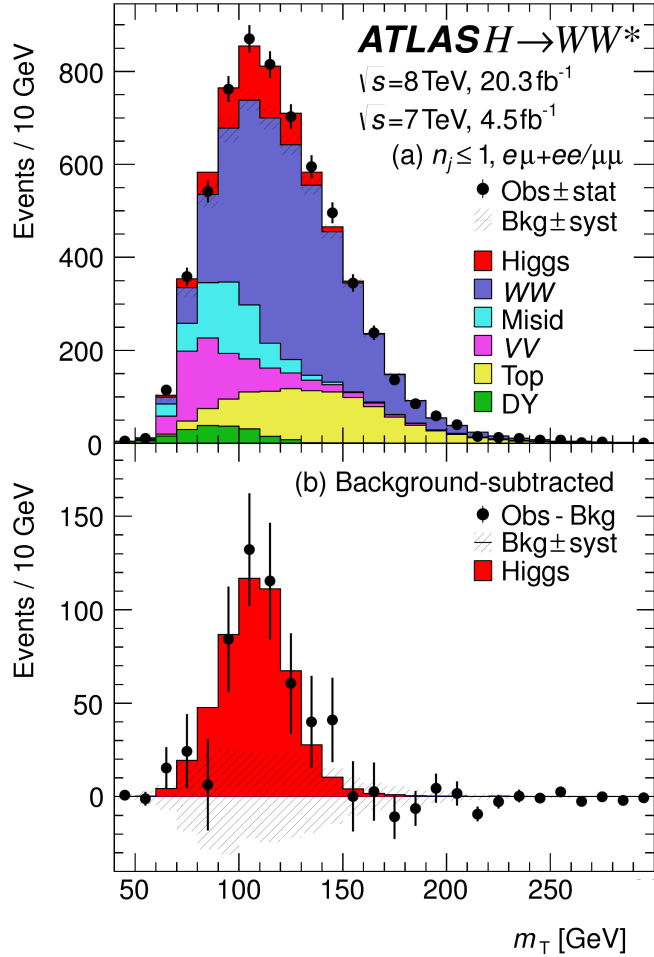


Figure 6.2: Post-fit m_T distribution in the $n_j \leq 1$ regions [74].

2308

2309 in chapter 5, for the physical interpretation of results presented in subsequent sections.

2310 6.3 SIGNAL STRENGTH MEASUREMENTS IN GGF AND VBF PRODUCTION

2311 A combined measurement of the signal strength, as well as the individual ggF and VBF signal strengths,
 2312 is extracted when all of the signal regions are combined in the fit. A total cross section for the combined
 2313 gluon fusion and vector boson fusion Higgs processes is measured, and this sum is normalized to theory
 2314 prediction to obtain a value for the combined signal strength. The final measured combined signal strength

²³¹⁵ μ is

$$\begin{aligned} \mu &= 1.09 \quad {}^{+0.16}_{-0.15} \text{ (stat.)} \quad {}^{+0.08}_{-0.07} \left(\begin{array}{l} \text{expt} \\ \text{syst} \end{array} \right) \quad {}^{+0.15}_{-0.12} \left(\begin{array}{l} \text{theo} \\ \text{syst} \end{array} \right) \quad \pm 0.03 \left(\begin{array}{l} \text{lumi} \\ \text{syst} \end{array} \right) \\ &= 1.09 \quad {}^{+0.16}_{-0.15} \text{ (stat)} \quad {}^{+0.17}_{-0.14} \text{ (syst)} \\ &= 1.09 \quad {}^{+0.23}_{-0.21}. \end{aligned} \tag{6.1}$$

²³¹⁶ Figure 6.3 gives the best fit signal strength $\hat{\mu}$ as a function of the hypothesized Higgs mass. The value at
²³¹⁷ a mass of 125.36 GeV corresponds to the μ quoted in equation 6.1. This value of the Higgs mass is used
²³¹⁸ because it is the most precise mass measurement from ATLAS, a result of the combined $\gamma\gamma$ and ZZ mass
²³¹⁹ measurements [107]. The figure also illustrates that the $H \rightarrow WW^* \rightarrow \ell\nu\ell\nu$ channel would have been
²³²⁰ sensitive to the Higgs boson at higher masses as well¹.

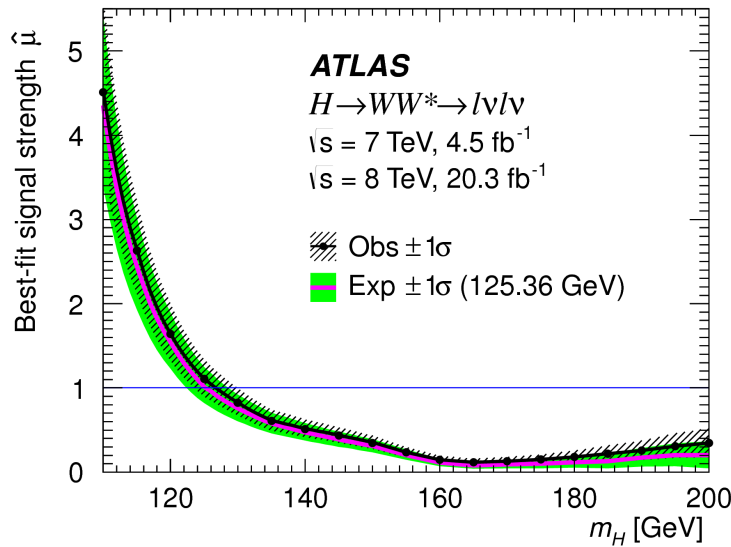


Figure 6.3: Best fit signal strength $\hat{\mu}$ as a function of hypothesized m_H [74].

²³²¹ As explained in chapter 3, a probability p_0 can be computed using the test statistic q_0 to quantify the
²³²² probability that the background could fluctuate to produce an excess at least as large as the one observed
²³²³ in the data. The local p_0 value is shown in figure 6.4 as a function of m_H . The minimum p_0 value is at
²³²⁴ $m_H = 130$ GeV and corresponds to a significance of 6.1σ . The curve is relatively flat and the significance
²³²⁵ is the same at 125.36 GeV within the quoted precision. The expected significance for a signal with strength

¹A μ far below unity at higher masses indicates that there were many more expected events than were observed.

²³²⁶ $\mu = 1.0$ is 5.8σ . This represents the first discovery level observation of Higgs production using only the
²³²⁷ $H \rightarrow WW^* \rightarrow \ell\nu\ell\nu$ analysis.

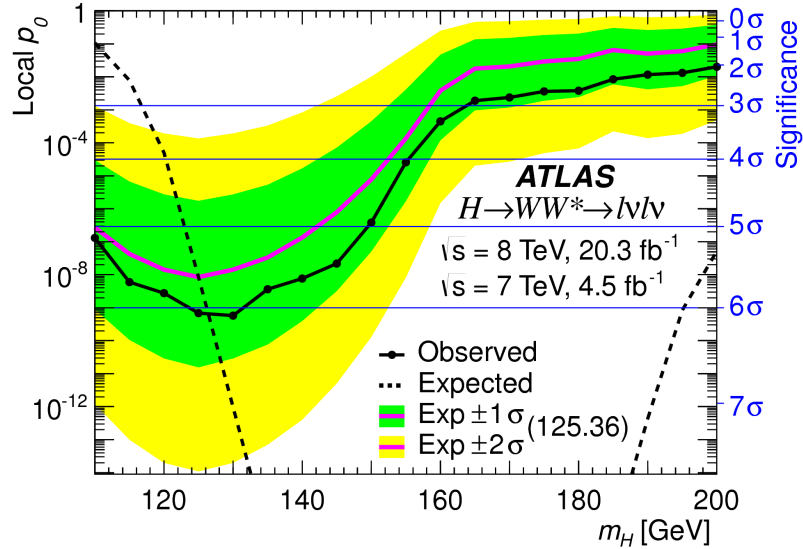


Figure 6.4: Local p_0 as a function of m_H [74].

²³²⁸ All the results presented so far in this section have been for the combined gluon fusion and VBF pro-
²³²⁹ duction modes. However, each signal strength can be calculated separately in the likelihood as well. There
²³³⁰ are two ways to do this. First, the likelihood can be parameterized in terms of a single parameter, the ratio
²³³¹ of the VBF and gluon fusion signal strengths. With this method, the statistical significance of the VBF
²³³² Higgs result can be evaluated. Figure 6.5 shows the likelihood as a function of the ratio $\mu_{\text{VBF}}/\mu_{\text{ggF}}$. The
²³³³ best fit value of the ratio of signal strengths is shown in equation 6.2. Within the quoted uncertainties, it
²³³⁴ is consistent with a ratio of unity.

$$\frac{\mu_{\text{VBF}}}{\mu_{\text{ggF}}} = 1.26^{+0.61} (\text{stat.})^{+0.50} (\text{syst.}) = 1.26^{+0.79}_{-0.53} \quad (6.2)$$

²³³⁵ The null hypothesis for VBF production corresponds to a ratio of $\mu_{\text{VBF}}/\mu_{\text{ggF}} = 0$. The likelihood in
²³³⁶ figure 6.5 gives a significance of 3.2σ at $\mu_{\text{VBF}}/\mu_{\text{ggF}} = 0$, as quoted in chapter 5.

²³³⁷ In addition to the ratio of signal strengths, each signal strength can be varied independently in the like-
²³³⁸ lihood as well. Figure 6.6 shows the two dimensional likelihood scan in the $\mu_{\text{ggF}}-\mu_{\text{VBF}}$ plane. The best fit

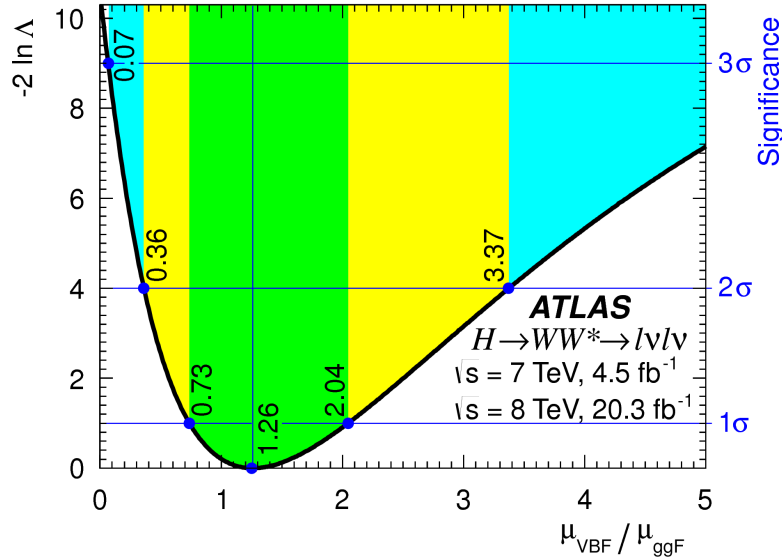


Figure 6.5: Likelihood as a function of $\mu_{\text{VBF}} / \mu_{\text{ggF}}$ [74].

values of the two signal strengths are shown in equation 6.3. Both are consistent with unity within their uncertainties.

$$\begin{aligned}
 \mu_{\text{ggF}} &= 1.02 \pm 0.19 {}^{+0.22}_{-0.18} = 1.02 {}^{+0.29}_{-0.26} \\
 \mu_{\text{VBF}} &= 1.27 {}^{+0.44}_{-0.40} {}^{+0.29}_{-0.21} = 1.27 {}^{+0.53}_{-0.45}. \\
 &\quad (\text{stat.}) \quad (\text{syst.})
 \end{aligned} \tag{6.3}$$

6.4 MEASUREMENT OF HIGGS COUPLINGS TO VECTOR BOSONS AND FERMIONS

The couplings of the Higgs to fermions and bosons are also measured relative to theoretical prediction. The parameter of interest in this case is referred to as κ , or the ratio of the measured coupling to the Standard Model expectation². Both the fermion and boson couplings have these so-called scale factors, κ_F for fermions and κ_V for bosons. Gluon fusion production is sensitive to the fermion couplings through the top quark loops in its production, while VBF production is sensitive to the vector boson couplings in its production. Both modes are sensitive to the vector boson couplings in their decays. The signal strengths

² κ is to coupling measurements what μ is to cross section measurements.

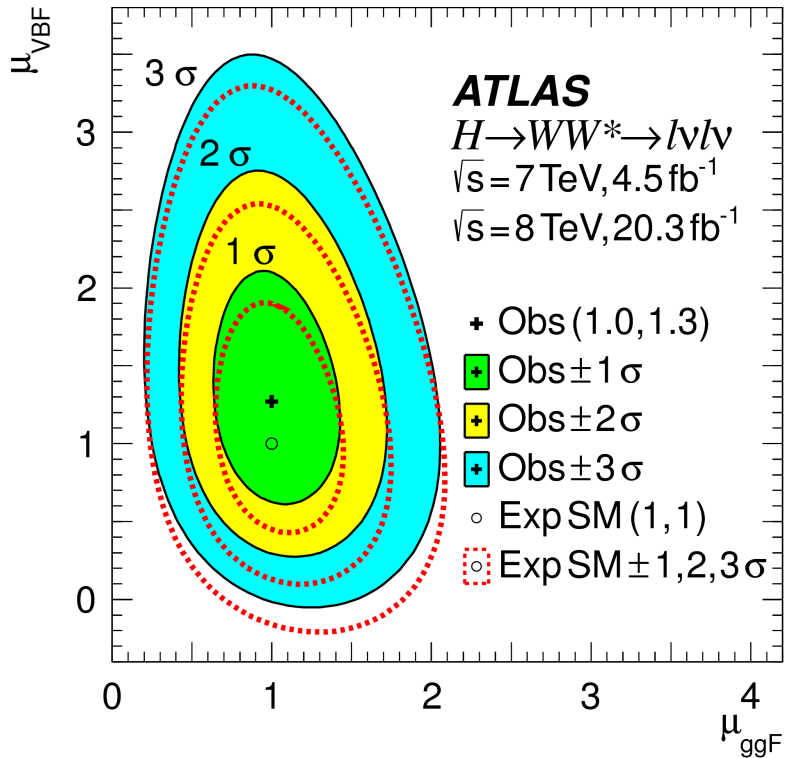


Figure 6.6: Two dimensional likelihood scan as a function of μ_{VBF} and μ_{ggF} [74].

²³⁴⁸ will have dependence on the coupling scale factors [18].

$$\begin{aligned} \mu_{\text{ggF}} &\propto \frac{\kappa_F^2 \cdot \kappa_V^2}{(\mathcal{B}_{H \rightarrow f\bar{f}} + \mathcal{B}_{H \rightarrow gg}) \kappa_F^2 + (\mathcal{B}_{H \rightarrow VV}) \kappa_V^2} \\ \mu_{\text{VBF}} &\propto \frac{\kappa_V^4}{(\mathcal{B}_{H \rightarrow f\bar{f}} + \mathcal{B}_{H \rightarrow gg}) \kappa_F^2 + (\mathcal{B}_{H \rightarrow VV}) \kappa_V^2}. \end{aligned} \quad (6.4)$$

²³⁴⁹ Figure 6.7 shows the two-dimensional likelihood scan of κ_F and κ_V . The best-fit values are given in equation 6.5. The best-fit values are consistent with unity within their uncertainties.

$$\begin{aligned} \kappa_F &= 0.93 \quad {}^{+0.24}_{-0.18} \quad {}^{+0.21}_{-0.14} = 0.93 \quad {}^{+0.32}_{-0.23} \\ \kappa_V &= 1.04 \quad {}^{+0.07}_{-0.08} \quad {}^{+0.07}_{-0.08} = 1.04 \quad \pm 0.11. \end{aligned} \quad (6.5)$$

(stat.) (syst.)

²³⁵¹

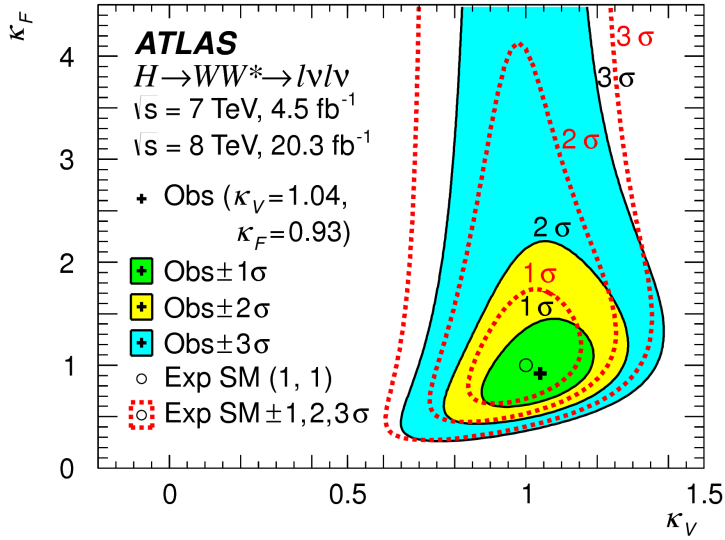


Figure 6.7: Likelihood scan as a function of κ_F and κ_V , the Higgs coupling scale factors [74].

2352 6.5 HIGGS PRODUCTION CROSS SECTION MEASUREMENT

2353 Another measurement that comes naturally from the signal strength measurements quoted earlier is the
 2354 production cross section at 7 and 8 TeV for both gluon fusion and VBF production. The general equation
 2355 for calculating the cross section is

$$\begin{aligned}
 (\sigma \cdot \mathcal{B}_{H \rightarrow WW^*})_{\text{obs}} &= \frac{(N_{\text{sig}})_{\text{obs}}}{\mathcal{A} \cdot \mathcal{C} \cdot \mathcal{B}_{WW \rightarrow \ell\nu\ell\nu}} \cdot \frac{1}{\int L dt} \\
 &= \hat{\mu} \cdot (\sigma \cdot \mathcal{B}_{H \rightarrow WW^*})_{\text{exp}}.
 \end{aligned} \tag{6.6}$$

2356 Here, $(N_{\text{sig}})_{\text{obs}}$ is the number of events observed in data. \mathcal{A} is the geometric and kinematic acceptance of
 2357 the detector, while \mathcal{C} is the efficiency of the signal region selection for events that are reconstructed in the
 2358 detector. The branching ratio of a WW system to leptons must also be divided out. The production cross
 2359 section depends on the center of mass energy and the production mode desired (gluon fusion or VBF), and

2360 so three separate cross section measurements are obtained:

$$\begin{aligned}\sigma_{\text{ggF}}^{\text{7TeV}} \cdot \mathcal{B}_{H \rightarrow WW^*} &= 2.0 \pm 1.7^{+1.2}_{-1.1} = 2.0^{+2.1}_{-2.0} \text{ pb} \\ \sigma_{\text{ggF}}^{\text{8TeV}} \cdot \mathcal{B}_{H \rightarrow WW^*} &= 4.6 \pm 0.9^{+0.8}_{-0.7} = 4.6^{+1.2}_{-1.1} \text{ pb} \\ \sigma_{\text{VBF}}^{\text{8TeV}} \cdot \mathcal{B}_{H \rightarrow WW^*} &= 0.51^{+0.17}_{-0.15} {}^{+0.13}_{-0.08} = 0.51^{+0.22}_{-0.17} \text{ pb.}\end{aligned}\tag{6.7}$$

(stat.) (syst.)

2361 These are the most precise measurements for the Higgs production cross sections from a single channel.
2362 The predicted cross section values (including the branching ratio of $H \rightarrow WW^*$) for gluon fusion are
2363 3.3 ± 0.4 pb at 7 TeV and 4.2 ± 0.5 pb at 8 TeV, consistent with the measured values within their uncer-
2364 tainties. For vector boson fusion, the predicted cross section at 8 TeV is 0.35 ± 0.02 pb, again consistent
2365 with the measured value.

2366 6.6 CONCLUSION

2367 The combined analysis of the gluon fusion and vector boson fusion processes in $H \rightarrow WW^* \rightarrow \ell\nu\ell\nu$
2368 in the 7 and 8 TeV datasets has yielded the first discovery level significance for Higgs production in this
2369 decay channel. Additionally, precise measurements of the couplings to vector bosons and fermions were
2370 obtained. Finally, signal strengths and cross sections for each production mode were measured. Figure 6.8
2371 shows the $H \rightarrow WW^* \rightarrow \ell\nu\ell\nu$ measurements in comparison with other Higgs decay channels in
2372 ATLAS. The measurement of signal strength from this channel remains the most sensitive in both the
2373 gluon fusion and VBF production modes for the Run 1 dataset.

ATLAS

Individual analysis

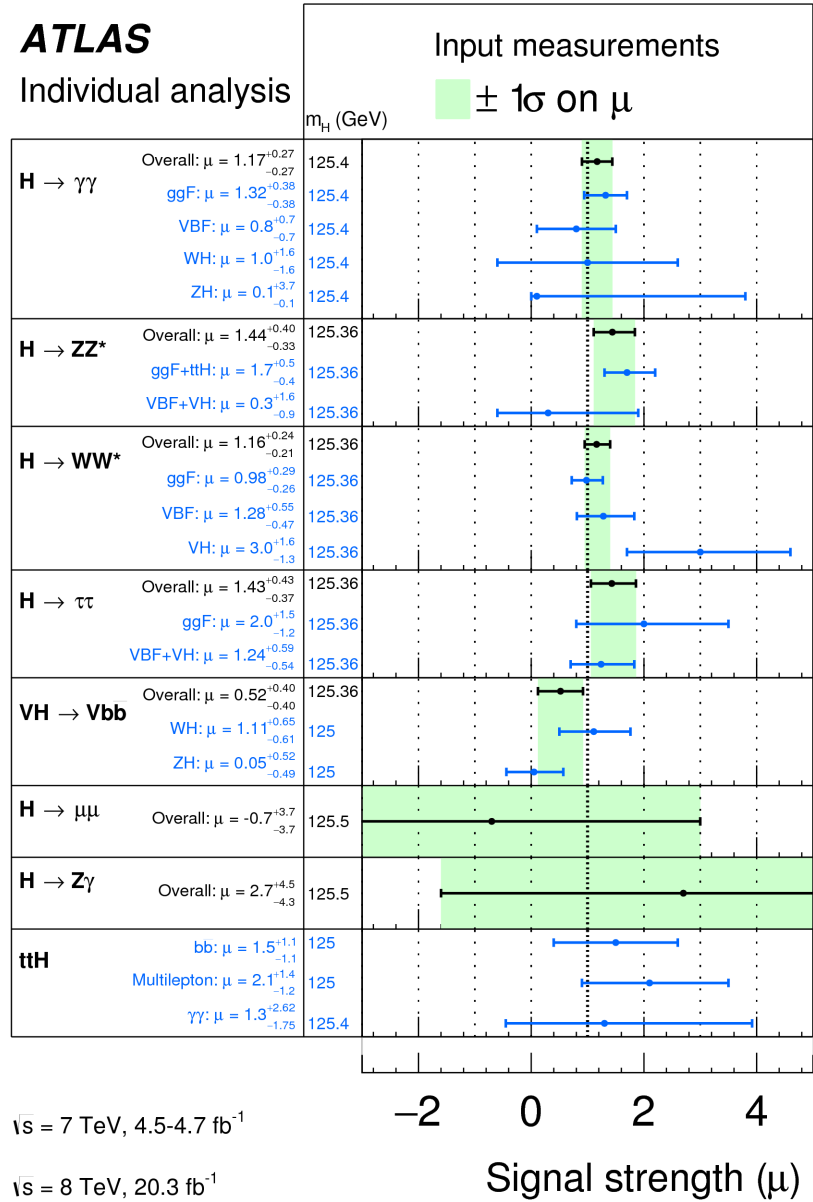


Figure 6.8: Comparison of signal strength measurements in different Higgs decay channels on ATLAS [io8].

2374

Part III

2375

Search for Higgs pair production in the

2376

$HH \rightarrow b\bar{b}b\bar{b}$ channel in LHC Run 2 at $\sqrt{s} =$

2377

13 TeV

Passion is in all great searches and is necessary to all creative endeavors.

W. Eugene Smith

7

2378

2379 Search for Higgs pair production in boosted 2380 $b\bar{b}b\bar{b}$ final states

2381 7.1 INTRODUCTION

2382 This chapter presents a search for resonant production of a Higgs pair in the $X \rightarrow HH \rightarrow b\bar{b}b\bar{b}$ final
2383 state in 3.2 fb^{-1} of data collected at $\sqrt{s} = 13 \text{ TeV}$. In particular, this chapter focuses on a search for this
2384 final state in the regime where m_X is large ($\gtrsim 1 \text{ TeV}$) and the Higgs bosons in the decay are significantly
2385 boosted. A tailored selection for this boosted selection, using novel techniques in jet substructure and b -
2386 tagging, is discussed. Then, the data-driven background estimate is presented. Finally, the results of the
2387 search are shown. The signal models used as benchmarks are a spin-2 Randall Sundrum graviton (RSG)
2388 and a narrow width spin zero resonance. These models are described in more detail in Chapter 1. Limits
2389 on signal models are reserved for the next chapter where the results of this chapter are combined with the

2390 results of a separate selection dedicated to the lower m_X regime.

2391 **7.2 MOTIVATION**

2392 With the center of mass energy increase from $\sqrt{s} = 8 \text{ TeV}$ to $\sqrt{s} = 13 \text{ TeV}$, the LHC and ATLAS are
2393 able to probe new resonances at higher mass scales than previously accessible in Run 1. This is a powerful
2394 motivator for searching for a new resonance in the early 13 TeV data. Figure 7.1 shows the ratios of parton
2395 luminosities between 8 and 13 TeV for different resonance masses. For a resonance of $M_X = 2 \text{ TeV}$, the
2396 cross section at $\sqrt{s} = 13 \text{ TeV}$ is roughly a factor of 10 larger than at $\sqrt{s} = 8 \text{ TeV}$.

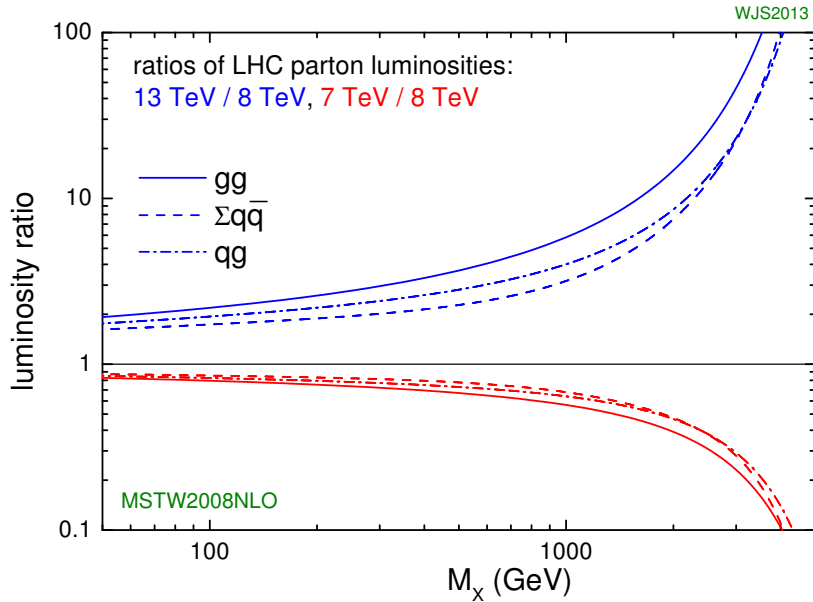


Figure 7.1: Parton luminosity ratios as a function of resonance mass M_X for 13/8 TeV and 7/8 TeV [109].

2397 Higgs pair production offers a vast array of unprobed regions of phase space where searches for BSM
2398 physics can be made. Chapter 1 discusses some possibilities for both resonant and non-resonant enhance-
2399 ment of the di-Higgs production cross section. Given the increased mass reach of the LHC in Run 2, it is
2400 particularly important to focus on resonant searches at high m_X . When conducting a search in the HH
2401 final state, the different possible decay modes of each Higgs must be considered. Figure 7.2 shows the
2402 branching ratio of the HH final state for different combinations of decays of each individual Higgs. As

²⁴⁰³ the largest branching ratio for the 125 GeV Higgs is $H \rightarrow b\bar{b}$, the $HH \rightarrow b\bar{b}b\bar{b}$ branching ratio is also the
²⁴⁰⁴ largest at 33%.

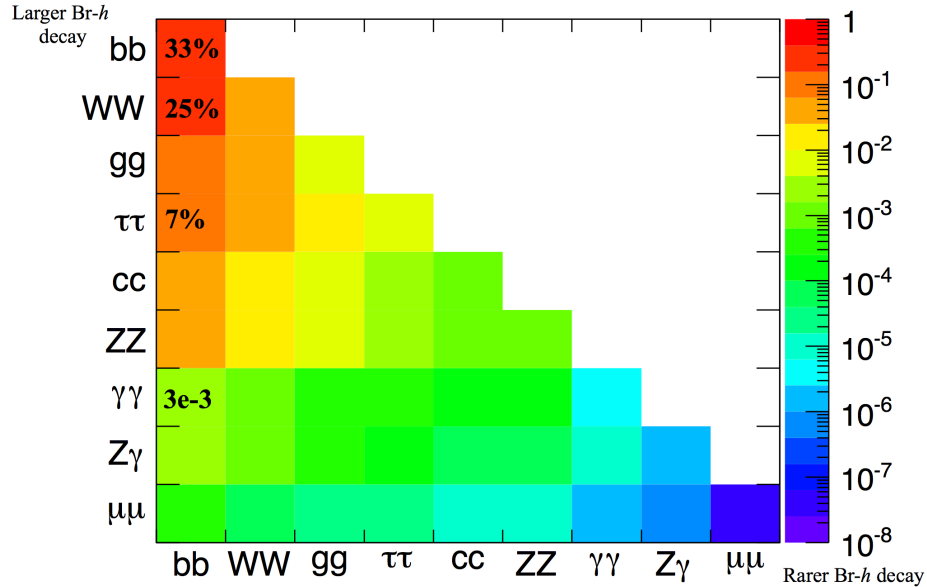


Figure 7.2: Summary of HH branching ratios [110].

²⁴⁰⁵ At high m_X , the Higgs bosons resulting from the decay of a heavy resonance will have large p_T ¹. The
²⁴⁰⁶ angular separation between the decay products of the Higgs, $\Delta R \equiv \sqrt{(\Delta\eta)^2 + (\Delta\phi)^2}$, is inversely
²⁴⁰⁷ proportional to the Higgs p_T , as shown in equation 7.1.

$$\Delta R \approx \frac{2m}{p_T} \quad (7.1)$$

²⁴⁰⁸ Figure 7.3 shows the minimum ΔR between truth level B decay vertices in simulation samples for Randall-
²⁴⁰⁹ Sundrum gravitons of different masses. The figure shows that as the mass of the graviton increases, the ΔR
²⁴¹⁰ distribution between the b quarks in the Higgs decay tends to shift to lower values. Because of this effect,
²⁴¹¹ it is necessary to tailor a selection to target these merged b -jets.

¹In the limit that the resonance mass is much larger than the Higgs mass, the Higgs p_T is roughly $m_X/2$.

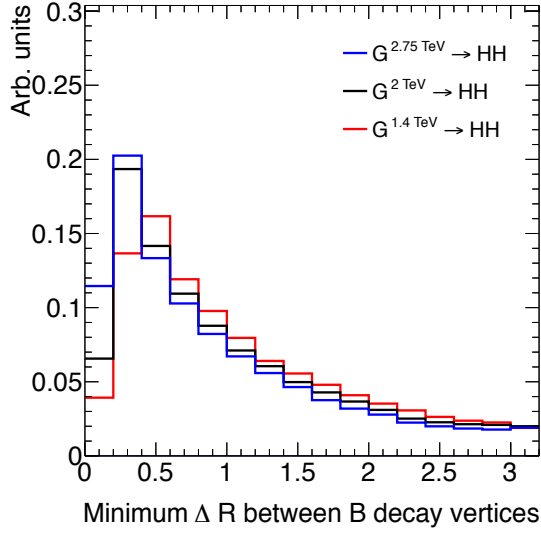


Figure 7.3: Minimum ΔR between B decay vertices for different RSG masses in a $G_{KK}^* \rightarrow HH \rightarrow 4b$ sample with $c = 1$.

2412 7.3 DATA AND SIMULATION SAMPLES

2413 7.3.1 SIGNAL MODELS

2414 While the resonance search is by its nature generic (as it is a simple search for a peak in the $4b$ invariant mass
 2415 spectrum), there are two signal models that the selection requirements have been optimized for. The first
 2416 is Randall-Sundrum (RSG) model, where a tower of massive spin-2 Kaluza-Klein gravitons is predicted.
 2417 The second is a heavy narrow scalar resonance, the so-called “heavy Higgs”. This type of resonance arises,
 2418 for example, in the two Higgs doublet model (2HDM). More details about the physics of these models
 2419 and their motivation is given in chapter 1.

2420 Signal graviton (G_{KK}^*) events are generated at leading order (LO) with **MADGRAPH5 v2.2.2** [ii]. The
 2421 PDF set used is the **NNPDF2.3 LO** set [ii]. For modeling parton shower and hadronization in jets, **PYTHIA**
 2422 8.186 is used with the A14 tune [90, ii]. The free parameters in the RSG model are the graviton mass
 2423 and the coupling constant $c \equiv k/\bar{M}_{\text{Pl}}^2$. Both the production cross section and width of the graviton are
 2424 proportional to c^2 . Samples are generated at both $c = 1$ and $c = 2$ for a variety of mass points between

² k is the curvature constant for the warped extra dimension and \bar{M}_{Pl} is the Planck mass divided by 8π

2425 300 GeV and 3 TeV.

2426 The second signal sample is a heavy spin-0 resonance H with a fixed width of $\Gamma_H = 1$ GeV. This
2427 is generated with **MADGRAPH5** and uses the **CT10** PDF set [93]. The parton shower and hadronization
2428 are handled by **HERWIG ++** with the **CTEQ6L1** PDF set and the **UEEE5** event tune [94, 114, 115]. Because
2429 the width and branching ratios depend on 2HDM parameters, each mass point generated with this fixed
2430 width corresponds to a different point in the 2HDM parameter phase space. Mass points are generated
2431 between 300 GeV and 3 TeV as with the RSG signal samples.

2432 **7.3.2 BACKGROUND SAMPLES**

2433 While the dominant **QCD** multijet background is estimated with a fully data-driven method, the sub-
2434 dominant backgrounds $t\bar{t}$ and Z +jets are modeled with some input from simulation.

2435 $t\bar{t}$ events are simulated at next-to-leading order (NLO) with the **POWHEG-BOX** version 1 generator us-
2436 ing the **CT10** PDF set [116]. The parton shower, hadronization, and underlying event are simulated with
2437 **PYTHIA 6.428** with the **CTEQ6L1** PDF set [89]. The Perugia 2012 tune is used [117]. NNLO **QCD** correc-
2438 tions to the cross sections are computed in **Top++ 2.0** [118]. The top quark mass is set to 172.5 GeV. The
2439 shapes of distributions in $t\bar{t}$ are taken from MC while the normalization is taken from data.

2440 The Z +jets background is simulated with **PYTHIA 8.186** and the **NNPDF2.3** LO PDF set. This back-
2441 ground is negligible compared to the others and is taken fully from MC.

2442 **7.3.3 DATA SAMPLE AND TRIGGER**

2443 This analysis is done on 3.2 fb^{-1} of data taken in 2015 at $\sqrt{s} = 13$ TeV. The details of the machine
2444 conditions during this time can be found in Chapter 2. Only data which was taken during stable beam
2445 conditions with all detectors functioning is used. Events must pass a trigger which requires a single large
2446 radius ($R = 1.0$) jet with $p_T > 360$ GeV to be reconstructed in the HLT. Figure 7.4 shows the trigger
2447 efficiency for various trigger options as a function of graviton mass. Above $m_{G_{KK}^*} > 1$ TeV, the single
2448 large radius jet trigger is 99% efficient for events passing the signal selection.

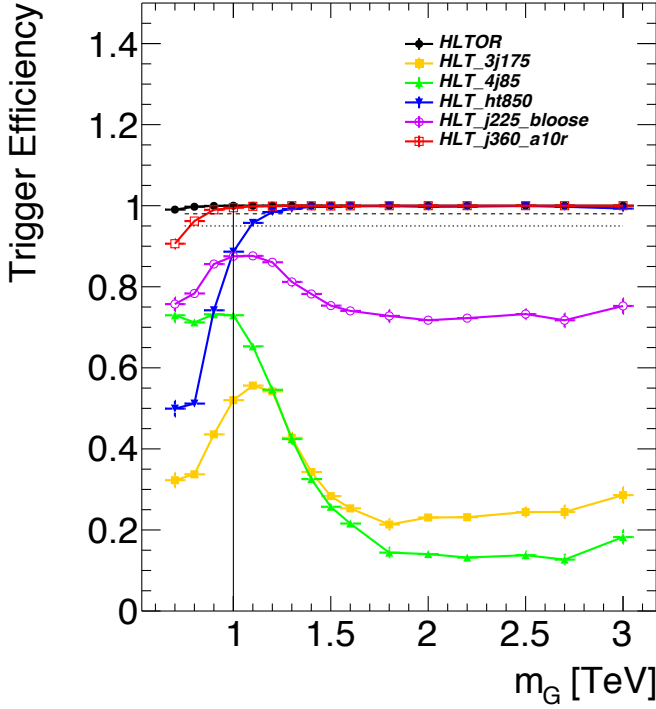


Figure 7.4: Trigger efficiency for events passing all signal region selections as a function of mass in a $G_{KK}^* \rightarrow HH \rightarrow 4b$ sample with $c = 1$ [19]. In the trigger names, “j” refers to a jet or jets. “ht” refers to H_T , the scalar sum of transverse momenta in the event. “bloose” refers to a loose b -tagging requirement applied to the jet. “a10r” refers to anti- k_T jets with $R = 1.0$. The numbers at the end of each trigger name are the thresholds on the given quantity in GeV.

2449 7.4 EVENT RECONSTRUCTION AND OBJECT SELECTION

2450 The boosted selection first begins by defining a unique set of objects that can be exploited to increase signal
 2451 efficiency in the kinematic regime where the final state b -jets are very merged.

2452 7.4.1 LARGE RADIUS ($R = 1.0$) JETS

2453 The first step towards reconstructing the final state is to define objects that can be used to measure the
 2454 kinematics of the Higgs bosons. In the boosted selection anti- k_T jets with a radius parameter of 1.0 are
 2455 used. These jets are much larger in angular size than the typical $R = 0.4$ jets and are intended to encompass
 2456 all of the products of the Higgs decay³. The jets are built from clusters in the calorimeter calibrated with

³This is in contrast to the resolved selection, which uses two $R = 0.4$ anti- k_T jets for each Higgs.

local calibration weighting [69].

Because of the large extent of these jets, great care must be taken to remove potential contributions of calorimeter clusters from pile-up. This is done using a technique called jet trimming [120]. With trimming, the constituents of the large radius jet are re-clustered with a smaller radius using the k_T algorithm. Then, these so-called subjets are removed from the larger jet if $p_T^{\text{subjett}} / p_T^{\text{jet}} < f_{\text{cut}}$. In this analysis, the subjet radius is $R = 0.2$ and $f_{\text{cut}} = 0.05$. Trimming has been shown to improve the mass resolution of large radius jets. Figure 7.5 shows the effect of trimming on the large radius jet mass (M_J). Because the large radius jet fully contains the Higgs decay products, its invariant mass should correspond to the 125 GeV mass of the Higgs. The trimming algorithm brings the jet mass much closer to the expected Higgs mass and improves the mass resolution.

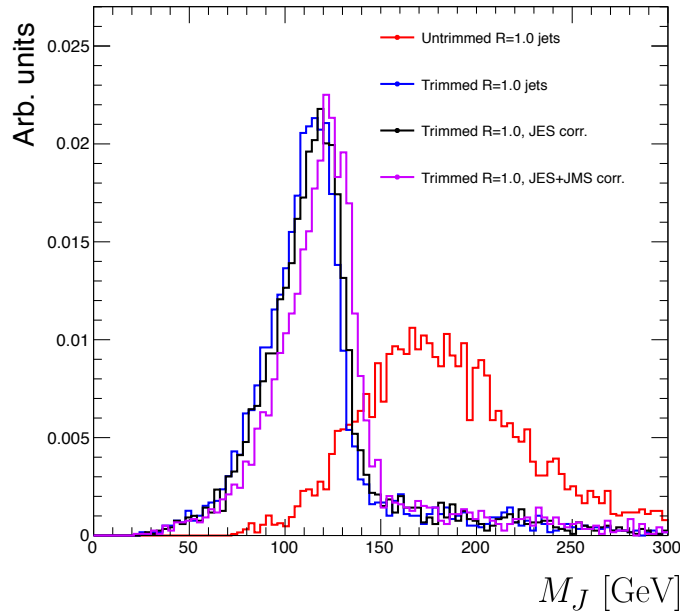


Figure 7.5: Comparison of untrimmed and trimmed jet masses for large radius jets in a RSG sample with $m_{G_{\text{KK}}^*} = 1 \text{ TeV}$. JES (JMS) refers to the standard jet energy (mass) scale calibration for ATLAS [69].

The large radius jets are required to satisfy $250 < p_T < 1500 \text{ GeV}$. They must also be within $|\eta| < 2.0$ in order to ensure that the full jet is within the inner detector tracking volume. Finally, they are required to have $M_J > 50 \text{ GeV}$. The upper p_T cut and lower threshold on mass are applied to correspond to the kinematic range where uncertainties are available in ATLAS calibrations [121, 122].

2471 7.4.2 TRACK JETS AND b -TAGGING

2472 Because the b -jets from boosted Higgs decays are so close together (as illustrated in figure 7.3), narrow radius
 2473 jets are required to fully resolve both b -jets. The minimum radius feasible for jets based on calorimeter
 2474 deposits is determined by the calorimeter granularity. However, because b -tagging relies on information
 2475 from the inner detector, it is possible to define another type of jet that can have a smaller radius and better
 2476 b -tagging resolution. These jets are called “track jets” [122, 123].

2477 Track jets are formed by applying the usual anti- k_T clustering algorithm to tracks that are required to be
 2478 consistent with the primary vertex. After the jet axis has been determined using these tracks, a second step
 2479 of track association is also performed to add tracks that can be useful for b -tagging [123]. In this analysis,
 2480 the tracks are clustered with a radius parameter of $R = 0.2$. This radius has been shown to give good
 2481 performance in boosted Higgs tagging [122, 123]. Figure 7.6 shows a comparison among different track jet
 2482 radii of the efficiency for reconstructing two b -jets from each Higgs in a RSG sample as a function of mass.
 Track jets with radius of 0.2 give the best performance, especially at high mass. In this analysis, track jets

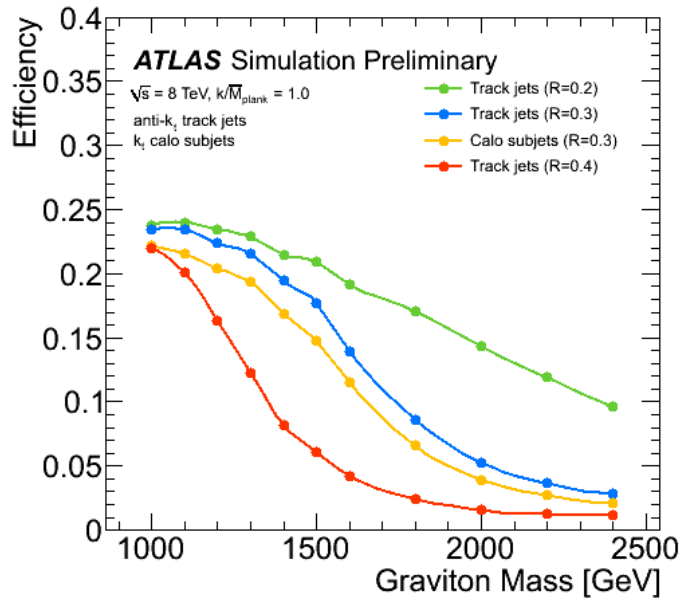


Figure 7.6: Efficiency of finding two b -jets from each Higgs in an RSG event using calorimeter jets with $R = 0.3$ and track jet radii of $R = [0.2, 0.3, 0.4]$ [123].

2483

2484 are required to have $p_T > 10$ GeV and $|\eta| < 2.5$. They must also have at least two tracks.

2485 7.4.3 MUONS

2486 Muons are used in this study to correct the four-momenta of calorimeter jets by accounting for semi-
2487 leptonic b decays. The muons used are combined ID and MS muons which must satisfy tight identification
2488 requirements [65]. The muons must have $p_T > 4 \text{ GeV}$ and $|\eta| < 2.5$. Table 7.1 summarizes the object
2489 requirements described in this section.

	R	p_T	$ \eta $	M
Calorimeter jets	1.0	$250 < p_T < 1500 \text{ GeV}$	< 2.0	$> 50 \text{ GeV}$
Track jets	0.2	$> 10 \text{ GeV}$	< 2.5	-
Muons	-	4 GeV	< 2.5	-

Table 7.1: Summary of requirements on objects used in the $X \rightarrow HH \rightarrow b\bar{b}b\bar{b}$ search.

2490 7.5 EVENT SELECTION

2491 The first requirement in the boosted event selection is for ≥ 2 large radius jets satisfying the selections
2492 outlined above. The two highest momentum large- R jets in the event are referred to as “Higgs candidates”.
2493 The leading jet is required to have $p_T > 350 \text{ GeV}$.

2494 Track jets satisfying the object selections are matched to Higgs candidate jets via ghost association [124].
2495 This matching technique uses zero momentum particles to identify regions in the η - ϕ plane that would
2496 have been clustered into a particular jet. It is used in this context to identify track jets that are the result
2497 of substructure inside of a large- R calorimeter jet. Each Higgs candidate must have at least 2 track jets
2498 associated with it. These basic requirements are illustrated graphically in figure 7.7.

2499 The QCD multijet background produces less central jets than high mass resonances, so there is an ad-
2500 ditional requirement that the two Higgs candidates be close together in η . The large- R jets are required to
2501 satisfy $|\Delta\eta(JJ)| < 1.7$.

2502 7.5.1 MASS REQUIREMENTS

2503 The final set of requirements ensures that the Higgs candidates are consistent with expected properties of
2504 the 125.0 GeV Higgs. First, a variable (X_{hh}) is defined to measure the consistency of both of the Higgs

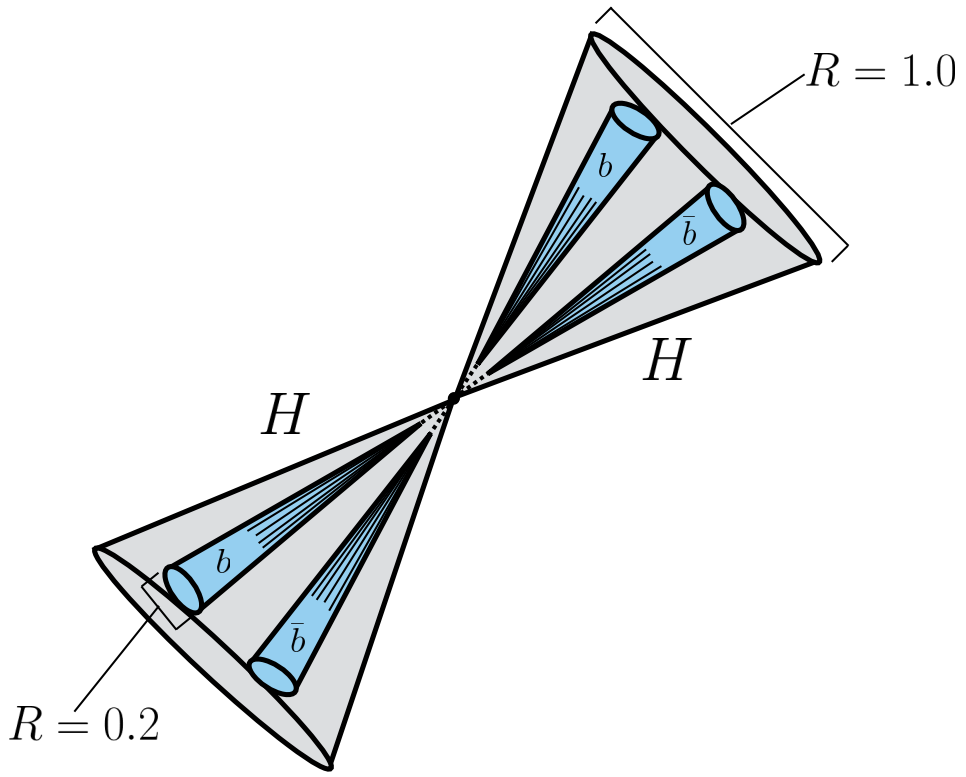


Figure 7.7: Illustration of the boosted selection requirements on Higgs candidates. Each large-radius calorimeter jet (Higgs candidate) must contain two track jets.

candidate jets with the SM Higgs mass:

$$X_{hh} = \sqrt{\left(\frac{M_J^{\text{lead}} - 124 \text{ GeV}}{0.1 M_J^{\text{lead}}}\right)^2 + \left(\frac{M_J^{\text{sublead}} - 115 \text{ GeV}}{0.1 M_J^{\text{sublead}}}\right)^2}. \quad (7.2)$$

The mass values in the X_{hh} formula are optimized to maximize signal efficiency. The sub-leading jet typically has a lower mass due to semi-leptonic b decays and final state radiation. X_{hh} effectively acts as a χ^2 measurement of the consistency of the two Higgs candidate masses with the signal hypothesis. The denominators of each term ($0.1 M$) give the uncertainty on the mass measurement for the large radius jets. Events are required to satisfy $X_{hh} < 1.6$.

Before making the requirement on X_{hh} , the masses of the Higgs candidates are corrected for semi-leptonic b decays using muons with the criteria outlined in the previous section. Any muons within a $\Delta R < 0.2$ of a b -tagged track jet (as described in the next section) have their four-momenta added to the

2514 four-momentum of the Higgs candidate. This correction does not affect the pre-selection requirements
 2515 but does affect the X_{hh} requirement and the final invariant mass discriminant.

2516 **7.5.2 b-TAGGING REQUIREMENTS**

2517 The last requirement applied is on the number of b -tagged track jets. There are two signal regions defined.
 2518 The first requires exactly four b -tagged track jets, two in each Higgs candidate (known as the $4b$ signal re-
 2519 gion). At high resonance masses, this requirement is inefficient, so an additional signal region requiring
 2520 only three b -tagged track jets is also defined (known as the $3b$ signal region). While this has a larger back-
 2521 ground it is also more efficient for high resonance masses. For both signal regions, the MV2c2o algorithm,
 2522 where the training sample for the algorithm has 20% charm events is used. More details for this algorithm
 2523 can be found in Chapter 2.

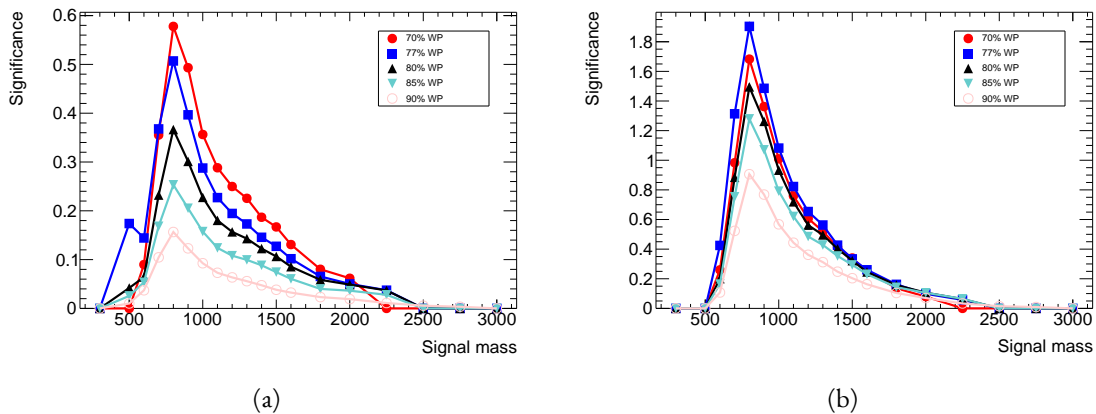


Figure 7.8: Estimated significance as a function of signal mass for RSG $c = 1$ models in the $3b$ (a) and $4b$ (b) regions for different b -tagging efficiency working points.

2524 Once the algorithm is selected, an efficiency working point must also be chosen. This working point
 2525 defines the efficiency with which true b -jets are tagged and also fixes the overall background rejection of the
 2526 algorithm. Higher efficiency working points accept more true b -jets but also allow for more background.
 2527 Five different working points (70%, 77%, 80%, 85%, 90%) are tested. With each working point, the
 2528 full data driven background estimation method is run to quantify the amount of background that will be
 2529 present in the final signal region. The significance is quantified using the median discovery significance for

2530 signal and background with Poisson errors, given in equation 7.3 [125].

$$Z = \sqrt{2 \left((s + b) \ln \left(1 + \frac{s}{b} \right) - s \right)} \quad (7.3)$$

2531 Here, s is the expected number of signal events and b is the expected number of background events. This
 2532 formula is derived using Poisson statistics with errors on both the signal and background. It is used because
 2533 it is valid in the regime where s and b are of the same order. Note that in the limit where s is much smaller
 2534 than b , this equation reduces to the more well known s/\sqrt{b} . Figure 7.8 shows the estimated significance as
 2535 a function of signal mass in RSG $c = 1$ models for the $3b$ and $4b$ signal regions. The 77% working point
 2536 gives the best performance over a wide range of masses in the $4b$ signal region. As this is the region which
 2537 contributes the most to the total discovery significance, the 77% efficiency working point is chosen for the
 2538 analysis.

2539 7.5.3 SELECTION EFFICIENCY

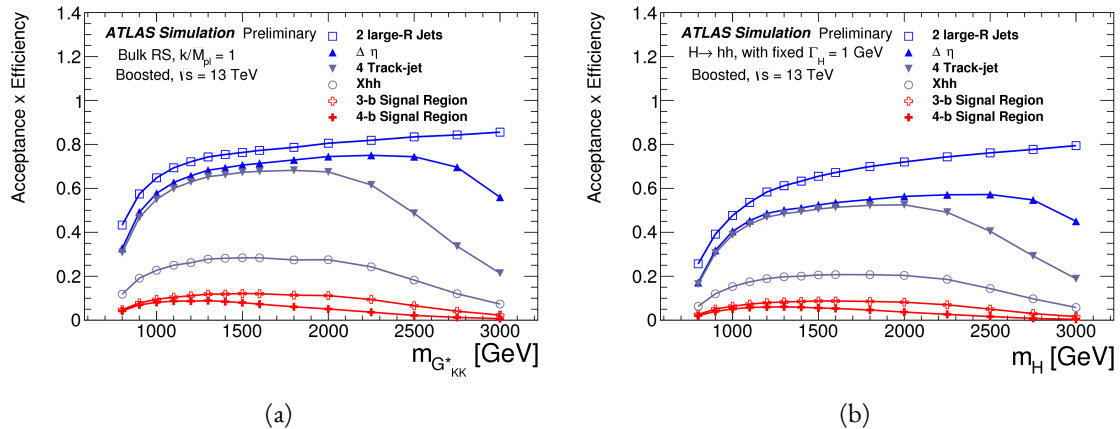


Figure 7.9: Acceptance \times efficiency as a function of mass for (a) RSG and (b) narrow heavy scalar signal models [126]. Each curve corresponds to one of the selection requirements used to define the signal region. The requirements are made sequentially in the order shown in the legend.

2540 Figure 7.9 shows the product of acceptance and efficiency as a function of mass for both the RSG and
 2541 narrow heavy scalar resonance signal models. After $m_X > 1$ TeV, the efficiency of the $4b$ requirement
 2542 begins to decline. After $m_X > 2$ TeV, the efficiency of requiring two track jets in each Higgs candidate

begins to decline as well. Both of these behaviors illustrate the difficulty of resolving the merged decay products at high mass. Figure 7.10 shows a more detailed comparison of the signal efficiency in the $3b$ vs $4b$ signal regions for the RSG model. The efficiencies shown here are relative to all prior selection requirements. It can be seen there that at high masses the $3b$ signal region is more efficient for signal.

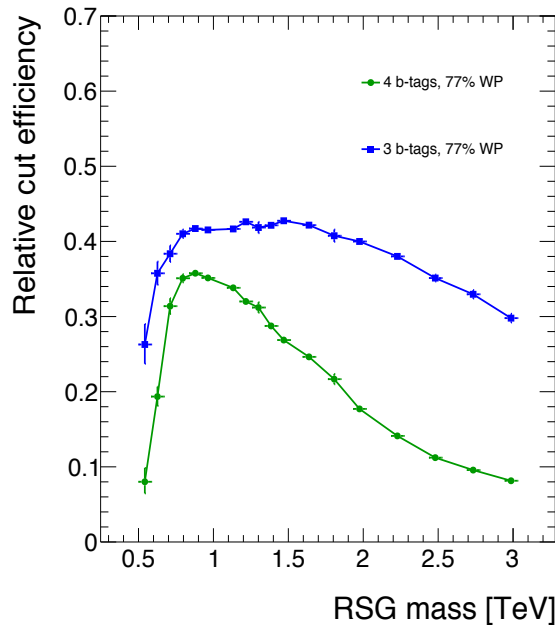


Figure 7.10: Efficiency of requiring 3 or 4 b -tagged track jets vs. RSG mass. The efficiency quoted is relative to the previous selection requirements (rather than an absolute efficiency).

To investigate the degradation of b -tagging efficiency at high p_T , the individual jet tagging efficiencies can be compared as a function of signal mass. This is shown in figure 7.11. The figure shows that the leading jet tagging efficiency in both calorimeter jets degrades heavily, while the sub-lead jet tagging efficiency remains relatively constant. This suggests that the degradation is related to the track jet p_T rather than the merging of decay products in the final state. More details on the cause of this efficiency degradation are shown in appendix A.

The final discriminating variable used in the boosted analysis is M_{2J} , the invariant mass of the two Higgs candidates. In order to improve the mass resolution, the four-momenta of each Higgs candidate are scaled by m_h/M_J . The effect of this correction is small in the boosted analysis but is done for consistency with the resolved selection. Table 7.2 shows the effect of the selection requirements on signal and

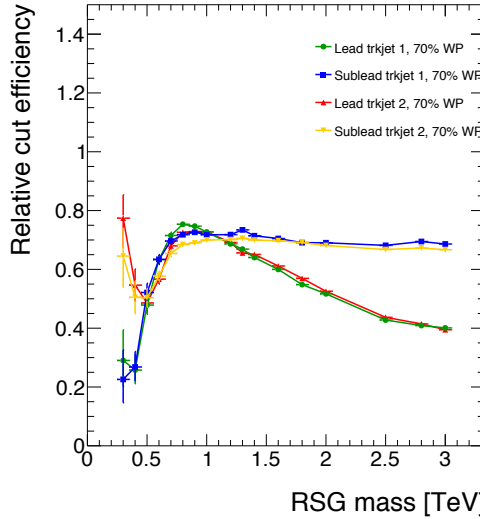


Figure 7.11: MV2c20 b -tagging efficiency for each of the four track jets in the boosted $4b$ selection as a function of RSG mass for $c = 1$ models.

background simulations as well as data.

Selection	Data	$m_{G_{KK}^*} = 1\text{TeV}$	$m_{G_{KK}^*} = 2\text{TeV}$	$t\bar{t}$	$Z + \text{jets}$
$N(\text{fiducial large-R jets}) \geq 2$	2202396	23.3	0.48	32345.2	4255.7
leading large-R jet $p_T > 350\text{ GeV}$	1873741	22.9	0.48	26511.7	3649.9
Both large-R jet $m > 50\text{ GeV}$	1854625	21.2	0.47	24369.8	3575.8
Both large-R jet $p_T < 1500\text{ GeV}$	1853601	21.2	0.46	24346.5	3572.9
$ \Delta\eta(JJ) < 1.7$	1435273	20.8	0.44	20751.0	3265.8
≥ 2 track-jets per large-R jet	1224727	19.8	0.40	18234.5	2692.6
3 b -tags, $X_{hh} < 1.6$	316	3.4	0.067	46.7	2.0
4 b -tags, $X_{hh} < 1.6$	20	2.9	0.030	1.4	0.0

Table 7.2: Effect of boosted selection on data, RSG signal models, $t\bar{t}$, and $Z + \text{jets}$. The numbers from simulation are normalized with the MC generator cross section and do not take into account the data driven estimates described in section 7.6 [127].

7.6 DATA-DRIVEN BACKGROUND ESTIMATION

The largest background to the $X \rightarrow HH \rightarrow b\bar{b}b\bar{b}$ final state is QCD multijet production, constituting 80-90% of the total background. Because of the difficulties in modeling higher order QCD processes, this background is estimated with a fully data-driven method. The only other non-negligible background

2562 is $t\bar{t}$, constituting 10-20% of the total background⁴. Due to the presence of $t\bar{t}$ in the sideband region
 2563 where the QCD background will be estimated, the normalization of the QCD and $t\bar{t}$ backgrounds are
 2564 simultaneously estimated.

2565 **7.6.1 MASS REGION DEFINITIONS**

2566 The first step in the data-driven background estimate is to define a sideband mass region where the back-
 2567 ground normalization can be derived. Additionally, a control region is defined where the background
 2568 estimate can be validated. The control (CR) and sideband (SB) regions are defined using a radial distance
 2569 in the two-dimensional large-R jet mass plane, R_{hh} :

$$R_{hh} = \sqrt{(M_J^{\text{lead}} - 124 \text{ GeV})^2 + (M_J^{\text{sublead}} - 115 \text{ GeV})^2}. \quad (7.4)$$

2570 Events in the control region are required to fail the signal region $X_{hh} < 1.6$ requirement and have
 2571 $R_{hh} < 35.8 \text{ GeV}$. The control region definition is optimized to be kinematically similar to the signal re-
 2572 gion (thus allowing for robust background validation) while still having enough events to make a meaning-
 2573 ful comparison between data and the background estimate. The sideband region consists of those events
 2574 which are not in the signal or control regions. Figure 7.12 shows the definition of the signal, control, and
 2575 sideband mass regions. Table 7.3 summarizes the mass region selections for the three different regions used
 2576 in the analysis.

Region	Requirement	Notes
Signal Region (SR)	$X_{hh} < 1.6$	-
Control Region (CR)	$R_{hh} < 35.8 \text{ GeV}$ and $X_{hh} > 1.6$	Used for validation of background estimates
Sideband Region (SB)	$R_{hh} > 35.8 \text{ GeV}$	Used to derive background normalization

Table 7.3: Mass region definitions used for background estimation.

⁴The $Z + \text{jets}$ background is a sub-percent level contribution.

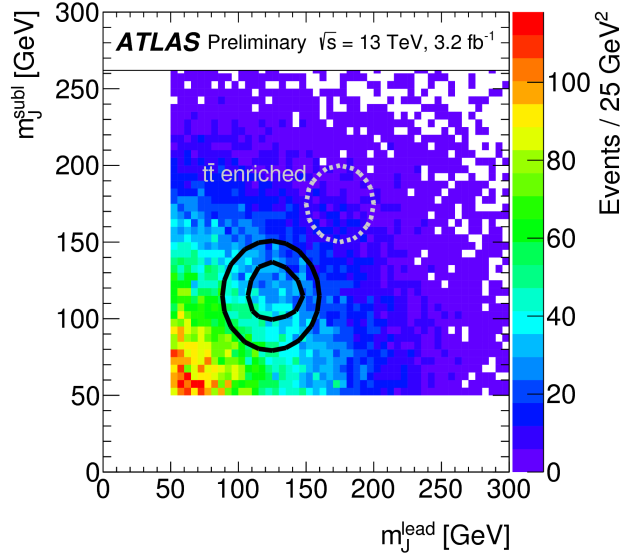


Figure 7.12: M_j^{sublead} vs. M_j^{lead} in a 2 b -tag data sample. The signal region is defined by the inner black contour ($X_{hh} < 1.6$) and the sideband region is defined by the outer contour ($R_{hh} > 35.8 \text{ GeV}$). The region between the black contours is the control region. The mass region which is enriched in $t\bar{t}$ background is also shown for illustration [126].

2577 7.6.2 BACKGROUND ESTIMATION

2578 The method for estimating the background in this analysis is similar to the ABCD method presented in
 2579 Chapter 5. In this case, the two handles used to define different regions for the estimate are the number
 2580 of b -tagged track jets and the mass requirements. A region requiring exactly two b -tagged track jets in one
 2581 large-R jet (referred to as the 2-tag or 2 b region) is defined for use in the background estimate. The number
 2582 of expected background events in the 3 b and 4 b signal regions is then given by

$$N_{\text{bkg}}^{3(4)-\text{tag},\text{SR}} = \mu_{\text{Multijet}} N_{\text{Multijet}}^{2-\text{tag},\text{SR}} + \beta_{t\bar{t}} N_{t\bar{t}}^{3(4)-\text{tag},\text{SR}} + N_{Z+\text{jets}}^{3(4)-\text{tag},\text{SR}}. \quad (7.5)$$

2583 In this equation, $N_{\text{bkg}}^{3(4)-\text{tag}}$ is the expected number of background events in the 3 b or 4 b signal regions.
 2584 $N_{\text{Multijet}}^{2-\text{tag}}$ is the number of multijet events in the 2-tag region. $N_{t\bar{t}}^{3(4)-\text{tag}}$ is the number of $t\bar{t}$ events pre-
 2585 dicted in the MC for the 3 b or 4 b signal region, and the variable is similarly defined for the $Z+\text{jets}$ back-
 2586 ground. The $\beta_{t\bar{t}}$ parameter is a scale factor used to correct the normalization of the $t\bar{t}$ estimate in the
 2587 signal region. A QCD multijet extrapolation factor, μ_{Multijet} , is derived in the sideband region and used

2588 to estimate the ratio of 2-tag events to 3(4)-tag events in the signal region:

$$\mu_{\text{Multijet}} = \frac{N_{\text{Multijet}}^{3(4)\text{-tag,SB}}}{N_{\text{Multijet}}^{2\text{-tag,SB}}} = \frac{N_{\text{data}}^{3(4)\text{-tag,SB}} - \beta_{t\bar{t}} N_{t\bar{t}}^{3(4)\text{-tag,SB}} - N_{Z+\text{jets}}^{3(4)\text{-tag,SB}}}{N_{\text{data}}^{2\text{-tag,SB}} - \beta_{t\bar{t}} N_{t\bar{t}}^{2\text{-tag,SB}} - N_{Z+\text{jets}}^{2\text{-tag,SB}}}. \quad (7.6)$$

2589 The $t\bar{t}$ scale factor and the QCD multijet extrapolation factor are estimated together in a simultaneous fit
 2590 in the sideband region. Then, the number of events in the 2-tag signal region is used, along with the $t\bar{t}$
 2591 estimate in the 3b and 4b signal regions and μ_{Multijet} , to estimate the total number of background events
 2592 in the two final signal regions. The shape of the final discriminant M_{2J} is also taken from the 2-tag signal
 region where there are more events. This method is illustrated graphically in figure 7.13. In the 3b region,

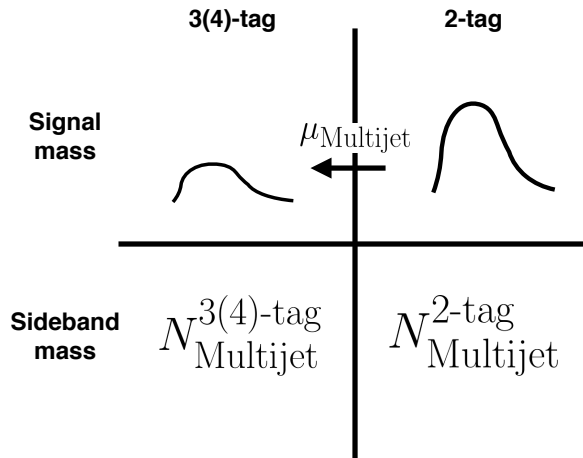


Figure 7.13: An illustration of the data-driven background estimation technique for the boosted analysis

2593

2594 the fit yields values of $\mu_{\text{Multijet}} = 0.160 \pm 0.03$ and $\beta_{t\bar{t}} = 1.02 \pm 0.09$. In the 4b region, the fit gives
 2595 $\mu_{\text{Multijet}} = 0.0091 \pm 0.0007$ and $\beta_{t\bar{t}} = 0.82 \pm 0.39$. The uncertainties quoted are statistical only. The
 2596 larger uncertainties in the 4b values indicate the lower statistics available in that region.

2597 Figure 7.14 shows the distributions of data and background estimates in the 3b and 4b sideband regions
 2598 after the background fit has been done. The normalizations are constrained from the fit to match that of
 2599 the data, but good modeling of the shape of the mass of the leading large-R jet is seen as well. The shapes
 2600 of the kinematic distributions for the $t\bar{t}$ background in the 4b region are taken from the 3b region due to
 2601 the better MC statistics in that region.

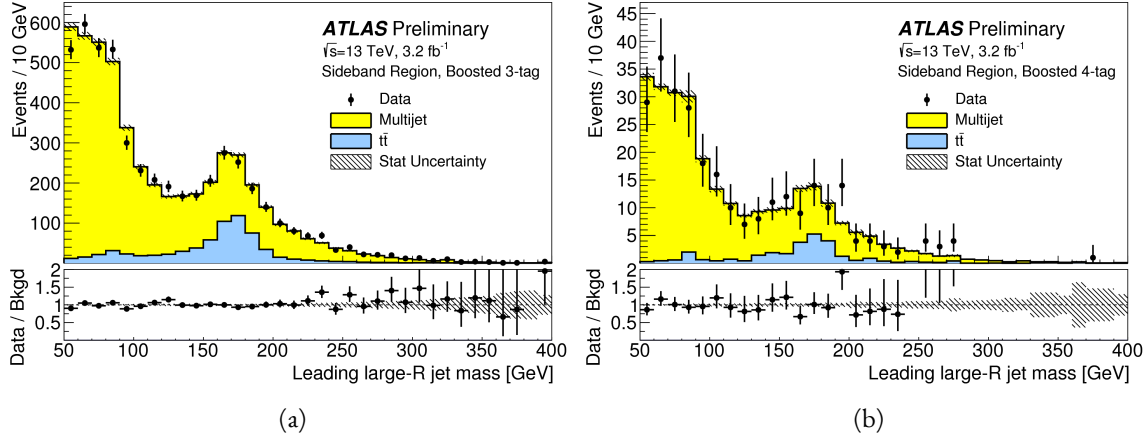


Figure 7.14: Leading large-R jet mass in the $3b$ (a) and $4b$ (b) sideband regions. The multijet and $t\bar{t}$ backgrounds are estimated using the data-driven methods described in the text. Because their normalizations are derived in the sideband region, the total background normalization is constrained by default to match the normalization of the data [126].

2602 7.6.3 BACKGROUND SHAPE FIT

2603 As mentioned in the previous section, the background shape in the 3-tag and 4-tag signal regions is taken
 2604 from the 2-tag signal mass region. Due to the limited statistics available, the background shapes are addi-
 2605 tionally smoothed after being extrapolated to the 3-tag and 4-tag signal regions. Only the data in the range
 2606 $900 < M_{2J} < 2000$ GeV is included in the shape fit due to the limited statistics available above 2 TeV.
 2607 Both the $t\bar{t}$ and QCD multijet background are independently fit with an exponential shape, $y = e^{ax+b}$.
 2608 Other shapes are considered and used for the systematic uncertainties. Table 7.4 shows the fit values for
 2609 the parameters. Because both the $3b$ and $4b$ QCD shapes come from the 2-tag region, the slopes derived
 2610 are very similar.

	a	b
QCD ($4b$)	0.00545 ± 0.00021	5.44 ± 0.24
$t\bar{t}$ ($4b$)	0.00746 ± 0.00021	4.88 ± 0.36
QCD ($3b$)	0.00545 ± 0.00021	8.30 ± 0.24
$t\bar{t}$ ($3b$)	0.00746 ± 0.00021	8.58 ± 0.36

Table 7.4: Parameters derived for exponential fit to background M_{2J} shape in the $3b$ and $4b$ signal regions [127].

2611 7.6.4 VALIDATION OF BACKGROUND ESTIMATE

2612 The background estimate can be validated by using the method to estimate the number of events in the
 2613 control mass region rather than the signal mass region. Figure 7.15 shows the M_{2J} distribution in the 3b
 2614 and 4b control regions, comparing data and background estimates. In both cases, both the background
 2615 shape and normalization are consistent with the data, indicating good agreement. The ratio of data to the
 2616 background estimates is also fit to a line in the figure to test for any shape difference. The slope of the
 2617 line is within 1σ (from the fit uncertainties) of flat, further indicating that the data is consistent with the
 2618 background estimate in the control region.

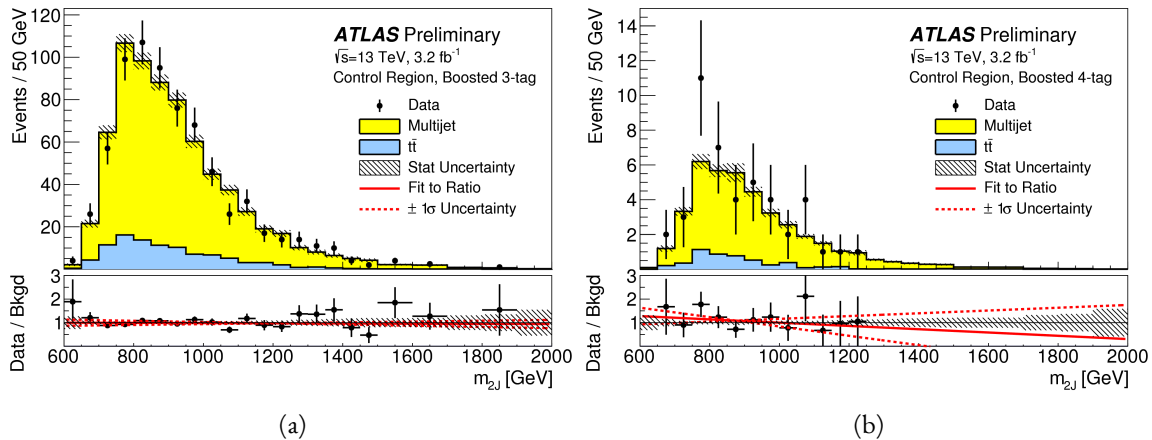


Figure 7.15: Di-jet invariant mass (M_{2J}) in the 3b (a) and 4b (b) control regions. The multijet and $t\bar{t}$ backgrounds are estimated using the data-driven methods described in the text [126].

2619 Table 7.5 shows the yields in data and background estimates in the 3-tag and 4-tag sideband and control
 2620 regions. Again, here, it can be seen that the total number of predicted background events from the data
 2621 driven method is consistent with the number of data events in the region.

2622 7.7 SYSTEMATIC UNCERTAINTIES

2623 The systematic uncertainties in this analysis can be divided into two broad categories. The first type is
 2624 uncertainties associated with the modeling of the signal processes. The second type of uncertainty is asso-
 2625 ciated with both the shape and normalization of the background prediction.

Sample (3-tag)	Sideband Region	Control Region
Multijet	4328 ± 27	607 ± 10
$t\bar{t}$	683.5 ± 8.1	99.6 ± 3.1
$Z+jets$	31.8 ± 3.7	7.7 ± 1.8
Total	5043 ± 28	715 ± 11
Data	5043	724
Sample (4-tag)	Sideband Region	Control Region
Multijet	247.4 ± 1.5	34.7 ± 0.6
$t\bar{t}$	28.4 ± 1.5	5.1 ± 0.7
$Z+jets$	3.4 ± 1.2	0.6 ± 0.5
Total	279.2 ± 2.5	40.3 ± 1.0
Data	279	45

Table 7.5: The number of events in data and predicted background events in the boosted 3-tag and 4-tag sideband and control regions [126]. The uncertainties shown are statistical only.

2626 7.7.1 SIGNAL MODELING UNCERTAINTIES

2627 The signal modeling uncertainty has three main components: theoretical uncertainty on the acceptance,
 2628 experimental uncertainties on the large-R jets, and experimental uncertainties on the track jets related to
 2629 b -tagging. In this analysis the experimental uncertainties are the most significant.

2630 The first uncertainty on signal modeling is the theoretical uncertainty on the acceptance. As explained
 2631 in section 5.6.1, there are four components to this uncertainty. The first is related to missing higher order
 2632 terms from the matrix element calculations which is estimated by varying the QCD renormalization and
 2633 factorization scales. The second is uncertainty due to the PDF set used. The third is a generator uncer-
 2634 tainty which is estimated by modifying the generator used to model the underlying event and hadroniza-
 2635 tion. Finally, there is an uncertainty associated with the modeling of the initial state and final state radia-
 2636 tion (ISR/FSR). The total theoretical uncertainty on the signal yield is 3%, and this is dominated by the
 2637 ISR/FSR modeling.

2638 There are uncertainties on the large-R jets in both the jet energy scale (JES) and jet energy resolution
 2639 (JER) as well as the jet mass scale (JMS) and jet mass resolution (JMR). These are evaluated using $\sqrt{s} =$

2640 8 TeV data from Run 1 of ATLAS and extrapolated to the Run 2 beam and detector conditions using
2641 MC⁵. The details of these uncertainties can be found in reference [128].

2642 Uncertainties on the track jets are related to the b -tagging efficiency. The total uncertainty on the signal
2643 yield due to b -tagging is evaluated by propagating variations of the b -tagging efficiency through the boosted
2644 selection requirements. The uncertainties are calculated jet-by-jet and parameterized as a function of b -jet
2645 p_T and η [106]. For high p_T b -jets (with $p_T > 300$ GeV), the uncertainties are extrapolated using MC
2646 simulation from the lower p_T b -jets [129].

2647 Table 7.6 shows the systematic uncertainties on the signal normalization for models with $m_{G_{KK}^*} =$
2648 1.5 TeV and both $c = 1$ and $c = 2$ as well as a narrow width heavy scalar. The dominant uncertainty
2649 comes from b -tagging and this uncertainty is larger in the 4-tag region than the 3-tag region.

2650 7.7.2 BACKGROUND UNCERTAINTIES

2651 Uncertainties on the QCD multijet background normalization and shape are estimated using the control
2652 mass region. As shown previously, the background predictions in the control region match with the data
2653 yields within the statistical uncertainty in both the 3-tag and 4-tag control regions. Additionally, the statis-
2654 tical uncertainty on the background prediction in the control region is assigned as a systematic uncertainty
2655 on the normalization of the QCD background.

2656 Additional robustness tests are done by varying the definition of the control mass region and the b -
2657 tagging requirements used to define the 2-tag sample. In all cases, the effect of the variations is found to be
2658 within the statistical uncertainties on the background normalization in the control region.

2659 Shape uncertainties on the background are evaluated using two techniques. First, as shown in fig-
2660 ure 7.15, the ratio between the data and background prediction is fit with a linear function. The uncer-
2661 tainties on the slope of this fit are assigned as shape uncertainties. An additional uncertainty is assigned by
2662 using alternate power law fit functions for the smoothing of the background shape. Table 7.7 shows the
2663 alternate shapes used. The largest difference between the nominal fit function and the alternates, taking
2664 into account the 1σ uncertainty band on each fit as well, is taken as a shape uncertainty.

⁵The uncertainties are correspondingly larger due to the uncertainty of this extrapolation.

Source	Background	G_{KK}^*		H
		$c = 1$	$c = 2$	
Luminosity	-	5.0	5.0	5.0
3-tag				
JER	< 1	< 1	< 1	< 1
JES	2	< 1	< 1	< 1
JMR	1	12	12	11
JMS	5	14	13	17
<i>b</i> -tagging	1	23	22	23
Theoretical	-	3	3	3
Multijet Normalization	3	-	-	-
Statistical	2	1	1	1
Total	7	31	30	33
4-tag				
JER	< 1	< 1	< 1	< 1
JES	< 1	< 1	< 1	< 1
JMR	4	12	13	13
JMS	5	13	13	14
<i>b</i> -tagging	2	36	36	36
Theoretical	-	3	3	3
Multijet Normalization	14	-	-	-
Statistical	3	1	1	1
Total	15	42	42	43

Table 7.6: Summary of systematic uncertainties in the total background and signal event yields (expressed in %) in the boosted 3-tag and 4-tag signal regions. Systematic uncertainties on the signal normalization are shown for models with $m_{G_{\text{KK}}^*} = 1.5 \text{ TeV}$ and both $c = 1$ and $c = 2$ as well as a narrow width heavy scalar.

2665 The uncertainties on the $t\bar{t}$ background are obtained by propagating the various experimental variations
 2666 (JES, JER, JMS, JMR, *b*-tagging) through the analysis selection requirements. Table 7.6 summarizes the
 2667 background uncertainties in the 3-tag and 4-tag regions.

2668 7.8 RESULTS

2669 Table 7.8 shows the observed yields in the 3-tag and 4-tag signal regions for the boosted analysis compared
 2670 to the predicted number of background events. In the 3-tag region, 316 events are observed with a pre-

Functional Form
$f_1(x) = p_0(1-x)^{p_1}x^{p_2}$
$f_2(x) = p_0(1-x)^{p_1}e^{p_2 x^2}$
$f_3(x) = p_0(1-x)^{p_1}x^{p_2}x$
$f_4(x) = p_0(1-x)^{p_1}x^{p_2}\ln x$
$f_5(x) = p_0(1-x)^{p_1}(1+x)^{p_2}x$
$f_6(x) = p_0(1-x)^{p_1}(1+x)^{p_2}\ln x$
$f_7(x) = \frac{p_0}{x}(1-x)^{p_1-p_2}\ln x$
$f_8(x) = \frac{p_0}{x^2}(1-x)^{p_1-p_2}\ln x$

Table 7.7: Alternate fit functions used to model the M_{2J} distribution in the QCD multijet background. In the equations, $x = M_{2J}/\sqrt{s}$.

dicted background of 285 ± 19 . In the 4-tag region, 20 events are observed with a predicted background of 14.6 ± 2.4 . Figure 7.16 shows the M_{2J} distribution in the 3-tag and 4-tag regions. There are some small excesses in the data, in particular in the 3-tag region around $M_{2J} \approx 900$ GeV and in the region of $1.6 < M_{2J} < 2.0$ TeV. The significance of these excesses will be evaluated in the next chapter in the statistical combination with the resolved results.

Sample	Signal Region (3-tag)	Signal Region (4-tag)
Multijet	235 ± 14	13.5 ± 2.4
$t\bar{t}$	48 ± 22	1.2 ± 1.0
$Z + \text{jets}$	2.0 ± 2.2	-
Total	285 ± 19	14.6 ± 2.4
Data	316	20
$G_{\text{KK}}^*(1000 \text{ GeV}), c = 1$	3.4 ± 0.9	2.9 ± 1.1

Table 7.8: Observed yields in the 3-tag and 4-tag signal regions for the boosted analysis compared to the predicted number of background events Errors correspond to the total uncertainties in the predicted event yields. The yields for a graviton with $m_{G_{\text{KK}}^*} = 1$ TeV and $c = 1$ are also shown [126].

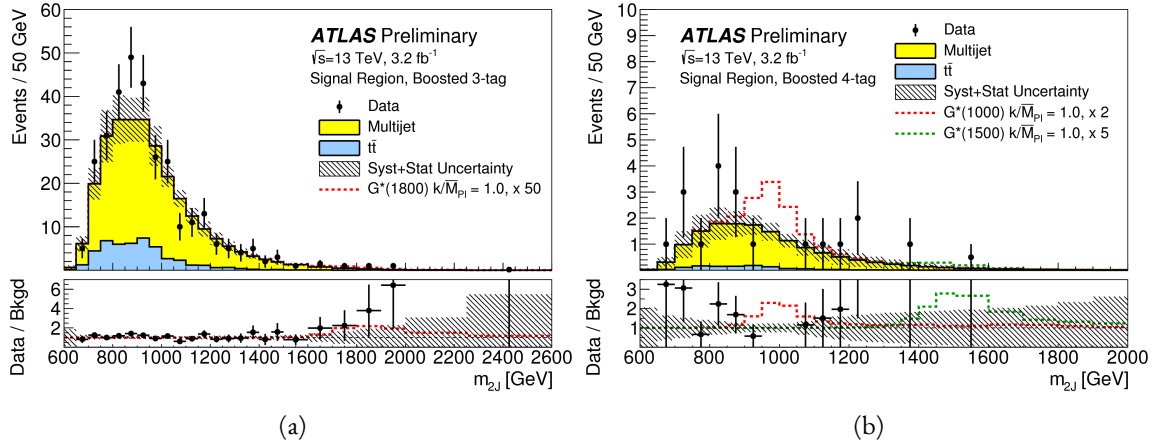


Figure 7.16: Di-jet invariant mass (M_{2J}) in the $3b$ (a) and $4b$ (b) signal regions. The multijet and $t\bar{t}$ backgrounds are estimated using the data-driven methods described in the text. In the $3b$ region, a graviton signal with $m_{G_{KK}^*} = 1.8 \text{ TeV}$ and $c = 1$ is overlaid, with the cross section multiplied by a factor of 50 so that the signal is visible. In the $4b$ region, signals with $m_{G_{KK}^*} = 1.0 \text{ TeV}$ and $m_{G_{KK}^*} = 1.5 \text{ TeV}$ are overlaid, both with $c = 1$ and the yields multiplied by factors of 2 and 5 respectively [126].

*There is no real ending. It's just the place where you stop
the story.*

Frank Herbert

8

2676

2677

Combined limits from boosted and resolved searches

2678

2679

8.1 INTRODUCTION

2680 In order maximize the explored mass range of possible resonances decaying to di-Higgs final states, two
2681 distinct tailored selections were produced. The resolved selection is more sensitive in the mass range of
2682 $400 < m_X < 1100$ GeV while the boosted selection is more sensitive to masses in the range $1100 <$
2683 $m_X < 3000$ GeV. Chapter 7 presents the details of the boosted selection and results. In setting limits
2684 on spin-2 Randall-Sundrum graviton (RSG) and narrow width heavy scalar (H) models, the results of the
2685 boosted selection are combined with the results of the resolved selection to cover a larger mass range.

2686 This chapter presents limits on signal models resulting from the $X \rightarrow HH \rightarrow b\bar{b}b\bar{b}$ search in both
2687 the resolved and boosted selections. It first presents a brief overview of the resolved results that go into

2688 the limit setting. Then, an overview of the statistical methods used for the search and limit setting is given.
 2689 Finally, limits on the RSG and heavy scalar models are presented.

2690 **8.2 RESOLVED RESULTS**

2691 The details of the resolved selection will not be presented here and can be found in reference [126]. In
 2692 basic terms, the selection searches for four $R = 0.4$ b-tagged calorimeter jets (where each pair of jets is
 2693 one Higgs candidate). This selection is distinct from the boosted methodology which searches for merged
 2694 decay products. The backgrounds to the resolved selection are the same as those presented in Chapter 7
 2695 for the boosted analysis.

2696 Table 8.1 shows the results for data yields and expected background in the resolved signal region. Fig-
 2697 ure 8.1 shows the M_{2J} distribution in the resolved signal region. The total number of events is consistent
 2698 with the prediction and no significant excess is seen. One event in the boosted 4-tag signal is shared with
 2699 the resolved signal region and has a mass of 852 GeV.

Sample	Signal Region Yield
Multijet	43.3 ± 2.3
$t\bar{t}$	4.3 ± 3.0
$Z + \text{jets}$	-
Total	47.6 ± 3.8
Data	46
SM hh	0.25 ± 0.07
$G_{\text{KK}}^*(800 \text{ GeV}), c = 1$	5.7 ± 1.5

Table 8.1: Observed yields in the resolved selection 4-tag signal region compared to the predicted number of background events Errors correspond to the total uncertainties in the predicted event yields. The yields for a graviton with $m_{G_{\text{KK}}^*} = 800$ GeV and $c = 1$ are also shown [126].

2700 **8.3 STATISTICAL TECHNIQUE AND RESULTS**

2701 The statistical technique used for the search in this analysis is the same as that used in the $H \rightarrow WW^*$
 2702 analysis presented in section 3.6.2. The test statistic q_0 is used to define the p -values which measure the

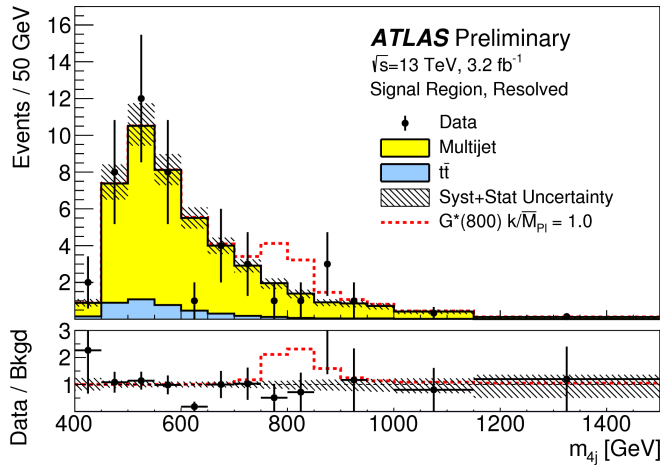


Figure 8.1: Di-jet invariant mass (M_{2J}) in the resolved signal region. The expected signal from a graviton with $m_{G_{KK}^*} = 800$ GeV and $c = 1$ is overlaid. [126].

compatibility of the data with the background-only hypothesis corresponding to a signal strength $\mu = 0$.

Local p_0 values are computed to quantify the probability that the background could produce a fluctuation greater than or equal to the one observed in the data. In the resolved analysis, no significant excesses are observed. The largest discrepancy with respect to the background only hypothesis occurs near a resonance mass of 900 GeV and is found to be less than 2σ in significance.

In the boosted selection, the largest local excess is a broad excess in the $3b$ signal region that begins near $M_{2J} \approx 1.7$ GeV. Assuming a G_{KK}^* with this mass and $c = 1.0$, the local significance of this excess is 2.0σ .

8.4 LIMIT SETTING

In the absence of any significant excess observed in the data, limits on different signal models can be set. This section describes the limit setting procedure and presents combined results of the resolved and boosted analyses.

8.4.1 LIMIT SETTING PROCEDURE

The procedure used for setting exclusion limits in this analysis is the CL_s method [130]. The first step in setting the limits is to define a test statistic which will be used. For limit setting, the test statistic is shown

2718 in equation 8.1.

$$\tilde{q}_\mu = \begin{cases} -2 \ln \frac{L(\mu, \hat{\theta}(\mu))}{L(0, \hat{\theta}(0))} & \hat{\mu} < 0 \\ -2 \ln \frac{L(\mu, \hat{\theta}(\mu))}{L(\hat{\mu}, \hat{\theta})} & 0 \leq \hat{\mu} < \mu \\ 0 & \hat{\mu} > \mu \end{cases} \quad (8.1)$$

2719 In the above equation, μ is the value of the signal strength under test, $\hat{\mu}$ is the best fit μ , $\hat{\theta}$ is the best fit
2720 value of the nuisance parameters, $\hat{\theta}$ is the best fit value of the nuisance parameters under the fixed μ value,
2721 and L is the Poisson likelihood of the data (as described in section 3.6.2).

2722 The test statistic \tilde{q}_μ is constructed to protect against two interesting corner cases when setting the upper
2723 limit on the cross section. First, it protects against negative signal strengths μ which are unphysical. Second,
2724 it does not count excesses in the data larger than those expected by a signal strength μ as evidence against
2725 the μ hypothesis.

2726 The CL_s statistic is constructed by taking a ratio of two probabilities. CL_{s+b} is the probability that the
2727 signal+background hypothesis would produce a value of the test statistic that is less than or equal to the
2728 observed valueⁱ. CL_b is the probability that the background only hypothesis will produce a value of the test
2729 statistic less than or equal to the observed. The CL_s statistic is the ratio CL_{s+b}/CL_b . A 95% upper limit
2730 on the cross section is set at the value of μ that makes the CL_s statistic less than 5%. In practice, the limits
2731 are computed numerically within an asymptotic approximation for the distribution of the test statistic \tilde{q}_μ .
2732 The details of this approximation can be found in reference [76].

2733 The resolved and boosted analyses are combined using a very simple procedure rather than a full statis-
2734 tical combination. For each mass point tested, the limit which gives the most stringent constraint is used.
2735 This means that for mass points below 1.1 TeV the resolved signal region is used, while at and above this
2736 point the combination of the orthogonal 3b and 4b boosted signal regions is used.

2737 8.4.2 LIMIT SETTING RESULTS

2738 Figure 8.2 shows the combined 95% upper bounds as a function of mass for three different models: G_{KK}^*
2739 with $c = 1$, G_{KK}^* with $c = 2$, and a narrow heavy scalar H .

ⁱLower values of \tilde{q}_μ mean better compatibility.

2740 The cross section of $\sigma(pp \rightarrow G_{\text{KK}}^* \rightarrow hh \rightarrow b\bar{b}b\bar{b})$ with $c = 1$ is constrained to be less than 70 fb
2741 for masses in the range $600 < m_{G_{\text{KK}}^*} < 3000$ GeV. For the RSG model with $c = 2$, cross sections limits
2742 between 40 fb and 200 fb are set for the mass range of $500 < m_{G_{\text{KK}}^*} < 3000$ GeV. Masses in the range
2743 of $475 < m_{G_{\text{KK}}^*} < 785$ GeV are excluded with $c = 1$ (with an exclusion of the range 465 to 745 GeV
2744 expected). Masses less than 980 GeV are excluded with $c = 2$ (with an exclusion for masses less than
2745 1 TeV expected).

2746 In the heavy Higgs model, the cross section upper limits for $\sigma(pp \rightarrow H \rightarrow hh \rightarrow b\bar{b}b\bar{b})$ ranges from
2747 30 to 300 fb in the mass range of $500 < m_H < 3000$ GeV. The resolved analysis can also set an upper
2748 limit on the Standard Model di-Higgs production cross section discussed in chapter 3. The upper limit on
2749 $\sigma(pp \rightarrow hh \rightarrow b\bar{b}b\bar{b})$ in the Standard Model is constrained to be less than 1.22 pb.

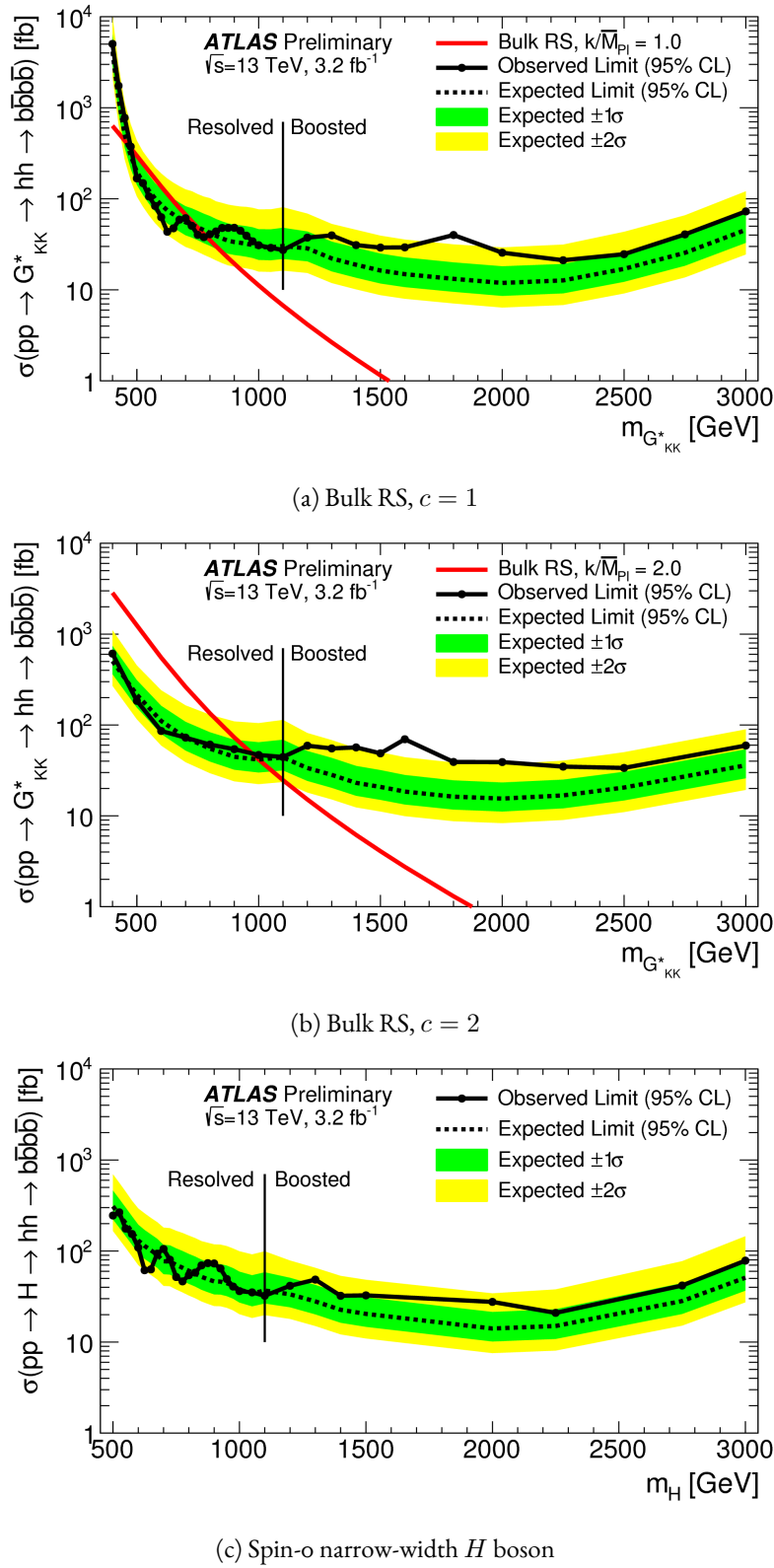


Figure 8.2: Expected and observed upper limit as a function of mass for G^*_{KK} in the RSG model with (a) $c = 1$ and (b) $c = 2$, as well as (c) H with fixed $\Gamma_H = 1$ GeV, at the 95% confidence level in the CL_s method [126].

2750

Part IV

2751

Looking ahead

9

2752

2753

Conclusion

2754 After being sought for many years at different collider experiments, the Higgs boson was discovered by
2755 the ATLAS and CMS experiments in 2012, confirming the leading theory for the source of electroweak
2756 symmetry breaking and filling in the last missing piece of the Standard Model. After its discovery, mea-
2757 surements of the particle's detailed properties and searches for new particles decaying to Higgs final states
2758 were both extremely important in constraining physics beyond the Standard Model. This dissertation
2759 presented this evolution through two results: the observation and measurement of the Higgs boson in the
2760 $H \rightarrow WW^* \rightarrow \ell\nu\ell\nu$ channel at $\sqrt{s} = 7$ TeV and $\sqrt{s} = 8$ TeV and a search for Higgs pair production
2761 in the $HH \rightarrow b\bar{b}b\bar{b}$ channel at $\sqrt{s} = 13$ TeV in pp collisions.

2762 In the $H \rightarrow WW^* \rightarrow \ell\nu\ell\nu$, results from both the discovery of the Higgs boson and the full ATLAS
2763 Run 1 dataset were presented. The Higgs boson was discovered with a 5.9σ significance in a combination
2764 of the $H \rightarrow \gamma\gamma$, $H \rightarrow ZZ \rightarrow 4\ell$, $H \rightarrow WW^* \rightarrow \ell\nu\ell\nu$ with 4.2 fb^{-1} at $\sqrt{s} = 7$ TeV and 5.2 fb^{-1} at
2765 $\sqrt{s} = 8$ TeV. The $H \rightarrow WW^*$ channel was expected to contribute approximately one-third of the total

2766 sensitivity to the Higgs signal at the time. With the full 20.3 fb^{-1} at $\sqrt{s} = 8 \text{ TeV}$ and 4.2 fb^{-1} at $\sqrt{s} =$
2767 7 TeV , ATLAS achieved discovery level significance in the $H \rightarrow WW^*$ channel alone and obtained the
2768 first evidence of vector boson fusion production of the Higgs. The combined signal strength was measured
2769 to be $\mu = 1.09^{+0.23}_{-0.21}$. The total observed significance of the $H \rightarrow WW^*$ process was observed to be 6.1σ
2770 (with 5.8σ expected). Advanced methods for background reduction and estimation, particularly in same-
2771 flavor lepton final states, were shown. The VBF signal strength was measured to be $\mu_{\text{VBF}} = 1.27^{+0.53}_{-0.45}$
2772 with an observed significance of 3.2σ (with 2.7σ expected).

2773 These results required many novel innovations. The increase of pileup interactions in the higher in-
2774 stantaneous luminosity LHC conditions of 2012 led to a degradation of missing transverse momentum
2775 resolution. As a result, the prominent $Z/\gamma^* + \text{jets}$ background of the same flavor $H \rightarrow WW^* \rightarrow \ell\nu\ell\nu$
2776 final states increased greatly. New variables, including a track-based missing transverse momentum and a
2777 measurement of the balance between the dilepton system and recoiling jets, allowed for significant reduc-
2778 tion of this background. In the VBF channel, selections were optimized to exploit the unique VBF final
2779 state topology. Incorporating these variables into a boosted decision tree technique allowed the analysis
2780 to exceed the 3σ statistical significance threshold.

2781 After the end of Run 1, the results of Higgs measurements from ATLAS were combined with those
2782 from CMS to produce the most precise measurements of the Higgs boson so far [131]. Figure 9.1 shows the
2783 combination of ATLAS and CMS data for the Higgs signal strength and coupling measurements. In the
2784 signal strength measurements of gluon fusion and vector boson fusion, the $H \rightarrow WW^*$ channel provides
2785 the tightest constraints. Additionally, the Higgs coupling to W bosons is the most precisely measured with
2786 a relative uncertainty of 10%.

2787 With the discovery of the Higgs firmly established and its properties measured, a natural next step was
2788 to search for new physics with Higgs final states. At $\sqrt{s} = 13 \text{ TeV}$, a search for Higgs pair production
2789 in the $b\bar{b}b\bar{b}$ final state with 3.2 fb^{-1} was conducted. A signal region optimized for the boosted final states
2790 arising from high mass resonances was constructed. This signal region utilized large-radius calorimeter jets
2791 and b -tagging with small radius track jets to maximize the signal acceptance. No significant excesses were
2792 observed, and upper limits on cross sections are placed for spin-2 Randall Sundrum gravitons (RSG) and

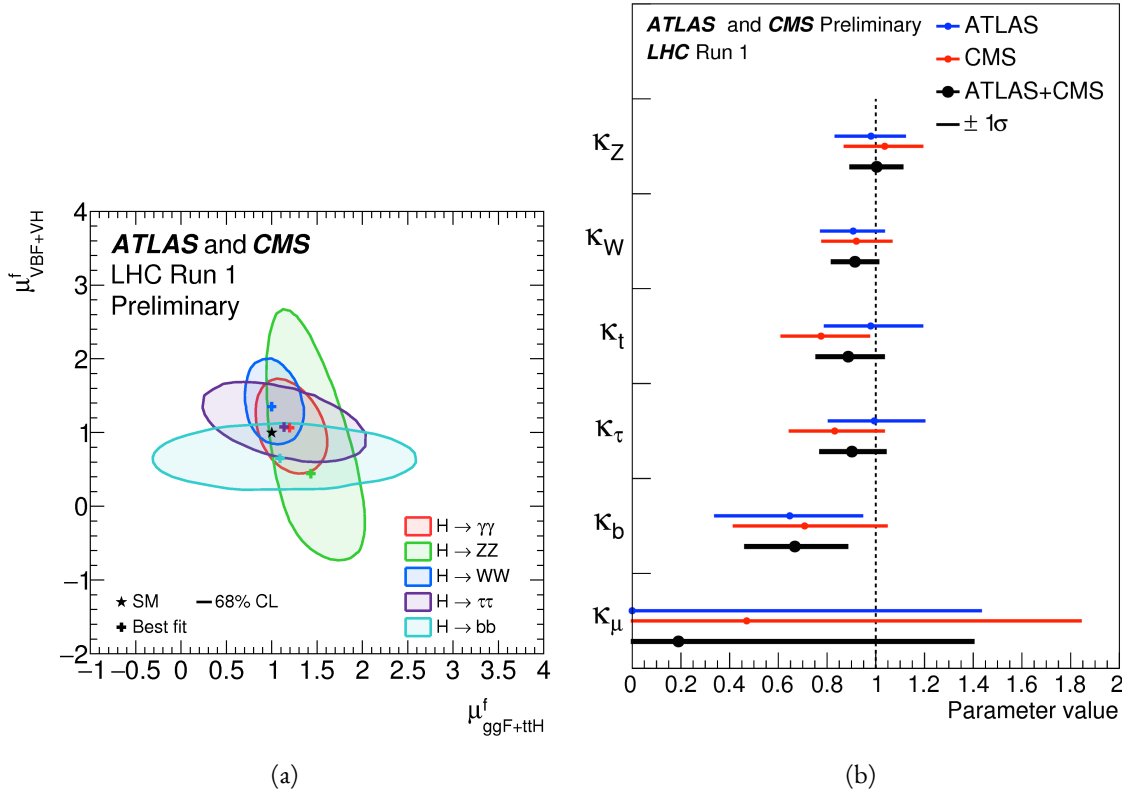


Figure 9.1: Combined ATLAS and CMS measurements in Run 1 for (a) Higgs signal strength in gluon fusion and VBF and (b) Higgs couplings normalized to their SM predictions

heavy narrow scalar resonances. The increase in center of mass energy in Run 2 allowed this analysis to quote upper cross section up to masses 3 TeV. The cross section of $\sigma(pp \rightarrow G_{\text{KK}}^* \rightarrow hh \rightarrow b\bar{b}b\bar{b})$ with $k/\bar{M}_{\text{Pl}} = 1$ was constrained to be less than 70 fb for masses in the range $600 < m_{G_{\text{KK}}^*} < 3000$ GeV. For the RSG model with $k/\bar{M}_{\text{Pl}} = 2$, cross sections limits between 40 fb and 200 fb are set for the mass range of $500 < m_{G_{\text{KK}}^*} < 3000$ GeV. The cross section upper limits for $\sigma(pp \rightarrow H \rightarrow hh \rightarrow b\bar{b}b\bar{b})$ ranges from 30 to 300 fb in the mass range of $500 < m_H < 3000$ GeV.

While there has been a rigorous program of measurements and searches involving the Higgs, there is still much room for improvement at the High Luminosity LHC (HL-LHC) and beyond. The measured signal strength for VBF production in $H \rightarrow WW^*$ still has a relative error at the level of 40%, largely dominated by statistical uncertainty. Projections for the HL-LHC show that the uncertainty on the VBF signal strength can be reduced to approximately 15% with 3000 fb^{-1} [132, 133]. This projection also assumes that theoretical uncertainties on the signal, which would be the largest contribution in the future

dataset, remain as they are now. Improvements in the theoretical understanding of the Higgs signal would also reduce the signal strength uncertainty dramatically. Such results allow for measurements of the Higgs coupling to vector bosons to reach precisions at the level of a few percent, therefore giving much power to constrain or discover new physics.

The prospects for detection of beyond the Standard Model resonant di-Higgs production at the HL-LHC are also quite promising. Figure 9.2 shows projections for the discovery significance of RSG signals at the HL-LHC in the $X \rightarrow HH \rightarrow b\bar{b}b\bar{b}$ search [133]. In all detector budget scenarios, a 1.5 TeV resonance is above or near 5σ significance, while a 2 TeV resonance is between $4-5\sigma$ except for the lowest budget scenario.

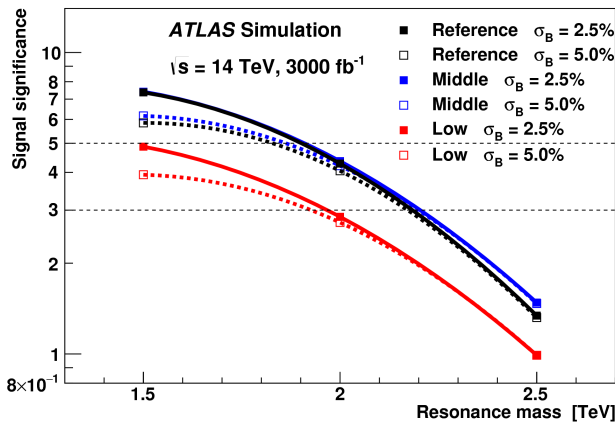


Figure 9.2: Discovery significance for RSG models at the HL-LHC in three different budget scenarios [133]. Systematic uncertainties on the background prediction (σ_B) of 2.5% and 5.0% are both tested.

The Higgs will continue to be an incredibly powerful tool in the understanding of nature at the HL-LHC and beyond. Through both precision measurements and searches, the nature of electroweak symmetry breaking will be better understood and the potential for the discovery of physics beyond the Standard Model has never been greater.

A

2818

2819

b-tagging performance at high p_T

2820 One of the limiting factors of the signal acceptance in the $X \rightarrow HH \rightarrow b\bar{b}b\bar{b}$ search at high resonance
2821 masses is the degradation of the *b*-tagging efficiency for high p_T jets. This appendix presents a study of the
2822 underlying causes of this degradation.

2823 A.I CHANGES IN MV₂ SCORE AT HIGH p_T

2824 The degradation of *b*-tagging at high p_T was studied in particular in the context of RSG models at high
2825 mass. Figure A.I shows the p_T of the leading track jet inside of the leading calorimeter jet in RSG events.
2826 At high $m_{G_{KK}^*}$, the p_T spectrum of track jets is much harder than at lower masses due to the increased
2827 Higgs p_T .

2828 Figure A.2 shows the MV_{2c2o} algorithm score for the leading and subleading track jets inside of the
2829 leading calorimeter jet. In both cases, it can be seen that at higher RSG masses the MV₂ score shifts towards
2830 more background like (negative) values. Additionally, this effect is more pronounced in the leading track

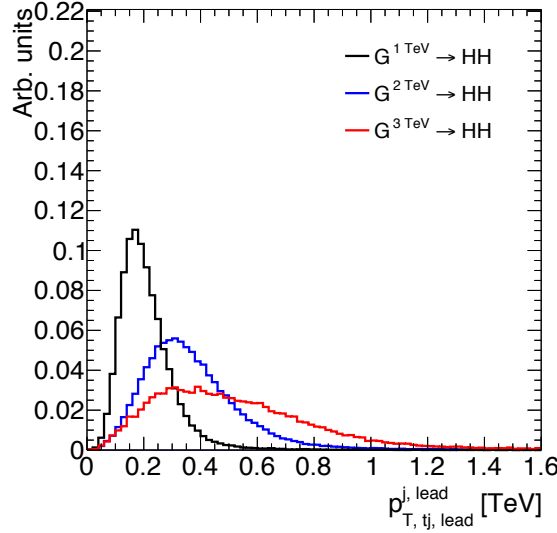


Figure A.1: p_T of the leading track jet in the leading calorimeter jet for different signal masses in RSG $c = 1$ models.

²⁸³¹ jet than the subleading.

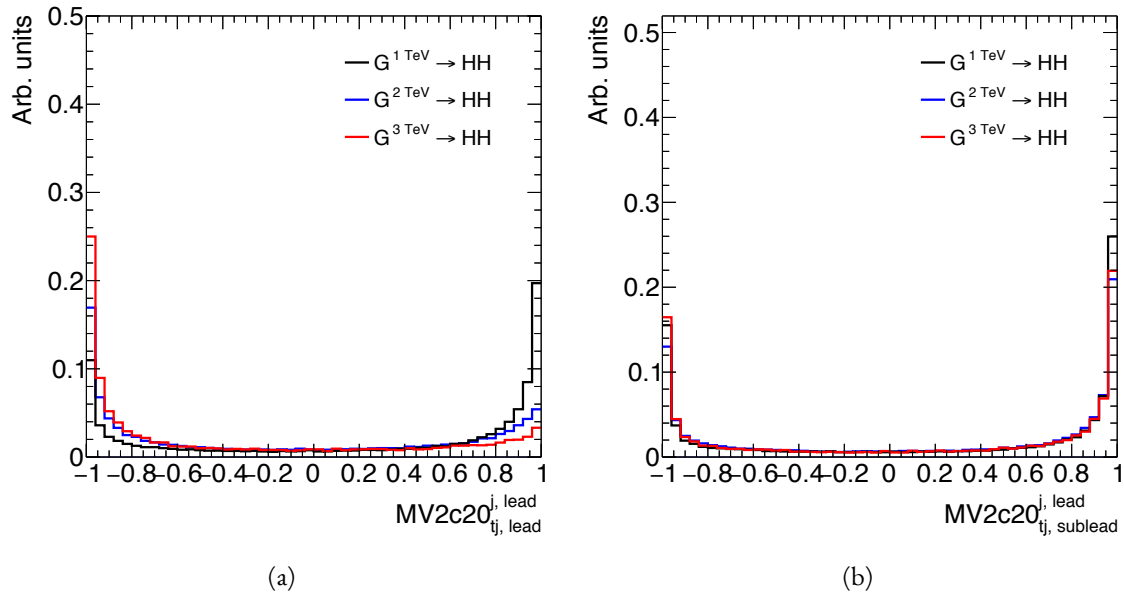


Figure A.2: MV2c20 score for the leading track jet (a) and subleading track jet (b) of the leading calorimeter jet for different signal masses in RSG $c = 1$ models.

²⁸³² To understand what is causing this change in the MV2c20 score, the same comparisons can be made for
²⁸³³ the input variables of MV2c20. The focus in these comparisons will be on the leading track jet as this is the
²⁸³⁴ one seen to have the largest difference in MV2 score. Figure A.3 shows the log likelihood ratio $\log(p_b/p_u)$

2835 from the IP₃D (three dimensional impact parameter) algorithm. At higher masses, the IP₃D likelihood
 2836 ratio distribution does become more background-like.

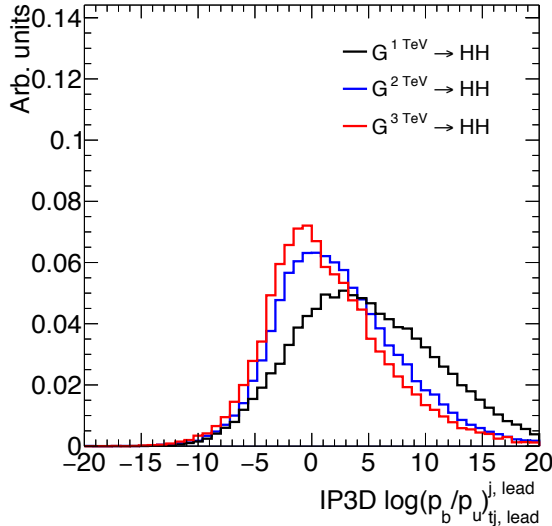


Figure A.3: IP₃D log-likelihood ratio ($\log(p_b/p_u)$) of the leading track jet in the leading calorimeter jet for different signal masses in RSG $c = 1$ models.

2837 Figure A.4 shows the mass and number of tracks at the secondary vertex computed by the SV1 algorithm.
 2838 When there is no secondary vertex found, the algorithm assigns a default negative value for these quantities.
 2839 Both of these distributions show that there is a significantly larger fraction of jets where no secondary vertex
 2840 is found in the high mass samples compared to the $m_{G_{KK}^*} = 1$ TeV sample. The SV1 algorithm's inability
 2841 to find a secondary vertex could be an important factor in the overall MV₂ score shift, as this eliminates
 2842 eight of the input variables that would normally contribute information to the algorithm.

2843 Figure A.5 shows the same quantities for the JetFitter algorithm. In this case, there is also a change in
 2844 the fraction of jets which have their secondary vertices successfully reconstructed, but this change is not as
 2845 drastic as that seen in SV1. There is also an increase in the number of jets which have high values of mass.

2846 A.2 EFFECT OF MULTIPLE b -QUARKS INSIDE ONE JET

2847 One hypothesis for why the efficiency of b -tagging the leading track jet degrades is that at high masses, the
 2848 b quarks get close enough together that both of them are inside of the leading track jet. Because MV₂ is not

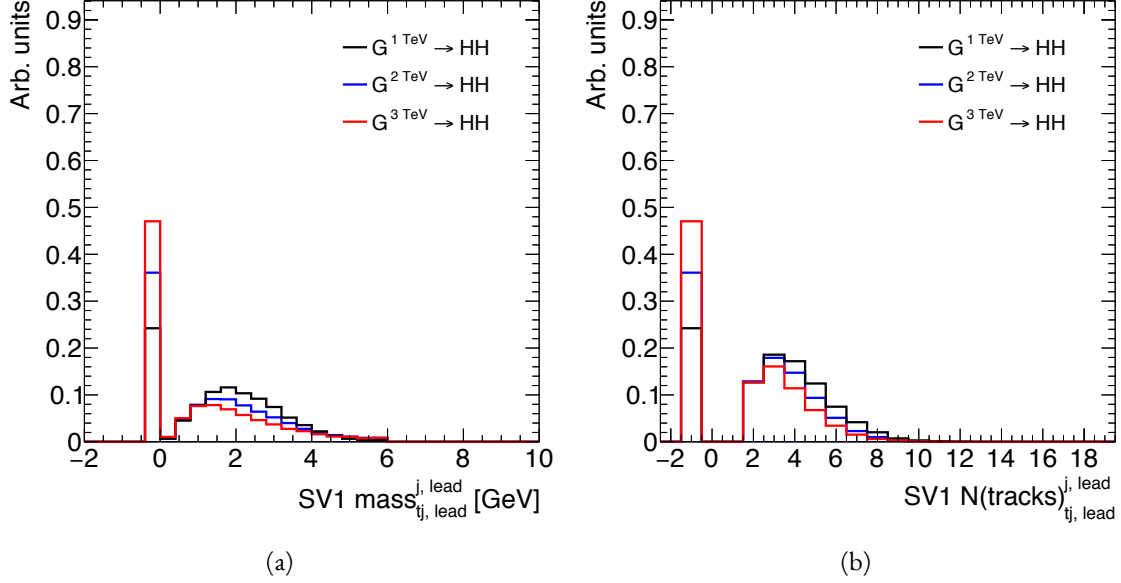


Figure A.4: Mass (a) and number of tracks (b) for the secondary vertices computed with the SV1 algorithm. When no secondary vertex is found, the quantities are assigned to default negative values.

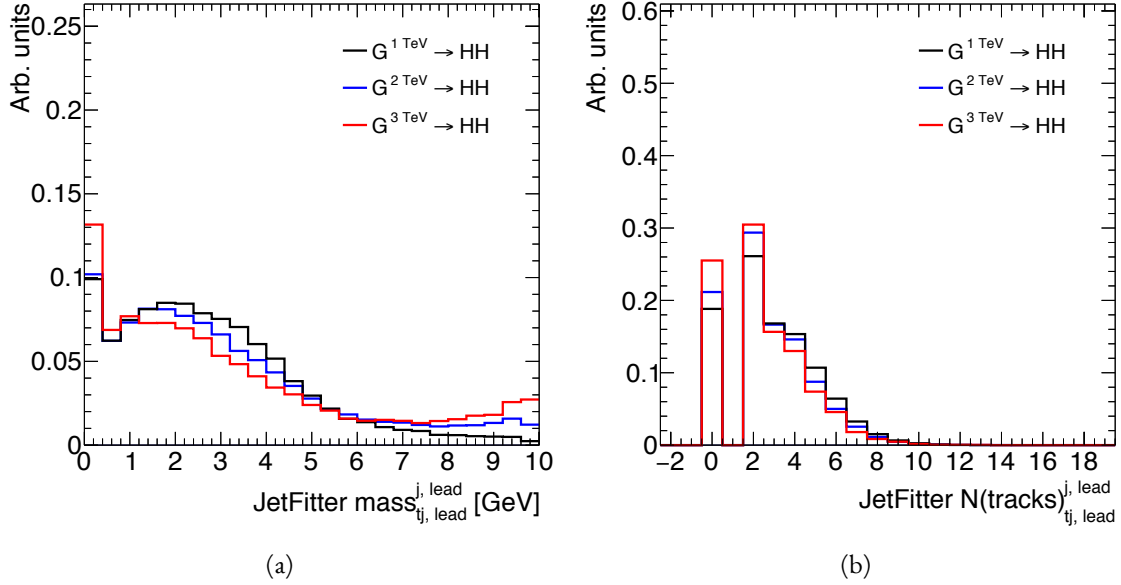


Figure A.5: Mass (a) and number of tracks (b) for vertices computed with the JetFitter algorithm. When no vertices are found, the quantities are assigned to default negative values.

2849 tuned for tagging multiple b quarks inside one jet, the tagging efficiency could degrade. Figure A.6 shows
 2850 MV2 scores and SV1 mass for cases where there are two b quarks at truth level within the radius of the

leading track jet compared to cases where there is only one true b ¹. This figure suggests that the presence

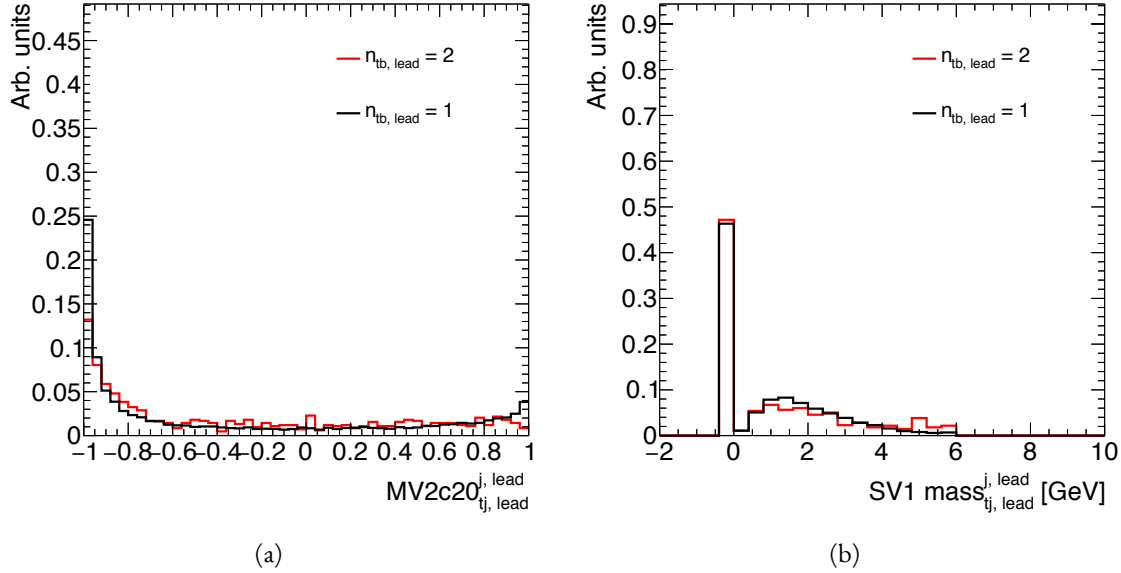


Figure A.6: MV₂c20 score (a) and SV1 mass (b) for leading track jets with two truth b quarks ($n_{tb, \text{lead}} = 2$) compared to those with only one truth b ($n_{tb, \text{lead}} = 1$).

of two b -quarks inside the leading jet is not the cause of the degradation in efficiency. There is a change in the shape of the MV₂ score distribution, but it is not nearly as pronounced as that seen in A.2 at higher masses. Additionally, the fraction of jets with no secondary vertex found is nearly identical in the track jets with two truth b -quarks.

A.3 CHANGES IN TRACK QUALITY AT HIGH p_T

Another hypothesis for the degradation of the b -tagging efficiency is a decrease in track quality for high p_T b jets. One way to check the overall quality of the tracking inside the jet is to investigate quantities related to the leading track inside of the track jet. Figure A.7 shows the fit χ^2/n_{DOF} and number of hits in the pixel detector for the leading track of the leading track jet. In both cases, the figure shows that in higher mass samples, the quality of the leading track inside of the track jet degrades substantially. The fit quality is lessened and the tracks have less hits in the pixel detector. This is likely due to the fact that at higher p_T ,

¹When two truth b quarks are required in the leading jet, the subleading jet is required to have zero. When one is required for the leading, one is also required for the subleading.

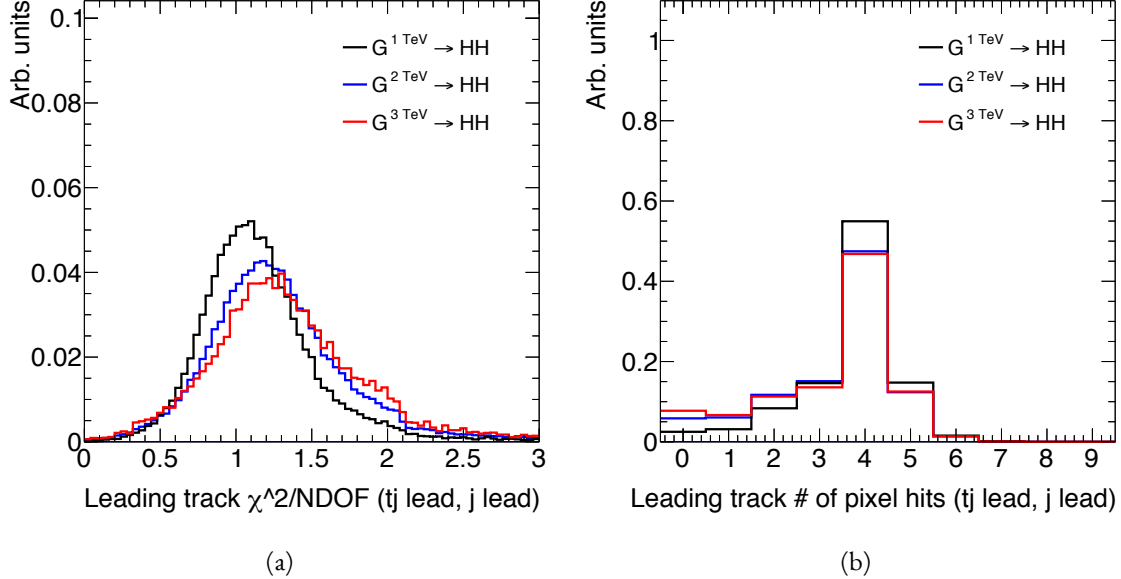


Figure A.7: Track fit χ^2/n_{DOF} (a) and number of pixel detector hits (b) for the leading track of the leading track jet in different mass RSG $c = 1$ samples.

the B -hadron will sometimes live long enough to miss the IBL and first pixel layer, thus decreasing the number of hits on the track. Figure A.8 shows the distance traveled in the transverse plane by B -hadrons for three different masses of gravitons. At higher masses, a larger fraction of B -hadrons decay within the IBL and first pixel layer.

To check whether this is the cause for the shift in the MV_2 score and the higher difficulty in reconstructing secondary vertices, jets whose leading track have at least four pixel hits are compared with those whose tracks have less than four pixel hits. The results for the MV_2 score and SVI mass are shown in figure A.9. Track jets where the leading track does not have at least four pixel hits are more likely to not have a secondary vertex reconstructed. Additionally, their $\text{MV}_{2\text{c}20}$ score is shifted more significantly to background-like values. This seems to confirm the hypothesis that degrading track quality is responsible for the lowered b -tagging efficiency at high p_T .

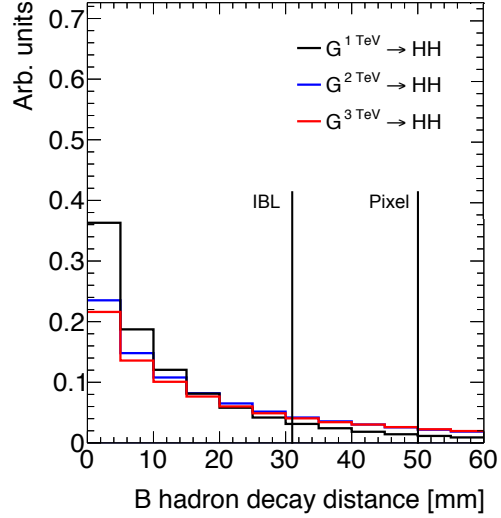


Figure A.8: Distance traveled (in the transverse plane) by B -hadrons before decay for different signal masses in RSG $c = 1$ models. Vertical lines denote where the IBL and first pixel layers begin.

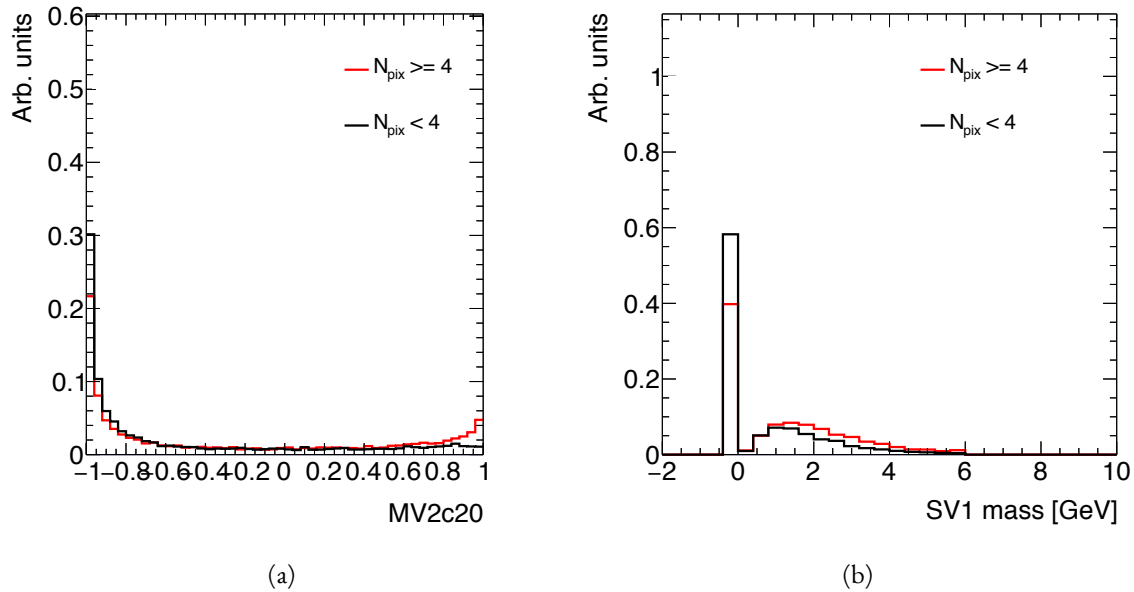


Figure A.9: MV2c20 score (a) and SV1 mass (b) for leading track jets whose leading track jet has at least four pixel hits ($N_{\text{pix}} \geq 4$) compared to those which do not ($N_{\text{pix}} < 4$).

References

2874

- 2875 [1] Georges Aad et al. Observation of a new particle in the search for the Standard Model Higgs boson
2876 with the ATLAS detector at the LHC. *Phys. Lett.*, B716:1–29, 2012. doi: 10.1016/j.physletb.2012.
2877 08.020.
- 2878 [2] Serguei Chatrchyan et al. Observation of a new boson at a mass of 125 GeV with the CMS experi-
2879 ment at the LHC. *Phys. Lett.*, B716:30–61, 2012. doi: 10.1016/j.physletb.2012.08.021.
- 2880 [3] David Griffiths. *Introduction to elementary particles*. 2008.
- 2881 [4] F. Halzen and Alan D. Martin. *QUARKS AND LEPTONS: AN INTRODUCTORY COURSE*
2882 *IN MODERN PARTICLE PHYSICS*. 1984. ISBN 0471887412, 9780471887416.
- 2883 [5] Christopher G. Tully. *Elementary particle physics in a nutshell*. 2011.
- 2884 [6] K. A. Olive et al. Review of Particle Physics. *Chin. Phys.*, C38:090001, 2014. doi: 10.1088/1674-1137/
2885 38/9/090001.
- 2886 [7] Matthew D. Schwartz. *Quantum Field Theory and the Standard Model*. Cambridge University
2887 Press, 2014. ISBN 1107034736, 9781107034730. URL <http://www.cambridge.org/us/academic/subjects/physics/theoretical-physics-and-mathematical-physics/quantum-field-theory-and-standard-model>.
- 2888 [8] S. Dawson. Introduction to electroweak symmetry breaking. In *High energy physics and cosmology. Proceedings, Summer School, Trieste, Italy, June 29-July 17, 1998*, pages 1–83, 1998. URL <http://alice.cern.ch/format/showfull?sysnb=0301862>.
- 2889 [9] S. L. Glashow. Partial Symmetries of Weak Interactions. *Nucl. Phys.*, 22:579–588, 1961. doi: 10.
2890 1016/0029-5582(61)90469-2.
- 2891 [10] Steven Weinberg. A Model of Leptons. *Phys. Rev. Lett.*, 19:1264–1266, 1967. doi: 10.1103/
2892 *PhysRevLett*.19.1264.
- 2893 [11] A. Salam. *Elementary Particle Theory*. Almqvist and Wiksell, Stockholm, 1968.
- 2894 [12] J. Iliopoulos S.L. Glashow and L. Maiani. *D2*:1285, 1970.
- 2895 [13] R. Keith Ellis, W. James Stirling, and B. R. Webber. *QCD and collider physics*. *Camb. Monogr. Part. Phys. Nucl. Phys. Cosmol.*, 8:1–435, 1996.

- 2901 [14] P. W. Higgs. Broken symmetries and the masses of gauge bosons. 13:508, 1964.
- 2902 [15] P. W. Higgs. Spontaneous symmetry breakdown without massless bosons. 145:1156, 1966.
- 2903 [16] F. Englert and R. Brout. Broken symmetry and the mass of gauge vector mesons. 13:321, 1964.
- 2904 [17] G. S. Guralnik, C. R. Hagen, and T. W. .B. Kibble. Global conservation laws and massless particles.
Phys. Rev. Lett., 13:585, 1964. doi: 10.1103/PhysRevLett.13.585.
- 2905 [18] LHC Higgs Cross Section Working Group, S. Heinemeyer, C. Mariotti, G. Passarino, and
R. Tanaka (Eds.). Handbook of LHC Higgs Cross Sections: 3. Higgs Properties. 2013.
- 2906 [19] Charalampos Anastasiou and Kirill Melnikov. Higgs boson production at hadron colliders in
NNLO QCD. *Nucl. Phys.*, B 646:220, 2002. doi: 10.1016/S0550-3213(02)00837-4.
- 2907 [20] M. Spira, A. Djouadi, D. Graudenz, and P. M. Zerwas. Higgs boson production at the LHC. *Nucl.*
Phys., B 453:17, 1995. doi: 10.1016/0550-3213(95)00379-7.
- 2908 [21] Giuseppe Degrassi and Fabio Maltoni. Two-loop electroweak corrections to Higgs production at
hadron colliders. *Phys. Lett.*, B 600:255, 2004.
- 2909 [22] U. Aglietti, R. Bonciani, G. Degrassi, and A. Vicini. Master integrals for the two-loop light fermion
contributions to $gg \rightarrow H$ and $H \rightarrow \gamma\gamma$. 600:57, 2004. doi: 10.1016/j.physletb.2004.
09.001.
- 2910 [23] D. de Florian and M. Grazzini. Higgs production at the LHC: updated cross sections at $\sqrt{s} =$
8 TeV. *Phys. Lett.*, B 718:117, 2012.
- 2911 [24] P. Bolzoni, F. Maltoni, S.-O. Moch, and M. Zaro. Higgs production via vector-boson fusion at
NNLO in QCD. 105:011801, 2010. doi: 10.1103/PhysRevLett.105.011801.
- 2912 [25] Tao Han, G. Valencia, and S. Willenbrock. Structure function approach to vector boson scattering
in $p p$ collisions. *Phys. Rev. Lett.*, 69:3274–3277, 1992. doi: 10.1103/PhysRevLett.69.3274.
- 2913 [26] Mariano Ciccolini, Ansgar Denner, and Stefan Dittmaier. Electroweak and QCD corrections to
Higgs production via vector-boson fusion at the LHC. *Phys. Rev.*, D 77:013002, 2008. doi: 10.
1103/PhysRevD.77.013002.
- 2914 [27] S. Catani, D. de Florian, M. Grazzini, and P. Nason. Soft-gluon re-summation for Higgs boson
production at hadron colliders. *JHEP*, 0307:028, 2003. doi: 10.1088/1126-6708/2003/07/028.
- 2915 [28] Abdelhak Djouadi. The Anatomy of electro-weak symmetry breaking. I: The Higgs boson in the
standard model. *Phys. Rept.*, 457:1–216, 2008. doi: 10.1016/j.physrep.2007.10.004.

- 2930 [29] J. Baglio, A. Djouadi, R. Gröber, M. M. Mühlleitner, J. Quevillon, and M. Spira. The mea-
 2931 surement of the Higgs self-coupling at the LHC: theoretical status. *JHEP*, 04:151, 2013. doi:
 2932 10.1007/JHEP04(2013)151.
- 2933 [30] Matthew J. Dolan, Christoph Englert, and Michael Spannowsky. New Physics in LHC Higgs boson
 2934 pair production. *Phys. Rev.*, D87(5):055002, 2013. doi: 10.1103/PhysRevD.87.055002.
- 2935 [31] Roberto Contino, Margherita Ghezzi, Mauro Moretti, Giuliano Panico, Fulvio Piccinini, and An-
 2936 drea Wulzer. Anomalous Couplings in Double Higgs Production. *JHEP*, 08:154, 2012. doi:
 2937 10.1007/JHEP08(2012)154.
- 2938 [32] R. Grober and M. Mühlleitner. Composite Higgs Boson Pair Production at the LHC. *JHEP*, 06:
 2939 020, 2011. doi: 10.1007/JHEP06(2011)020.
- 2940 [33] Lisa Randall and Raman Sundrum. A Large mass hierarchy from a small extra dimension. *Phys.*
 2941 *Rev. Lett.*, 83:3370–3373, 1999. doi: 10.1103/PhysRevLett.83.3370.
- 2942 [34] Kaustubh Agashe, Hooman Davoudiasl, Gilad Perez, and Amarjit Soni. Warped Gravitons at the
 2943 LHC and Beyond. *Phys. Rev.*, D76:036006, 2007. doi: 10.1103/PhysRevD.76.036006.
- 2944 [35] A. Liam Fitzpatrick, Jared Kaplan, Lisa Randall, and Lian-Tao Wang. Searching for the Kaluza-
 2945 Klein Graviton in Bulk RS Models. *JHEP*, 09:013, 2007. doi: 10.1088/1126-6708/2007/09/013.
- 2946 [36] Julien Baglio, Otto Eberhardt, Ulrich Nierste, and Martin Wiebusch. Benchmarks for Higgs Pair
 2947 Production and Heavy Higgs boson Searches in the Two-Higgs-Doublet Model of Type II. *Phys.*
 2948 *Rev.*, D90(1):015008, 2014. doi: 10.1103/PhysRevD.90.015008.
- 2949 [37] G. C. Branco, P. M. Ferreira, L. Lavoura, M. N. Rebelo, Marc Sher, and Joao P. Silva. Theory and
 2950 phenomenology of two-Higgs-doublet models. *Phys. Rept.*, 516:1–102, 2012. doi: 10.1016/j.physrep.
 2951 2012.02.002.
- 2952 [38] Howard E. Haber and Oscar Stål. New LHC benchmarks for the \mathcal{CP} -conserving two-Higgs-
 2953 doublet model. *Eur. Phys. J.*, C75(10):491, 2015. doi: 10.1140/epjc/s10052-015-3697-x.
- 2954 [39] Jose M. No and Michael Ramsey-Musolf. Probing the Higgs Portal at the LHC Through Resonant
 2955 di-Higgs Production. *Phys. Rev.*, D89(9):095031, 2014. doi: 10.1103/PhysRevD.89.095031.
- 2956 [40] Johan Alwall, Michel Herquet, Fabio Maltoni, Olivier Mattelaer, and Tim Stelzer. MadGraph
 2957 5:Going Beyond. *JHEP*, 1106:128, 2011. doi: 10.1007/JHEP06(2011)128.
- 2958 [41] Oleg Antipin, Tuomas Hapola. CP3 Origins implementation of Randall-Sundrum model. 2013,
 2959 URL <http://cp3-origins.dk/research/units/ed-tools>.

- 2960 [42] Georges Aad et al. Constraints on new phenomena via Higgs boson couplings and invisible decays
 2961 with the ATLAS detector. *JHEP*, 11:206, 2015. doi: 10.1007/JHEP11(2015)206.
- 2962 [43] Lyndon R Evans and Philip Bryant. LHC Machine. *J. Instrum.*, 3:S08001. 164 p, 2008. URL
 2963 <https://cds.cern.ch/record/1129806>. This report is an abridged version of the LHC De-
 2964 sign Report (CERN-2004-003).
- 2965 [44] ATLAS Collaboration. The ATLAS experiment at the CERN Large Hadron Collider. *JINST*, 3:
 2966 S08003, 2008. doi: 10.1088/1748-0221/3/08/S08003.
- 2967 [45] CMS Collaboration. The cms experiment at the cern lhc. *Journal of Instrumentation*, 3(08):S08004,
 2968 2008. URL <http://stacks.iop.org/1748-0221/3/i=08/a=S08004>.
- 2969 [46] LHCb Collaoration. The LHCb Detector at the LHC. *JINST*, 3:S08005, 2008. doi: 10.1088/
 2970 1748-0221/3/08/S08005.
- 2971 [47] ALICE Collaboration. The alice experiment at the cern lhc. *Journal of Instrumentation*, 3(08):
 2972 S08002, 2008. URL <http://stacks.iop.org/1748-0221/3/i=08/a=S08002>.
- 2973 [48] Lyndon Evans. The Large Hadron Collider. In Holstein, BR and Haxton, WC and Jawah-
 2974 ery, A, editor, *ANNUAL REVIEW OF NUCLEAR AND PARTICLE SCIENCE, VOL*
 2975 *61*, volume 61 of *Annual Review of Nuclear and Particle Science*, pages 435–466. 2011. doi:
 2976 {10.1146/annurev-nucl-102010-130438}.
- 2977 [49] ATLAS Collaboration. Luminosity Determination in pp Collisions at $\sqrt{s} = 7$ TeV Using the
 2978 ATLAS Detector at the LHC. *Eur. Phys. J.*, C 71:1630, 2011. doi: 10.1140/epjc/s10052-011-1630-5.
- 2979 [50] Mike Lamont for the LHC team. The First Years of LHC Operation for Luminosity Production.
 2980 International Particle Accelerator Conference, 2013. URL <https://accelconf.web.cern.ch/>
 2981 accelconf/IPAC2013/talks/moyab101_talk.pdf.
- 2982 [51] Paul Collier for the LHC team. LHC Machine Status. CERN Resource Review Board, 2015. URL
 2983 <https://cds.cern.ch/record/2063924/files/CERN-RRB-2015-119.PDF>.
- 2984 [52] Track Reconstruction Performance of the ATLAS Inner Detector at $\sqrt{s} = 13$ TeV. Technical
 2985 Report ATL-PHYS-PUB-2015-018, CERN, Geneva, Jul 2015. URL <http://cds.cern.ch/>
 2986 [record/2037683](https://cds.cern.ch/record/2037683).
- 2987 [53] M Capeans, G Darbo, K Einsweiller, M Elsing, T Flick, M Garcia-Sciveres, C Gemme, H Perneg-
 2988 ger, O Rohne, and R Vuillermet. ATLAS Insertable B-Layer Technical Design Report. Techni-
 2989 cal Report CERN-LHCC-2010-013. ATLAS-TDR-19, CERN, Geneva, Sep 2010. URL [https:](https://)
 2990 [//cds.cern.ch/record/1291633](https://cds.cern.ch/record/1291633).

- 2991 [54] ATLAS Collaboration. ATLAS Trigger Operations Public Results. 2015. URL <https://twiki.cern.ch/twiki/bin/view/AtlasPublic/TriggerOperationPublicResults>.
- 2992
- 2993 [55] ATLAS Collaboration. ATLAS Luminosity Public Results, Run 1. 2012. URL <https://twiki.cern.ch/twiki/bin/view/AtlasPublic/LuminosityPublicResults>.
- 2994
- 2995 [56] ATLAS Collaboration. ATLAS Luminosity Public Results, Run 2. 2015. URL <https://twiki.cern.ch/twiki/bin/view/AtlasPublic/LuminosityPublicResultsRun2>.
- 2996
- 2997 [57] T Kawamoto, S Vlachos, L Pontecorvo, J Dubbert, G Mikenberg, P Iengo, C Dallapiccola,
2998 C Amelung, L Levinson, R Richter, and D Lellouch. New Small Wheel Technical Design Re-
port. Technical Report CERN-LHCC-2013-006. ATLAS-TDR-020, CERN, Geneva, Jun 2013.
3000 URL <https://cds.cern.ch/record/1552862>. ATLAS New Small Wheel Technical Design
3001 Report.
- 3002 [58] Y. Giomataris, Ph. Rebours, J.P. Robert, and G. Charpak. Micromegas: a high-granularity
3003 position-sensitive gaseous detector for high particle-flux environments. *Nuclear Instruments
3004 and Methods in Physics Research Section A: Accelerators, Spectrometers, Detectors and As-
3005 sociated Equipment*, 376(1):29 – 35, 1996. ISSN 0168-9002. doi: [http://dx.doi.org/10.1016/0168-9002\(96\)00175-1](http://dx.doi.org/10.1016/0168-9002(96)00175-1). URL <http://www.sciencedirect.com/science/article/pii/0168900296001751>.
- 3006
- 3007
- 3008 [59] T. Alexopoulos, J. Burnens, R. de Oliveira, G. Glonti, O. Pizzirussi, V. Polychronakos, G. Sekhni-
3009 aidze, G. Tsipolitis, and J. Wotschack. A spark-resistant bulk-micromegas chamber for high-
3010 rate applications. *Nuclear Instruments and Methods in Physics Research Section A: Acceler-
3011 ators, Spectrometers, Detectors and Associated Equipment*, 640(1):110 – 118, 2011. ISSN 0168-9002.
3012 doi: <http://dx.doi.org/10.1016/j.nima.2011.03.025>. URL <http://www.sciencedirect.com/science/article/pii/S0168900211005869>.
- 3013
- 3014 [60] Joao Pequenao and Paul Schaffner. An computer generated image representing how ATLAS de-
3015 tects particles. Jan 2013. URL <https://cds.cern.ch/record/1505342>.
- 3016
- 3017 [61] Improved electron reconstruction in ATLAS using the Gaussian Sum Filter-based model for
3018 bremsstrahlung. Technical Report ATLAS-CONF-2012-047, CERN, Geneva, May 2012. URL
<https://cds.cern.ch/record/1449796>.
- 3019
- 3020 [62] Electron efficiency measurements with the ATLAS detector using the 2012 LHC proton-proton
3021 collision data. Technical Report ATLAS-CONF-2014-032, CERN, Geneva, Jun 2014. URL
<https://cds.cern.ch/record/1706245>.
- 3022
- 3023 [63] Georges Aad et al. Electron and photon energy calibration with the ATLAS detector using LHC
Run 1 data. *Eur. Phys. J.*, C74(10):3071, 2014. doi: 10.1140/epjc/s10052-014-3071-4.

- 3024 [64] Georges Aad et al. Measurement of the muon reconstruction performance of the ATLAS detector
 3025 using 2011 and 2012 LHC proton–proton collision data. *Eur. Phys. J.*, C74(11):3130, 2014. doi:
 3026 10.1140/epjc/s10052-014-3130-x.
- 3027 [65] Georges Aad et al. Muon reconstruction performance of the ATLAS detector in proton–proton
 3028 collision data at $\sqrt{s}=13$ TeV. 2016.
- 3029 [66] W Lampl, S Laplace, D Lelas, P Loch, H Ma, S Menke, S Rajagopalan, D Rousseau, S Snyder,
 3030 and G Unal. Calorimeter Clustering Algorithms: Description and Performance. Technical Re-
 3031 port ATL-LARG-PUB-2008-002. ATL-COM-LARG-2008-003, CERN, Geneva, Apr 2008. URL
 3032 <https://cds.cern.ch/record/1099735>.
- 3033 [67] Georges Aad et al. Topological cell clustering in the ATLAS calorimeters and its performance in
 3034 LHC Run 1. 2016.
- 3035 [68] Matteo Cacciari, Gavin P. Salam, and Gregory Soyez. The Anti- $k(t)$ jet clustering algorithm. *JHEP*,
 3036 04:063, 2008. doi: 10.1088/1126-6708/2008/04/063.
- 3037 [69] Monte Carlo Calibration and Combination of In-situ Measurements of Jet Energy Scale, Jet Energy
 3038 Resolution and Jet Mass in ATLAS. Technical Report ATLAS-CONF-2015-037, CERN, Geneva,
 3039 Aug 2015. URL <http://cds.cern.ch/record/2044941>.
- 3040 [70] Georges Aad et al. Performance of b -Jet Identification in the ATLAS Experiment. 2015.
- 3041 [71] Expected performance of the ATLAS b -tagging algorithms in Run-2. Technical Report
 3042 ATL-PHYS-PUB-2015-022, CERN, Geneva, Jul 2015. URL <http://cds.cern.ch/record/2037697>.
- 3043 [72] Georges Aad et al. Performance of Missing Transverse Momentum Reconstruction in Proton-
 3044 Proton Collisions at 7 TeV with ATLAS. *Eur. Phys. J.*, C72:1844, 2012. doi: 10.1140/epjc/
 3045 s10052-012-1844-6.
- 3046 [73] Performance of Missing Transverse Momentum Reconstruction in ATLAS studied in Proton-
 3047 Proton Collisions recorded in 2012 at 8 TeV. Technical Report ATLAS-CONF-2013-082, CERN,
 3048 Geneva, Aug 2013. URL <http://cds.cern.ch/record/1570993>.
- 3049 [74] ATLAS Collaboration. Observation and measurement of Higgs boson decays to WW^* with the
 3050 ATLAS detector. *Phys. Rev. D*, 92(012006), 2015.
- 3051 [75] Aaron James Armbruster. Discovery of a Higgs Boson with the ATLAS detector. 2013. CERN-
 3052 THESIS-2013-047.
- 3053 [76] G. Cowan, K. Cranmer, E. Gross, and O. Vitells. Asymptotic formulae for likelihood-based tests
 3054 of new physics. *Eur. Phys. J.*, C71:1554, 2011. doi: 10.1140/epjc/s10052-011-1554-0.

- 3056 [77] R.K. Ellis, I. Hinchliffe, M. Soldate, and J.J. Van Der Bij. Higgs decay to $\tau+\tau$ –a possible signature
 3057 of intermediate mass higgs bosons at high energy hadron colliders. *Nuclear Physics B*, 297(2):221
 3058 – 243, 1988. ISSN 0550-3213. doi: [http://dx.doi.org/10.1016/0550-3213\(88\)90019-3](http://dx.doi.org/10.1016/0550-3213(88)90019-3). URL <http://www.sciencedirect.com/science/article/pii/0550321388900193>.
- 3060 [78] ATLAS Collaboration. Limits on the production of the Standard Model Higgs Boson in pp
 3061 collisions at $\sqrt{s} = 7$ TeV with the ATLAS detector. *Eur. Phys. J.*, C 71:1728, 2011. doi:
 3062 [10.1140/epjc/s10052-011-1728-9](https://doi.org/10.1140/epjc/s10052-011-1728-9).
- 3063 [79] Leo Breiman, Jerome Friedman, Charles J Stone, and Richard A Olshen. *Classification and regres-*
 3064 *sion trees*. CRC press, 1984.
- 3065 [80] Yoav Freund and Robert E Schapire. A decision-theoretic generalization of on-line learning and an
 3066 application to boosting. *Journal of Computer and System Sciences*, 55(1):119 – 139, 1997. ISSN 0022-
 3067 0000. doi: <http://dx.doi.org/10.1006/jcss.1997.1504>. URL <http://www.sciencedirect.com/science/article/pii/S00220009971504X>.
- 3069 [81] Jerome H. Friedman. Stochastic gradient boosting. *Computational Statistics and Data Analysis*, 38
 3070 (4):367 – 378, 2002. ISSN 0167-9473. doi: [http://dx.doi.org/10.1016/S0167-9473\(01\)00065-2](http://dx.doi.org/10.1016/S0167-9473(01)00065-2). URL <http://www.sciencedirect.com/science/article/pii/S0167947301000652>. Non-
 3072 linear Methods and Data Mining.
- 3073 [82] ATLAS Collaboration. Performance of the ATLAS muon trigger in pp collisions at $\sqrt{s} = 8$ TeV.
 3074 *Eur. Phys. J. C*, (arXiv:1408.3179. CERN-PH-EP-2014-154):75, 19 p, Aug 2014. URL <https://cds.cern.ch/record/1749694>.
- 3076 [83] ATLAS collaboration. Electron trigger performance in 2012 ATLAS data, 2015. ATLAS-COM-
 3077 DAQ-2015-091.
- 3078 [84] Paolo Nason. A new method for combining NLO QCD with shower Monte Carlo algorithms.
 3079 *JHEP*, 11:040, 2004.
- 3080 [85] B. P. Kersevan and E. Richter-Was. The Monte Carlo event generator AcerMC version 2.0 with
 3081 interfaces to PYTHIA 6.2 and HERWIG 6.5. 2004.
- 3082 [86] Nikolas Kauer and Giampiero Passarino. Inadequacy of zero-width approximation for a light Higgs
 3083 boson signal. 2012.
- 3084 [87] T. Gleisberg, Stefan Hoeche, F. Krauss, M. Schonherr, S. Schumann, et al. Event generation with
 3085 SHERPA 1.1. *JHEP*, 0902:007, 2009. doi: <10.1088/1126-6708/2009/02/007>.
- 3086 [88] Michelangelo L. Mangano et al. ALPGEN, a generator for hard multiparton processes in hadronic
 3087 collisions. *JHEP*, 0307:001, 2003. doi: <10.1088/1126-6708/2003/07/001>.

- 3088 [89] Torbjorn Sjostrand, Stephen Mrenna, and Peter Z. Skands. PYTHIA 6.4 Physics and Manual.
 3089 *JHEP*, 0605:026, 2006. doi: [10.1088/1126-6708/2006/05/026](https://doi.org/10.1088/1126-6708/2006/05/026).
- 3090 [90] Torbjorn Sjostrand, Stephen Mrenna, and Peter Z. Skands. A Brief Introduction to PYTHIA 8.1.
 3091 *Comput.Phys.Commun.*, 178:852–867, 2008. doi: [10.1016/j.cpc.2008.01.036](https://doi.org/10.1016/j.cpc.2008.01.036).
- 3092 [91] G. Corcella et al. HERWIG 6: An event generator for hadron emission reactions with interfering
 3093 gluons (including super-symmetric processes). *JHEP*, 01:010, 2001. doi: [10.1088/1126-6708/2001/01/010](https://doi.org/10.1088/1126-6708/2001/01/010).
- 3095 [92] J. M. Butterworth, Jeffrey R. Forshaw, and M. H. Seymour. Multiparton interactions in photo-
 3096 production at HERA. *Z. Phys.*, C 72:637, 1996. doi: [10.1007/s002880050286](https://doi.org/10.1007/s002880050286).
- 3097 [93] Jun Gao, Marco Guzzi, Joey Huston, Hung-Liang Lai, Zhao Li, et al. The CT10 NNLO Global
 3098 Analysis of QCD. *Phys.Rev.*, D89:033009, 2014. doi: [10.1103/PhysRevD.89.033009](https://doi.org/10.1103/PhysRevD.89.033009).
- 3099 [94] P. M. Nadolsky. Implications of CTEQ global analysis for collider observables. *Phys. Rev.*, D 78:
 3100 013004, 2008. doi: [10.1103/PhysRevD.78.013004](https://doi.org/10.1103/PhysRevD.78.013004).
- 3101 [95] A. Sherstnev and R. S. Thorne. Parton distributions for the LHC. *Eur. Phys. J.*, C 55:553, 2009. doi:
 3102 [10.1140/epjc/s10052-008-0610-x](https://doi.org/10.1140/epjc/s10052-008-0610-x).
- 3103 [96] A. Bredenstein, Ansgar Denner, S. Dittmaier, and M. M. Weber. Precise predictions for the Higgs-
 3104 boson decay $H \rightarrow WW/ZZ \rightarrow 4$ leptons. *Phys. Rev.*, D74:013004, 2006.
- 3105 [97] A. Djouadi, J. Kalinowski, and M. Spira. HDECAY: A program for Higgs boson decays in the
 3106 standard model and its supersymmetric extension. *Comput. Phys. Commun.*, 108:56, 1998. doi:
 3107 [10.1016/S0010-4655\(97\)00123-9](https://doi.org/10.1016/S0010-4655(97)00123-9).
- 3108 [98] S. Agostinelli et al. GEANT4, a simulation toolkit. *Nucl. Instrum. Meth.*, A 506:250, 2003. doi:
 3109 [10.1016/S0168-9002\(03\)01368-8](https://doi.org/10.1016/S0168-9002(03)01368-8).
- 3110 [99] Eilam Gross and Ofer Vitells. Transverse mass observables for charged Higgs boson searches at
 3111 hadron colliders. *Phys. Rev.*, D81:055010, 2010. doi: [10.1103/PhysRevD.81.055010](https://doi.org/10.1103/PhysRevD.81.055010).
- 3112 [100] J. R. Andersen et al. Les Houches 2013: Physics at TeV Colliders: Standard Model Working Group
 3113 Report. 2014.
- 3114 [101] I. Stewart and F. Tackmann. Theory uncertainties for Higgs mass and other searches using jet bins.
 3115 *Phys. Rev.*, D 85:034011, 2012. doi: [10.1103/PhysRevD.85.034011](https://doi.org/10.1103/PhysRevD.85.034011).
- 3116 [102] ATLAS Collaboration. Luminosity Determination in pp Collisions at $\sqrt{s} = 7$ TeV Using the
 3117 ATLAS Detector at the LHC. *Eur. Phys. J.*, C 71:1630, 2011. doi: [10.1140/epjc/s10052-011-1630-5](https://doi.org/10.1140/epjc/s10052-011-1630-5).

- 3118 [103] Jet energy scale and its systematic uncertainty in proton-proton collisions at $\sqrt{s} = 7$ tev with atlas
 3119 2011 data. *ATLAS-CONF-2013-004*, 2013.
- 3120 [104] Calibrating the b -tag efficiency and mistag rate in 35 pb^{-1} of data with the atlas detector. *ATLAS-*
 3121 *CONF-2011-089*, 2011.
- 3122 [105] ATLAS Collaboration. Measurement of the b -tag Efficiency in a Sample of Jets Containing Muons
 3123 with 5 fb^{-1} of Data from the ATLAS Detector. *ATLAS-CONF-2012-043*, 2012. URL <http://cdsweb.cern.ch/record/1435197>.
- 3125 [106] ATLAS Collaboration. Calibration of b -tagging using dileptonic top pair events in a combinatorial
 3126 likelihood approach with the ATLAS experiment. (ATLAS-CONF-2014-004), 2014. URL <http://cds.cern.ch/record/1664335>.
- 3128 [107] Georges Aad et al. Measurement of the Higgs boson mass from the $H \rightarrow \gamma\gamma$ and $H \rightarrow ZZ^* \rightarrow$
 3129 4ℓ channels with the ATLAS detector using 25 fb^{-1} of pp collision data. *Phys. Rev.*, D90(5):052004,
 3130 2014. doi: 10.1103/PhysRevD.90.052004.
- 3131 [108] Georges Aad et al. Measurements of the Higgs boson production and decay rates and coupling
 3132 strengths using pp collision data at $\sqrt{s} = 7$ and 8 TeV in the ATLAS experiment. *Eur. Phys. J.*,
 3133 C76(1):6, 2016. doi: 10.1140/epjc/s10052-015-3769-y.
- 3134 [109] W.J. Stirling. $7/8$ and $13/8$ TeV LHC luminosity ratios. 2013. URL http://www.hep.ph.ic.ac.uk/~wstirlin/plots/lhclumi7813_2013_v0.pdf.
- 3136 [110] J Alison. Experimental Studies of hh. Oct 2014. URL <http://cds.cern.ch/record/1952581>.
- 3137 [111] J. Alwall et al. The automated computation of tree-level and next-to-leading order differential cross
 3138 sections, and their matching to parton shower simulations. *JHEP*, 07:079, 2014.
- 3139 [112] Richard D. Ball et al. Parton distributions with LHC data. *Nucl. Phys. B*, 867:244, 2013.
- 3140 [113] ATLAS Collaboration. ATLAS Run 1 Pythia8 tunes. (ATL-PHYS-PUB-2014-021), Nov 2014.
 3141 URL <https://cds.cern.ch/record/1966419>.
- 3142 [114] M. Bahr et al. Herwig++ Physics and Manual. *Eur. Phys. J. C*, 58:639–707, 2008. doi: 10.1140/
 3143 epjc/s10052-008-0798-9.
- 3144 [115] Stefan Gieseke, Christian Rohr, and Andrzej Siódmiok. Colour reconnections in Herwig++. *Eur.*
 3145 *Phys. J. C*, 72:2225, 2012. doi: 10.1140/epjc/s10052-012-2225-5.
- 3146 [116] Simone Alioli, Paolo Nason, Carlo Oleari, and Emanuele Re. A general framework for implement-
 3147 ing NLO calculations in shower Monte Carlo programs: the POWHEG BOX. *JHEP*, 06:043,
 3148 2010.

- 3149 [117] Peter Zeiler Skands. Tuning Monte Carlo Generators: The Perugia Tunes. *Phys. Rev. D*, 82:074018,
 3150 2010. doi: 10.1103/PhysRevD.82.074018.
- 3151 [118] Michal Czakon and Alexander Mitov. Top++: A Program for the Calculation of the Top-Pair
 3152 Cross-Section at Hadron Colliders. 2011.
- 3153 [119] Baojia (Tony) Tong. Private communication.
- 3154 [120] D. Krohn, J. Thaler, and L.-T. Wang. Jet Trimming. *JHEP*, 02:084, 2010. doi: 10.1007/
 3155 JHEP02(2010)084.
- 3156 [121] ATLAS Collaboration. Identification of Boosted, Hadronically Decaying W Bosons and Compar-
 3157 isons with ATLAS Data Taken at $\sqrt{s} = 8$ TeV. 2015.
- 3158 [122] Expected Performance of Boosted Higgs ($\rightarrow b\bar{b}$) Boson Identification with the ATLAS Detector
 3159 at $\sqrt{s} = 13$ TeV. Technical Report ATL-PHYS-PUB-2015-035, CERN, Geneva, Aug 2015. URL
 3160 <https://cds.cern.ch/record/2042155>.
- 3161 [123] Flavor Tagging with Track Jets in Boosted Topologies with the ATLAS Detector. Technical Report
 3162 ATL-PHYS-PUB-2014-013, CERN, Geneva, Aug 2014. URL <https://cds.cern.ch/record/1750681>.
- 3163 [124] Matteo Cacciari and Gavin P. Salam. Pileup subtraction using jet areas. *Phys. Lett. B*, 659:119, 2008.
 3164 doi: 10.1016/j.physletb.2007.09.077.
- 3165 [125] Glen Cowan, Eilam Gross. Discovery significance with statistical uncertainty in the background
 3166 estimate. 2008. URL <http://www.pp.rhul.ac.uk/~cowan/stat/notes/SigCalcNote.pdf>.
- 3167 [126] Search for pair production of Higgs bosons in the $b\bar{b}b\bar{b}$ final state using proton-proton collisions
 3168 at $\sqrt{s} = 13$ TeV with the ATLAS detector. Technical Report ATLAS-CONF-2016-017, CERN,
 3169 Geneva, Mar 2016. URL <https://cds.cern.ch/record/2141006>.
- 3170 [127] Qi Zeng. Private communication.
- 3171 [128] ATLAS Collaboration. Identification of boosted, hadronically-decaying W and Z bosons in
 3172 $\sqrt{s} = 13$ TeV Monte Carlo Simulations for ATLAS. (ATL-PHYS-PUB-2015-033), Aug 2015. URL
 3173 <https://cds.cern.ch/record/2041461>.
- 3174 [129] ATLAS Collaboration. Performance of b -Jet Identification in the ATLAS Experiment. 2015.
- 3175 [130] Alexander L. Read. Presentation of search results: The CL(s) technique. *J. Phys. G*, 28:2693, 2002.
 3176 doi: 10.1088/0954-3899/28/10/313.

- 3179 [131] Measurements of the Higgs boson production and decay rates and constraints on its couplings
3180 from a combined ATLAS and CMS analysis of the LHC pp collision data at $\sqrt{s} = 7$ and 8 TeV.
3181 Technical Report ATLAS-CONF-2015-044, CERN, Geneva, Sep 2015. URL <http://cds.cern.ch/record/2052552>.
3182
- 3183 [132] Projections for measurements of Higgs boson signal strengths and coupling parameters with the
3184 ATLAS detector at a HL-LHC. Technical Report ATL-PHYS-PUB-2014-016, CERN, Geneva,
3185 Oct 2014. URL <http://cds.cern.ch/record/1956710>.
- 3186 [133] ATLAS Phase-II Upgrade Scoping Document. Technical Report CERN-LHCC-2015-020. LHCC-
3187 G-166, CERN, Geneva, Sep 2015. URL <http://cds.cern.ch/record/2055248>.